TESIS DE LA UNIVERSIDAD DE ZARAGOZA

2020 129

Eduardo Arias Egido

GROWTH AND OPTIMIZATION OF THIN FILMS BASED ON IRIDIUM OXIDE FOR SPINTRONICS

Departamento
Física de la Materia Condensada

Director/es
Laguna Marco, Mª Ángeles
Piquer Oliet, Cristina Luisa

ISSN 2254-7606

Prensas de la Universidad
Universidad Zaragoza

ISSN 2254-7606

Universidad Zaragoza
1542

Tesis Doctoral

GROWTH AND OPTIMIZATION OF THIN FILMS BASED ON IRIDIUM OXIDE FOR SPINTRONICS

Autor

Eduardo Arias Egido

Director/es

Laguna Marco, Mª Ángeles
Piquer Oliet, Cristina Luisa

UNIVERSIDAD DE ZARAGOZA

Física de la Materia Condensada

2020

Universidad Zaragoza
1542

Tesis Doctoral

GROWTH AND OPTIMIZATION OF THIN FILMS BASED ON IRIDIUM OXIDE FOR SPINTRONICS

Autor

Eduardo Arias Egido

Directores

Laguna Marco, Mª Ángeles
Piquer Oliet, Cristina

UNIVERSIDAD DE ZARAGOZA

Física de la Materia Condensada

2020

Growth and Optimization of Thin Films Based on Iridium Oxide for Spintronics

Memoria presentada por

Eduardo Arias Egido

Para optar al grado de

DOCTOR

(PROGRAMA DE FÍSICA)

Directores:

Dra. Mª Ángeles Laguna Marco

Dra. Cristina Piquer Oliet

Zaragoza, 2020

Instituto de Ciencia de Materiales de Aragón

Consejo Superior de Investigaciones Científicas

Agradecimientos

Terminar una tesis doctoral marca un momento importante en la vida. Es el resultado de mucho esfuerzo y aprendizaje, gran parte del cual no queda explícitamente recogido en el manuscrito. Es un trabajo que, de una manera u otra, involucra a muchas personas. A todas ellas me gustaría darles las gracias.

En primer lugar quiero agradecer a M. Ángeles todo su apoyo, su paciencia, y sus consejos. Gracias por compartir conmigo tus conocimientos y por haber estado siempre disponible, incluso en momentos difíciles. Quiero también agradecer a Cristina la aportación de su sabiduría en muchos aspectos. Sin vuestra labor esta tesis no habría sido posible.

Gracias a Daniel y José Ángel, mis directores del proyecto de fin de carrera, que me contagiaron su entusiasmo por la ciencia y son grandes "culpables" de que haya llegado hasta aquí.

A la empresa *Fersa Bearings*, que me recibió con los brazos abiertos al terminar la carrera permitiéndome iniciarme en el mundo laboral. De la misma manera me apoyaron cuando, después de darle muchas vueltas, tomé la decisión de embarcarme en la tesis.

A todo el personal del SAI de la universidad, en especial, a Pedro de instrumentación, que nos ayudó con la puesta a punto del *sputtering*; a Ana del servicio de medidas físicas por los quebraderos de cabeza que le han dado nuestras muestras; y a Concha del servicio de difracción por los infinitos difractogramas que le he pedido.

Gracias a todas las colaboraciones. A Jacobo y a todo el GF*Ñ*C de la universidad complutense de Madrid. Tenéis un grupo de trabajo y un ambiente laboral envidiable. Hicisteis que me sintiese como en casa y que se me hicieran cortos los 4 meses de mi estancia allí. A Pilar e Irene, por las muestras de PLD y por estar siempre

dispuestas a ayudar. A Jesús por los cálculos de XANES. A las muchas personas que han colaborado durante los largos experimentos en sincrotrón contribuyendo a que salieran adelante, en especial, gracias a Daniel, Carlos, Yong, Gilberto, Roberto, Sofía, Vera y Leyre.

Gracias también a Fernando por acogerme en los últimos meses de la tesis.

Al personal administrativo del ICMA y del departamento por intentar facilitarnos el papeleo.

A toda la gente que hace posible el *Hercules European School*, especialmente, a los muchos compañeros de fatigas que tuve la suerte de conocer allí. Fue una experiencia muy enriquecedora, tanto a nivel académico como personal.

A Adrián, compañero tanto de despacho como de penas y alegrías de la vida del doctorando, y a Jorge por 4 años de cafés y desconexión momentánea.

Para finalizar, quiero dar las gracias a los seres más importantes de mi vida: mis amigos y mi familia, tanto a los que están como a los que ya se han ido. Sin su apoyo este trabajo hubiese costado un poquito más. En especial gracias a mis padres, porque todo lo que soy es gracias a vosotros, gracias por vuestro esfuerzo diario, por darme la mejor educación y la mejor vida, gracias por TODO.

Por último, y por ello precisamente la más importante, gracias a Paula. Durante el inicio del doctorado tuve la suerte de conocerte. Gracias por haber llegado en el momento oportuno, gracias por una infinidad de motivos, por ya casi 4 años de una relación maravillosa y por hacerme tan feliz cada día. *Now I'm a believer*.

Contents

Chapter 1

Introduction

During the last years the interest in iridium oxide (IrO_2) has been growing due to its great technological importance, with current or potential applications in diverse areas, namely: optical information storage [1], electrochromic devices [2], semiconductor electronics [3], gas sensing [4], pH measurement [5], catalysis [6] or spintronics [7]. Since this dissertation is devoted to explore the potential of IrO_2 in the field of spintronics, first of all, the overall spintronics context is shortly introduced in section 1.1. Then, as some of the main aspects determining the physics behind IrO_2 are common to other iridium oxides (iridates), section 1.2 provides a general overview of their electronic structure and their electrical transport and magnetic properties. This is followed by a survey of IrO_2 in section 1.3, where the state of art of the research published so far is presented. At the end of the chapter, an outlook and an overview of this thesis are given in sections 1.4 and 1.5, respectively.

1.1. Spintronics

In standard electronic devices, equal number of spin–up and spin–down electrons make up the electric current. By introducing an imbalance in the amount of electrons with different spin, one can start to envisage electronic devices that function on the spin of the carriers rather than on its charge. This new concept gives rise to what is known as **spintronics**. Spintronics is a relatively new science which aims at manipulating the intrinsic spin of the electron (and its associated magnetic moment) instead of, or in addition, to its fundamental electronic charge in the electron transport processes [8, 9]. Born in 1988 with the discovery of giant magnetoresistance (GMR),

it has since been largely exploited on the market. It is found, for instance, at the base of each read head of every hard disk.

One of the most modern trends in spintronics focuses on exploiting the **spin–orbit coupling** (SOC) for manipulating the spin in a memory device or for operating with spin currents (generation, injection, transport and detection) [7, 10–13]. This coupling connects the spin of an electron to its orbital momentum, so it provides a pathway for generating and manipulating spins solely by electric fields [14]. One can achieve the generation (or detection) of spin currents through the spin Hall effect (SHE): a novel phenomenon which converts a charge current without any spin polarization into a pure spin current through the SOC (or *vice versa*: inverse spin Hall effect, ISHE) [15–18]. The spin current generated from a charge current (via SHE) can be further used for spin–orbit torque (SOT) magnetization switching [19–21]. This is a promising phenomenon that can be used to manipulate the magnetization of ferromagnets by current injection, thus improving the performance of magnetoresistive random–access memory (RAM) devices. SOT switching allows the read and write paths to be separated, thus enabling the independent co–optimization of readability, access latency and energy consumption [22].

As a result, the quest for new materials with significant spin–orbit interactions in the electronic ground state is an increasingly explored area which represents a promising approach towards the development of new spintronic devices. Since the SOC rapidly increases with the atomic number, *Z*, materials containing heavy elements are natural candidates for this field of inquiry. Among them, iridium oxides (**iridates**) are specially promising. Indeed, the simplest binary oxide of iridium, **IrO_2**, exhibits a remarkably large SHE and a moderately high resistivity, which makes this material the most promising to date for spin–current detection [7]. It is striking that IrO_2 presents not only a good behavior as a spin detector material in the polycrystalline state, but even also a better one in the practically important amorphous state. Strong SOC iridates are currently playing a key role also in the development of modern “antiferromagnetic spintronics”, where magneto–transport is governed by an antiferromagnet instead of a ferromagnet [23–25]. A further example of the potential

of high SOC iridates was recently illustrated by the pioneer work by *D. Yi et al.* [26], who showed that even paramagnetic iridates can be used successfully to manipulate the magnetism of a neighbor 3*d* TMO film.

1.2. Iridates

Oxide materials containing heavy Ir atoms, commonly known as iridates, have proven to display not only a **strong SOC**, but also remarkable properties related to this interaction. They are found to host exotic phases, such as spin–orbit coupled Mott insulators [27, 28], topological insulators [29, 30], superconductors [31, 32], Weyl semimetals [33, 34], spin liquids and spin ices [35, 36]. This has led to an active community of theoreticians and experimentalists investigating the properties of these complex systems. In this sense, during the last decade much work has been carried out in iridates of the Ruddlesden–Popper series: $Sr_{n+1}Ir_nO_{3n+1}$ (with n = 1, 2, ∞); in pyrochlore iridates: $R_2Ir_2O_7$ (where R is a rare earth element or Y); in honeycomb iridates: $(Na/Li)_2IrO_3$; or even in the simplest iridate: IrO_2. The common characteristic of all these Ir^{4+} iridates is the existence of an unusual **delicately balanced ground state** created as a consequence of the different **competing interactions** present in these materials.

1.2.1. Electronic Structure: Basic Concepts

Before discussing in detail the physics behind iridates, it is constructive to start looking at the electronic description of an isolated Ir atom. Iridium (Ir) is a heavy 5*d* transition metal (TM) with electronic configuration: [Xe] $4f^{14}5d^{7}6s^{2}$. Therefore, it has conduction electrons in both, the 6*s* and 5*d* subshell levels, and the remaining electrons can be considered as core–electrons. In the common Ir^{4+} ion, the Ir 6*s* electrons and two of the 5*d* electrons are removed from the Ir atom, reducing the Ir valence electrons down to $5d^5$. According to quantum mechanics, the 5 remaining electrons in the 5*d* subshell would occupy the orbitals formed by linear combinations of $|l, m_l\rangle$ states, with l = 2 (*d* atomic orbitals) and m_l = -2, -1, 0, 1, 2 (from $-l$ to $+l$), where l determines the magnitude of the orbital angular momentum of the electron,

and m_l indicates the orientation of the orbital angular momentum is space. According to Hund's first rule, the energy of a half–filled *d* subshell is minimum when the total spin quantum number, $S = \Sigma_i s_i$ (s_i is the spin of the i^{th} electron), is maximized. In this sense, the **Hund's coupling energy**, $\boldsymbol{J_H}$, is defined basically as the energy saved by aligning a pair of spins. Therefore, due to the Pauli's exclusion principle, the orbitals of the subshell would be occupied singly with electrons of parallel spin before double occupation occurs, thus minimizing the electrostatic repulsion as shown in Fig. 1.1(a). As a result of maximizing the total spin, $S = 5/2$, the sum of the m_l values would be zero, and *L* should be 0.

This theory is valid for the case of a free Ir^{4+} ion where the *d* orbitals are energetically degenerate. However, in 5*d* TMOs the *d* orbitals are no longer degenerate due to electrostatic interactions and orbital overlap with the neighboring ligands, *i.e.*, the **crystalline electric field (CEF)** comes into play. The orbital overlap with the neighboring ligands in a crystal also results in the formation of electronic bands with a characteristic **bandwidth**, ***W***. Moreover, the effect of other additional interactions must also be taken into account, namely: the strong **SOC** associated to the high atomic number of Ir, and the reduced **on–site Coulomb repulsion**, ***U***, as a consequence of the relatively extended nature of the 5*d* orbitals. As a result, an unusual energy hierarchy emerges, where Hund's coupling (J_H), crystal electric field splitting (Δ_{CEF}), bandwidth (W), spin–orbit coupling energy (E_{SOC}), and on–site Coulomb repulsions (U) become comparable.

Crystal Electric Field (CEF)

The crystalline field theory is a model that describes the breaking of degeneracies of electron orbital states (usually *d* or *f* orbitals) due to the static electric field produced by a surrounding charge distribution (anion neighbors).

As illustrated in Fig. 1.1(b), in the **IrO_6 octahedra** environment, typical of most Ir^{4+} oxides [37], the electron cloud of the $d_{x^2-y^2}$ and d_{z^2} orbitals is directed towards the negatively charged oxygen ions surrounding iridium, while the d_{xy}, d_{yz} and

d_{xz} orbitals have their lobes directed along the diagonals in between the oxygens. Therefore, due to electrostatic repulsion, the $d_{x^2-y^2}$ and d_{z^2} orbitals are higher in energy than the d_{xy}, d_{yz} and d_{xz} ones [38]. These two sets of orbitals are commonly referred to by their group theoretical names: e_g for $d_{x^2-y^2}$ and d_{z^2} orbitals; and t_{2g} for d_{xy}, d_{yz} and d_{xz} orbitals.

As the degeneracy of the *d* orbitals has been removed, the electrons start filling the low energy orbitals, *i.e.*, the t_{2g} orbitals. The filling up depends on the competition between the crystal–field splitting (Δ_{CEF}) and the Hund's coupling (J_H). This means that, if the crystal–field splitting is greater than the energy saved by aligning a pair of spins ($\Delta_{CEF} > J_H$), the electrons will partially fill the t_{2g} levels before filling the e_g orbitals, in accordance with Pauli's exclusion principle [39–41]. Hence, the 5 electrons will be in the lower t_{2g} state (known as "low–spin state", $S = 1/2$), as shown in Fig. 1.1(b).

The occupation of the valence electrons has now been reduced to only one hole in the Ir 5*d* t_{2g} level. However, the strong interaction between the spin and orbital momenta of the electrons found in 5*d* elements has yet to be accounted for. Such interaction has profound implications on the states of the valence electrons.

Spin–Orbit Coupling (SOC)

The spin–orbit coupling (SOC) is a relativistic interaction between the spin of the electron and its orbital motion around the nucleus. Thus, the energy associated to this interaction is proportional to the total spin ($\boldsymbol{S}$) and orbital ($\boldsymbol{L}$) momentum vectors, $E_{\mathrm{SOC}} = \lambda \boldsymbol{S} \cdot \boldsymbol{L}$, where λ states for the spin–orbit splitting parameter. As $\lambda \propto Z^4$, the SOC is usually treated as a small perturbation in 3*d* TMs ($\lambda \approx 0.01$ eV) [42]. In contrast, Ir has $Z = 77$ and $\lambda \approx 0.5$ eV [43–45], so that the SOC does play a major role.

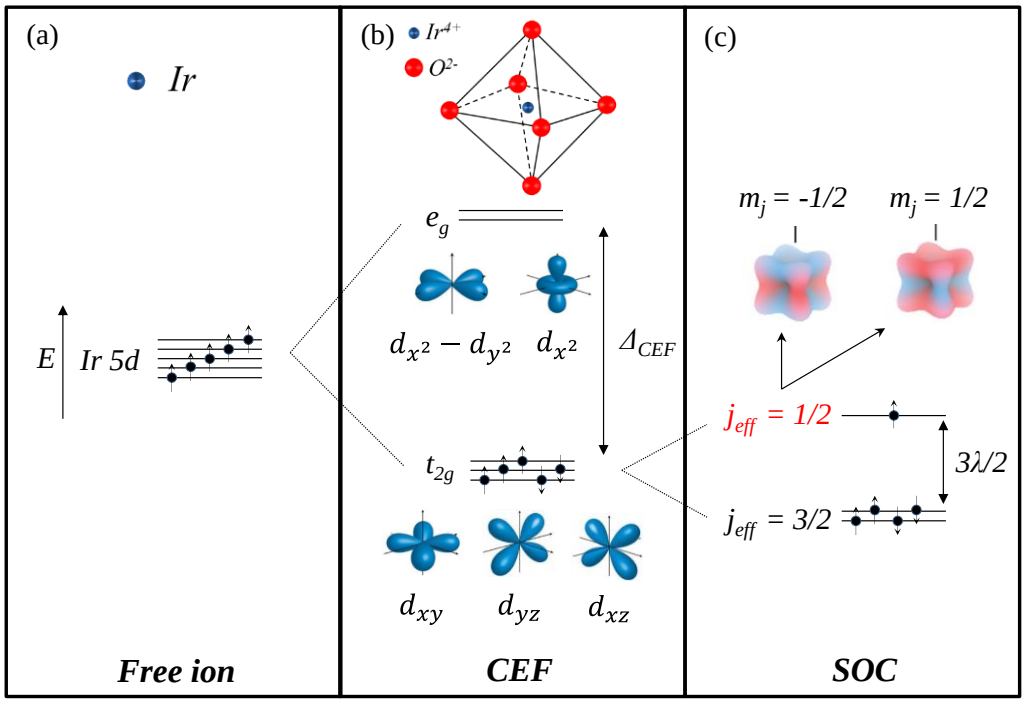

Figure 1.1 (a) Lowest energy arrangement of the valence electrons among the 5*d* orbitals for an Ir^{4+} ion according to Hund's rules. (b) Illustration of the octahedral geometry of Ir^{4+}. The five degenerate 5*d* orbitals split into three three–fold (t_{2g}) and two–fold multiplets (e_g) by the octahedral crystal field of the O^{2-} anions. The magnitude of the splitting is called the crystal–field splitting, Δ_{CEF}. (c) In the presence of SOC, the t_{2g} orbitals split into two levels: a doubly degenerate $j_{eff} = 1/2$ and a quadruply degenerate $j_{eff} = 3/2$, where the spin and orbital degrees of freedom are entangled in a complex manner. The atomic $j_{eff} = 1/2$ orbitals are illustrated.

The orbital angular momentum is generated when an electron in an orbital of a degenerate set of orbitals is moved to another orbital in the set. In complexes of low symmetry certain rotations are not possible. In such a case, the orbital angular momentum is said to be "quenched", and L is smaller than it might be expected (partial quenching), or zero (complete quenching). In the octahedral environment of iridates mentioned above, the large crystal field between e_g and t_{2g} quenches the orbital momentum $l = 2$ down to $l_{eff} = 1$ [41, 46]. As a consequence, there is only one unpaired electron in the t_{2g} levels, with $S = 1/2$ and with an effective angular momentum $l_{eff} = 1$. The strong SOC regime makes that the spin and orbital degrees of freedom cannot be treated separately. This results in new states described by the

effective total angular momentum, j_{eff}, given by (l_{eff} + S) or (l_{eff} - S). Thus, these energy states are split into two levels: a quadruply degenerate j_{eff} = 3/2 (m_j = ± 3/2 and ± 1/2), and a doubly degenerate j_{eff} = 1/2 (m_j = ± 1/2), with 3λ/2 higher in energy than the first [38], as illustrated in Fig. 1.1(c). The j_{eff} = 3/2 state is completely filled, and the j_{eff} = 1/2 state is half occupied. Therefore, by including the strong SOC the valence electron states are now described by $|j_{eff}, m_j\rangle$, in which both **the t_{2g} orbitals and the spin of the electron are strongly entangled in a complex manner**.

On–site Coulomb Interaction (U)

A single hole in the j_{eff} = 1/2 state should naively lead to a metallic behavior. However, several 5d^5 iridates are found to be insulating [27, 28, 47–51]. In TMOs an insulating gap can be induced in the valence band structure by including electron correlations described by the on–site Coulomb interaction, U. In general, a gap opens if the bandwidth, W, of the valence electrons is smaller than U (systems where this happens are known as Mott insulators [52]). In TMOs, W is determined by the hybridization of the d orbitals of the TM atom with the p orbitals of the adjacent oxygens surrounding it. In principle, due to the large spatial extension of 5d orbitals, the bands of the TMs are relatively broad, and hence, a metallic state is expected. In fact, without inclusion of the SOC, the width of the Ir t_{2g} bands is so large that band–structure calculations with a reasonable U fail to open an insulating gap (Fig. 1.2(a)). However, upon inclusion of the SOC, the t_{2g} manifold is split into lower j_{eff} = 3/2 and much narrower half–filled upper j_{eff} = 1/2 bands, as shown in Fig. 1.2(b). Now, the application of a small U can split the j_{eff} = 1/2 bands into an "upper–Hubbard band" (UHB) and a "lower–Hubbard band" (LHB). For the 5d^5 state depicted in Fig. 1.2(c), the UHB is totally empty and the LHB is totally filled and separated by U. This gives rise to a new Mott insulating state mediated by SOC, and so this material is commonly referred to as j_{eff} = 1/2 spin–orbit Mott insulator. As a consequence, the system has now a single electron localized to each site, so that each site has a magnetic moment. This is why insulator iridates often present (anti)ferromagnetism, while metallic iridates are paramagnetic.

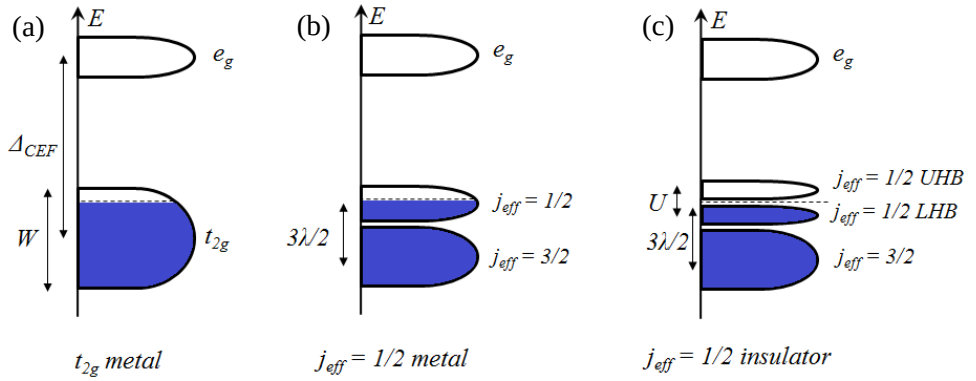

Figure 1.2 Schematic band picture of insulating $5d^5$ iridates. (a) If SOC is not considered, the width (W) of the t_{2g} bands is much larger than the on–site Coulomb repulsion (U) and hence, the system is metallic. (b) With inclusion of SOC, the t_{2g} manifold is split into j_{eff} = 1/2 and j_{eff} = 3/2 subbands, whose W are significantly narrower. (c) Even a relatively small U may then induce a finite Mott–like gap in the upper j_{eff} = 1/2 states.

Distortions

The model employed so far is based on large and highly symmetric octahedral crystal field splitting of the 5*d* orbitals. However, oxygen octahedra in TMOs are not rigid. Various factors such as the crystal structure or external uniaxial pressure can distort the octahedra. The most common distortions of IrO_6 octahedra are tetragonal and trigonal, illustrated in Fig. 1.3. In the simplest picture, tetragonal elongation splits the degenerate t_{2g} orbitals into an upper d_{xy} singlet and lower $d_{xz/yz}$ doublet. This comes about because the $d_{xz/yz}$ orbitals have a larger *z*–component than d_{xy} and hence, they will be lowered in energy as the apical oxygens move further away from the central atom. The opposite occurs under tetragonal compression. Under a trigonal distortion the degenerate t_{2g} orbitals split into a singlet, a_{1g} state, and a doublet, e'_g state.

Since non–cubic CEF competes with SOC, their combined effect on the energy splitting of the t_{2g} levels is non–trivial. A small non–cubic CEF contribution would give rise to split j_{eff} = 3/2 levels by Δ, as shown in Fig. 1.3. A strong non–cubic CEF contribution may result in a negligible effect of the SOC. Finally, it should be noted that, usually, no mixing between t_{2g} and e_g happens in trigonal distortion, though it may happen in case of tetragonal distortion [53, 54].

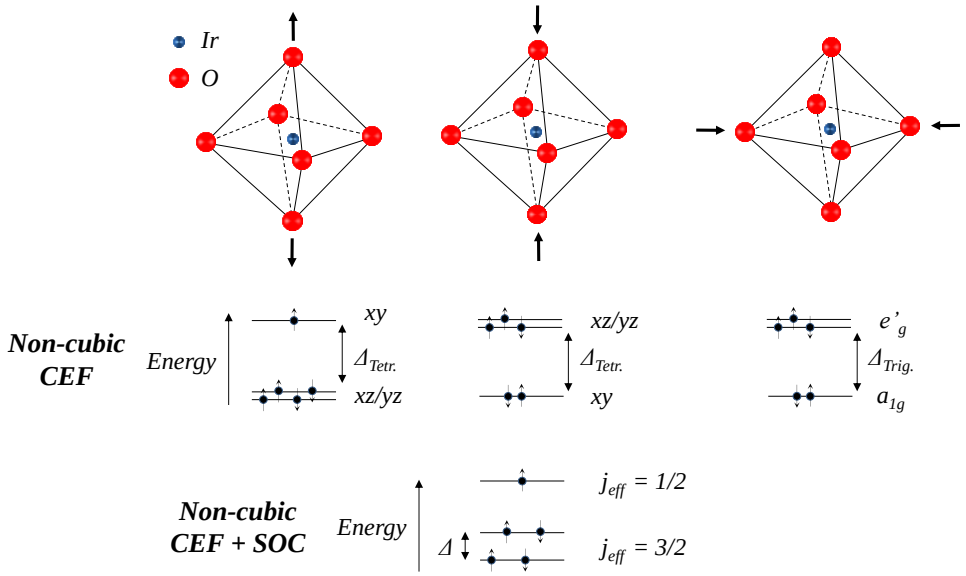

Figure 1.3 Schematic evolution of the Ir 5*d* t_{2g} levels in the presence of an octahedral oxygen cage with tetragonal distortion (elongation and compression) and trigonal distortion (compression). In the bottom image the SOC is also included.

1.2.2. Electrical Transport and Magnetic Properties

An interesting consequence of the complex and delicately balanced ground state described from the interactions explained above is the wide variety of electrical and magnetic behaviors observed in Ir^{4+} iridates. They range from insulators with an electrical resistivity at room temperature $\rho_{RT} > 10^7$ μΩ cm [55], to Fermi metals with $\rho_{RT} < 10^2$ μΩ cm [56]; and from canted antiferromagnets with a magnetic moment up to ~0.4 μ_B/at. Ir [57], to paramagnets [58]. As a result, they are potential candidates to host tunable metal–insulator and nonmagnetic–magnetic transitions.

Some of the most important mechanisms that underlay metal–insulator transitions (MITs) in correlated systems are interaction–driven (or correlation–driven) Mott localization, magnetic–order–driven Slater localization, and disorder–driven Anderson localization. A short description of these mechanisms is given below.

Mott localization emerges when $U > W$ in partially–filled band systems, so that, if the kinetic energy of the electrons is not high enough to overcome U, an energy

gap (E_g) is created, as already shown in Fig. 1.2. The size of such gap is $E_g \approx U - W$. Thus, as for large distances between atoms the orbital overlap is small, then W is small, which usually leads to $U >> W$ (insulator). Contrary, for $U << W$ a single half–filled band is predicted (metal). Finally, if $U \approx W$, a MIT is expected [52].

Many insulating systems, especially TMOs, often exhibit antiferromagnetic ground states. The magnetically driven localization was first proposed by *J. C. Slater* [59], who suggested that antiferromagnetism alone can trigger a MIT. The establishment of a long–range antiferromagnetic order induces an opposite potential on each nearest electron site, which doubles the magnetic unit cell. This fact results in a splitting of the occupied bands and, in case of half–filling, a gap for charge excitations is created. In consequence, this MIT is closely connected with disappearance of the magnetic ordering at Néel temperature (T_N). Therefore, the main difference between a Mott insulator and a Slater insulator is that for a Mott insulator the system remains insulating even above T_N, whereas a Slater insulator should be metallic above T_N.

Disorder (defects, impurities, etc.) is unavoidable in real physical systems, being an important factor in determining the transport properties. In ordinary metals, a random potential due to disorder (D) is much smaller than the kinetic energy of the electrons, and thus, it can be treated as a small perturbation. However, in low carrier density systems (bad metals) the disorder potential could become comparable or even exceed the Fermi energy, localizing the electrons and yielding the system to an Anderson–type MIT [60]. The localized and delocalized states do not coexist at the same energy, but they are separated by a barrier called the mobility edge. At a finite temperature, the carriers can hop from one localized state to another due quantum tunneling. This phenomenon is known as variable range hopping (VRH).

Analogously, the magnetic behavior of Ir^{4+} iridates has been found to be strongly dependent on structural details as well as on the delicate balance among the different interactions present in the system [57, 58, 61–63]. Thus, while most of these iridates present antiferromagnetic order, minor differences in the electronic structure,

such as slightly wider bands, seem to be enough to promote paramagnetism. Moreover, it is still under strong debate whether the insulating state is driven by magnetic order (Slater insulators) or not [63–67]. The nature of the atomic magnetic moment itself may also be diverse: on the one hand, the interplay between SOC, distortions and correlations can lead to two different scenarios: a $S = 1/2$ or a $j_{eff} = 1/2$ magnetic moment. On the other hand, the presence of 3*d* magnetic atoms (Fe, Cr, etc.) may give rise to an induced magnetic moment in Ir as a result of 3*d*–Ir polarization.

Some of the key parameters mentioned above, such as bandwidth (*W*), Coulomb repulsions (*U*), disorder (*D*) or strength of the SOC, can be tuned to some extent by dimensionality effects (*i.e.*, by reducing the film thickness), lattice strain (by using different lattice mismatched substrates), doping, or by physical pressure, among others. This way, the overall change in the effective correlations (*U*/*W*) or the increase in the effective disorder (*D*/*W*) may induce metal–insulator and/or nonmagnetic–magnetic transitions in the system. A short review about the electrical transport and magnetic properties of some of the most common Ir^{4+} iridates is given below.

The compounds of the **Ruddlesden–Popper series** are a family of perovskite materials with stoichiometry $Sr_{n+1}Ir_nO_{3n+1}$ ($n = 1, 2, \infty$), being *n* the number of Ir–O layers separated by Sr–O layers. Sr_2IrO_4 ($n = 1$) is notable for being the first proposed experimental realization of a $j_{eff} = 1/2$ spin–orbit Mott insulator [27, 28, 47, 51, 68]. This compound develops canted antiferromagnetic order below $T_N \approx 240$ K [28]. As *n* increases, the electronic structure progresses towards a metallic ground state, as evidenced by the charge gap softening in $Sr_3Ir_2O_7$ ($n = 2$). However, even the latter compound remains an as insulating weak ferromagnet. A further increase in the number of Ir–O layers eventually yields the $n = \infty$ member of the series, $SrIrO_3$, which shows a paramagnetic metallic ground state [61]. Therefore, it can be postulated that an insulator–metal transition occurs at some point beyond $n > 2$. Qualitatively, this transition was proposed to occur due to a bandwidth broadening caused by the increase of the number of Ir nearest neighbors (by adding Ir–O layers, *n*), until *W* reaches *U* [50]. However, the microscopic picture is likely more complex and even the nature of the insulating states in Sr_2IrO_4 and $Sr_3Ir_2O_7$ is under strong debate. Many

studies argue that itineracy effects are significant in these materials and the above picture of a j_{eff} = 1/2 spin–orbit Mott insulator is insufficient, as the insulating state exhibits both, Slater and Mott characteristics [66, 69–71].

In the last years, much work has been focused on $SrIrO_3$ and Sr_2IrO_4 **thin films**, as they allow tuning the *U*/*W* and *D*/*W* ratio by varying the film thickness or the lattice strain [65, 67, 72–74]. In the two–dimensional limit, the coordination of constituent ions at the interfaces is reduced, typically yielding a decrease in *W*. Thus, at a critical thickness depending on the relative magnitude of *W* and *U*, a MIT can take place [75]. This approach was applied by *D. J. Groenendijk et al.* [65], who found a thermal MIT in $SrIrO_3$ deposited on $SrTiO_3$(100) at a film thickness of 3–4 unit cells. Similarly, *A. Biswas et al.* [67] observed two different thermal MITs in $SrIrO_3$: in the first one, reducing the thickness (dimensionality) of $SrIrO_3$ films deposited on $GdScO_3$ from 35 nm down to 3 nm led to an Anderson (disorder) type MIT, where interactions did not seem to play a significant role. In a second approach, they grew 35 nm–thick $SrIrO_3$ films with an increasing compressive strain via lattice mismatched substrates. They also observed a MIT here, though seemingly of "Mott–Anderson" type, where both correlation and disorder play a significant role. Regarding the insulating Sr_2IrO_4, *J. S. Lee et al.* [72] proved that the Mott gap collapses (insulator–metal transition) upon Rh or Ru doping due to a reduction of the SOC and increasing *U*/*W* ratio. On the other hand, *C. R. Serrao et al.* [73] observed that by increasing the in–plane tensile strain up to ~0.3%, a charge gap reduction from 200 meV down to 50 meV for the thinnest and most epitaxy–distorted film occurred.

Similarly, the family of **pyrochlore iridates**, $A_2Ir_2O_7$, where *A* is a rare earth, also gained interest with the discovery of a MIT accompanied by magnetic ordering as a function of the rare earth ion [76]. It was shown that the conductivity increases with increasing the *A* atomic radius. Early calculations of the electronic structure and X–ray diffraction measurements found that the width of the conduction band and resultant MIT in these iridates are greatly affected by small changes in the Ir–O–Ir bond angles and Ir–O bond lengths [77, 78]. Moreover, magnetization measurements revealed that

all insulating samples undergo a magnetic transition to a presumed antiferromagnetic or spin–glass state in the 130–150 K range [79].

1.3. IrO_2

1.3.1. Structure

IrO_2 crystallizes in the rutile–type structure ($P4_2/mnm$ space group) with two units formula per unit cell, whose dimensions are $a = b = 4.50$ Å and $c = 3.16$ Å, as illustrated in Fig. 1.4. Each Ir is bonded to six O atoms in a slightly distorted octahedral environment, which leads to four long planar (1.99 Å) and two short apical (1.96 Å) Ir–O bonds with Ir–O–Ir angles of ~105 and ~127° in the *xy* plane. As can be seen in Fig. 1.4, the IrO_6 octahedra in the three–dimensional network share corners along *x* and *z*, while they share edges along *y*. This is in contrast to perovskite iridates, which exhibit only corner–sharing octahedra. These details determine that *W* in IrO_2 is greater than in $SrIrO_3$ [80] and hence, its more metallic character. Besides, the fact that the IrO_6 octahedra are sharing edges in the IrO_2 structure makes this system more rigid than perovskite iridates against distortions, such as tilts in the Ir–O–Ir angles or variations in the Ir–O bond lengths.

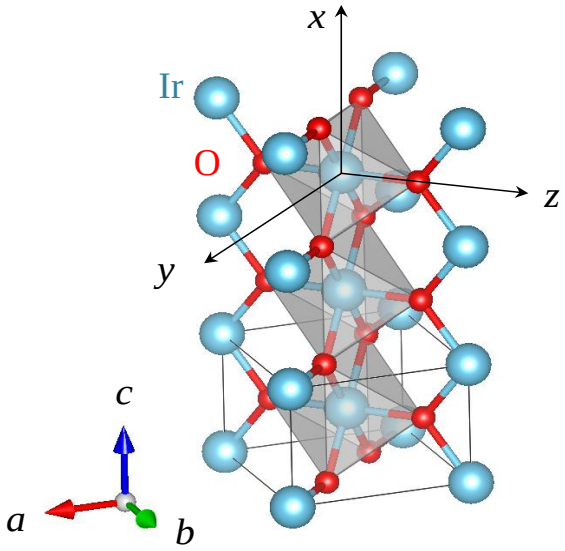

Figure 1.4 Ball and stick representation of the crystal structure of rutile IrO_2.

1.3.2. Electronic Band Structure, Electrical Transport and Magnetic Properties

The role of SOC in the IrO_2 electronic structure is still under extensive debate. Some studies claim that the intriguing $j_{eff} = 1/2$ state (Fig. 1.1) is applicable even in metallic IrO_2 [37, 56, 81–83]. However, due to the itinerant nature and relatively large values of W in metallic compounds, other groups argue that the $j_{eff} = 1/2$ state is not relevant in IrO_2 [84–86]. In other words, even if strong SOC exist in IrO_2, it does not seem to be responsible for any of the major features of the band structure. According to these works, the $j_{eff} = 1/2$ state could be attained by reducing W.

Regardless of whether the electronic structure is well described by the $j_{eff} = 1/2$ state or not, a wide consensus is reached regarding the **metallic and non–magnetic nature of bulk IrO_2**. However, theoretical studies suggest that this ground state can indeed be tuned through structural modifications [82–84]. In this sense, *S. K. Panda et al*. [82] came up with an interesting phase diagram, where the non–magnetic metallic IrO_2 becomes an antiferromagnetic metal and eventually an antiferromagnetic Slater insulator upon increasing U. On the other hand, *J. M. Kahk et al.* [84] predicted that the metallicity of IrO_2 should be quite robust with respect to external influences, such as doping or non–stoichiometry. In contrast, effects that change the relative nature of the t_{2g} orbitals, as epitaxial strain along the c axis, could lead to a marked change in the observed behavior. With a similar view, *X. Ming et al.* [83] focused on the evolution of the electronic structure as a function of the IrO_2 layer thickness, m, in $(IrO_2)_m(TiO_2)_{10}$ heterostructures. They predicted, by density functional theory simulations, that the heterostructures do exhibit a thickness–controlled MIT, evolving from metal ($m = 6$) to bad metal ($m = 4$), and finally, to insulator ($m = 2$). According to their work, the subtle interplay between U and SOC leads to an almost pure $j_{eff} = 1/2$ spin–orbit insulating state at the level of atomically thin IrO_2 monolayer.

However, these predicted emerging insulating states are still waiting for experimental confirmation. The work carried out by *J. K. Kawasaki et al.* [87], which is, to the best of our knowledge, the only experimental work published on this subject,

did not succeeded in finding the insulating phase suggested in Ref. [83]. They grew (110)–oriented $(IrO_2)_n/(TiO_2)_2$ superlattices with $n \geq 3$. Despite the resistivity of the films clearly increased upon decreasing the number of IrO_2 layers, it was not enough to observe a clear MIT. Nevertheless, they predicted the electronic properties of the superlattices to be highly dependent on orientation.

Finally, regarding the electrical conductivity of IrO_2, *M. Uchida et al.* [56] proved that the Hall voltage on IrO_2 epitaxial films can be reversed and also even turned to zero. This means that the dominant charge carrier type can be controlled in IrO_2 by the direction of the applied magnetic field. This is an additional interesting feature that should also be taken into account when envisaging possible spintronic applications

1.4. Outlook of This Dissertation

The above presented scenario suggests the enormous potential of IrO_2 for spintronic applications. However, the study of this compound is on a relatively early stage and it is still necessary to **find experimental evidence of the predicted tunable electrical transport and magnetic properties** [82, 83]. Lot of work is yet necessary to clarify the mechanisms determining the electrical and magnetic properties of IrO_2, as well as the possibility of tuning these properties through diverse routes such as dimensionality (ultrathin films, ~2D), structural modifications affecting bond lengths and angles, doping or incorporation of exchange interactions. From the applied point of view, the control of its electronic state may be one key step to find optimized spintronic devices. Thus, for instance, increasing the electrical resistivity of IrO_2 without compromising its high SOC is a challenge that would make this compound even more attractive as spin current detector material.

Another promising approach in the development of spintronics devices is based on the growth of iridate/3*d*–TMO structures. One can envisage the fabrication of controlled 5*d*–TMO/3*d*–TMO structures where the SOC of the 5*d* compound (IrO_2) is combined with the high magnetic moment and Curie temperature (T_C) of the 3*d*

compound to obtain a system with a tunable magnetic response and to modify the magnetic properties of IrO_2. It should be noted that, compared to rare earths elements, the broad spatial extension of the 5*d* orbitals may prove to be more efficient in inducing hardness on the neighboring 3*d*–TM. It is still necessary, however, to find these optimized iridate/3*d*–TMO structures aimed at creating spin–polarized currents and/or manipulating nanomagnets, as well as a better understanding of the widely unknown 5*d*/3*d* interactions.

Therefore, in order to gain a deeper knowledge about these issues, a systematic study on IrO_2–based thin films was carried out. Three different approaches were followed aimed at modifying the electrical transport and magnetic properties of this compound. In particular, the main goal of this thesis is to **synthesize and characterize IrO_2–based thin films that are prospective to present insulating behavior and/or magnetic ordering**. The 1st approach was focused on obtaining pure IrO_2 thin films with differentiated microstructure, crystallography and thickness by using different fabrication methods and growing conditions. In the 2nd approach, a negative chemical pressure via substitutional doping was applied. This was expected to reduce the electronic bandwidth of IrO_2, as it reduces the direct overlap between the Ir 5*d* orbitals. To this end, we synthesized and characterized $Ir_{1-x}Sn_xO_2$ dilutions, being *x* the Sn concentration. The binary oxide SnO_2 presents an insulating behavior, which was expected to increase the resistivity of the samples without considerably affecting the SOC of Ir. Finally, the 3rd approach consisted on studying the effect of adding a magnetic 3*d* element. The combination of the high magnetic moment and high Curie temperature (T_c) of a 3*d* atom with the high anisotropy of Ir was expected to lead to electronic and magnetic changes, such as high coercive fields or 3*d*–induced polarization of the Ir atoms. In this sense, two different systems were studied: $Ir_{1-x}Cr_xO_2$ monolayers (with *x* the Cr concentration) and Ir–/Fe–based heterostructures. With such 3*d*–5*d* metals combination we expected to obtain materials which are not only potentially interesting for spintronics, but also with the large magnetization and large magnetic hardness required for permanent magnets.

1.5. Dissertation Overview

A brief introduction to this dissertation has been given in Chapter 1.

Chapter 2 comprises the technical information about the experimental procedures, including sample preparation methods and characterization techniques implicated in the development of this thesis.

Conventional reactive magnetron sputtering, high oxygen pressure sputtering and pulsed laser deposition techniques were used to grow all the IrO_2 films under study in this thesis. In Chapter 3, it is shown how the different parameters involved in the fabrication process affect the microstructure of such samples.

Chapter 4 presents the electronic, electrical and magnetic characterization of IrO_2 thin films as a function of the microstructure, thickness and strain.

Chapter 5 is devoted to the synthesis and characterization of Sn–doped IrO_2 thin films. In order to better understand and tailor the performance of IrO_2 as spin current detector material, special attention is paid on the electrical response and strength of the SOC as a function of the Sn content.

Similarly, Chapter 6 shows the synthesis and characterization of Cr–doped IrO_2 thin films, where the interest here lies in the magnetic properties resulting from the 3*d*/5*d* interaction through substitution.

In Chapter 7 the synthesis and characterization of Ir– and Fe–based multilayers is reported. In contrast to the previous chapter, the 3*d*/5*d* interaction takes place through the interface. Composition, structure, and magnetic behavior are carefully analyzed for each sample series.

Lastly, the general conclusions and some general comments from the current work will be drawn.

Chapter 2

Experimental Techniques and Procedures

This chapter is addressed to briefly describe the main experimental techniques and procedures employed in the synthesis and characterization of the samples studied in this thesis. The majority of them were grown by means of the sputtering technique. Thus, in section 2.1 the sputtering deposition process is presented along with a description of the equipment employed. The diverse set–up operations and implementations carried out during this dissertation are also shown. Other few samples were grown by pulsed laser deposition; thus, such technique is shortly introduced in section 2.2. Finally, in section 2.3 the annealing treatment performed in the samples (when necessary) is described.

After introducing the fabrication procedures, the different characterization techniques employed are presented, grouped into: structural and morphological (section 2.4), compositional (section 2.5), magnetic (section 2.6) and electrical (section 2.7). Basic concepts about these techniques are given in Appendix B.

2.1. Sputtering Deposition

2.1.1. Basic Principles and Operation

The sputtering technique is a physical vapor deposition (PVD) process in which a bulk starting material, called **target**, is eroded by an energetic–particle

bombardment. The ejected atoms from such target are subsequently deposited on a **substrate**. The main process, schematized in Fig. 2.1, has the following steps:

1) The target is placed parallel to the substrate to be coated in a vacuum chamber filled with a particular process gas (Ar in Fig. 2.1) and set on a negative potential (cathode).
2) This potential accelerates the few electrons (*e*) present in the chamber towards the grounded wall.
3) While traversing the chamber, the electrons collide with the gas atoms (Ar) and generate, if the electric field is strong enough, electron–ion pairs (e + Ar^+).
4) These ions (Ar^+) are then accelerated towards the target and create, upon impact with its surface, an atomic collision cascade ejecting those atoms which acquire enough energy to overcome the surface binding energy.
5) Finally, the ejected atoms are condensed onto the surrounding surfaces. Here, the deposition rate (DR) is defined as the thickness of the layer deposited on the substrate during 1 minute of sputtering (in nm/min).

In order to prevent the gas from reacting with the target it is necessary to use noble gases. Since the pulverizing ions must be relatively heavy, **Ar** is the most employed gas because of its atomic weight/price rate [88].

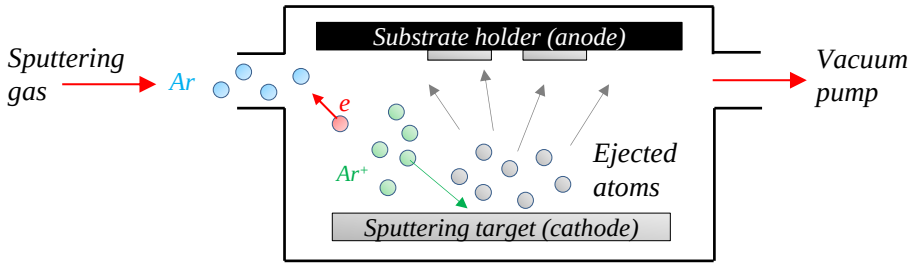

Figure 2.1 Basic sputtering process.

In order to increase the ionization rate of the Ar gas and, in turn, the DR, a magnetic field is commonly used to confine the electrons near the target surface. This method, widely known as **magnetron sputtering**, can not only increase the DR, but

also sustain the discharge at a lower pressure compared to that required if no magnetic field is present.

By using reactive working gases the deposition of some compounds (such as oxides, for instance) can be carried out, what is known as **reactive sputtering**. This is, however, a more complex process usually exhibiting a non–linear behavior with respect to the main process parameters [89–91]. Provided a metallic target, as the reactive gas flow is increased, the topmost layer of the material may change from metallic to compound, commonly known as "target poisoning". This fact often implies a change from conducting into non–conducting. Accordingly, the former sputtering condition is commonly referred to as "metal mode", whilst the latter is known as "compound mode", which is generally accompanied by a dramatic decay in the DR [89–91]. Note that, for Ir targets (most employed targets in this thesis), this should not represent a problem, since the resistivity of the oxide phase, IrO_2, is only ~10 times greater than that of the metallic phase, preserving the conducting behavior.

Depending on how the power is supplied, the sputtering technique is usually classified as **RF** (alternating current) or **DC** (direct current) sputtering. The use of a DC source requires electrically conductive electrodes. If one, or both electrodes are non–conductive (or if the target is "poisoned"), the insulator will charge up and, either the discharge will be terminated, or the charge accumulation will be dissipated in the form of an arc. In the latter case, droplets of material are produced and could be further deposited onto the substrate surface, leading to undesirable film properties and performance. The use of an alternating current source or **pulsed DC** bias can alleviate this problem, since positive charges accumulated during one half–cycle can be neutralized by electron bombardment during the next cycle. In RF deposition, the power is applied to the target material using an impedance matching box to transfer the maximum power. In this configuration, the target and the substrate holder act as the electrodes with the electrons oscillating between both. Because of the power being split between the two electrodes, the effective power at the cathode is typically only 50% of the power delivered in DC sputtering. Thus, usually considerably lower DRs are found in RF than in an equivalent DC process [92–96]. Magnetron sputtering using

pulsed DC power delivery is also used in processes which are prone to arcing. The primary advantage of pulsed DC sputtering is that at optimum pulsing frequencies and duty cycles, higher DRs can be achieved compared to RF sputtering [97].

2.1.2. Experimental Equipment

Most of the samples studied during this dissertation were synthesized in a stainless steel sputtering chamber designed by our group, fabricated by *Cryovac*, and mounted at *Instituto de Ciencia de Materiales de Aragón* (ICMA) right before the beginning of this Ph.D. work. During the thesis, several implementations were carried out to improve the performance of the equipment (see Appendix A). The complete system is shown in Fig. 2.2, where the main components, described below, are exposed: the main (1) and the load–lock (2) chambers, the vacuum system (3), the different power sources (4), the gas circuit (5), the substrate–temperature controller (6) and the monitored system (7) can be seen in Fig. 2.2(a). Fig. 2.2(b) shows the inside of the main chamber. When operating at room temperature, the substrates (typically Si(100) properly cut from a wafer) are attached with rubber cement on the sample holder. Such sample holder is introduced into the main chamber through a transfer bar and inserted into a rotatory arm (8) placed at a distance of 100 mm above the surface of the magnetrons (9). For high–temperature growths, the substrates are directly attached with silver paste to the heater (10), positioned 75 mm above the surface of the magnetrons. A stainless steel shutter (11) separates one magnetron from the other when co–sputtering deposition is not used. As an example, the Ar + O_2 plasma generated during deposition is shown in the inset of Fig. 2.2(b).

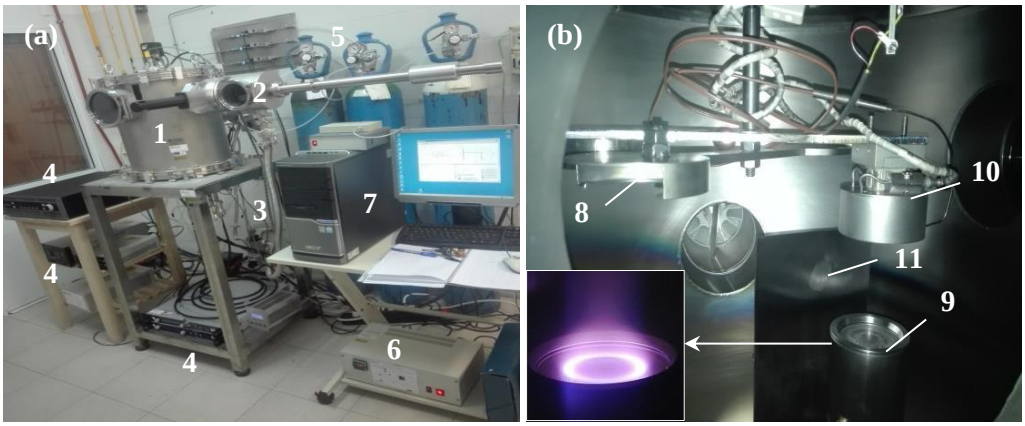

Figure 2.2 (a) Sputtering equipment used for thin film deposition. (b) Interior of the main chamber. The inset shows the Ar + O_2 plasma created during deposition.

A base pressure in the 10^{-7} mbar range can be achieved in the main (growing) chamber by means of a *Pfeiffer* **vacuum system**, which consists of a DUO 10 M rotatory vane pump and a HiPace 300 turbo–pump controlled by a display and control unit (DCU). An additional small load–lock chamber, placed at the right side of the deposition chamber, allows manipulating the sample holder without breaking the vacuum in any other part of the system when operating at room temperature. This secondary chamber is connected to the main chamber by a guillotine valve and to the rotatory pump as well.

Two water–cooled ferromagnetic–materials–compatible IONI'X UHV planar **magnetrons** (2" diameter) from *Thin Film Consulting* are placed inside the main chamber, what allows the deposition of the desired material. These magnetrons can be tilted in order to carry out co–sputtering growths, *i.e.*, sputtering of more than one material simultaneously with the power supplied to each of the targets controlled independently, as shown in Fig. 2.3. In this configuration, the magnetrons are tilted respect to its vertical axis, so that the substrate is placed at the intersection of the magnetron axes.

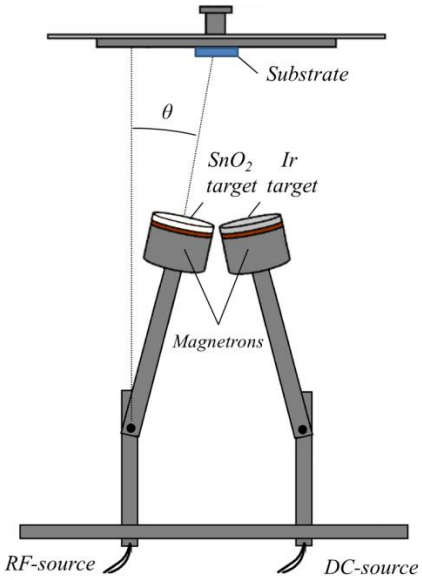

Figure 2.3 Magnetrons configuration for co–sputtering growths.

The magnetrons were operated by different **power sources** depending on the requirements, as explained above: OL400W DC source from *HiTek Power Limited*, R301 RF source (operating at 13.56 MHz) from *Kurt J. Lesker*, or Pinnacle Plus+ 5 kW pulsed DC source from *Advanced Energy Industries*. It has to be said that, while in these RF and pulsed DC sources the output power can be directly tuned, in the DC source the tunable output parameter is the intensity. Because of this, usually small differences are found in the output power for the same applied intensity, since the output voltage slightly varies in each growth.

Regarding the **working gases**, Ar, O_2 and N_2, with 99.995%, 99.999%, and 99.999% purities, respectively, can be introduced inside the chamber through F–201CV mass flow controllers (MFCs) from *Bronkhorst Hi–Tech*. The gas circuit is also equipped with particulate filters and non–return valves. A valve was installed in the system right after each controller in order to achieve the base pressure mentioned above (10^{-7} mbar). Without these valves, the vacuum worsens one order of magnitude due to uncontrolled internal leaks in the MFCs. Additionally, an overpressure is settled at the other end of the MFCs to prevent air from entering into the system.

To grow films on substrates at temperatures up to 950 ºC, a home–designed **substrate heating system** based on a heater and a thermocouple controller was used.

Finally, through a home–made software developed with the technical support of the *Servicio de Instrumentación Electrónica* at University of Zaragoza, it is possible to **monitor**: (i) the movement of the sample–holder arm, so that the substrate holder can be alternatively moved between several defined positions; (ii) the gas supply introduced in the chamber by the three MFCs, and (iii) the sputtering times (very useful to prepare multilayers).

Systematically before each growth, a 5 minutes pre–sputtering (15 min for new targets or when the equipment has not been used for more than a week) was performed to clean the target surface. Usually, this procedure is carried out in Ar atmosphere. However, a greater amount of metallic Ir was found in (nominally) IrO_2 films grown under the same conditions but during less deposition time (*i.e.*, thinner samples). From this fact, it was concluded that, during the pre–sputtering process, a very thin metallic Ir film (~1–2 nm) is deposited in the substrate if a pure Ar atmosphere is used. In consequence, the pre–sputtering process was carried out in an O_2 + Ar mixture atmosphere.

It is noted that some of the Ir– and Fe–based multilayers studied in Chapter 7 were grown in a similar equipment located in the sputtering laboratory of the "Heterostructures for Optics and Optoelectronics" group at *Instituto de Ciencia de Materiales de Madrid* (ICMM).

2.1.3. High Oxygen Pressure Sputtering

The high oxygen pressure deposition technique was used to grow high–quality epitaxial films. In this variant from conventional sputtering, a complete thermalization of the extracted species is favored and, at the same time, prevents them from back–sputtering and losing oxygen in the final crystal structure. Under these conditions, the DRs are very slow (commonly < 1 nm/min) and high–quality epitaxial films are

usually obtained [98]. Given those DRs, this technique was only used to grow ultrathin (≤ 5 nm) epitaxial films on TiO_2 substrates.

These samples were synthesized in collaboration with the group of *Física de Materiales Complejos* (GFMC) during a stay of four months at *Universidad Complutense de Madrid* (UCM). The equipment employed, exposed in Fig. 2.4(a), consists of a growing chamber in which a high vacuum of about 10^{-6} mbar is previously realized by a turbo–molecular pump supported by a membrane pump. A constant oxygen flow is injected and controlled by a system of needle valves. The substrate is placed on a heater located at the bottom of the chamber parallel to the target. An example of the plasma generated in the powered target is given in Fig. 2.4(b). More detailed information about this equipment, as well as about its performance, can be found in Refs. [98–100].

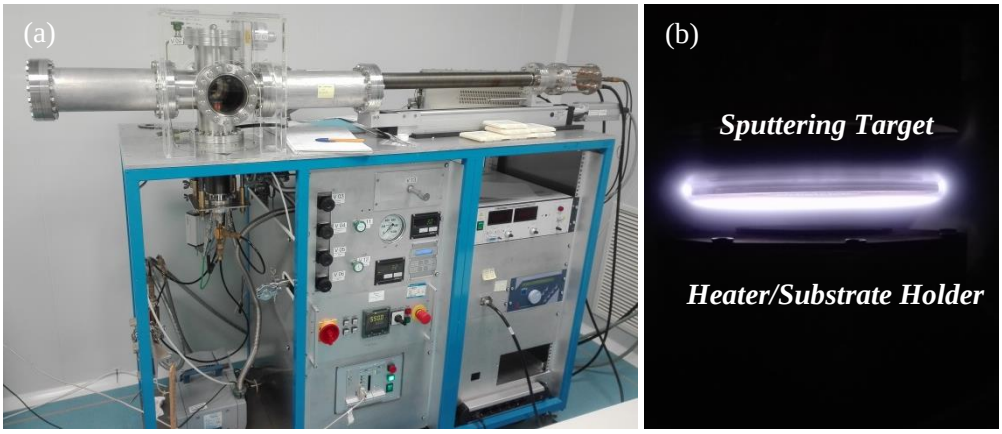

Figure 2.4 (a) High oxygen pressure sputtering equipment employed for thin film deposition. (b) Enlarged view of the powered target on the substrate.

2.2. Pulsed Laser Deposition (PLD)

The pulsed laser deposition (PLD) technique is also a PVD process commonly employed in the deposition of high–quality epitaxial thin films, in which the material that is to be deposited is vaporized from the target by a pulsed laser beam and transported in a plasma plume to the substrate [101]. A simple scheme of the process is represented in Fig. 2.5(a). The laser is focused and directed towards a vacuum

chamber thanks to an external optical set. Then, the laser strikes the surface of the target and a plasma plume is formed by the ejected atoms interacting with the chamber atmosphere. Finally, these atoms are deposited on the surrounding areas and on the substrate, which is placed on a heater opposite to the target.

Since the DRs obtained by PLD are relatively high compared to those from high oxygen pressure sputtering, this technique was used to grow epitaxial films of thickness up to 100 nm using TiO_2 and SnO_2 substrates. It is worth mentioning that the growth of the thickest films (~100 nm) had to be done in 3 steps to calibrate the energy of the laser. For thinner films, the deposition process could be performed in 1 step.

The samples obtained by means of such technique were synthesized in collaboration with Pilar Jiménez and Dr. Irene Lucas at *Instituto de Nanociencia de Aragón* (INA). The system employed, shown in Fig. 2.5(b), is equipped with a vacuum chamber evacuated by a cryogenic pump to a base pressure in the 10^{-7} mbar range. The PLD module includes a high–energy excimer KrF laser whose spot is focused on the target surface by means of an external optical system. The PLD equipment also includes a load–lock chamber evacuated by a turbo–molecular pump to facilitate the manipulation of the substrate holder without breaking the vacuum in any other part of the system. More detailed information about this equipment and its performance can be found in Ref. [102].

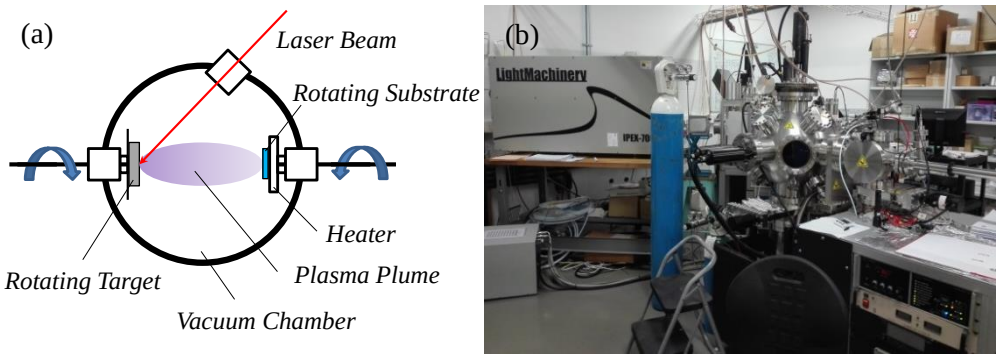

Figure 2.5 (a) Simple PLD process scheme and (b) equipment employed for thin film deposition.

2.3. Sample Annealing

In order to improve (when necessary) the crystallinity of the deposited films grown by conventional sputtering, a subsequent annealing treatment was carried out. A natural–convection muffle furnace allowed performing such treatment in air atmosphere at several temperatures (typically 600 ºC). For probing other atmospheres (O_2 and Ar), a tube furnace was employed. In all the cases both, the heating and cooling rates, were 5 ºC/min (except in specific circumstances where an air or water quenching was performed).

2.4. Structural and Morphological Characterization

2.4.1. X–Ray Diffraction (XRD) and Reciprocal Space Maps (RSM)

X–ray diffraction (XRD) measurements were systematically performed to obtain structural information about the deposited films, more specifically: phase identification, preferred orientation (texture), grain size and lattice parameters.

Conventional XRD experiments were carried out by Dr. Concepción Sánchez from *Servicio de Difracción de Rayos X y Análisis por Fluorescencia* at University of Zaragoza. Data collection was performed at room temperature in a *Rigaku* D/max 2500 and in a *Rigaku* D/Max Ru300 diffractometers, working at 40 kV and 80 mA. High–resolution XRD measurements (HR–XRD) were performed in epitaxial films, also at room temperature, at *Laboratorio de Microscopías Avanzadas* (LMA) at University of Zaragoza in a D8 Advance diffractometer from *Bruker*, working at 40 kV and 40 mA; and at UCM by Ignacio Carabías in an X'Pert PRO MRD diffractometer from *Malvern Panalytical*, working at 45 kV and 40 mA. In all the cases, the K_α radiation line of Cu was used.

The diffraction patterns of polycrystalline samples were analyzed with the Rietveld method using the FullProf software [103]. This is a refinement technique that allows accurately determining structural and compositional parameters of the sample

from the construction of a theoretical model that fits the experimental diffraction pattern by a least squares method [104]. It provides reliable information about phase identification, texture or lattice parameters even when the peak–to–background ratio is small and the peak width is relatively large (other structural parameters have not been fitted). With the FullProf software, the preferred orientation can be quantified by means of the *Pref.* parameter. A *Pref.* $\neq$ 1 means that the sample has grown with a preferred orientation. If the *Pref.* parameter is < 1, it indicates a platy habit; and if it is > 1, a needle–like habit [105, 106]. Additionally, the refinements have allowed discerning the presence of a small amount of metallic Ir (< 1%) which otherwise would easily go unnoticed. Finally, the sample displacement error is corrected with the refinement procedure, giving thus, in general, more precise values of the lattice parameters. Such error has been corrected in all the diffractograms from polycrystalline samples displayed in this thesis.

The grain size of the films in the out–of–plane direction was obtained by measuring the full width half maximum (FWHM) of the diffraction peaks, which is directly related to the crystallite size through the Scherrer equation [107]:

$$GS = \frac{K\lambda}{B(2\theta)cos\theta} \tag{2.1}$$

where *GS* is the grain size, λ is the wavelength of the X–ray source (1.54 Å for the Cu K_α radiation line), *B* is the FWHM of the specific peak, θ is the Bragg angle of such peak, and *K* is the Scherrer constant (0.94 for our samples).

Regarding the epitaxial films, reciprocal space maps (RSM) were recorded to determine with precision their lattice parameters [108]. They were collected and analyzed with the assistance of Pilar Jiménez at LMA in a D8 Advance diffractometer from *Bruker*. 2θ–ω scans were recorded from different values of ω, being 2θ the angle between the incident beam and the detector (detector angle), and ω the angle between the X–ray source and the sample (incident angle). This configuration allows determining the position of $|\boldsymbol{\sigma}_{hkl}|$ for the substrate ($|\boldsymbol{\sigma}_{substrate}|$) and the film ($|\boldsymbol{\sigma}_{film}|$) as shown in Fig. 2.6, being $\boldsymbol{\sigma}_{hkl}$ the reciprocal space vector defined as that normal to the

(*hkl*) planes with a modulus the inverse of the inter–planar distance, $1/d_{hkl}$. When the lattice parameters are orthogonal, as in a tetragonal crystalline structure of IrO_2, next expression applies:

$$|\boldsymbol{\sigma}_{hkl}| = \sqrt{\frac{h^2}{a^2} + \frac{k^2}{b^2} + \frac{l^2}{c^2}} \tag{2.2}$$

Defining $\boldsymbol{\sigma}_{//}$ and $\boldsymbol{\sigma}_{\perp}$ as the parallel and perpendicular component of the $\boldsymbol{\sigma}_{hkl}$ vector to the sample surface (see Fig. 2.6) and considering, for instance, a (001)–oriented film, where *a* and *b* are the in–plane lattice parameters and *c* the out–of–plane parameter, Eq. 2.2 gives:

$$|\boldsymbol{\sigma}_{//}| = \sqrt{\frac{h^2}{a^2} + \frac{k^2}{b^2}} \qquad |\boldsymbol{\sigma}_{\perp}| = \frac{l}{c} \tag{2.3}$$

Then, using (*h0l*)– and (*0kl*)–type reflections the lattice parameters of the deposited film are easily obtained from Eq. 2.3.

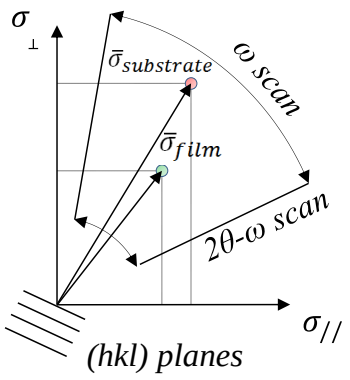

Figure 2.6 Schematic description of a RSM measurement.

2.4.2. X–Ray Reflectivity (XRR)

The X–ray reflectivity (XRR) technique was systematically used to extract information about the thickness, density and surface roughness of the deposited films. The experiments were performed in a D8 Advance diffractometer from *Bruker* located at LMA working at 40 kV and 40 mA using the K_α radiation line of Cu.

The main parameters that can be easily obtained from a XRR curve are displayed in Fig. 2.7(a). The period of the signal is related to the film thickness, the position of the critical angle, θ_c (angle under which the X–rays are totally reflected), provides information about the film density; and the decay rate of the curve, as well as the visible number and amplitude of the oscillations, give information about the film and substrate roughness.

On the other hand, in the XRR curve of a multilayer, as that depicted in Fig. 2.7(b), the following maxima can be resolved: (i) *satellite maxima*, whose angular spacing depends on the bilayer thickness; and (ii) *Kiessig fringes*, whose period depends on the total multilayer thickness.

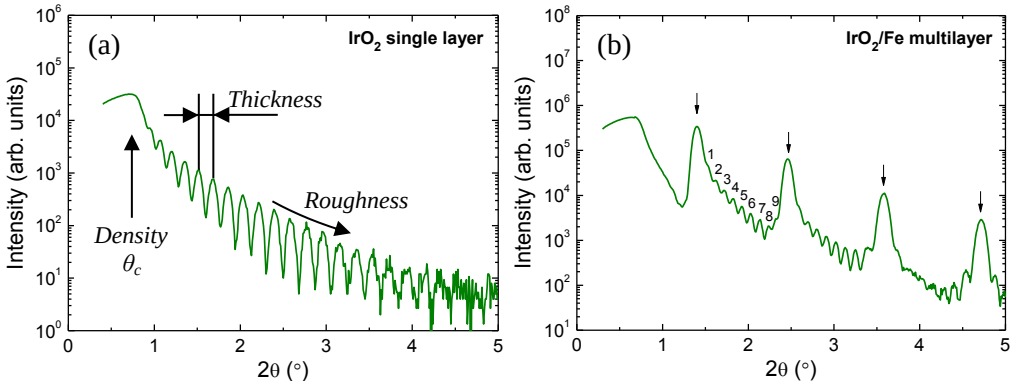

Figure 2.7 Examples of XRR curves measured in (a) an IrO_2 single layer and in (b) a IrO_2/Fe multilayer (10 repetitions). The *satellite maxima* are indicated by vertical arrows (bilayer thickness) and the *Kiessig fringes* by numbers (total thickness).

The Leptos software was employed for fitting the experimental curves of single films, thus obtaining precise values of layer thickness and film density. In several cases, a reliable fit of the surface roughness was not achieved, and hence, the study of such parameter was limited to a more qualitatively analysis. On the other hand, the fittings of the Ir– and Fe–based multilayers were not trivial. In these samples, the total and bilayer thickness was determined by fitting the position of the *Kiessig fringes* or the *satellite maxima*, as appropriated, to next expression [109]:

$$\theta_m^2 - \theta_c^2 = m^2 \left(\frac{\lambda}{2t}\right)^2 \quad (2.4)$$

where θ_m is the incident angle, m is the order of the interference, and t the bilayer thickness or the total layer thickness, as appropriated (*satellite maxima* or *Kiessig fringes* period).

2.4.3. X–Ray Absorption Spectroscopy (XAS)

X–ray absorption spectroscopy (XAS) is a well–established analytical technique for local structural determination (namely: the local environment of an atom). From the analysis of XAS spectra, information about the electronic state (oxidation state, density of states and local orbital symmetry) can also be obtained [110]. As explained in Appendix B, the absorption spectrum is in general divided into two regions: the XANES (X–ray absorption near edge structure) and the EXAFS (extended X–ray absorption fine structure). XANES experiments were performed to gain knowledge about the electronic structure of the absorbing atom (Ir, Fe or Cr), more specifically, about the strength of the spin–orbit coupling and the oxidation states; while EXAFS experiments provided information about the short–range crystal structures around Ir and Fe centers (interatomic distances and structural disorder).

As the layers of interest are Ir, IrO_2, Cr–based oxides, Fe, and Fe–based oxides, XAS experiments were performed at (i) the Ir $L_{2,3}$ edges, which corresponds to $2p \rightarrow 5d$ transitions; and (ii) at the K-edge of both Cr and Fe, *i.e.*, $1s \rightarrow 4p$ transitions. All these absorption edges lie within the so–called hard X–rays region, which allows probing the whole sample instead of just the surface (typically 4–10 nm), and using a single beamline to probe both, the 5*d* and 3*d* elements. In addition, choosing the K edge of the 3*d* metal over the $L_{2,3}$ edges ($2p \rightarrow 3d$ transitions) has several advantages, such as an easier and more accurate phase identification. As high–energy (hard) X–rays are required, synchrotron radiation is practically the unique source capable of producing X–rays of such high intensity. Given the scarce measuring time which is usually granted at these facilities (and as long as the required proposal is accepted), the experiments were performed on representative samples.

Standard XANES and EXAFS spectra were collected in fluorescence yield mode at CLAESS beamline at ALBA synchrotron (Barcelona). A Si(111) double crystal monochromator was used to obtain a monochromatic beam, and Rh–coated collimating and toroidal mirrors were used to optimize the energy resolution, focus the beam and reject higher harmonics. The incoming beam was monitored by an N_2–filled ionization chamber and the fluorescence lines were detected using a Si–drift detector.

Due to the high intensity of the white line at the Ir L_3 edge and the significant broadening due to the core–hole lifetime [111], high–energy resolution fluorescence detected XANES (HERFD–XANES) instead of conventional fluorescence XANES is required to record good spectra with optimized resolution. This technique makes it possible to overcome some of the main limitations of conventional XAS by measuring the X–ray absorption spectrum via monitoring the intensity of a fluorescence line corresponding to a specific excited state decay process using a narrow energy resolution. This is generally achieved by using a crystal analyzer to select a narrow energy band from the emission line of the sample. This way, the HERFD–XANES enhances features present in the edge region of the absorption spectrum resolving structures that are not visible in a conventional XANES spectrum [112, 113]. Such resolution enhancement allows determining the amplitude, position and width of the white line more accurately, which is crucial for a more precise determination of the spin–orbit coupling strength.

HERFD–XANES measurements were carried out at Diamond Light Source facility (Oxford) at I20–Scanning beamline. Such beamline is equipped with a four–bounce scanning Si(111) monochromator [114] and the harmonic rejection was achieved by using two Rh–coated mirrors operating at 4.0 mrad incidence angle. An X–ray emission spectrometer based on a 1 m–diameter Rowland circle operating in the Johann configuration in the vertical plane was used for the experiments [115]. Three 100 mm Si(555) spherical analyzer crystals were used to select the $L_{\beta 1}$ (10708 eV) emission line, while three 100 mm Si(642) crystals were used in the case of the $L_{\alpha 1}$ (9175 eV) emission line. An ion chamber filled with the optimum gas mixture to absorb 15% of the incident radiation at the Ir $L_{2,3}$ edges energies was used as incident

monitor, while a Medipix area detector [116] was used to collect the intensity of the emission line.

Once XAS spectra are recorded, a normalization procedure is necessary before data can be compared (see Appendix B). In this sense, XANES and EXAFS spectra have been analyzed according to standard procedures [117] using the HORAE–IFEFFIT (Athena, Artemis) software package.

Particular attention must be payed to the re–absorption of fluorescence photons in the sample, especially when grazing incidence is used. In order to correct self–absorption effects, the XANDA software was used [118]. As an example, Fig. 2.8(a) shows the normalized XANES spectra of a 100 nm–thick amorphous IrO_2 film measured at the Ir L_3 edge for three configurations of the incident angle, ϕ, namely: normal incidence ($\phi \approx 90º$), $\phi = 45º$, and grazing incidence ($\phi \approx 0º$). Although identical profiles should be expected, the intensity of the white line at grazing incidence is clearly lowered. In Fig. 2.8(b), the same spectra are displayed after correcting the self–absorption effects by XANDA, showing now the three configurations practically identical profiles.

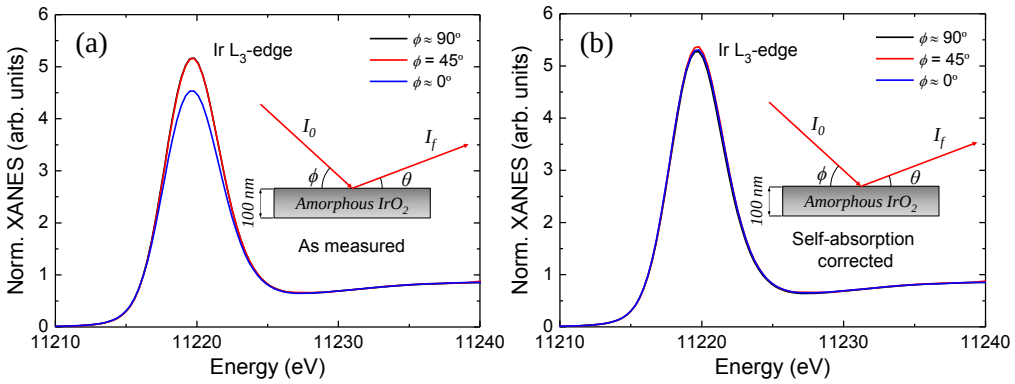

Figure 2.8 Normalized XANES spectra recorded for different values of the incident angle, ϕ, (a) before and (b) after correcting self–absorption effects.

Finally, for the sake of better understanding the XANES spectra, additional calculations of the Ir $L_{2,\ 3}$–edges and the Cr and Fe K–edge XANES spectra were carried out by Dr. Jesús Chaboy using the multiple–scattering code Continuum [119]

included in the MXAN software package [120]. A complete discussion of the followed procedure can be found in Refs. [121–123].

2.4.4. Transmission Electron Microscopy (TEM)

Cross–sectional TEM images were recorded on representative samples to gain a deeper knowledge about structural details of the deposited IrO_2 films, such as crystallinity or porosity. Additionally, by means of this technique the layered structure in the Ir– and Fe–based multilayers could be observed. The diffraction mode of the microscope also allowed registering diffraction patterns of selected areas.

Both, the sample preparation (standard procedure [124]) and image acquisition of these samples, were performed with the assistance of Dr. M. Ángeles Laguna Gómez at 200 kV using a JEOL–2000FXII microscope located at *Servicio de Microscopía Electrónica de Materiales* at University of Zaragoza.

Additionally, for better characterizing the IrO_2 epitaxial films, a high–resolution TEM was used. Sample preparation (standard procedure [124]) and image acquisition were performed with the assistance of Dra. Mariona Cabero in a JEM ARM200cF microscope working at 120 kV at *Centro Nacional de Microscopía Electrónica* (Madrid). In these samples an alumina capping was needed on top, as shown in Fig. 2.9, otherwise the IrO_2 layer was degraded under the beam.

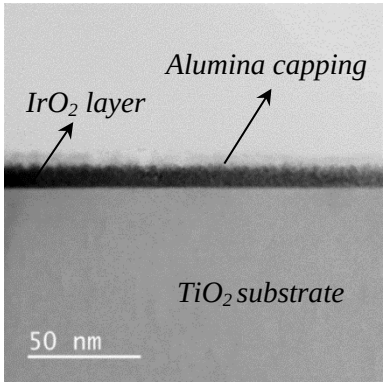

Figure 2.9 Illustrative low–magnification TEM image of an epitaxial IrO_2 film in which an alumina capping was deposited to prevent beam damaging.

Gatan Digital Micrograph software was used for image capture and further analysis.

2.4.5. Field Electron Scanning Electron Microscopy (FE–SEM)

FE–SEM images were recorded on the surface of representative samples to get a deeper knowledge about microstructural details, such as grain size and surface roughness. On the other hand, the cross–sectional configuration allowed discerning the layer thickness in those samples in which XRR experiments could not provide further information.

Image recording was performed with the assistance of Cristina Gallego at 1–5 kV in a Carl Zeiss MERLIN microscope located at *Servicio de Microscopía Electrónica de Materiales* at University of Zaragoza.

For surface image acquisition, the samples were attached to a sample holder with carbon tape, as shown in Fig. 2.10(a). For cross–sectional image acquisition a small portion of the sample was cut and attached perpendicularly to the sample holder with silver paste with the cut part at the top, as exposed in Fig. 2.10(b). As the samples under study are metallic at room temperature, further preparation was not needed.

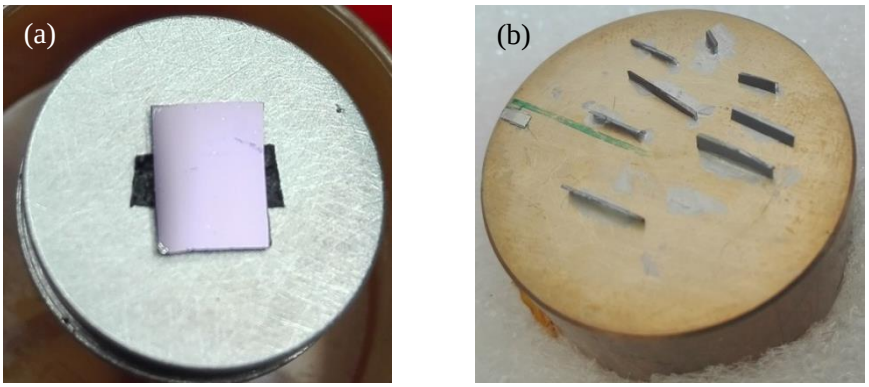

Figure 2.10 Sample configuration for (a) surface and (b) cross–sectional FE–SEM image acquisition.

2.5. Compositional Characterization

2.5.1. Rutherford Backscattering Spectroscopy (RBS)

The Rutherford backscattering spectrometry (RBS) technique was employed to determine the elemental composition and thickness of the Ir– and Fe–based multilayers in terms of atoms/cm^2. The results obtained by means of such technique were used to further ahead normalize the magnetization measurements into μ_B/at. Fe.

The RBS experiments were carried out and analyzed by Dr. Javier García at *Centro Nacional de Aceleradores* (Sevilla). 3.016 MeV He^{2+} and 1.514 MeV He^{2+} beams, with a beam diameter of ~1 mm and scattering angle of 110º were employed. The first beam energy allowed separating the Ir and Fe signals and measuring the total multilayer thickness, as well as determining the mean concentration of the elements making up the samples (Ir, Fe, and O). The second beam energy has a better depth resolution and allowed individually discerning the monolayer in the thickest monolayers (> 40x10^{15} at/cm^2).

2.5.2. Energy Dispersive X–Ray Spectroscopy (EDX)

The energy dispersive X–ray spectroscopy (EDX) technique was used to determine the concentration of the doping element in the Sn– and Cr–doped IrO_2 films.

The experiments were carried out with the assistance of Gala Simón and Laura Casado at LMA in an INSPECT 50 FE–SEM working at 30 kV for the Sn–doped samples (in order to reach the Sn K_α line at ~25 kV) and at 10 kV for the Cr–doped samples (highest–energy principal line is Ir L_α at ~9 kV). Although at those voltages the beam penetrates relatively deep in the substrate, this is not a problem since the interest here lies on determining the amount of the dopant element relative to the Ir concentration.

Sample configuration is identical to that shown in Fig. 2.10(a). Systematically, to prove the homogeneity of the samples three different regions were scanned: two at opposite corners and one at the center.

2.6. Electrical Characterization

The electrical properties of the synthesized samples were studied by measuring the temperature–dependent electrical resistivity, ρ(T), by the Van der Pauw method [125].

The measurements were carried out in a *Quantum Design* PPMS 9 T at *Servicio de Medidas Físicas* at University of Zaragoza. During the stay at UCM, the measurements on the samples synthesized there were performed in a cryostat capable of reaching temperatures of ~15 K and Keithly current sources and nano–voltmeters were used. More detailed information about this equipment can be found in Ref. [126]. In both cases, an electrical current of 100 μA was applied from room temperature to 10 K (~15 K with the UCM equipment set up).

Fig. 2.11(a) shows the connections necessary to carry out the measurements. During the experiment two scans are performed: when cooling down the sample, the current (I) is applied from A to B, and the potential difference V_D - V_C is measured. This way, the quotient V_{CD}/I_{AB} provides the electrical resistance $R_{AB, CD}$ as a function of the temperature. Secondly, during a warm up scan the connections are accordingly exchanged, so that, I is applied from B to C and V is measured between A and D. Thus, the quotient V_{DA}/I_{BC} provides the electrical resistance $R_{BC, DA}$.

As shown in Fig. 2.11(b), for measuring with the PPMS device the electrical contacts were made with an aluminum–wire bonding equipment. Such equipment allows establishing a connection, with the aid of an optical microscope, between a micrometer–sized region of the sample and the millimeter–sized conducting pads from the "puck". With the equipment employed at UCM, the four electrical contacts were

made on the surface of the sample by silver evaporation, and then connected to 50 μm–size copper wires with silver paste, as shown in Fig. 2.11(c).

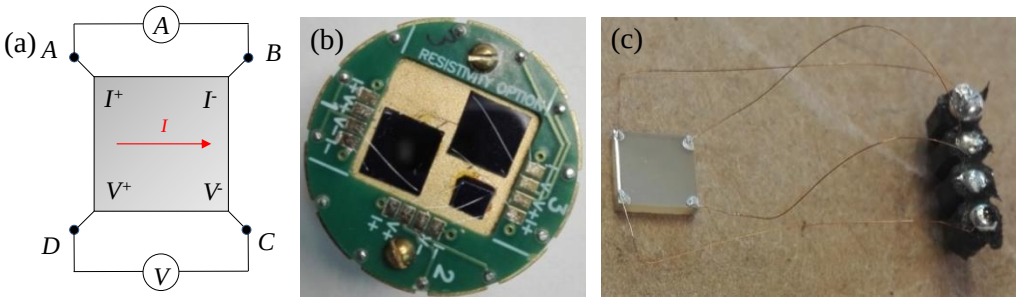

Figure 2.11 Van der Pauw configuration for (a) temperature–dependent resistivity measurements (*I* states for the applied intensity). Panel (b) shows a photograph of three samples mounted in a "puck" to be measured in the PPMS, and panel (c) a photograph of the sample disposition for measuring with the equipment used at UCM.

As can be seen in Fig. 2.11(b), whenever possible (*e.g.*, when large 2" Si wafers are used), the substrates are previously cut, so roughly square samples are obtained. In such a case, for homogeneous samples $R_{AB,CD} \approx R_{BC,\,DA}$ and it holds:

$$\rho(T) = \frac{\pi R(T) t}{\ln(2)} \tag{2.5}$$

where $R = (R_{AB,CD} + R_{BC,\,DA})/2$ and t is the film thickness.

This procedure markedly simplifies the resistance to resistivity conversion. When this approximation cannot be made (for 5 x 8 mm TiO_2 and SnO_2 substrates), a mathematical software is needed to perform such conversion (see Appendix B). In this dissertation, Mathematica software was used with the assistance of a code written by Dr. David Zueco.

2.7. Magnetic Characterization

2.7.1. Superconducting QUantum Interference Device (SQUID)

The magnetic characterization of the samples was systematically performed in a SQUID (superconducting quantum interference device) MPMS XL (5 T) magnetometer from *Quantum Design* at *Servicio de Medidas Físicas* at University of Zaragoza.

Methodically, a "magnet reset" was performed before introducing the samples in the device in order to remove the possible magnetic flux trapped in the superconducting magnet windings. Then, two different modes were used to carry out the measurements: "no–overshoot" and "hysteresis". The no–overshoot mode is more precise but much slower than the hysteresis mode, being the latter more suitable for measuring samples with large magnetic moment [127]. All the measurements were carried out in the RSO option (4 cm of sample movement and 1 Hz of repetition frequency) and DC mode.

Two types of measurements were recorded: temperature–dependent, M(T), and field–dependent, M(H). For the M(T) curves, commonly a zero–field–cooled (ZFC) measurement is first carried out, where the sample is cooled down to 5 K in the absence of a magnetic field, and a constant magnetic field (typically 1 kOe) is applied during the warm up scan. Secondly, in the field–cooled (FC) measurement, the sample is again cooled down to 5 K, but now in the presence of a constant magnetic field, and a warm up scan is performed also with the same applied field. Regarding the M(H) loops, the sample is subjected to a magnetic field cycling typically from 50 kOe to -50 kOe at a particular temperature (usually 5 and 300 K). For low temperatures, the samples were zero–field–cooled before carrying out any measurement.

When measuring a thin film, the sample is ideally placed inside a straw as shown in Fig. 2.12(a). Nevertheless, when the sample is not big enough to be placed in the straw without falling, it is introduced inside a gelatin capsule (employed for

measuring powder samples), as shown in Fig. 2.12(b). Additionally, for measuring the magnetic response with the magnetic field applied in the out–of–plane direction, the sample is placed between the ends of two straws and wrapped up by another straw attached with Kapton tape to the first ones, as exposed in Fig. 2.12(c).

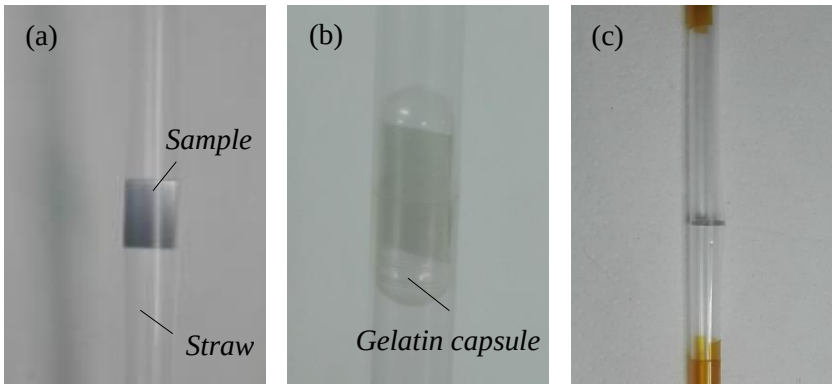

Figure 2.12 Different sample configurations employed for measuring thin films in the SQUID magnetometer, as explained in the main text.

It is of crucial importance to very carefully manipulate low–magnetization samples [128], as it is the case of most of the samples in this dissertation. One of the mean contamination sources which might introduce spurious effects in magnetization measurements is the use of metallic tools (tweezers, awls, blades, etc.). These objects can introduce Fe micro–impurities and mask the actual sample signal. As an example, in Fig. 2.13, two M(H) cycles measured on identical Si substrates are compared. In the first one, no metallic tools were used during the process, while for the second substrate an awl was employed to make small holes in the straw to prevent the film from falling. The first measurement shows a typical diamagnetic signal with a slope of **-6.9×10^{-9} emu/cm^{2}Oe**. However, in the second substrate a clear ferromagnetic component appears over the same diamagnetic signal. This fact proves that Fe micro–particles coming from the awl can indeed stick to the straw at the contact points.

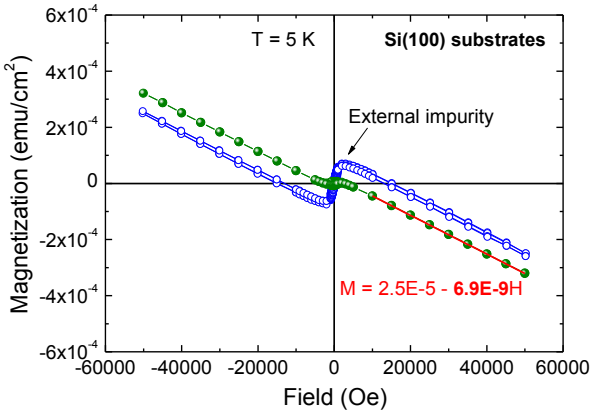

Figure 2.13 M(H) cycles on Si substrates without external spurious contributions (solid symbols) and with impurities from an awl (open symbols).

In addition, not only is a careful manipulation needed, but also a careful data analysis. More specifically, in the magnetization measurements carried out in the IrO_2 films, to obtain the IrO_2–layer magnetization (M_{IrO2}) the background contribution, defined as $M_{bck} = M_{capsule} + M_{substrate,}$ must be subtracted. In general, this is a straightforward procedure, but it may become complicated in some situations when small magnetic signals are expected, as for the case of IrO_2 thin films. In such cases, the main spurious or unwanted contributions must be identified in order to discern them from any magnetic signal coming from the deposited layer.

Ideally, the substrates should be measured before and after depositing the IrO_2 layer and employing the same capsule (when necessary) to correctly remove M_{bck}. Nevertheless, the dependence on external equipment, the fact that sometimes the capsule breaks, and that measuring the substrates before depositing the IrO_2 layer would probably mess up the surface, prevents from doing so. Therefore, the differences among using different **gelatin capsules** and **substrates** must be taken into account. Additionally, other unwanted effects might come from the **electronic noise** of the SQUID magnetometer, due to, for instance, the use of different measuring modes. Thus, several backgrounds were measured under diverse conditions with a view to obtaining an estimation of the error bar when determining M_{IrO2}.

The M(H) curves measured in three different empty gelatin capsules are depicted in Fig. 2.14(a). A diamagnetic signal is observed in the three of them with a maximum difference of $0.8x10^{-4}$ emu at the maximum applied magnetic field (M_{max}). Taking the typical ~5 x 8 mm–size of our samples, this is translated into a maximum indetermination of **$2.0x10^{-4}$ emu/cm^2** when obtaining the IrO_2 maximum magnetization ($M_{max, IrO2}$). In view of this, to remove such contribution (if possible) it is better to use a second straw as in Ref. [129] to perform the measurements.

Fig. 2.14(b) shows the M(H) curves measured in three different Si substrates (without capsule). The three of them show a similar diamagnetic response with slight variations in the slope. At M_{max}, this difference is translated into **$0.3x10^{-4}$ emu/cm^2**. Similarly, Fig. 2.14(c) shows the M(H) curves measured on TiO_2 substrates for three different growing orientations (capsule included). The signal recorded in all the cases presented again a diamagnetic behavior. If the three different substrates are compared at M_{max}, a maximum difference of **$2.1x10^{-4}$ emu/cm^2** is observed between them.

As a representation, Fig. 2.14(d) compares the same TiO_2(100) substrate measured using consecutively the two measuring modes mentioned above. Such substrate was also measured on two different days, labeled as (1) and (2). Additionally, another TiO_2(100) substrate, labeled as (3), is also represented in order to illustrate the importance of the noise coming from the equipment. When both measuring modes are compared at M_{max}, a maximum difference of **$0.2x10^{-4}$ emu/cm^2** is observed. On the other hand, when measuring on different days (electronic noise), the variations are found to be around **$1.4x10^{-4}$ emu/cm^2**. A clear artifact was recorded in the sample labeled as (3) at low magnetic field (see inset), and a maximum difference of **$1.8x10^{-4}$ emu/cm^2** at M_{max} is observed respect to the other substrates. As a consequence, though the measuring mode seems not to affect much the measurements at high applied fields (compared to other effects), the electronic noise might become important. In order to minimize this error, the measurements had to be repeated and compared to be sure they are reproducible.

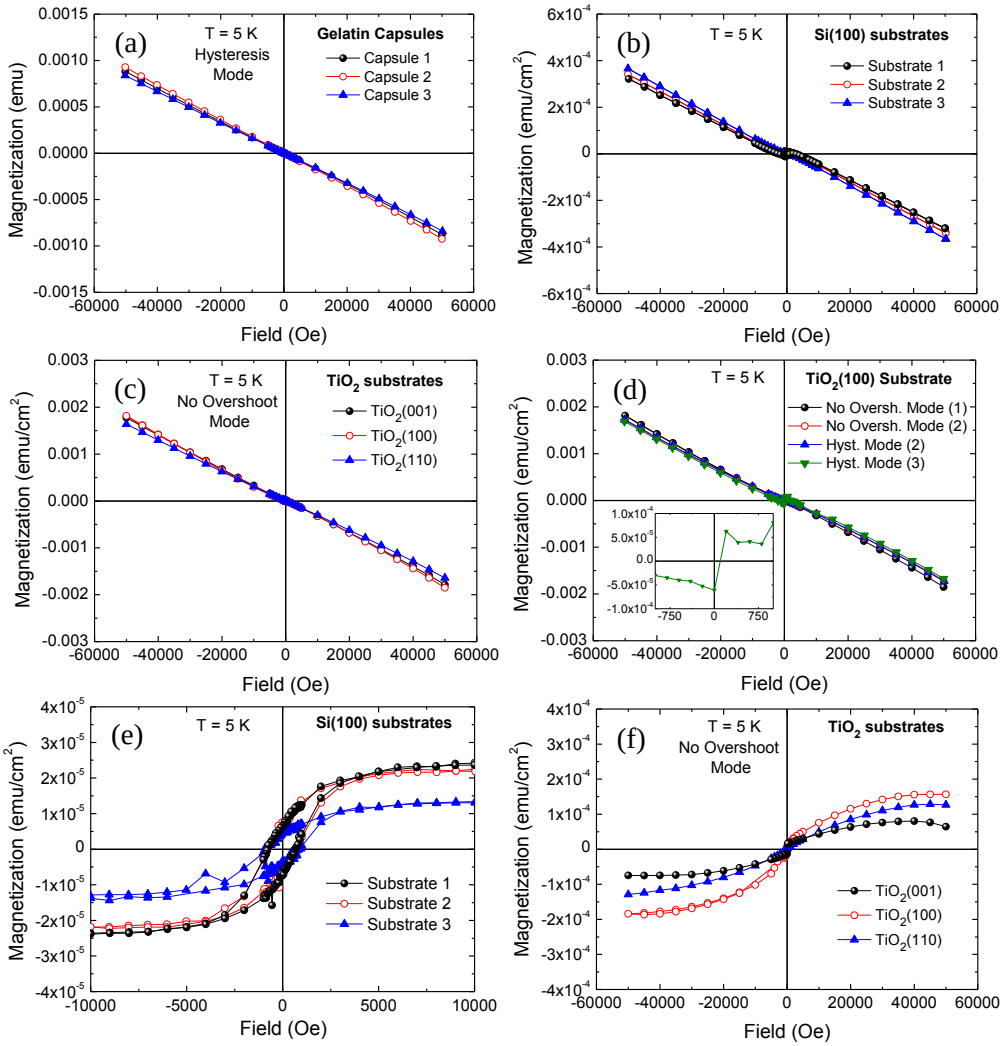

Figure 2.14 M(H) curves measured at 5 K in (a) three different empty gelatin capsules, (b) three different Si substrates, (c) TiO_2 substrates with different growing orientations, and (d) TiO_2 substrates using different measuring modes and recorded on two different days labeled as (1) and (2). An additional substrate (3) illustrates the importance of the electronic noise. Panels (e) and (f) show Si and TiO_2(100) substrates with diamagnetic contribution removed.

Finally, the presence of magnetic impurities in the substrates must also be taken into account. If the diamagnetic slope is subtracted in the M(H) curves of the Si substrates, a small soft ferromagnetic impurity is observed (Fig. 2.14(e)). This signal has a saturation magnetization of **1.0–2.5x10^{-5} emu/cm^2** and a coercive field of **~700 Oe**. In this sense, *A. Singh et al.* [130] already found Fe and Cu micro–impurities in

silicon wafers by synchrotron techniques with a concentration of both elements in the order of 10^{-8} at./cm^2, probably being responsible for these loops. Similarly, in the TiO_2 substrates a paramagnetic–like impurity is revealed (Fig. 2.14(f)), possibly due to Ti^{3+} centers [131]. Here, a maximum magnetization of ~**1.5x10^{-4} emu/cm^2** is measured.

In view of this, it can be concluded that the error introduced by the unwanted or uncontrolled effects are in the order of **~2.5x10^{-4} emu/cm^2**. This means that a magnetic signal from the IrO_2 layer smaller than such value cannot be considered reliable. In addition to this uncertainty, careful attention must be paid to properly interpret the origin of possible small hysteresis loops. Along this work special attention was also paid to avoid/correct other possible sources of experimental errors as those reported in Refs. [128, 129, 132].

2.7.2. X–Ray Magnetic Circular Dichroism (XMCD)

The X–ray magnetic circular dichroism (XMCD) is a powerful tool for studying magnetic materials, capable of providing element and shell specific information about orbital and spin magnetic moments [133, 134]. In order to gain a deeper insight into the magnetic properties of the samples, and in particular about the orbital and spin magnetic moments of Ir in the different scenarios probed, XMCD spectra were recorded on selected films.

The experiments were carried out at 4–ID–D beamline at Advanced Photon Source (Chicago). XMCD spectra were recorded in fluorescence mode at 10 K and under an applied magnetic field of 35 or 50 kOe. Since the main interest lies on the magnetic state of the Ir (5*d*) band, XMCD spectra were recorded at the Ir $L_{2,3}$ edges ($2p \rightarrow 5d$ transitions). Additionally, the Cr K edge ($1s \rightarrow 4p$ transition) was also measured. Note that the K edge provides magnetic information of the *d* states indirectly through the 3*d*–4*p* hybridization. In order to remove spurious signals in the XMCD spectra, the scans were collected for the two directions of the applied magnetic field, *i.e.,* along and opposite the direction of the beam propagation. Undulator radiation was monochromatized with double Si(111) crystals and its polarization

converted from linear to circular with a diamond quarter–wave plate operated in Bragg transmission geometry. XMCD was measured by switching X–ray helicity and detecting the related modulation in absorption coefficient with a lock–in amplifier.

The orbital (m_l) and spin (m_s) magnetic moments of the Ir atom were determined from the magneto–optical sum rules derived by *B. T. Thole et al.* [135] and by *P. Carra et al.* [136], as explained in Appendix B.

Chapter 3

Synthesis and Optimization of IrO_2 Thin Films

3.1. Introduction

As shown in Chapter 1, small structural changes in iridates can lead to vastly different electrical and magnetic responses [56, 65, 67, 72, 73, 76, 82, 83, 87]. Therefore, **being able to grow IrO_2 with diverse structure** might be crucial for tuning the macroscopic properties of this material.

Up to now, IrO_2 has been deposited by a variety of methods, including reactive sputtering [137–142], laser ablation [143], pulsed laser deposition [144–146], sol–gel [147], electrochemical deposition [148, 149], chemical vapor deposition [150] or molecular beam epitaxy [56]. The film characteristics, such as thickness, porosity, roughness, crystallinity or chemical composition have been found to rely much on the exact process conditions for each of these techniques. Unfortunately, the available literature reporting how the structure of the films depends on the growing conditions is relatively scarce, unsystematic, and in some cases, contradictory. As a consequence, **a systematic work to understand the links between growing conditions and structure** of the resulting film is required.

The work presented along this chapter focusses on the synthesis of IrO_2 thin films deposited by means of three different techniques, namely: reactive magnetron sputtering (RMS), high O_2 pressure sputtering (HPS), and pulsed laser deposition (PLD). Regarding the RMS, the films were grown in our recently mounted sputtering

chamber. This enabled us to perform a systematic study about the influence of a wide range of sputtering deposition and annealing parameters on the thin film microstructure that barely exists in the literature. From such study, it was possible to grow IrO_2 thin films with relevant microstructural differences in a controlled manner (section 3.2). On the other hand, the synthesis of IrO_2 films by HPS and PLD, shown in sections 3.3 and 3.4, respectively, did not aim at growing films with different microstructure, but epitaxial films with the highest crystallographic quality to compare with those previously synthesized.

3.2. Reactive Magnetron Sputtering (RMS)

Fig. 3.1 schematizes the correlations between the synthesis conditions (growing and annealing) and the structural properties of the IrO_2 thin films which have been studied. Within the growing conditions, the sputtering power (supplied by a DC source)[1] and the Ar flux were increased from the lowest values at which the plasma could be sustained, namely: ~4 W and 10 ml Ar/min, respectively. The O_2 flux was varied according to the typical oxygen mixing ratios found in the literature (~10–30% range) [140–142], being 2 ml/min the lowest O_2 flux which can be supplied by the mass flow controller. As for the samples grown at high temperatures, the substrate temperature, T_s, was increased until metallic Ir was formed [151]. On the other hand, for finding the optimal annealing conditions, the annealing temperature, T_{ann}, was progressively increased up to the temperature at which volatile IrO_3 was formed [143]. Moreover, oxidizing and reducing atmospheres were probed. In general, Si(100) substrates have been used to carry out this study, but also the effect of growing a few selected films on substrates with the same structure than IrO_2 (rutile–like) was probed. Besides, the effect of quenching some selected samples was also considered. The results from these studies are included in Appendix C.

[1] For the sake of completeness several series of samples were also grown by a RF source. In all the cases the structural quality (roughness, crystallinity, density, etc.) was worse and their study has not been included here.

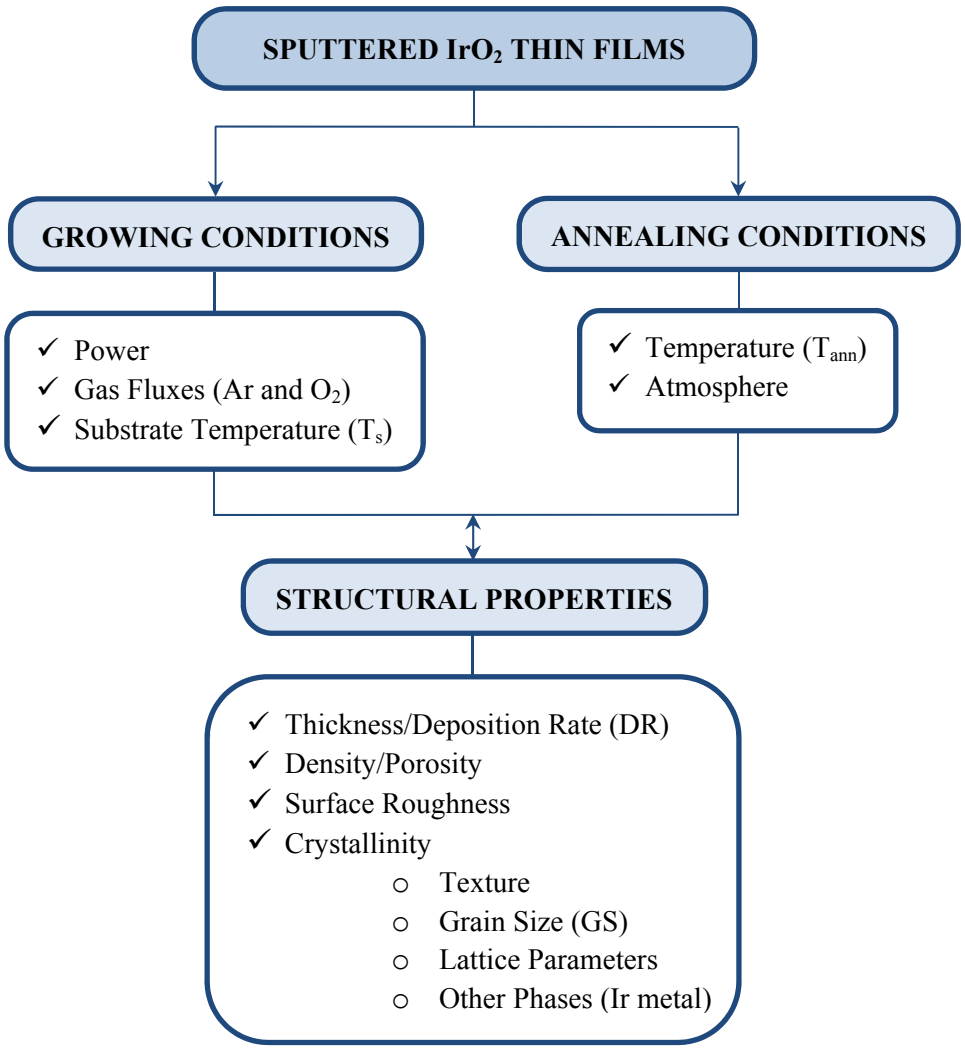

Figure 3.1 Scheme of parameters varied in the synthesis of IrO_2 thin films by RMS deposition and structural characteristics studied.

Concerning the structural characteristics, the films were first grown at RT with the main goal of having a good control over the thickness of the deposited layer (in other words, the deposition rate, DR) and to gain knowledge about the film density and surface roughness. Then, the crystallinity of several ~100 nm–thick samples was compared in terms of texture, grain size (GS), lattice parameters and presence of secondary phases (metallic Ir). For that to be possible, the films were either annealed or grown at high temperatures. Note that, as illustrated in Fig. 3.2, the as–grown samples at RT showed an amorphous–like diffractogram only exhibiting the broad

feature at 2θ ≈ 34º typical of IrO_2 [140, 143, 144]. Henceforth, all the diffraction patterns displayed (for samples grown at RT) correspond to annealed samples.

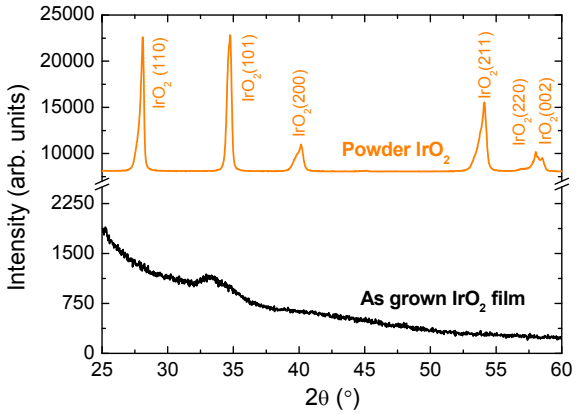

Figure 3.2 Representative diffractograms of an as–grown IrO_2 film at RT and commercial powder IrO_2 (*Sigma Aldrich*, 99.9% purity). The diffractograms are vertically shifted for the sake of clarity.

As one might expect, the amount of samples compared along this section is considerable in number. For the sake of making simpler this comparison, Table 3.1 is given as a compilation of the parameters employed for growing and annealing (if applied) each IrO_2 film. The main structural characteristics determined by X–ray reflectivity (XRR) and X–ray diffraction (XRD) are also included. As mention in Chapter 2, a precise quantitative analysis for the surface roughness could not be performed by XRR, and hence, the analysis of such parameter has been carried out in a more qualitative way.

It is noted that only the trends should be considered and not the absolute values of each growing parameter which are given throughout the chapter. The exact optimal values depend on the equipment and must be checked periodically as they may depend on other factors such as the target thickness, the materials deposited on the walls of the chamber, the performance of the magnetrons, etc.

Table 3.1: Synthesis parameters for IrO_2 films using different sputtering powers, Ar and O_2 fluxes, and substrate temperatures (T_s); as well as different annealing temperatures (T_{ann}) and atmospheres. The layer thickness (t) and film density are extracted from the XRR curves. The preferred orientation (in terms of the *Pref.* parameter, explained in section 2.4.1), grain size (GS), lattice parameters with their difference respect to bulk IrO_2 (ε_a and ε_c), and percentage of metallic Ir phase are extracted from XRD experiments.

Sample	**Power (W)**	**Ar Flux (ml/min)**	**O_2 Flux (ml/min)**	**T_s (ºC)**	**T_{ann} (ºC)**	**Ann. Atm.**	***t*** **(nm)**	**Density (g/cm^3)**	***Pref.***	**GS (nm)**	***a = b*** **(Å)**	**ε_a (%)**	***c*** **(Å)**	**ε_c (%)**	**Ir (%)**
IO_01	3.8	10	2.0	RT	–	–	44.8	10.0							
IO_02	6.0	10	2.0	RT	–	–	66.3	10.7							
IO_03	8.0	10	2.0	RT	–	–	85.6	11.2							
IO_04	3.9	10	3.0	RT	–	–	47.8	9.9							
IO_05	5.8	10	3.0	RT	–	–	67.5	10.3							
IO_06	8.2	10	3.0	RT	–	–	93.2	10.7							
IO_07	3.8	10	5.0	RT	–	–	50.4	9.5							
IO_08	5.9	10	5.0	RT	–	–	71.9	9.9							
IO_09	8.2	10	5.0	RT	–	–	98.2	10.0							
IO_10	3.6	11	2.0	RT	–	–	45.8	10.3							
IO_11	3.6	12	2.0	RT	–	–	48.7	10.3							
IO_12	3.5	13	2.0	RT	–	–	43.3	10.2							
IO_13	3.6	12	2.0	RT	600	O_2	98.1	11.2	0.97	8	4.500	0.0	3.152	-0.3	0.5
IO_14	5.9	12	2.0	RT	600	O_2	136.4	11.6	0.60	29	4.486	-0.3	3.127	-1.0	2.0
IO_15	7.9	12	2.0	RT	600	O_2	106.7	10.9	0.46	30	4.494	-0.1	3.128	-1.0	2.6
IO_16	7.9	12	2.0	RT	600	Air	107.3	11.1	0.63	24	4.487	-0.3	3.126	-1.1	2.5

Sample	Power (W)	Ar Flux (ml/min)	O_2 Flux (ml/min)	T_s (ºC)	T_{ann} (ºC)	Ann. Atm.	*t* (nm)	Density (g/cm^3)	*Pref.*	GS (nm)	*a = b* (Å)	ε_a (%)	*c* (Å)	ε_c (%)	Ir (%)
IO_17	21.5	12	2.0	RT	600	Air	91.9	11.6	0.91	16	4.508	0.2	3.152	-0.3	43.3
IO_18	3.8	10	2.0	RT	600	Air	91.8	10.8	0.88	9	4.490	-0.2	3.138	-0.7	2.6
IO_19	5.9	10	2.0	RT	600	O_2	101.9	10.7	0.58	20	4.495	-0.1	3.131	-0.9	9.1
IO_20	8.1	10	2.0	RT	–	–	107.5	10.7							
IO_21	8.1	10	2.0	RT	400	Air	97.8	11.0	0.54	27	4.492	-0.2	3.115	-1.4	6.3
IO_22	8.1	10	2.0	RT	500	Air	104.2	11.0	0.54	26	4.491	-0.2	3.118	-1.3	4.9
IO_23	8.1	10	2.0	RT	600	Air	98.7	11.1	0.54	29	4.491	-0.2	3.128	-1.0	14.0
IO_24	8.1	10	2.0	RT	600	O_2	101.5	10.9	0.55	33	4.492	-0.2	3.130	-0.9	9.4
IO_25	8.1	10	2.0	RT	600	Ar	100.0	10.9	0.70	24	4.480	-0.4	3.127	-1.0	16.8
IO_26	8.1	10	2.0	RT	700	Air	100.3	10.8	0.54	33	4.501	0.0	3.147	-0.4	22.1
IO_27	8.1	10	2.0	RT	800	Air	–	–	–	–	–	–	–	–	–
IO_28	3.7	10	5.0	RT	600	Air	92.7	10.3	0.94	11	4.498	0.0	3.147	-0.4	0.4
IO_29	5.8	10	5.0	RT	600	O_2	147.6	9.6	0.98	12	4.493	-0.2	3.145	-0.5	0.1
IO_30	8.1	10	5.0	RT	600	O_2	96.3	10.6	0.89	9	4.500	0.0	3.145	-0.5	0.2
IO_31	7.9	11	2.0	RT	600	Air	102.5	11.2	0.58	32	4.492	-0.2	3.127	-1.0	4.5
IO_32	7.9	13	2.0	RT	600	Air	106.5	11.0	0.64	18	4.490	-0.2	3.127	-1.0	1.2
IO_33	3.7	11	2.0	RT	600	Air	91.3	10.5	0.86	10	4.495	-0.1	3.143	-0.5	0.0
IO_34	3.5	13	2.0	RT	600	Air	95.9	10.7	0.91	11	4.496	-0.1	3.138	-0.7	0.8
IO_35	3.7	10	3.5	RT	600	Air	88.2	10.4	0.86	10	4.495	-0.1	3.143	-0.5	1.2
IO_36	3.6	12	5.0	RT	–	–	87.1	9.8							
IO_37	3.6	12	5.0	RT	400	Air	88.1	10.0	1.03	6	4.494	-0.2	3.120	-1.3	0.0

Sample	**Power (W)**	**Ar Flux (ml/min)**	**O_2 Flux (ml/min)**	**T_s (ºC)**	**T_{ann} (ºC)**	**Ann. Atm.**	***t*** **(nm)**	**Density (g/cm^3)**	***Pref.***	**GS (nm)**	***a = b*** **(Å)**	**ε_a (%)**	***c*** **(Å)**	**ε_c (%)**	**Ir (%)**
IO_38	3.6	12	5.0	RT	500	Air	85.6	10.2	1.11	8	4.496	-0.1	3.137	-0.7	0.0
IO_39	3.6	12	5.0	RT	600	Air	80.5	10.3	1.01	10	4.499	0.0	3.146	-0.4	0.0
IO_40	3.6	12	5.0	RT	600	O_2	80.5	10.8	1.04	10	4.500	0.0	3.147	-0.4	0.2
IO_41	3.6	12	5.0	RT	600	Ar	75.8	10.2	0.96	8	4.496	-0.1	3.142	-0.6	0.0
IO_42	3.6	12	5.0	RT	700	Air	79.7	9.7	1.01	13	4.497	-0.1	3.148	-0.4	0.1
IO_43	3.6	12	5.0	RT	800	Air	–	–	–	–	–	–	–	–	–
IO_44	8.2	10	2.5	RT	600	Air	105.3	11.6	0.83	11	4.494	-0.1	3.134	-0.8	1.7
IO_45	8.1	10	2.8	RT	600	Air	106.4	11.5	1.00	10	4.491	-0.2	3.140	-0.6	0.6
IO_46	8.1	10	3.5	RT	600	O_2	104.9	11.1	0.87	10	4.494	-0.1	3.146	-0.4	1.0
IO_47	7.8	13	2.0	200	–	–	108.5	11.5	–	8	–	–	–	–	–
IO_48	7.7	13	2.0	300	–	–	106.0	11.7	0.41	13	4.558	1.3	3.141	-0.6	0.0
IO_49	7.7	13	2.0	400	–	–	104.4	11.8	0.46	16	4.576	1.7	3.159	0.0	0.0
IO_50	7.7	13	2.0	450	–	–	80.0	11.7	0.56	14	4.553	1.2	3.160	0.0	11.02
IO_51	7.7	13	2.0	500	–	–	40.2	22.5	–	–	–	–	–	–	100.0
IO_52	7.7	13	4.0	500	–	–	37.7	21.8	0.82	9	4.504	0.1	3.156	-0.1	76.2
IO_53	7.4	13	13.0	500	–	–	71.7	11.8	0.37	15	4.523	0.5	3.151	-0.3	5.6

The error bar for the thickness and density measured by XRR was established at 0.5% and 4.0%, respectively, according to the research in Ref. [152]. The error bar in the parameters determined by XRD is shown in the comparisons made below. No convergence was found during Rietveld refining neither the sample grown at 200 ºC nor those annealed at 800 ºC, and no further information could be obtained with this technique from these samples.

3.2.1. Sputtering Power

When first films are synthesized with a new sputtering equipment, one of the most important parameters to be controlled is the output power, since critical properties such as DR or film density strongly depend on it. These parameters are easily determined from XRR experiments. Thus, Fig. 3.3(a) shows the XRR curves measured in three representative samples grown at different sputtering powers. It can be seen that, the higher the sputtering power, the higher number of oscillations in the same 2θ range, indicative of an increasing **DR**. On the other hand, a very small shift in the position of the critical angle, θ_c, towards greater 2θ values can be discerned as the sputtering power is increased, indicating a slightly greater film **density** at higher powers. Finally, a similar curve decay is observed in the three samples, which implies a comparable surface **roughness** regardless of the sputtering power.

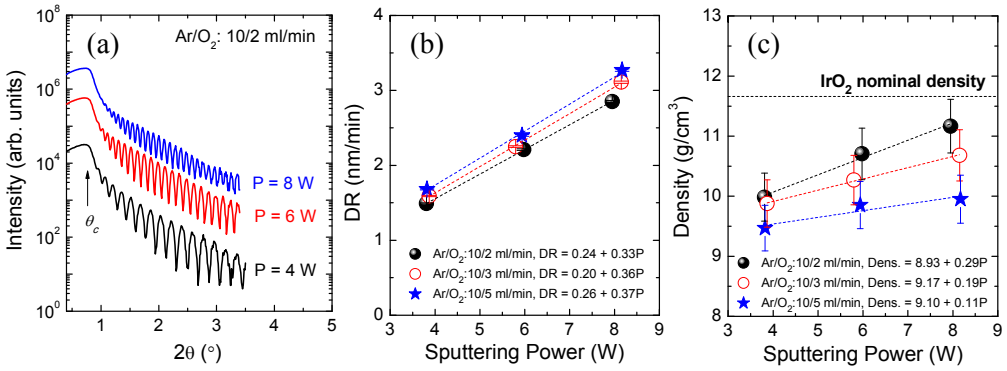

Figure 3.3 (a) Representative XRR curves measured in samples grown with different sputtering power for the same deposition time (30'). The curves are vertically shifted for clarity. Panels (b) and (c) show the dependence of DR and density with the sputtering power for three different O_2 fluxes. Dashed lines represent linear fits and dotted line in panel (c) is a reference for IrO_2 nominal density. Data correspond to the IO_01–09 samples in Table 3.1.

Precise information about the dependences of DR and density on the sputtering power was obtained by fitting the XRR curves. The **DR** (Fig. 3.3(b)) shows a linear increment with the sputtering power with a slope almost independent of the O_2 flux (~0.35 nm/minW). The film **density** (Fig. 3.3(c)) is in all the cases lower than the nominal one and also shows a linear increment with the sputtering power, though with

a more oxygen–dependent slope. Finally, a very small surface roughness (< 0.3 nm) is obtained regardless of the sputtering power.

The effect of the sputtering power on the sample crystallinity is reflected in Figs. 3.4(a) and 3.4(b), where the diffractograms of four different ~100 nm–thick films grown at 4, 6, 8 and 21 W, are compared. The diffraction patterns in Fig. 3.4(a) reveal a polycrystalline structure with well–defined diffraction peaks corresponding to the (110), (101), (200), (211), and (220) peaks of the rutile IrO_2 pattern, as those observed in bulk IrO_2 in Fig. 3.2. Moreover, it can be seen how the relative intensity of the (110) peak progressively increases with the sputtering power and the diffraction peaks become narrower. This indicates an increasing **preferred orientation** along such direction, as well as a greater **GS**, respectively. Regarding the **lattice parameters**, no clear dependence on the sputtering power can be inferred from the position of the diffraction peaks. However, a small shift in the Bragg positions towards greater angles (relative to those of bulk IrO_2) can be discerned for P = 6 and 8 W in all the visible peaks but in (110) and (220). This suggests slightly smaller values of the *c* parameter. Taking for instance the (101) reflection, a shift in 2θ around 0.2º respect to bulk IrO_2 is observed. Using Bragg's law and considering a = 4.50 Å (bulk value), such shift corresponds to a decrement in the *c* parameter around 0.03 Å.

In the diffractogram of the film grown with the highest sputtering power (21 W), two additional peaks at 2θ = 40.7º (111) and 2θ = 47.4º (200) identified as **metallic Ir phase** are clearly visible (Fig. 3.4(b)). On the other samples no secondary phase can be discerned. However, note that the (111) Ir–peak is located very close to the (200) IrO_2–peak (2θ = 40.2º) and it could be, either overlapped for small metallic Ir percentages, and/or confused with a peak displacement.

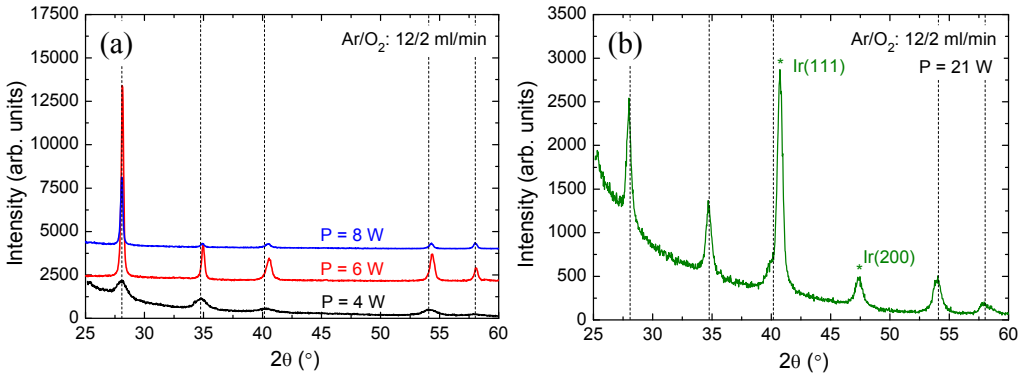

Figure 3.4 Representative diffractograms of ~100 nm–thick samples grown with (a) different and relatively low sputtering powers (from 4 to 8 W) and (b) with relatively high power (21 W). Dashed lines mark the diffraction peak positions of powder IrO_2. The diffractograms are vertically shifted for the sake of clarity. *Metallic Ir peaks. Data correspond to the IO_13–15, 17 samples in Table 3.1.

To obtain more precise information about the trends in the structural parameters mentioned above with the sputtering power, the diffractograms were Rietveld refined. The results from such refinements are given in Fig. 3.5. As for the **preferred orientation**, represented in Fig. 3.5(a), the refinements confirm that the samples become more textured along (110) when increasing the sputtering power. Similarly, it can be seen in Fig. 3.5(b) that the **GS** increases with the power. Nevertheless, the GS seems to be mainly dependent on whether the film is textured or not. In non–textured samples, a roughly constant GS ≈ 10 nm is obtained, while in textured samples the GS is found to be between 20 and 30 nm. Regarding the **lattice parameters**, represented in Fig. 3.5(c), no clear tendencies to increase or decrease when varying the sputtering power can be extracted, though a slightly smaller *c* parameter can be inferred as the sputtering power is increased. The refinements agree well with the estimation made above using the Bragg's law, obtaining in all the cases slightly smaller lattice parameters than those of bulk IrO_2, especially along *c*. The differences relative to the bulk values are given in Table 3.1 in terms of a *strain* parameter defined as follows:

$$\varepsilon(\%) = \frac{a_{film} - a_{bulk}}{a_{bulk}} * 100 \qquad (3.1)$$

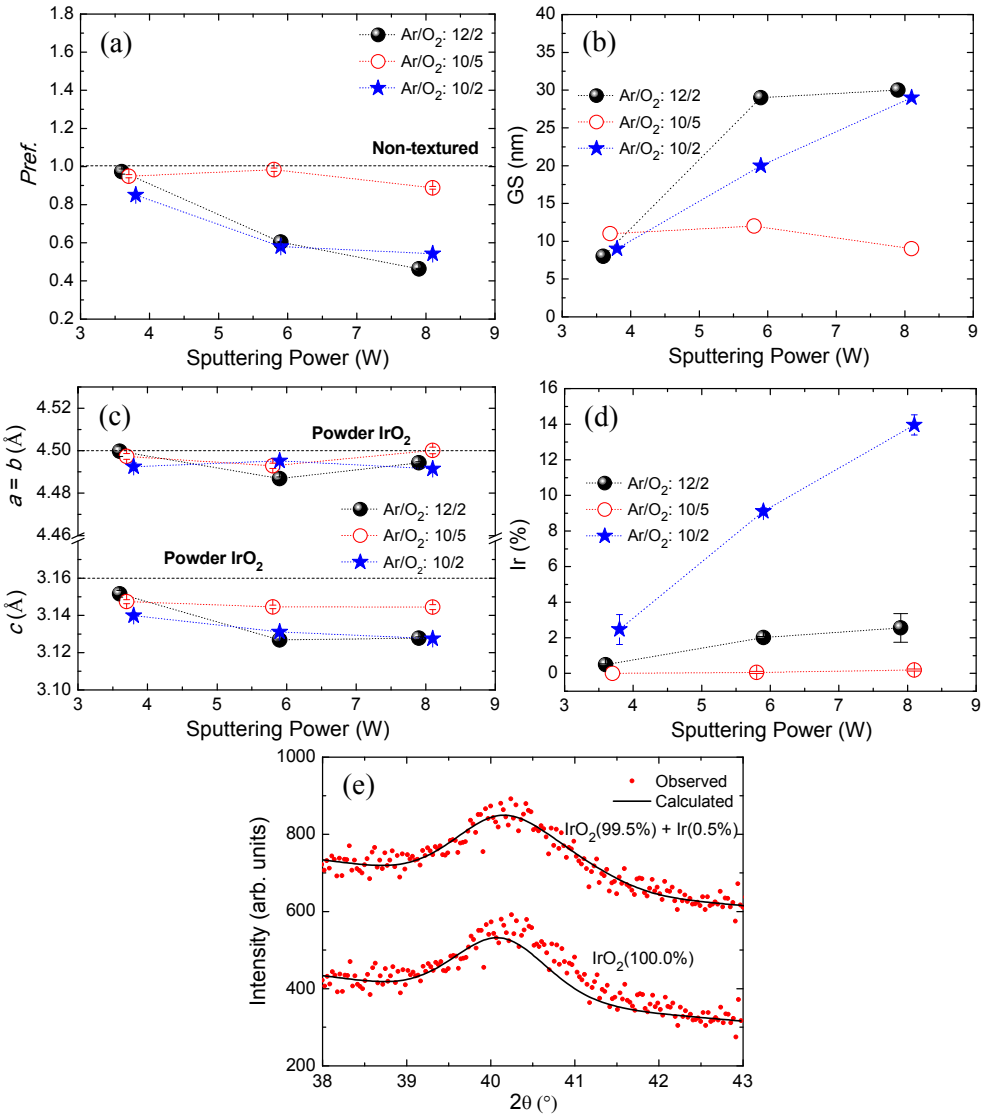

Figure 3.5 Influence of the sputtering power on the (a) preferred orientation, (b) GS, (c) lattice parameters, and (d) metallic phase concentration. Dashed lines are drawn in panel (a) as reference for *Pref.* = 1 (non–textured) and in panel (c) as references for the lattice parameters of powder IrO_2. Dotted lines are drawn as guides to the eye. Panel (e) shows a comparison of the Rietveld refinement for the IO_13 sample in the region from 2θ = 38–43º, depending on whether metallic Ir is included (0.5%) or not (R_{Bragg} parameter improves from 8.6 to 6.4%). Data correspond to IO_13–15, 18, 19, 23, 28–30 samples in Table 3.1. For clarity the sample grown at the highest power (21 W, IO_17) has not been included in the figure.

Thus, the values of ε obtained for these samples are between 0.0 and -0.3% in *a* and *b*, and between -0.3% and -1.0% in *c*. Note that there is a compressive strain in all the cases. Finally, as observed in Fig. 3.5(d), the **metallic Ir phase** is present in the majority of the samples, increasing almost linearly with the sputtering power. Additionally, the refinements indicate that the metallic phase grows preferentially along the (111) direction. This fact is actually what makes it not discernible directly over the diffractograms, since the expected (200) Ir–peak at $2\theta \approx 47^{\circ}$ is practically hidden and the (111) Ir–peak ($2\theta \approx 40.7^{\circ}$) overlaps with the (200) IrO_2–peak ($2\theta \approx 40.2^{\circ}$) (see Fig. 3.4(b)). Despite of that, the refinements are markedly improved after including the metallic phase, even for atomic percentages of Ir lower than 1%. As an example, Fig. 3.5(e) compares a detailed region around $2\theta = 40^{\circ}$ with the refinements performed using a single phase (IrO_2) or a phase mixture (Ir + IrO_2) in a sample with 0.5 at.% Ir (IO_13) according to the refinements.

Returning to the analysis of the film density differences, taking for instance the IO_13 sample (P = 4 W), a metallic Ir content of 0.5% would imply a film density of 11.7 g/cm^3. This is in contrast with the value of 11.2 g/cm^3 determined from XRR experiments. In order to explain such difference (~4.5%) between the estimated and experimental values, the effect of **porosity** must also be considered. If the same calculations are now performed in the IO_15 sample (P = 8 W), a difference of around 2% is observed between the estimated and experimental density. This fact suggests that, the higher the sputtering power, the lower porosity.

Further confirmation of this trend is observed in the cross–sectional TEM images displayed in Figs. 3.6(a) and 3.6(b), recorded in representative as–grown samples synthesized at 4 W and 8 W, respectively. These images show that the sample grown at 4 W is more porous and inhomogeneous than that grown at 8 W. As the pictures correspond to amorphous samples, the different gray scales cannot be associated to different crystal orientations. Besides, no other IrOx phase than IrO_2 is known. Therefore, the whitish areas in Fig. 3.6(a) (marked with arrows) can be associated to **porosity**, which agrees well with the less density observed in the samples grown at lower sputtering powers and with the calculations made above.

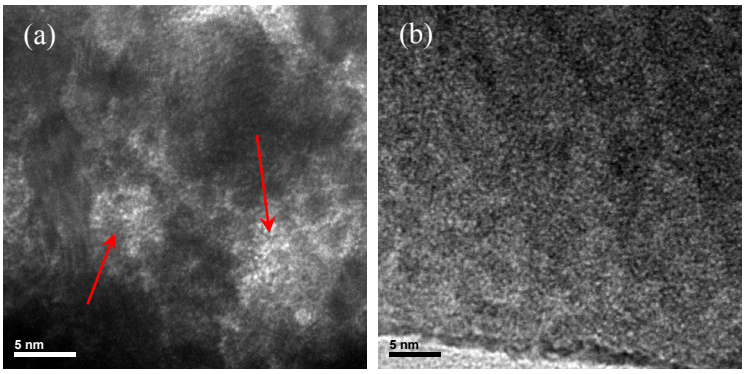

Figure 3.6 Illustrative TEM images taken in representative as–grown samples deposited (a) at P = 4 W, IO_04; and (b) at P = 8 W, IO_03.

The results obtained in this subsection, summarized in Table 3.2, can be explained in terms of atom mobility: at higher sputtering powers the bombarding ions have higher kinetic energy, and due to momentum transfer, the target atoms are more easily sputtered out, increasing thereby the **DR**. Similarly, at higher sputtering powers the ejected atoms also obtain more kinetic energy for surface diffusion when they arrive at the substrate, leading to less **porous** films (greater **density**). This fact also increases the probability of the atoms to reach equilibrium positions ((110) is the lowest energy plane for IrO_2 [153]), thus improving the film crystallinity (**texture** and **GS**) [154]. On the other hand, the more atoms ejected from the target, the more O_2 needed to oxidize them all, and hence, for a given atmosphere the percentage of **metallic Ir** in the film tends to increase. Finally, changing the sputtering power does not have any significant effect neither on the surface **roughness** nor on the **lattice parameters**, although smaller values than those measured in powder IrO_2 are observed, especially along *c*.

Table 3.2: Summary of the effects of increasing the sputtering power on the properties of IrO_2 thin films. Symbol (~) stands for roughly independent.

	DR	**Density**	**Roughness**	**Crystallinity**	**Latt. Parameters**	**% Ir**
P (↑)	↑	↑	~	↑	~	↑

3.2.2. Argon Flux

Several series of films were grown under different Ar fluxes to study its effect on the structure of IrO_2 films. As shown in Figs. 3.7(b) and 3.7(c), the **DR** is mainly independent on the Ar flux and the **density** slightly decreases. As for the surface **roughness**, the XRR curve decay is more pronounced as the Ar flux is increased (Fig. 3.7(a)), indicative of greater roughness. Indeed, the fits indicate an increment in the surface roughness from < 0.3 nm for 10 ml Ar/min, up to ~1.0 nm for 13 ml Ar/min.

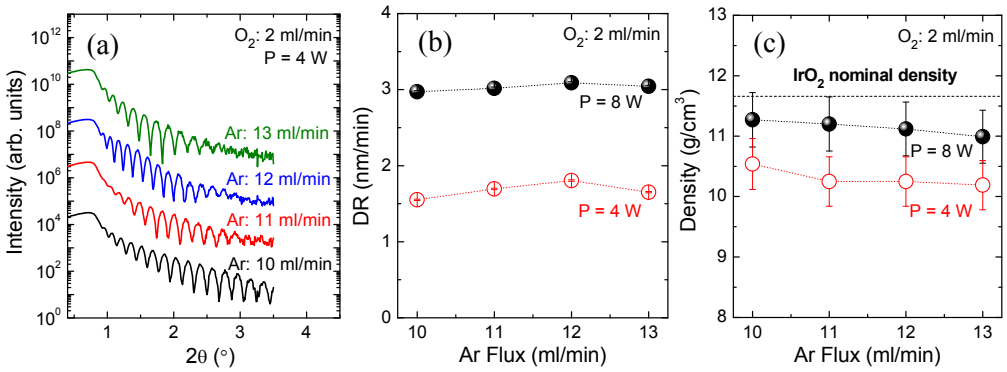

Figure 3.7 (a) XRR curves measured in representative samples grown with different Ar fluxes for the same deposition time (30'). The curves are vertically shifted for clarity. Panels (b) and (c) show the dependence of the DR and density with the Ar flux, respectively. Dashed lines are guides to eye and dotted line in panel (c) is a reference for the IrO_2 nominal density. The results have been conveniently normalized to remove the dependence with the power.[2] Data correspond to the IO_01, 10–12, 16, 23, 31, 32 samples in Table 3.1.

The diffractograms obtained in representative samples grown under different Ar fluxes are shown in Figs. 3.8(a) and 3.8(b) for a sputtering power of 4 and 8 W, respectively. The results from the Rietveld analyses are displayed in Figs. 3.8(c)–(f), where two additional samples grown at 6 W are also included for completeness. Regarding the **preferred orientation**, the trends in Fig. 3.8(c) indicate that the texture is slightly lost as the Ar flux is increased.

[2] As mentioned in section 2.1.2, small differences in the output power are obtained. Using the expressions in Fig. 3, the output power is normalized to 4 or 8 W, as appropriate.

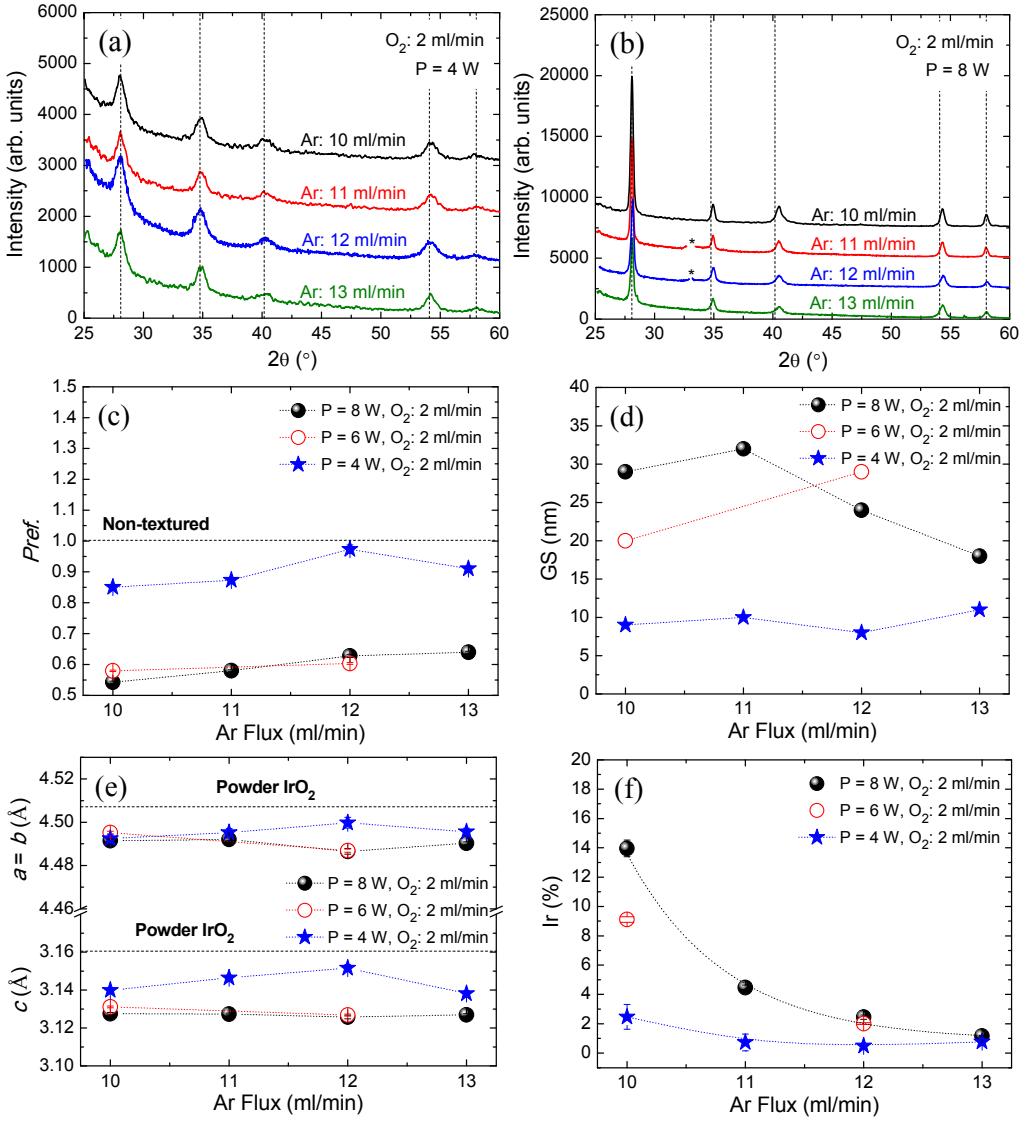

Figure 3.8 Diffractograms of ~100 nm–thick samples grown using different Ar fluxes for (a) P = 4 W and (b) P = 8 W. Dashed guidelines mark the diffraction peak positions of powder IrO_2. *Substrate peak removed for clarity. The diffractograms are vertically shifted for the sake of clarity. Panels (c)–(f) show the influence of the Ar flux on the preferred orientation, GS, lattice parameters, and metallic phase concentration, respectively. Dashed lines are drawn in panel (c) as reference for *Pref.* = 1 (non–textured) and in panel (e) as references for the lattice parameters of powder IrO_2. Dotted lines are guides to the eye. Data correspond to the IO_13, 14, 16, 18, 19, 23, 31–34 samples in Table 3.1.

As for the **GS** in Fig. 3.8(d), in non–textured samples it is found to be around 10 nm irrespective of the Ar flux. On the contrary, for textured samples (*i.e.*, the samples grown at higher powers) the trend in Fig. 3.8(d) indicates that the increment of the Ar flux reduces the GS (note that the sample grown at 6 W and 12 ml Ar/min has a greater thickness, hence its greater GS). As far as the **lattice parameters** are concerned, a clear dependence with the Ar flux is not detected within the probed range (Fig. 3.8(e)). Again, smaller lattice parameters than those of bulk IrO_2 are found: ε_a remains between 0.0 and -0.3%, and ε_c between -0.3 and -1.4%. Differently, the presence of **metallic Ir** within the film is importantly affected by the Ar flux. As shown in Fig. 3.8(f), there is a drastic reduction of the metallic phase percentage as the Ar flux is increased. In the sample series grown at 8 W, the metallic Ir percentage is reduced from ~14% when using 10 ml Ar/min, to ~1% when using 13 ml Ar/min.

Some of these trends were further confirmed by microscopy techniques. Fig. 3.9 compares surface FE–SEM images recorded in samples grown under different Ar fluxes. It can be seen that the sample grown with 10 ml Ar/min (Fig. 3.9 (a)) presents a **smoother** surface and greater **GS** respect to the sample grown with 13 ml/min (Fig. 3.9(b)). Moreover, from these images it can be seen that the GS is not homogeneous, with crystallite sizes ranging from a few nanometers up to ~200 nm in the sample grown with 10 ml/min, and up to ~100 nm in the sample grown with 13 ml/min.

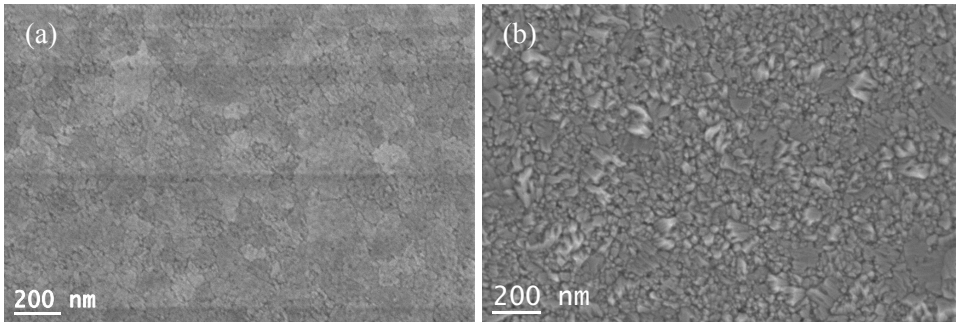

Figure 3.9 Illustrative FE–SEM images recorded in samples grown under different Ar fluxes: (a) 10 ml Ar/min (IO_23) and (b) 13 ml Ar/min (IO_32).

The remarkable difference between the average (out–of–plane) crystallite size determined from XRD and the GS observed in the surface SEM images confirms the

platy–like shape of the grains, in agreement with the values of the *Pref.* parameter (< 1) obtained from XRD.

The trends observed in the structural parameters of the IrO_2 films when increasing the Ar flux, summarized in Table 3.3, can be explained as follows: greater Ar fluxes increase the ion bombardment on the target surface. This boosts more target atoms to be ejected, but, at the same time, increases the atomic collisions, thus resulting in an essentially constant **DR**. These collisions also reduce the kinetic energy of the atoms when they arrive at the substrate surface, increasing the film **porosity** (less **density**) and the surface **roughness** [155–157]. The loss of kinetic energy also hinders the Ir atoms from reaching equilibrium positions. This causes the **texture** (if textured) to be slightly lost and the **GS** progressively decreases (worse crystallinity). Nevertheless, the advantage of increasing the atomic collisions is an enhanced probability of the Ir atoms to interact with the reactive gas (O_2). This leads to a drastic reduction in the **metallic phase** percentage within the film when increasing the Ar flux.

Table 3.3: Summary of the effects of increasing the Ar flux on the properties of IrO_2 thin films. Symbol (~) stands for roughly independent.

	DR	**Density**	**Roughness**	**Crystallinity**	**Latt. Parameters**	**% Ir**
Ar (↑)	~	↓	↑	↓	~	↓

3.2.3. Oxygen Flux

To study the influence of the O_2 flux in the DR, density and surface roughness, XRR curves (Fig. 3.10(a)) were recorded on samples synthesized using different O_2 fluxes for a given sputtering power (4, 6 or 8 W). It can be seen in Fig. 3.10(b) that the **DR** slightly increases with the O_2 flux, with a variation smaller than 10% in the probed range. This is somehow an unusual result, as typically more oxygen is translated into lower DRs [158–161]. As for the film **density**, it decreases almost linearly with the O_2 flux (Fig. 3.10(c)). Finally, the faster decay rate of the XRR curves for greater O_2 fluxes indicates greater surface **roughness**. Despite of that, the

deposited films still have a good surface quality, since the fittings indicate a surface roughness < 0.3 nm in these samples.

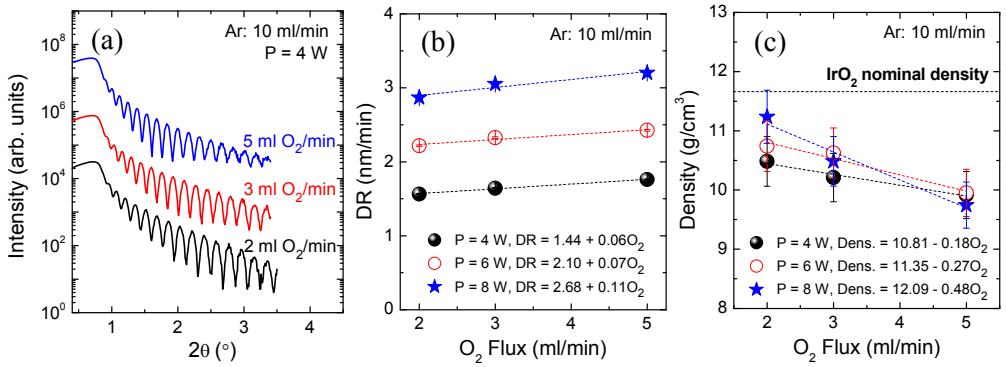

Figure 3.10 (a) XRR curves measured in representative samples grown with different O_2 fluxes for the same deposition time (30'). The curves are vertically shifted for clarity. Panels (b) and (c) show the dependence of the DR and density with the O_2 flux, respectively. Dashed lines represent linear fits and dotted line in panel (c) is a reference for the IrO_2 nominal density. The results have been conveniently normalized to remove the dependence with the power (explained in section 3.2.2). Data correspond to the IO_01–09 samples in Table 3.1.

The diffractograms measured in representative samples grown under different O_2 fluxes are given in Figs. 3.11(a) and 3.11(b) for a sputtering power of 4 and 8 W, respectively. The trends obtained from the Rietveld analyses are shown in Figs. 3.11(c)–(f), where two additional samples grown at 6 W, and two samples grown at 4 W and greater Ar flux (12 ml Ar/min), are also included for completeness. The results show that a substantial (110) **preferred orientation** is obtained only with the lowest O_2 flux (2 ml/min) and provided P ≥ 6 W (Fig. 3.11(c)). For greater O_2 fluxes the texture is lost regardless of the sputtering power. The drastic influence on the texture has a concomitant effect on the **GS** (Fig. 3.11(d)) [162, 163]: a relatively high GS (20–30 nm) is obtained only with the lowest O_2 flux (2 ml/min) and provided P ≥ 6 W. For O_2 fluxes greater than 2 ml/min, all the samples show a roughly constant GS ≈ 10 nm. As for the **lattice parameters**, no dependence with the O_2 flux is found (Fig. 3.11(e)). All the samples show lattice parameters smaller than those of bulk IrO_2, being this difference larger for the *c* parameter (the values of ε are around -0.2% in *a* and *b*, and from -0.3% to -1.0% in *c*).

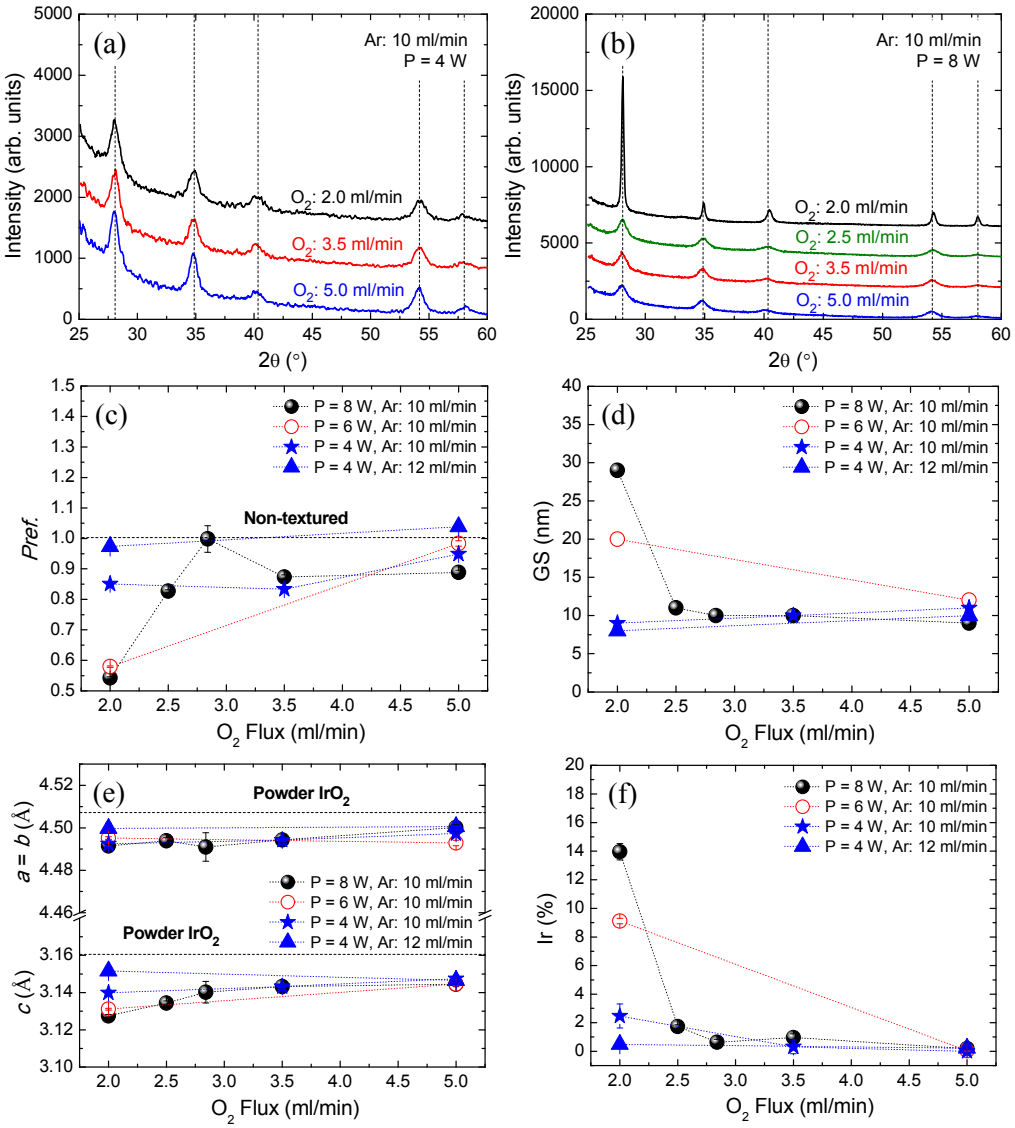

Figure 3.11 Diffractograms of ~100 nm–thick samples grown using different O_2 fluxes for (a) P = 4 W and (b) P = 8 W. Dashed guidelines mark the diffraction peak positions of powder IrO_2. The diffractograms are vertically shifted for clarity. Panels (c)–(f) show the influence of the O_2 flux on the preferred orientation, GS, lattice parameters, and metallic phase concentration, respectively. Dashed lines are drawn in panel (c) as a reference for *Pref.* = 1 (non–textured) and in panel (e) as references for the lattice parameters of powder IrO_2. Dotted lines are guides to the eye. Data correspond to the IO_13, 18, 19, 23, 28–30, 35, 39, 44–46 samples in Table 3.1.

Finally, the formation of **metallic Ir** decreases drastically as the O_2 flux is increased (Fig. 3.11(f)). For 2 ml O_2/min, the Ir content strongly depends on the sputtering power (already shown in section 3.2.1). For an O_2 flow ≥ 2.5 ml/min the Ir content is in all the cases smaller than 2% regardless of the sputtering power and tends to decrease as the O_2 flux is further increased.

The influence of the O_2 flux in the sample characteristics is summarized in Table 3.4. The increase of the O_2 flux results in greater **porosity** (lower **density**) and surface **roughness**, and worse–crystallized samples (**texture** and **GS**). This may be due to bombardment of oxygen on the growing film itself [95, 164–167]. Moreover, the greater O_2 pressure in the sputtering chamber obviously contributes to reduce the **metallic Ir** content within the film, further contributing to reduce the film **density**.

Table 3.4: Summary of the effects of increasing the O_2 flux on the properties of IrO_2 thin films. Symbol (~) stands for roughly independent.

	DR	**Density**	**Roughness**	**Crystallinity**	**Latt. Parameters**	**% Ir**
O_2 (↑)	↑	↓	↑	↓	~	↓

In view of the results obtained in sections 3.2.1, 3.2.2 and 3.2.3, it is clear that there are two competing trends in the synthesis of sputtered IrO_2 films by RSM at RT: increasing the sputtering power or decreasing the gas pressure (Ar or O_2) produces **better–crystallized** samples; however, both, the formation of **metallic phase**, as well as an increment in the surface **roughness**, are also promoted. This issue strongly limits the working conditions if a textured film is required. In fact, in our chamber the sputtering power must be set between 6 and 8 W and the Ar and O_2 fluxes fixed at 13 and 2 ml/min, respectively, to obtain polycrystalline textured samples with a reasonable amount of metallic Ir (< 1%) and surface roughness (< 1.5 nm). Nevertheless, for polycrystalline non–textured samples, there is a wide range of growing parameters that give rise to such microstructure with few metallic Ir and good roughness. This fact also allows classifying the "RT samples" into two groups: non–textured and (110)–textured. In the first group a roughly constant GS around 10 nm is

obtained in all the cases, while in the second group the GS ranges from 20–30 nm approximately.

3.2.4. Annealing Temperature (T_{ann})

The effect of the annealing temperature (T_{ann}) on the DR, density and surface roughness, is summarized in Figs. 3.12(a) and 3.12(b) (XRR curves), and in Figs. 3.12(c) and 3.12(d) (fitted parameters), where representative samples from both groups, non–textured and (110)–textured, are shown.[3]

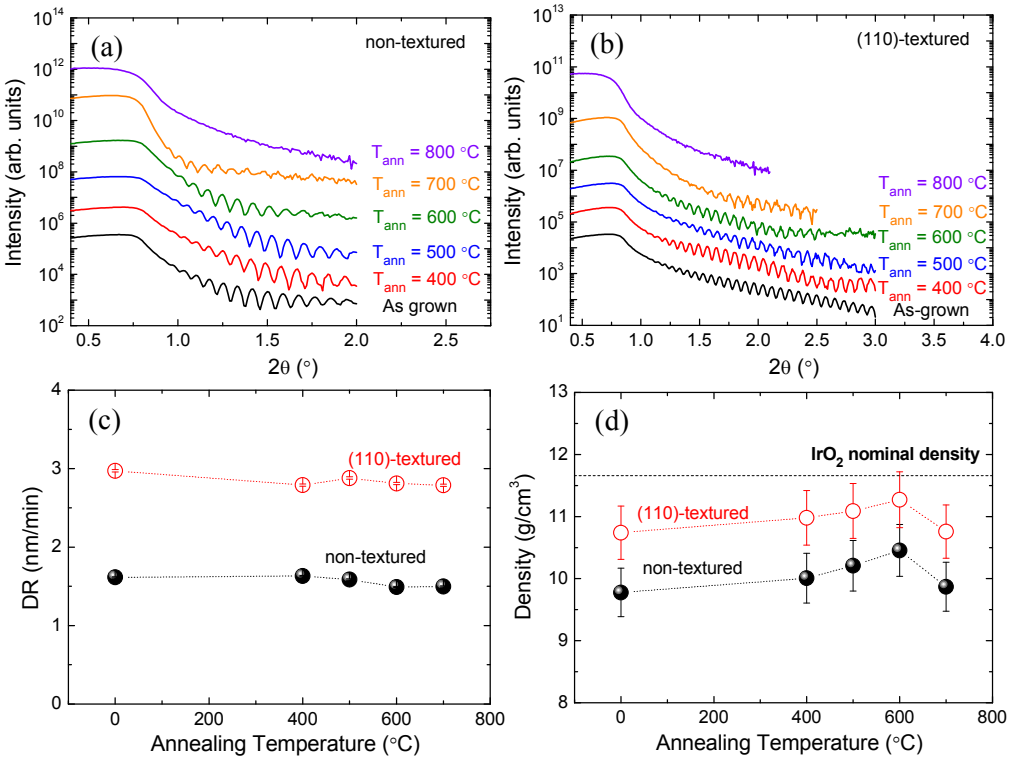

Figure 3.12 XRR experiments carried out in representative (a) non–textured and (b) (110)–textured samples annealed at different temperatures. The curves are vertically shifted for the sake of clarity. Panels (c) and (d) show the dependence of DR and density with T_{ann}. Dashed lines are guides to the eye and dotted line in panel (d) is a reference for the IrO_2 nominal density. Data correspond to the IO_20–23, 26, 27, 36–39, 42, 43 samples in Table 3.1.

[3] As proved below, little differences are obtained when using air or oxygen atmospheres for the annealing treatment. Thus, the influence of T_{ann} was studied solely using air.

As T_{ann} increases, there are a slight reduction in the thickness (**DR**) of the samples and a small increase in their **density**, approaching that of nominal IrO_2.[4] Nevertheless, for T_{ann} = 700 ºC there is a break on this trend and for T_{ann} = 800 ºC no oscillations are observed, suggesting the formation of volatile IrO_3 [143, 146]. As for the surface **roughness**, it progressively increases up to T_{ann} = 600 ºC, where a surface roughness around 1.5 and 1.0 nm are found in the non–textured and (110)–textured samples, respectively. Then, for T_{ann} = 700 ºC there is a rapid increment in the roughness of the films, as inferred for the faster decay rate of the XRR curves.

Figs. 3.13(a) and 3.13(b) show the diffractograms obtained in representative non–textured and (110)–textured samples, respectively, annealed at different temperatures. The results from the Rietveld refinements are given in Figs. 3.13(c)–(f). Regarding the **preferred orientation**, all the samples from the first group present a non–textured rutile–like structure, while all the samples from the second group are (110)–textured. The degree of texture does not depend on T_{ann} (Fig. 3.13(c)). On the contrary, the **GS**, represented in Fig. 3.13(d), does increase when increasing T_{ann} in the 400–700 ºC range, from 6 to 13 nm in the non–textured samples, and from 28 to 33 nm in the (110)–textured samples. Above this temperature, at 800 ºC, few IrO_2 was obtained, in agreement with the XRR experiments. On the other hand, as shown in Fig. 3.13(e), there is a slight increment in the **lattice parameters** as the annealing temperature is increased, becoming closer to those of powder IrO_2. ε_c evolves in both types of samples from around -1.3% for T_{ann} = 400 ºC to -0.4% for T_{ann} = 700 ºC. *a* and *b* remain similar to powder IrO_2 in all the temperature range. Finally, it can be seen in Fig. 3.13(b) that the formation of **metallic Ir** is favored at higher temperatures. In fact, the (111) Ir diffraction peak ($2\theta \approx 40.7$) is easily distinguished from the (200) IrO_2 peak ($2\theta \approx 40.2º$) in the (110)–textured sample annealed at 700 ºC. More specifically, in Fig. 3.13(f), it can be seen that, although the metallic phase does not arise in the non–textured samples (Ir(%) < 0.1%), in the (110)–textured films the percentage of metallic Ir increases from 6 to 22% in the 400–700 ºC range.

[4] Relative to the as–grown values, the reduction of the thickness is found to be always < 10% and the increase of the density < 6%.

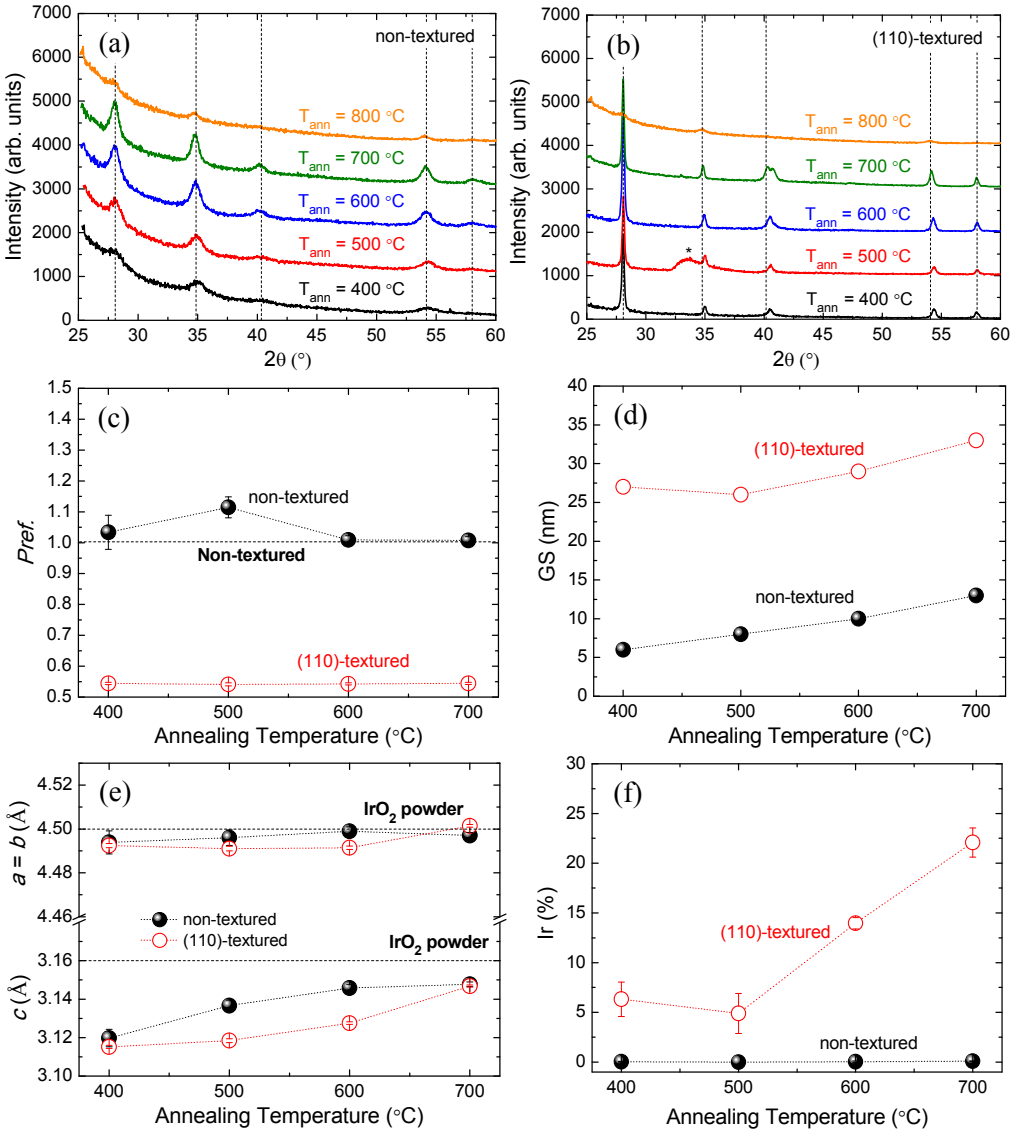

Figure 3.13 XRD measurements as a function of T_{ann} for representative (a) non–textured and (b) (110)–textured samples. *Si substrate. Dashed guidelines mark the diffraction peak positions of powder IrO_2. The diffractograms are vertically shifted for the sake of clarity. Panels (c)–(f) show the influence of T_{ann} on the preferred orientation, GS, lattice parameters, and metallic phase concentration, respectively. Dashed lines are drawn in panel (c) as reference for *Pref.* = 1 (non–textured) and in panel (e) as references for the lattice parameters of powder IrO_2. Dotted lines are guides to the eye. Data correspond to the IO_21–23, 26, 27, 37–39, 42, 43 samples in Table 3.1.

It is thus concluded (Table 3.5) that the annealing treatment produces a small variation in both, **thickness** (reduction) and **density** (increase), respect to the as–grown films, which is probably due to a slight film compaction by reducing internal defects. Such increase in the film density is greater at higher temperatures, provided that $T_{ann} \leq 600$ ºC. Furthermore, the annealing process is accompanied by an increment of the surface **roughness**, which is accentuated as T_{ann} increases.

The recrystallization is a thermally activated process and, as the temperature is raised, the grain growth is favored, thus reducing the internal energy by decreasing the total area of grain boundaries. Thus, as T_{ann} is increased up to 700 ºC the **GS** progressively increases and the **lattice parameters** approach those of bulk IrO_2. On the other hand, the **texture** of the films seems not to be much affected by T_{ann}. Finally, it has been seen that the formation of **metallic Ir** is favored at higher T_{ann}. This, however, only happens when nucleation of metallic phase has been produced during deposition of the films, and its growth is energetically favored during annealing at the expense of the oxidized phase. Notwithstanding this, above 700 ºC, few IrO_2 is obtained due to the formation of the volatile oxide phase, IrO_3 [143, 146].

Table 3.5: Summary of the effects of the annealing temperature on the properties of IrO_2 thin films. Symbol (~) stands for roughly independent.

	DR	**Density**	**Roughness**	**Crystallinity**	**Latt. Parameters**	**% Ir**
T_{ann} (↑)	~	↑	↑	↑	↑	↑

Therefore, although the annealing treatment at 700 ºC enhances the sample crystallinity, the markedly worse surface roughness, the high probably of volatile IrO_3 to be formed, as well as the fact that the growth of the metallic phase is favored, makes $T_{ann} = 600$ ºC a more appropriated annealing temperature.

3.2.5. Annealing Atmosphere

In order to find the optimum annealing atmosphere, representative samples were annealed under oxygen, air and argon (*i.e.*, oxidizing to reducing atmospheres). Figs. 3.14(a) and 3.14(b) show XRR curves measured in representative non–textured

and (110)–textured samples, respectively, annealed under these atmospheres. The **DR** and **density** extracted from such curves (Figs. 3.14(c) and 3.14(d), respectively) are found to be mainly independent on this parameter.

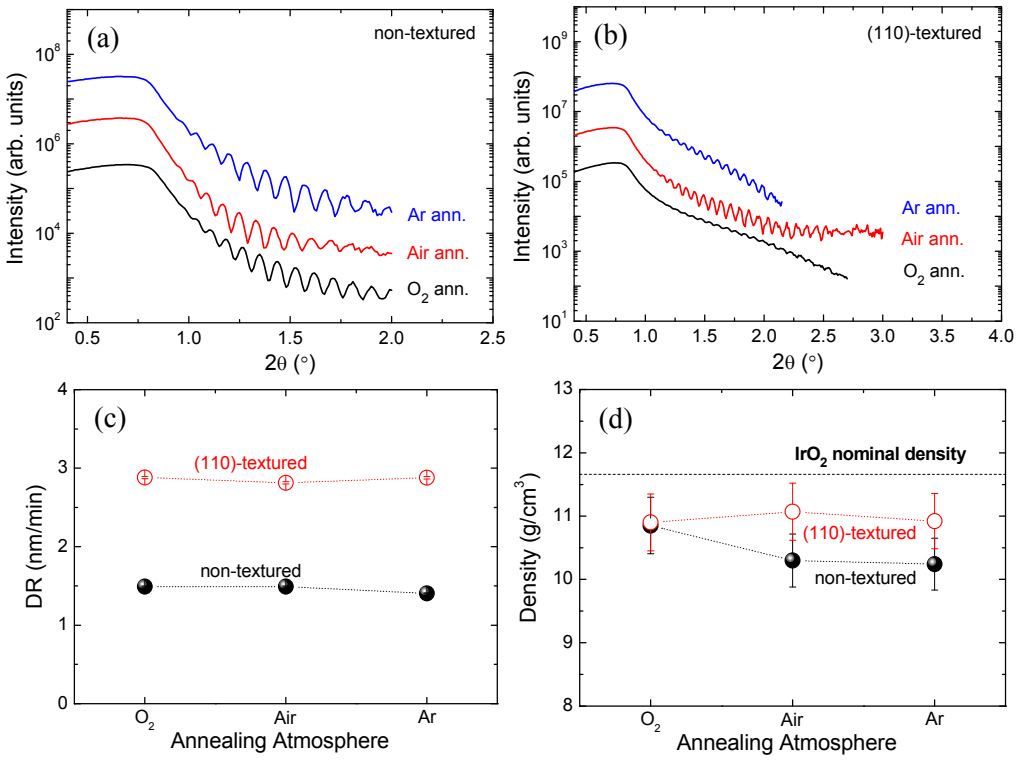

Figure 3.14 XRR experiments carried out in representative (a) non–textured and (b) (110)–textured samples annealed under different atmospheres. The curves are vertically shifted for clarity. Panels (c) and (d) show the dependence of DR and density with the annealing atmosphere, respectively. Dashed lines are guides to the eye and dotted line in panel (d) is a reference for the IrO_2 nominal density. Data correspond to the IO_23–25 and IO_39–41 samples in Table 3.1.

In addition, the curve decay is also not much affected by the atmosphere, obtaining a roughly constant surface **roughness** around 1.5 nm in non–textured samples, and ~1.0 nm in (110)–textured samples.[5]

At first sight, the recorded diffractograms seem to be independent **on the annealing atmosphere** for both, non–textured, Fig. 3.15(a), and (110)–textured samples, Fig. 3.15(b). Nevertheless, some small differences can be inferred. Regarding the **preferred orientation**, it is observed that the annealing atmosphere has only a minor effect. The non–textured samples show all similar random orientation of the grains regardless of the annealing atmosphere, while in textured samples the preferred orientation tends to be loosened when using an Ar (Fig. 3.15(c)). Similarly, it can be seen in Fig. 3.15(d) that there is a negligible influence of the gas in the **GS** of non–textured samples (remaining around 10 nm), though for textured films the GS decreases from 33 to 24 nm (~27% reduction) as more reducing atmosphere is used. The **lattice parameters**, represented in Fig. 3.15(e), are shown to be mainly independent on the atmosphere (the variations obtained are $< 0.3\%$). Finally, as observed in Fig. 3.15(f), the **metallic phase** does not arise ($\leq 0.2\%$) in non–textured samples regardless of the annealing atmosphere. On the contrary, in textured samples the atmosphere seems to play an important role, since the metallic phase percentage considerable increases as a more reducing atmosphere is used, from 9.4% in O_2 up to 16.8% in Ar.

[5] The apparent difference observed in the profile of the textured samples is not related to the IrO_2 films but to the substrate roughness, probably due to external contamination before deposition.

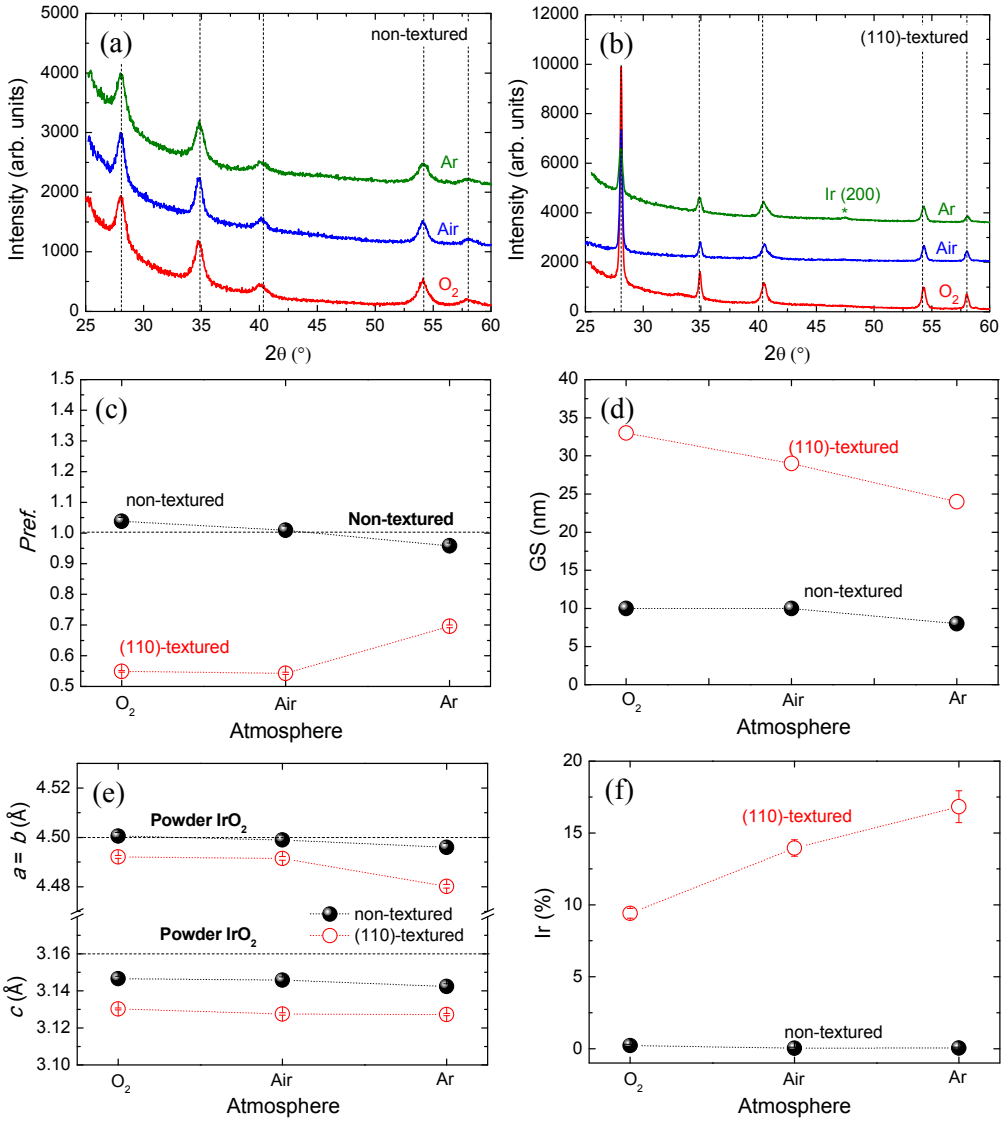

Figure 3.15 XRD measurements as a function of the annealing atmosphere for representative (a) non–textured and (b) (110)–textured samples. Dashed guidelines mark the diffraction peak positions of powder IrO_2. The diffractograms are vertically shifted for the sake of clarity. Panels (c)–(f) show the influence of the annealing atmosphere on the preferred orientation, GS, lattice parameters, and metallic phase concentration, respectively. Dashed lines are drawn in panel (c) as reference for *Pref.* = 1 (non–textured) and in panel (e) as references for the lattice parameters of powder IrO_2. Dotted lines are guides to the eye. Data correspond to the IO_23–25 and IO_39–41 samples in Table 3.1.

Therefore, it has been seen that the annealing atmosphere (see Table 3.6) has a negligible effect on determining the structural properties of non–textured samples. However, in textured films the annealing atmosphere does play an important role. A more reducing atmosphere hinders **texture** and relatively large **GSs**. Besides, annealing in a reducing atmosphere favors the formation of **metallic phase** when nucleation has been produced during deposition of the films, as happened with increasing T_{ann}.

Table 3.6: Summary of the effects of the annealing atmosphere on the properties of IrO_2 thin films. Symbol (~) stands for roughly independent.

	DR	Density	Roughness	Crystallinity	Latt. Parameters	% Ir
Atm. (↑ox.)	~	~	~	↑	~	↓

In conclusion, the results evidence that the annealing atmosphere has not a remarkable influence in the sample characteristics, especially when using oxygen or air. Hence, the annealing treatment was systematically performed in air atmosphere for the sake of readiness and availability.

3.2.6. Substrate Temperature (T_s)

Finally, to study the influence of the substrate temperature, T_s, several 100 nm–thick (nominal) samples were grown at different T_s without any further annealing treatment. The sputtering power was set at ~8 W and the Ar and O_2 fluxes were fixed at 13 and 2 ml/min, respectively. According to the results obtained in previous subsections, the samples with the best crystallinity/metallic Ir and surface roughness compromise are obtained under these conditions.

In Fig. 3.16(a), the very similar XRR profile discerned for $T_s \leq 400$ ºC indicates IrO_2 films with similar structure, while the disparity of the curve recorded in the sample grown at $T_s = 500$ ºC indicates the formation of a different phase. Note that the sample grown at $T_s = 450$ ºC shows an intermediate profile. More in detail, in the 200 to 400 ºC range there is a small reduction in the **DR**, from 5.4 to 5.2 nm/min (Fig. 3.16(c)). Above 400 ºC, the DR decreases dramatically down to 2.0 nm/min for $T_s =$

500 ºC.[6] On the other hand, the film **density** slightly increases in the 200 to 400 ºC range, from 11.5 to 11.8 g/cm^3, and then it rapidly increases up to 22.5 g/cm^3 for T_s = 500 ºC. Finally, the surface **roughness** is found to be between ~2.0 nm for $T_s \leq 400$ ºC, and ~2.5 nm for T_s = 500 ºC.

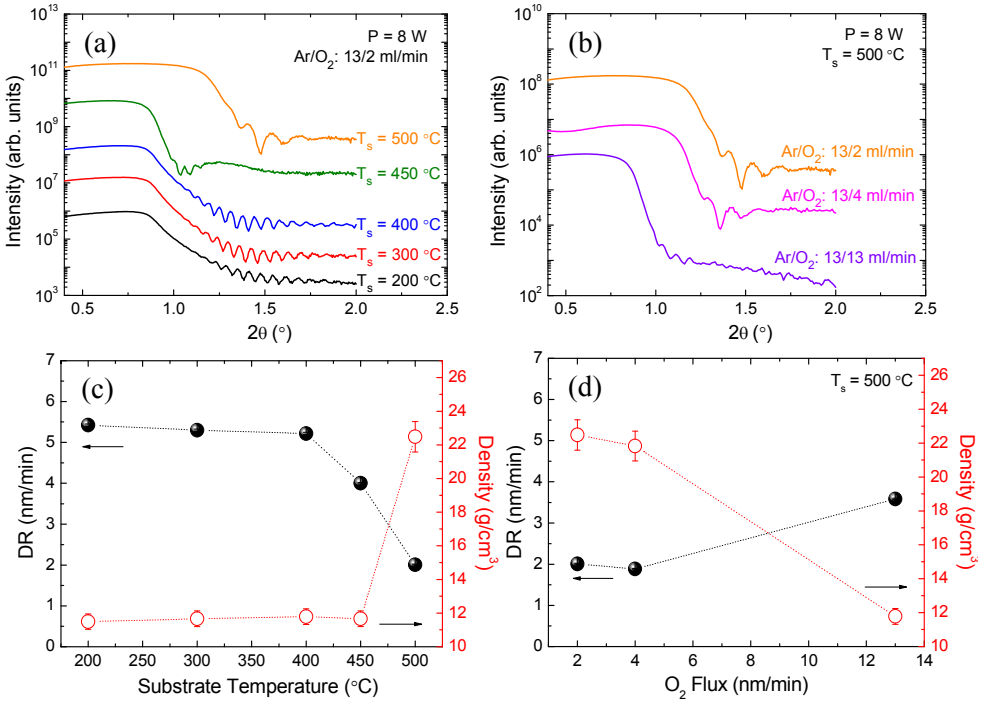

Figure 3.16 XRR measurements on samples grown at high T_s with (a) both gas flows fixed and different T_s, and (b) varying the O_2 flux while fixing T_s at 500 ºC. The curves are vertically shifted for clarity. Accordingly, panels (c) and (d) show the dependence of the DR and density with T_s. The same deposition time (20') and sputtering power was used in all the samples. Dashed lines are guides to the eye. Data correspond to the IO_47–53 samples in Table 3.1.

Both the drastic reduction of the DR (the ratio of molar volumes V_{IrO2}/V_{Ir} = 2.26) and the value of the film density (Ir nominal density: 22.6 g/cm^3), indicates the formation of a pure (or almost pure) metallic Ir layer for T_s = 500 ºC. For T_s = 450 ºC

[6] As mentioned in chapter 2, the substrate to target distance is fixed at 75 mm when using the heater and at 100 mm for RT growths. This explains the greater DR of the films grown with the heater (~5 nm/min for P = 8 W) respect to the films grown at RT (~3 nm/min for P = 8 W).

a metallic/oxide phase mixture (with a majority of the later) can be inferred from the shape of the reflectivity curve in Fig. 3.16(a), and the values of DR (4.0 nm/min) and film density (11.70 g/cm^3) in Fig. 3.16(c).

Trying to reduce the metallic Ir content in the samples grown at 500 ºC, the O_2 flux was increased up to 13 ml/min (50% O_2). From Figs. 3.16(b) and 3.16(d), it can be seen that, as the O_2 flux is increased, the **DR** increases again, while the film **density** decreases. This suggests an increase of the oxide phase. Nevertheless, the increment of the O_2 flux is accompanied by a considerable increase of the surface **roughness** (~4.0 nm for 13 ml O_2/min), in accordance with the results in section 3.2.3.

XRD provides complementary structural information. It can be seen in Fig. 3.17(a) that, already for T_s = 200 ºC, broad IrO_2 lines are revealed for these as–grown (non–annealed) samples. As T_s increases up to 400 ºC, a roughly similar degree of **texture** is found for all the samples (*Pref.* = 0.4–0.5 in Fig. 3.17(c)), being the (200) IrO_2–peak clearly dominant, *i.e.*, the samples are (100)–textured. Note that this preferred orientation is different from that found when the samples are deposited at RT. Moreover, the diffraction peaks become narrower and more intense, indicating a greater **GS** up to 16 nm for T_s = 400 ºC (Fig. 3.17(d)). For T_s = 450 ºC, the GS slightly decreases (14 nm). Another striking feature in Fig. 3.17(a) is the shift in the Bragg peaks position towards lower angles, suggesting greater **lattice parameters** than in powder IrO_2. Indeed, Fig. 3.17(e) shows that greater *a* and *b* lattice parameters are found in these samples compared to those of powder IrO_2. A maximum increase is reached in the sample grown at 400 ºC, with ε_a = 1.7% (tensile strain). On the contrary, *c* remains more similar to that of powder IrO_2 ($\varepsilon_c \geq$ -0.6%).

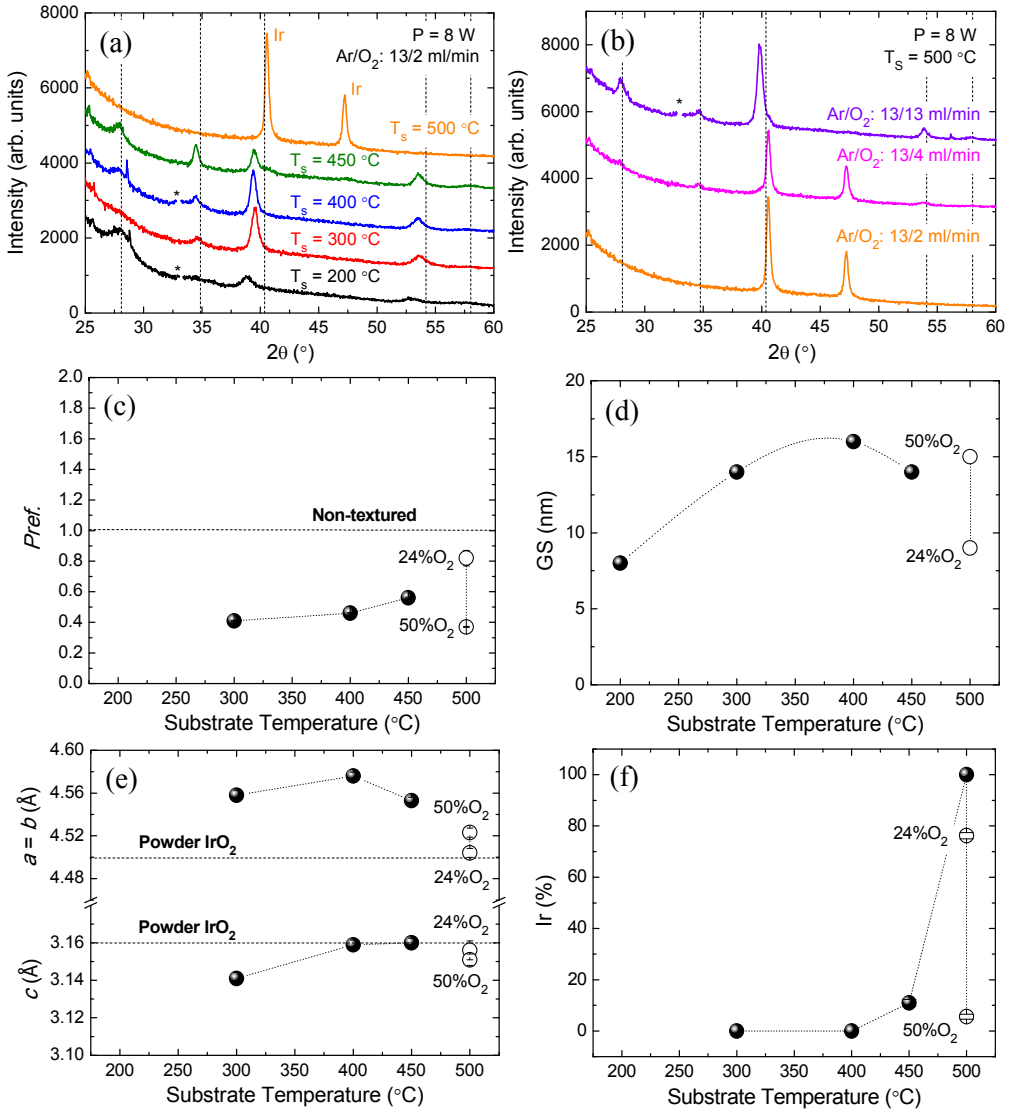

Figure 3.17 XRD measurements from samples grown at high T_s with (a) the O_2 flux fixed at 2 ml/min and different T_s, and (b) varying the O_2 flux while fixing T_s at 500 ºC. Dashed guidelines mark the diffraction peak positions of powder IrO_2. *Silicon peak subtracted for clarity. The diffractograms are vertically shifted for clarity. Panels (c)–(f) show the influence of T_s on the preferred orientation, GS, lattice parameters, and metallic phase concentration, respectively. Open symbols represent samples grown varying the O_2 flux with T_s fixed at 500 ºC. Dashed lines are drawn in panel (c) as reference for *Pref.* = 1 (non–textured) and in panel (e) as references for the lattice parameters of powder IrO_2. Dotted lines are guides to the eye. Data correspond to the IO_47–53 samples in Table 3.1.

Finally, as the XRR curves suggested, the amount of **metallic Ir** very rapidly increases with T_s in the 450–500 ºC range (Fig. 3.17(f)), to the extent that the IrO_2 peaks are no longer visible for T_s = 500 ºC and a pure Ir–like diffractogram is obtained (Fig. 3.17(a)). If under the same conditions of T_s (500 ºC), power (~8 W) and Ar flux (13 ml/min), the O_2 pressure is increased, the oxide phase arises again, as displayed in Fig. 3.17(b). However, the presence of a substantial amount of metallic Ir (~6%) persists up to a 50% O_2.

Therefore, it is concluded (summary in Table 3.7) that, by increasing T_s up to 400 ºC, slightly smaller **DRs** and greater film **densities** (more similar to that nominal of IrO_2) are obtained. This is compatible with a reduction of internal defects at higher temperatures due to an improved adatom mobility. The surface **roughness** remains roughly constant below this temperature. Such atomic mobility enhancement by increasing T_s also leads to greater **GS,** as happened with the annealing temperature. More importantly, two distinctive characteristics can be highlighted in these samples when compared to those grown at RT and subsequently annealed: the (100)–**preferred orientation** and the greater **lattice parameters** than those from bulk IrO_2. This agrees with the results previously reported by other groups [168–170]. Nevertheless, all these tendencies are valid only until **metallic Ir** is formed ($T_s \approx$ 450 ºC ($\approx$ 500 ºC) for Ar/O_2: 13/2 ml/min (Ar/O_2: 13/13 ml/min)) [151].

Table 3.7: Summary of the effects of increasing the substrate temperature on the properties of IrO_2 thin films (for $T_s \leq$ 400 ºC Symbol (~) stands for roughly independent.

	DR	Density	Roughness	Crystallinity	Latt. Parameters	% Ir
T_s (↑)	~	↑	~	↑	↑	↑

3.3. High Oxygen Pressure Sputtering (HPS)

The synthesis of IrO_2 thin films by high oxygen pressure sputtering (HPS) aims at growing epitaxial films with the highest crystallographic quality. The key factor for an epitaxial growth to be achieved in thin films is having directions of similar spacing between atoms in the substrate and in the deposited film, so that these

directions tend to line up with each other. Hence, IrO_2 thin films were deposited on (001), (100) and (110) single crystals TiO_2 substrates, which have the same crystalline structure and similar lattice parameters.[7]

Being to the best of our knowledge the first time IrO_2 is deposited by means of this technique, a similar study to that performed in our sputtering chamber was carried out for finding the optimal growing conditions. The difference here is that the goal is not growing films with a wide range of structural properties, but high–quality epitaxial films. As schematized in Fig. 3.18, in this system the substrate to target distance, sputtering power, oxygen pressure (P_{O2}) and substrate temperature (T_s) can be varied.

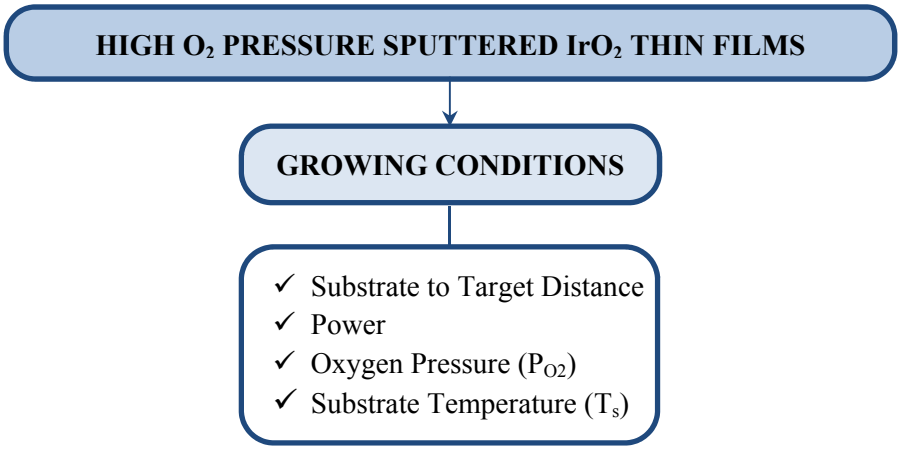

Figure 3.18 Scheme of parameters varied in the synthesis of IrO_2 thin films by HPS deposition.

The **substrate to target distance** is optimized when the plasma is tangent to the substrate holder, as represented in Fig. 3.19(a). Therefore, optimizing this parameter does not require depositing films at several testing distances, but a visual check is enough. In this case, the optimal substrate to target distance was 1.5 cm.

Similarly, the optimization of the **sputtering power** did not require a systematic film deposition. It was set at 110 W after the very poor plasma generated

[7] $SrTiO_3$ substrates were also probed but no XRD patterns were observed (amorphous structure).

for lower powers (the dependence here is typically exponential and negligible amount of material was deposited for lower sputtering power) and overheating at higher powers.

In this equipment, decreasing the **oxygen pressure (P_{O2})** has a similar effect than increasing the sputtering power, but without the risk of overheating. Thus, P_{O2} was varied in the 2.5–3.2 mbar range (the commonly used range [98–100]), being the main difference the greater thickness of the films deposited at lower pressures, as shown in Fig. 3.19(b). As no other differences were observed regarding the crystal quality, P_{O2} was set to 3.2 mbar.

The parameter which needed a more careful analysis is the **substrate temperature, T_s**. On the one hand, the synthesis of compounds carried out by means of this technique requires, in general, growing temperatures above 750 ºC [98–100, 171–173]. On the other hand, as shown in section 3.2.6, substrate temperatures below 450 ºC are required to grow IrO_2 by RMS. Therefore, to optimize T_s, thin films were grown at several temperatures from RT to 600 ºC. Fig. 3.19(c) shows the corresponding XRR curves. For $T_s \leq 200$ ºC clear oscillations are discerned, indicating a deposited layer of 8–9 nm, *i.e.*, a **DR** ≈ 0.07 nm/min.[8] For T_s = 400 ºC no oscillations are observed, which can be associated to a relatively high surface **roughness** given the fast curve decay. For T_s = 600 ºC, again no oscillations are observed, but this time the profile suggests that (practically) no material has been deposited. This could be due to the formation of the volatile IrO_3 phase emerging at lower temperatures than with RMS due to the high oxygen pressure.

Regarding the **crystallinity** of the films, the diffractograms in Figs. 3.19(b) and 3.19(d) show that only the IrO_2(002) reflection is revealed in the whole 2θ range. This proves that an IrO_2 layer has been epitaxially deposited on the TiO_2(001) substrate. Very little difference is observed in the samples grown with $T_s \leq 200$ ºC. The sample grown at T_s = 400 ºC also shows an IrO_2 single crystal–like structure,

[8] Note the extremely low DR compared to that of RMS, where DRs > 1 nm/min were found even for P ≈ 4 W.

despite not showing oscillations in the XRR curve. No diffraction peak is observed at T_s = 600 ºC confirming that no material has been deposited.

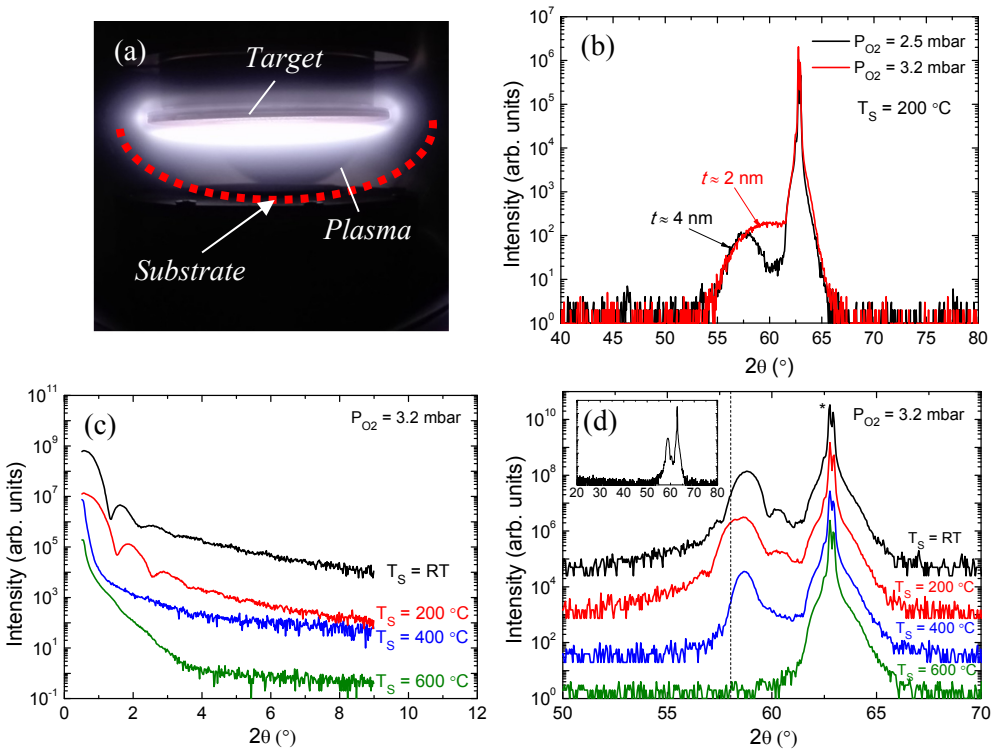

Figure 3.19 (a) Illustration of the optimized substrate to target distance. (b) HR–XRD signals for IrO_2 films grown on TiO_2(001) at different P_{O2}. Panels (c) and (d) show the XRR and HR–XRD signals, respectively, recorded in IrO_2 films grown on TiO_2(001) at different T_s. Dashed guideline in panel (d) marks the diffraction peak position of the (002) reflection from powder IrO_2. The inset in such figure proves that no other reflections than (002) are observed. The curves are vertically shifted for the sake of clarity. *TiO_2(001) substrate.

To further prove the high–quality of these epitaxial films Fig. 3.20(a) shows an illustrative HR–TEM image recorded on an additional 9 nm–thick sample. It confirms the high–quality epitaxial growth even at RT.

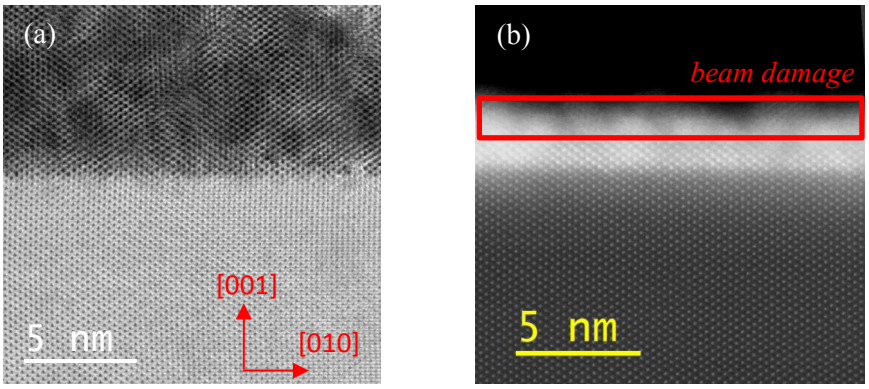

Figure 3.20 (a) Illustrative cross–sectional HR–TEM image recorded in a $t \approx 9$ nm (001)–epitaxial sample (T_s = RT and P_{O2} = 3.2 mbar). (b) Cross–sectional HR–TEM image recorded in a $t \approx 2$ nm (001)–epitaxial sample (T_s = 200 ºC and P_{O2} = 3.2 mbar). Note that the electron beam causes damage on the surface that prevented us from taking images in the samples studied in Chapter 4.

Therefore, high–quality epitaxial IrO_2 films can be deposited with this technique even at RT. Besides, it is found that lower substrate temperatures favor better surface roughness. This is quite an unexpected result, since, as commented above, the synthesis of oxides by means of this technique typically requires high growing temperatures [98–100, 171–173]. Note also the practical importance of this fact, which considerable reduces the overall production time.

3.4. Pulsed Laser Deposition (PLD)

In the previous section, epitaxial IrO_2 films were successfully grown by HPS. However, the DRs obtained there were very slow and for growing thicker films other techniques are more appropriated. Thus, with the aim of growing IrO_2 epitaxial films with a layer thickness up to ~100 nm (as the samples deposited by RMS in section 3.2), the PLD technique was used. As schematized in Fig. 3.21, the main parameters involved during the deposition process are the energy and frequency of the laser (equivalent to the sputtering power), the oxygen pressure (P_{O2}), the substrate temperature (T_s) and the rotation speed of the heater (substrate holder).

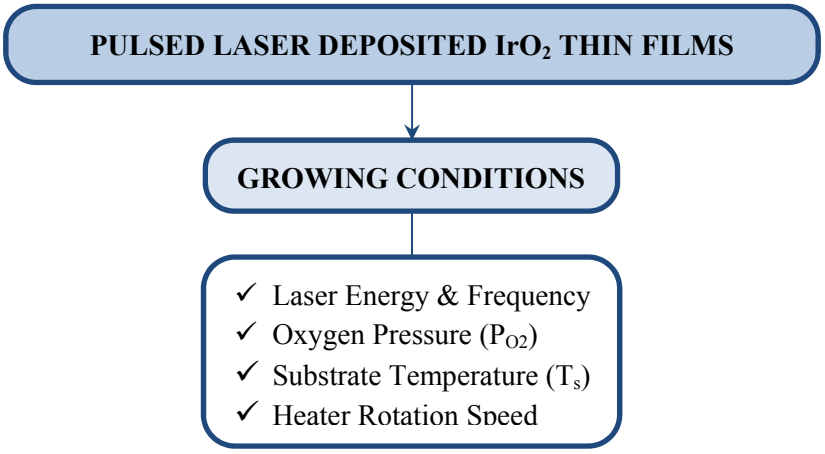

Figure 3.21 Scheme of parameters varied in the synthesis of IrO_2 thin films by PLD.

The equipment employed is a widely–tested equipment and, contrary to the previous section, several works on IrO_2 films deposited by PLD are available in the literature [144–146]. Thus, taking advantage of the previous experience of the group in charge of the PLD and the data from the literature, the **laser energy** after the attenuator was set at ~50 mJ and its **frequency** at 3 Hz.[9] The $\mathbf{P_{O2}}$ was 50 mTorr, and a heater was employed to warm the substrates during the growth up to 480 ºC ($\mathbf{T_s}$) with a **rotation speed** of 30 º/s.

For these growing conditions, Figs. 3.22(a) and 3.22(b) show the XRR and XRD data, respectively, measured in a representative IrO_2 film deposited on a TiO_2(100) substrate. From Fig. 3.22(a), a layer thickness of 90 nm is obtained. This gives a **DR** around 1 nm/min, *i.e.*, more than 1 order of magnitude faster than with the HPS technique, yet lower than the DRs obtained by RMS. The film **density** was found to be 11.63 g/cm^3 (very close to the nominal value, 11.66 g/cm^3) and the surface **roughness** around 2.5 nm. On the other hand, in the diffractogram shown in Fig. 3.22(b), only reflections from the ⟨100⟩ family of planes emerge, proving the **monocrystalline** character of the sample.

[9] A laser energy of ~80 mJ was first probed, but it turned out to be excessive energy and the target was rapidly eroded.

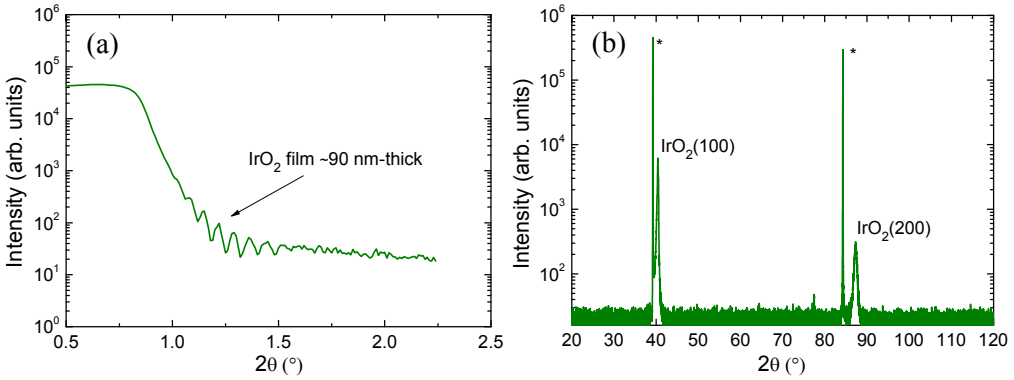

Figure 3.22 (a) XRR and (b) HR–XRD measurements carried out in a representative IrO_2 sample deposited on TiO_2(100) by PLD. *TiO_2(100) substrate signal.

Therefore, epitaxial films with variable thickness were successfully obtained by PLD on TiO_2(100) substrates. Similar results were obtained when depositing on TiO_2(001) and TiO_2(110) using the same growing conditions and measuring comparable values of DR, roughness, density and crystallinity (epitaxial films). The main difference here lies on the lattice parameters, which are different for the three growing orientations due to an effect of the substrate. This will be discussed in the next chapter.

3.5. Conclusions

IrO_2 thin films with a wide range of different structural properties have been successfully grown by **reactive magnetron sputtering** in our recently mounted sputtering chamber by using different growing and annealing conditions. The trends observed when varying these parameters are summarized in Table 3.8.

The **sputtering power** was found to be the only parameter which importantly affects the DR: the greater the sputtering power, the greater the DR. Increasing the sputtering power also favors lower porosity and better crystallinity. Indeed, two types of samples can be found when varying the power: non–textured samples with GS ≈ 10 nm at relatively low power, and (110)–textured samples with GS ≈ 20–30 nm when the power is increased. At the same time, for a given atmosphere, the higher the

sputtering power, the more likely the formation of Ir–metal clusters. Varying the sputtering power do not to have any significant effect on the lattice parameters. However, it should be noted that the lattice parameters obtained in films grown at RT (and annealed) are always slightly smaller than those found in bulk. This relative reduction is especially relevant for the *c* parameter ($-0.3\% \leq \varepsilon_c \leq -1.4\ \%$).

Increasing the **Ar flux** has no relevant effect on the DR, density or lattice parameters, but leads to rougher films and worse crystallized samples (loss of texture and smaller GS), as well as to less amount of metallic Ir impurity phase within the films.

The **O_2 flux** has a sharp effect on the microstructure of the films. Increasing the O_2 flux yields to an increased porosity, worse crystallinity (texture and GS), and rougher surfaces, while it does not affect much the DR or the lattice parameters. As an advantage, the percentage of metallic Ir within the film decreases.

The **annealing treatment** produces a density increase and a thickness reduction respect to the as–grown films due to a film compaction by reducing the internal defects. This effect is slightly enhanced at higher **annealing temperatures** (provided that $T_{ann} \leq 600$ ºC). Furthermore, the annealing process is accompanied by an increase in the surface roughness, which is accentuated as T_{ann} increases. The crystallinity of the films is improved and the lattice parameters progressively approach those of bulk IrO_2 as the temperature is increased. Rising T_{ann} also favors the formation of metallic Ir when nucleation of the metallic phase has been produced during deposition of the films. In such a case, its growth is energetically favored during the annealing at the expense of the oxidized phase. As T_{ann} approaches 800 ºC, the formation of volatile IrO_3 oxide phase is enhanced.

The values of the lattice parameters are not dependent on the type of **annealing atmosphere.** Regarding the crystallinity, no clear dependences are observed in non–textured samples, though in textured films a more oxidizing atmosphere is found to favor texture and larger GSs. If an Ir metallic seed is formed

during the growing process, the more reducing the atmosphere, the higher the amount of metallic Ir present in the film after the thermal treatment. This occurs at the expense of the GS of the oxide phase.

By increasing the **substrate temperature** up to 400 ºC, the atoms obtain extra thermal energy, increasing the film density (lower porosity) and enhancing the GS. However, above 400 ºC, the metallic Ir content is found to increase exponentially. Two distinctive characteristics can be highlighted in these samples: (i) a (100)– rather than (110)–texture is preferred, and (ii) greater lattice parameters than those from bulk IrO_2 ($1.2 \leq \varepsilon_a \leq 1.7$ %).

Table 3.8: Simplified scheme of the effects of varying a growing or annealing parameter on the properties of IrO_2 thin films. Symbol (~) stands for roughly independent.

	DR	**Density**	**Roughness**	**Crystallinity**	**Latt. Parameters**	**% Ir**
P (↑)	↑	↑	~	↑	~	↑
Ar (↑)	~	↓	↑	↓	~	↓
O_2 (↑)	↑	↓	↑	↓	~	↓
T_s (↑)	~	↑	~	↑	↑	↑
T_{ann} (↑)	~	↑	↑	↑	↑	↑
Atm. (↑ox.)	~	~	~	↑	~	↓

To sum up, two competing trends are clearly distinguished in the synthesis of reactively sputtered IrO_2 films: increasing the sputtering power, decreasing the Ar or the O_2 flux or increasing the substrate temperature produce (i) better–crystallized samples, but also (ii) increases the metallic phase content and the surface roughness. This issue strongly limits the working conditions if a textured film is required. On the other hand, for polycrystalline non–textured samples, there is a wider range of growing parameters that give rise to such microstructure.

Although highly oriented films can be easily grown in our sputtering chamber, for epitaxial growths other techniques are more appropriated. In this sense, **IrO_2 epitaxial films** were successfully obtained by HPS for small layer thicknesses (≤ 10

nm), and by PLD for layer thicknesses up to ~100 nm. Importantly, high–quality films are obtained by HPS even at RT.

Finally, it has to be noted that the expertise acquired during the growth of IrO_2 films by RMS will also help to optimize the synthesis of other compounds in our new sputtering chamber in a more straightforward way, as happened with the HPS and PLD techniques. Notwithstanding, it has to be taken into account that the synthesis and optimization of each compound can significantly differ.

1st Approach

Structure of IrO_2 Thin Films

Chapter 4

IrO_2 Thin Films: The Role of Structure and Dimensionality on the Electrical and Magnetic Behavior

4.1. Introduction

As a follow up to the work carried out in the preceding chapter, now the attention is focused on **studying the relationship between structure and physical (electrical and magnetic) properties of IrO_2 thin films**. Motivated by the theoretical predictions suggesting that IrO_2 can become magnetic as well as insulating through structural modifications [82, 83], a detailed characterization of representative IrO_2 thin films with relevant structural differences (crystallinity, thickness, growing direction and lattice parameters/strain) has been performed.

The effect of the layer **thickness** (*t*) has been studied prompted by the theoretical work by *X. Ming et al.* [83], who predicted a metal–insulator transition (MIT) and magnetic ordering in (001)–oriented IrO_2/TiO_2 superlattices at 2–3 IrO_2 atomic layers. In very thin films, the coordination of constituent ions at the surfaces and interfaces is reduced, typically yielding a decrease of the electronic bandwidth, *W*. This, in turn, yields an increase of the effective correlation (*U/W*, where *U* is the Coulomb repulsion). Moreover, lowering the thickness also makes the potential due to disorder (*D*) more effective in causing Anderson localization (weak localization) as *D/W* increases. As a consequence, by decreasing the layer thickness, a critical point

may be reached where a MIT is induced [75] (as explained in section 1.2.1). Experimental evidence of this thickness–dependent MIT has been recently reported for $SrIrO_3$ thin films, being the underlying mechanisms (Mott *vs.* Anderson) still under extensive debate [65, 67, 174]. Though first attempts of finding such thickness–dependent MIT by *J. K. Kawasaki et al.* [87] in (110)–oriented $(IrO_2)_n/(TiO_2)_2$ superlattices ($n \geq 3$) were unsuccessful, they predicted the electronic properties of such compounds to be highly dependent on orientation. In fact, the importance of orientation was already proved by *M. Uchida et al.* [56], who observed a change in the carrier type depending on this parameter. In view of these results, IrO_2 epitaxial films have been grown with **different orientations**. Besides, by epitaxially depositing the IrO_2 films on different substrates and orientations an additional parameter is introduced: the modification of the lattice parameters. The induced **strain** may reduce the orbital overlap and be a key factor in promoting the transitions mentioned above in an analogous way to that reported in $SrIrO_3$ [67, 175].

It should be highlighted that, whereas extensive work has been carried out on engineering (through thickness and strain) and studying MITs in thin film systems like $SrIrO_3$ and Sr_2IrO_4, to the best of our knowledge no experimental work other than that of *J. K. Kawasaki et al.* [87] has been published on IrO_2 so far. Thus, first along this chapter the structural characterization of different IrO_2 thin films is presented (section 4.2). The influence of (i) crystallinity, (ii) thickness, (iii) growing direction and (iv) substrate–induced strain/modification of the lattice parameters on the electronic band description (section 4.3) and on the electrical (section 4.4) and magnetic (section 4.5) response is then studied.

4.2. Structural Characterization

Table 4.1 summarizes the structural details of the samples studied along this chapter (the synthesis conditions have been given in the previous chapter). To investigate the effect of **crystallinity**, ~100 nm–thick amorphous, non–textured polycrystalline (henceforth labeled as non–textured) with a grain size (GS) of 6 and 10 nm, (110)–textured polycrystalline (labelled as (110)–textured), and epitaxial films

were considered. To explore the effect of **thickness**, ~100 nm, ~20 nm, ~5 nm, ~2 nm and, in some extra cases, ~1.5 nm–thick IrO_2 films were compared for the amorphous, polycrystalline and epitaxial samples. Regarding the **orientation**, epitaxial films were deposited on TiO_2 substrates with (001), (100) and (110) growing orientations. Finally, the epitaxial films were grown with different thicknesses and on substrates with different lattice parameters to study the effect of **strain**. For this purpose, TiO_2 and SnO_2 substrates (both rutile) with nominal lattice parameters $a = b = 4.59$ Å and $c = 2.96$ Å, for TiO_2; and $a = b = 4.74$ Å and $c = 3.19$ Å for SnO_2, were employed. Note that the differences in the IrO_2 lattice parameters obtained by using these lattice mismatched substrates will be presumably greater than those obtained "naturally" in the polycrystalline samples ($-0.4\% \leq \varepsilon_a \leq +1.7\%$ and $0 \leq \varepsilon_c \leq -1.3\%$ according to the results obtained in Chapter 3). For completeness, a ~100 nm–thick (100)–textured film grown at 400 ºC has also been included in the analysis because of presenting unusual large *a* and *b* lattice parameters respect to the nominal values.

Due to the great amount of samples compared throughout this chapter, a color code has been followed: black curves are drawn for amorphous samples, red for non–textured and (110)–textured polycrystalline samples, purple for the (100)–textured polycrystalline film, green for epitaxial films deposited on TiO_2, and blue for the epitaxial film deposited on SnO_2.

Table 4.1: Structural properties of the samples studied in this chapter: layer thickness (t) determined by XRR and lattice parameters determined by XRD in polycrystalline samples showing a diffraction pattern. The lattice parameters in $t \approx 100$ and 5 nm epitaxial samples were determined by RSMs. The difference in each lattice parameter with powder IrO_2 (ε) is given in brackets.

Sample Crystallinity	t (nm)	a (Å)	b (Å)	c (Å)
Amorphous	84.7‡	–	–	–
	17.4‡	–	–	–
	5.0	–	–	–
	4.1‡	–	–	–
	2.0‡	–	–	–
Non–textured (GS = 6 nm)	88.1‡	4.49 (-0.2%)	4.49 (-0.2%)	3.12 (-1.3%)
Non–textured (GS = 10 nm)	80.5‡	4.50 (0.0%)	4.50 (0.0%)	3.15 (-0.3%)
	16.4‡	–	–	–
	3.3	–	–	–
	2.0#	–	–	–
(110)–textured	106.5	4.49 (-0.2%)	4.49 (-0.2%)	3.13 (-0.9%)
	20.2‡	4.51 (+0.2%)	4.51 (+0.2%)	3.14 (-0.6%)
	6.3	–	–	–
	3.3	–	–	–
	1.4#	–	–	–
(100)–textured	104.4	4.58 (+1.7%)	4.58 (+1.7%)	3.16 (0.0%)
(001)–epitaxial	96.0	4.59–4.50§	4.59–4.50§	3.12–3.15§
	23.4	–	–	–
	5.7	4.59 (+2.0%)	4.59 (+2.0%)	3.11 (-1.6%)
	2.5*	–	–	–
	2.2*	–	–	–
	1.5*	–	–	–
(100)–epitaxial	89.0	4.46 (-0.9%)	4.59 (+2.0%)	3.13 (-0.9%)
	21.5	–	–	–
	5.1	4.48 (-0.4%)	4.59 (+2.0%)	3.10 (-1.9%)
	1.7*	–	–	–
	1.5*	–	–	–
(110)–epitaxial	92.2	4.53† (+0.7%)	4.53† (+0.7%)	3.12† (-1.3%)
	22.3	4.56† (+1.3%)	4.56† (+1.3%)	3.07† (-2.8%)
	5.3	4.58† (+1.8%)	4.58† (+1.8%)	3.05† (-3.5%)
	2.7*	–	–	–
	2.2*	–	–	–
(100)–epitaxial	5.1	4.30 (-4.4%)	4.72 (+4.7%)	3.16 (0.0%)

*Layer thickness calculated by XRD. #Estimated thickness from the deposition time. †Estimated lattice parameters (explained in the main text). §Relaxed film. ‡Samples prepared using a pure Ar atmosphere during the pre–sputtering step (see section 2.1.2).

4.2.1. X–Ray Reflectivity (XRR)

XRR experiments were carried out to determine the **thickness** of the samples. The corresponding curves are shown in Figs. 4.1(a)–(d) for a nominal thickness of 100, 20, 5 and 2 nm, respectively, and in Table 4.1 the values extracted from such curves are given. It can be seen in Fig. 4.1 that, as expected, the oscillation frequency becomes lower as the thickness becomes thinner, down to the ~2 nm–thick samples where, practically, no oscillations can be discerned. Such layer thickness is in the detection limit of the technique, which makes the values obtained here less reliable. This is why no more XRR experiments were carried out in samples with a nominal thickness $t \leq 2$ nm. Their thickness was further ahead determined by XRD (shown below). As can be seen in Table 4.1, in general, layer thicknesses close to the nominal values (within ± 20%) are obtained, so that the films are valid for our purpose.

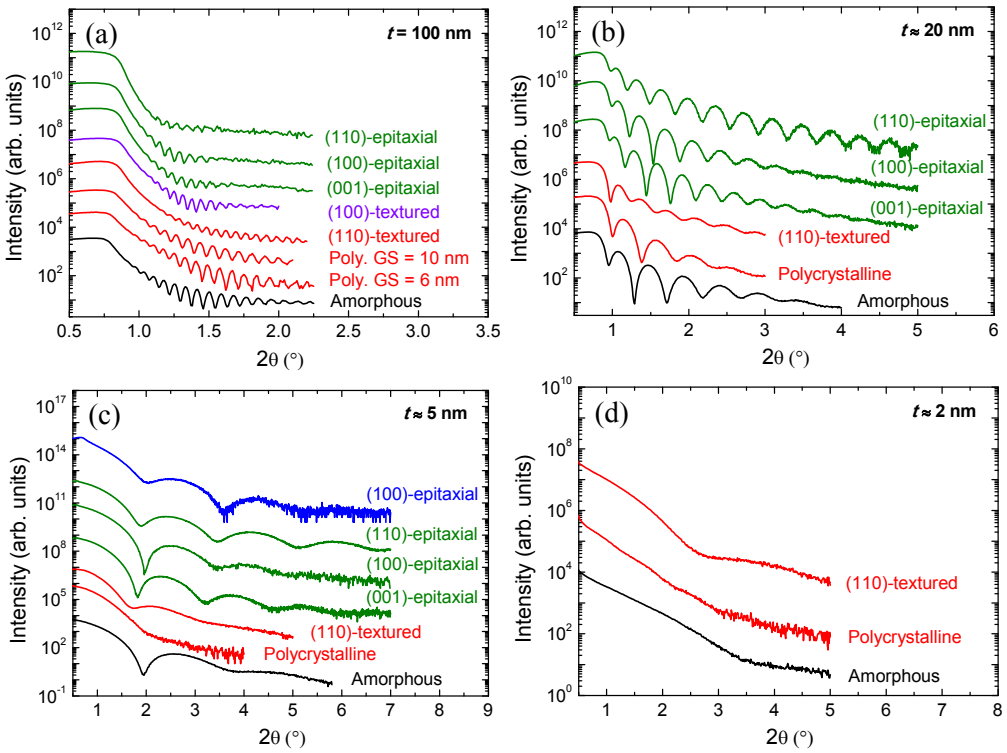

Figure 4.1 XRR measurements on IrO_2 thin films for nominal (a) t = 100 nm, (b) t = 20 nm (c) t = 5 nm and (d) t = 2 nm.

4.2.2. X–Ray Diffraction (XRD)

The sample **crystallinity** was probed by means of XRD, whose results are accordingly given in Fig. 4.2. As expected, amorphous samples do not present any diffraction peak (not shown).

Regarding the polycrystalline films, Figs. 4.2(a) and 4.2(b) show the corresponding diffractograms for the non–textured and textured films, respectively (the parameters of the (100)–textured sample were discussed in the previous chapter). For nominal t = 100 nm, both non–textured and (110)–textured samples display the typical features of rutile IrO_2, with the relative intensity of the (110)–peak clearly enhanced for the latter (in agreement with its textured character). In both set of samples, as t is reduced, the diffraction peaks become less pronounced. In fact, for nominal t = 20 nm, the non–textured sample only exhibits a small bump at the (110)–IrO_2 peak position. Contrary, the textured sample shows all the IrO_2 features observed in the ~100 nm–thick sample, but certainly with less intensity. Note that the texture is still conserved. Then, for smaller thicknesses ($t \leq 5$ nm), no features are discerned neither in the non–textured nor in the textured films. As the synthesis procedure of the samples is identical and only the sputtering time is varied, the disappearance of the diffraction peaks can be related to the smaller amount of material. A loss of crystallinity cannot be rule out, though.

A Rietveld refinement was performed in those samples exhibiting a diffraction pattern. The results are given in Table 4.1. In all the cases, differences in the lattice parameters smaller than 1.5% respect to powder IrO_2 (Fig. 3.2 in the previous chapter) are found. The refinements also confirm a percentage of metallic phase lower than 1% in the $t \approx 100$ nm samples and a significantly greater percentage (~10%) in the $t \approx 20$ nm textured sample (deposited during the pre–sputtering step, as mentioned in section 2.1.2). Finally, by means of the Scherrer equation (Eq. 2.1), GSs of 10 and 6 nm are obtained in the $t \approx 100$ nm–thick non–textured samples (the thinner non–textured samples were synthesized with the conditions that give a GS = 10 nm for $t \approx 100$ nm).

On the other hand, a GS = 18 nm is measured in the $t \approx 100$ and 20 nm–thick textured samples.

Figs. 4.2(c), 4.2(d), 4.2(e) and 4.2(f) show the HR–XRD experiments carried out in the epitaxially grown IrO_2 samples. The sharpest peaks observed in each diffractogram belong to the respective substrate signal. Only peaks corresponding to the substrate growing orientation are observed in all the samples, proving their epitaxy. Regarding the lattice parameters, some peak shifts can be discerned depending on the layer thickness. This indicates that the lattice parameters slightly vary for samples with different thickness. In other words, the effect of the substrate on straining the lattice depends on the thickness. For instance, in Fig. 4.2(c) a peak displacement towards greater 2θ angles is observed for samples with smaller thickness. As the Bragg peak corresponds to the (001) reflection, this would indicate a gradually smaller *c* parameter as the thickness is reduced. Similarly, in Figs. 4.2(d) and 4.2(e) the peak shift in the (100) and (110) reflections, respectively, is found to be towards smaller 2θ angles. This indicates greater *a* lattice parameter for (100)–epitaxial samples and greater $a + b$ parameters for (110)–epitaxial films on reducing the thickness. The lattice parameters were obtained by reciprocal space maps (shown below). However, for the (110)–epitaxial samples no proper reflections could be found and their lattice parameters were estimated from the XRD data by assuming $a = b$ and a constant cell volume. The results are given in Table 4.1.

As for the possible relaxation of the cell along the sample thickness, the thinnest films ($t < 20$ nm) do not present any sign of relaxation. Contrary, it draws attention the diffractogram of the ~100 nm–thick (001)–epitaxial sample, represented in Fig. 4.2(c), where a double peak is clearly discerned at $2\theta = 58.5^\circ$ and 59.0° (marked with arrows in the figure). This could suggest an abrupt relaxation of the film, so that two differentiated regions with two different lattice parameters exist in the sample. This may be tentatively associated to the three–step fabrication process explained in Chapter 2. No other sample shows clear signs of relaxation, though the asymmetric shape of the Bragg peak at $2\theta \approx 40.5^\circ$ observed in the ~100 nm–thick

(100)–epitaxial sample in panel (d) may be due to a strain gradient (gradual relaxation) [176].

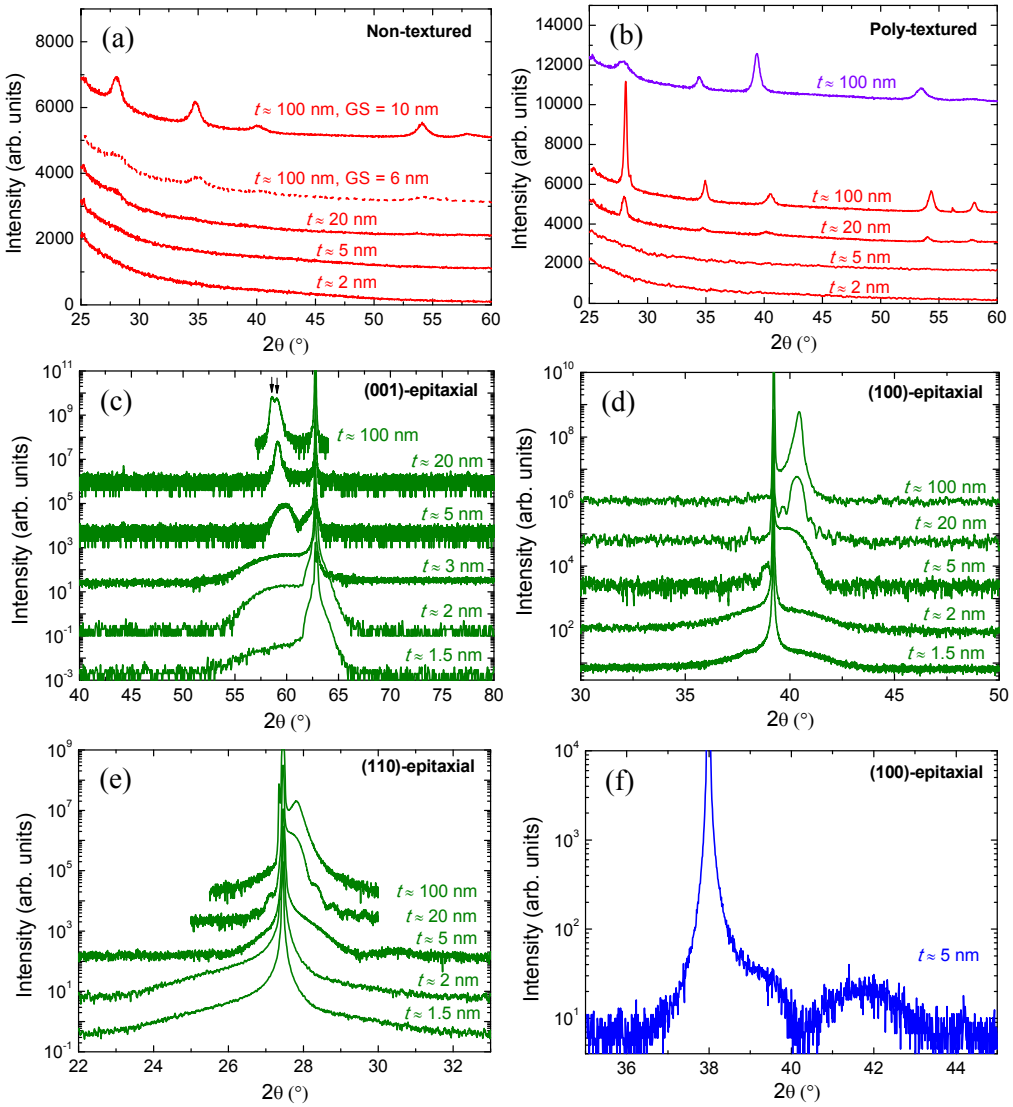

Figure 4.2 XRD measurements for (a) non–textured and (b) textured samples, and HR–XRD for epitaxial films deposited on (c) TiO_2(001), (d) TiO_2(100), (e) TiO_2(110) and (f) SnO_2(100).

Finally, the layer thickness was estimated by using the Scherrer equation in the thinnest epitaxial samples in which XRR experiments could not provide further information (nominal t = 2 and 1.5 nm). The results are given in Table 4.1, being close to the nominal values.

In order to obtain precise values of the lattice parameters for the (001)– and (100)–epitaxial films, reciprocal space maps were collected on representative samples ($t \approx 100$ and 5 nm). The corresponding maps are depicted in Fig. 4.3 and the extracted lattice parameters are given in Table 4.1.

First, in the ~100 nm–thick epitaxial film on TiO_2(001), the extended spot observed in Figs. 4.3(a) and 4.3(b) shows that the in–plane lattice parameters, *a* and *b*, present both a gradual relaxation along the thickness, from 4.59 Å (same as in substrate) to 4.50 Å; and the out–of–plane parameter, *c*, from 3.12 Å (greater than in substrate, 2.96 Å) to 3.15 Å. These measurements indicate certain disagreement with the XRD (Fig. 4.2(c)), which suggested an abrupt relaxation of the lattice parameters. Anyway, both techniques agree in the film relaxation of this sample. For the $t \approx 5$ nm film (Figs. 4.3(c) and 4.3(d)), the in–plane lattice parameters are perfectly matched with the substrate ($a = b = 4.59$ Å, tensile strain) and the out–of–plane parameter is compressed to compensate the tensile strain down to $c = 3.11$ Å. These differences are thus consistent with the gradually smaller *c* parameter inferred from the diffractograms in Fig. 4.2(c).

As for the ~100 nm–thick epitaxial film on TiO_2(100), represented in Figs. 4.3(e) and 4.3(f), it can be seen that the in–plane lattice parameter, *b*, is matched with the substrate (4.59 Å, tensile strain), although the spot seems to be slightly extended indicating a small relaxation, in accordance with the XRD data. The other in–plane lattice parameter, *c*, is compressed down to 3.13 Å, and hence, it does not completely match the value of the substrate (2.96 Å). The out–of–plane parameter, *a*, is compressed down to 4.46 Å. When the layer thickness is reduced to $t \approx 5$ nm (Figs. 4.3(g) and 4.3(h)), *b* is again matched (4.59 Å, tensile strain), while the other in–plane parameter, *c*, is more compressed down to 3.10 Å, though it is not yet fully matched with the substrate. The out–of–plane parameter, *a*, is now compressed down to 4.48 Å. Again, this is consistent with the diffractograms from Fig. 4.2(d), where a greater *a* lattice parameter was detected in the thinnest samples.

Regarding the 5 nm–thick epitaxial film on SnO_2(100), it presents in–plane lattice parameters, b = 4.72 Å (matched with SnO_2, tensile strain), and c = 3.16 Å (c = 3.19 Å for SnO_2), extracted from Figs. 4.3(i) and 4.3(j). The out–of–plane parameter, a, is compressed down to 4.30 Å. It is striking the notable difference between a and b, equal at first in the rutile structure while a difference of 0.42 Å has been measured in this sample.

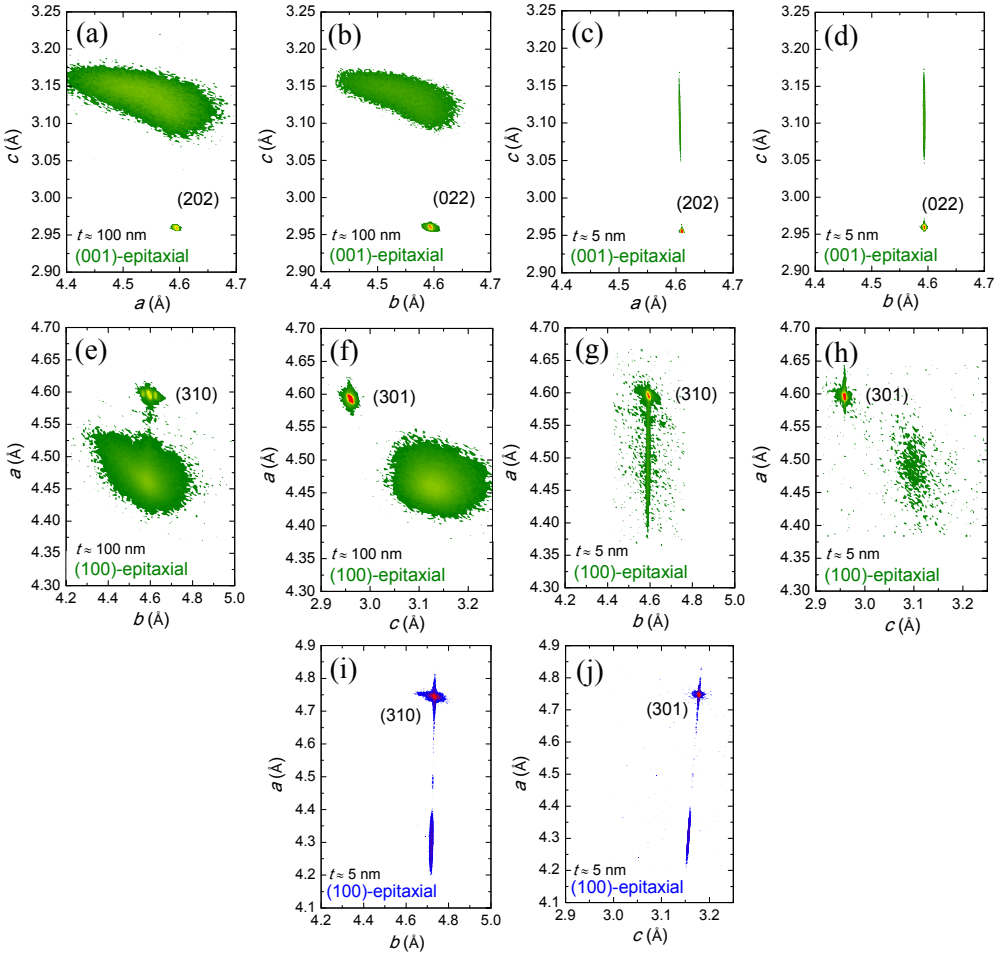

Figure 4.3 Reciprocal space maps for epitaxial films deposited on (a) and (b) TiO_2(001) with t ≈ 100 nm, (c) and (d) TiO_2(001) with t ≈ 5 nm, (e) and (f) TiO_2(100) with t ≈ 100 nm, (g) and (h) TiO_2(100) with t ≈ 5 nm, and (i) and (j) SnO_2(100) with t ≈ 100 nm.

4.2.3. Extended X–ray Absorption Fine Structure (EXAFS)

EXAFS spectrum provides information about structural factors, such as Ir–O distances, IrO_6 octahedra distortion and Ir–O–Ir angles, which have proven to be fundamental in determining the electrical and magnetic properties of iridates [67, 72–74, 77, 177]. However, since the allocated beam time at synchrotron facilities (if granted) is very limited, and much accumulation time is required in the thinnest films for achieving a measurement with a proper signal to noise ratio, EXAFS spectra were only collected in the ~100 nm–thick films. Additionally, the ~5 nm–thick amorphous sample could also be measured during the experiments.

Fig. 4.4(a) shows the Ir L_3–edge EXAFS signals recorded at RT on the selected samples and compared to a powder IrO_2 reference. To correlate the spectral features with specific structural changes, in Fig. 4.4(b) the Fourier transform is depicted. At first glance, the disparity observed between the spectra is subtle, though some differences are discerned. The amorphous samples exhibit no long range order beyond the first octahedral shell (feature at $R \approx 1.65$ Å, no phase correction applied). In contrast, all the polycrystalline and epitaxial samples present very similar profiles to that of the IrO_2 reference, with the typical features due to scattering from second ordered nearest neighbors (features between R ≈ 3–4 Å). This proves the good crystal quality of our polycrystalline sputtered films. On closer examination, the position of the main peak (marked with a solid line in panel (b)) is lightly shifted towards lower *R* values as the sample crystallinity is improved. For clarity, the evolution of the peak position with the sample crystallinity is represented in Fig. 4.4(c). Here, it can be seen that the position of such feature progressively shifts (~0.03 Å) from the amorphous films to the (100)– and (110)–epitaxial samples, where this value is very similar to that observed in powder IrO_2. This suggests greater Ir–O distances for samples with poorer crystallinity. Though the differences are small (note that the resolution is ~0.17 Å), the tendency seems to be robust.

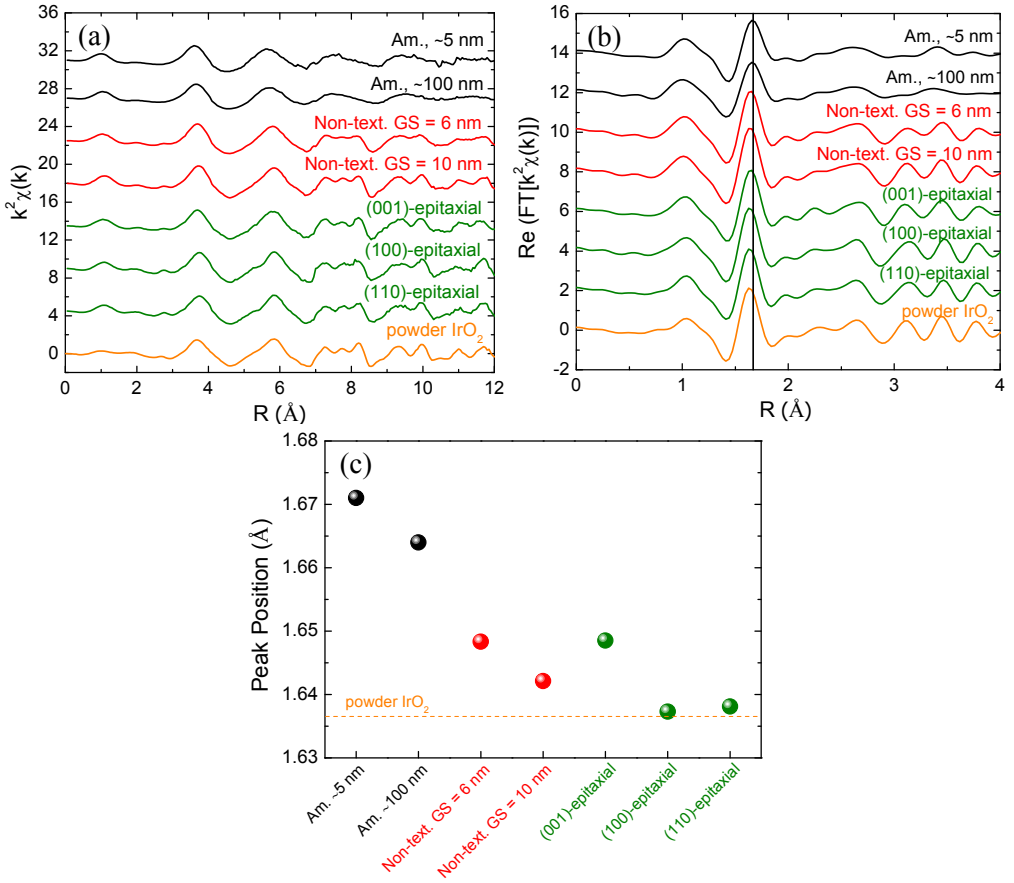

Figure 4.4 (a) EXAFS spectra recorded at the Ir L_3 edge for representative samples. (b) Fourier transforms (real part) of the k^2–weighted Ir L_3–edge EXAFS signals in the 3 $Å^{-1}$ to 12 $Å^{-1}$ range. (c) Evolution of the main–peak position. In all the samples t = 100 nm except in the amorphous films, where it is also represented the t = 5 nm sample. The solid line in panel (b) at ~1.67 Å is a guide to the eye.

Thus, the structural characterization allows concluding that the synthesized samples have indeed relevant differences as far as the **crystallinity**, **thickness**, **growing orientation** and lattice parameters/**strain** are concerned. In addition, it has been observed that the Ir–O bond lengths are slightly greater in amorphous samples. Bearing this in mind, the effect that these structural differences have in the electronic description and in the electrical and magnetic properties, is discussed in the following sections.

4.3. Electronic Characterization

Given the importance of SOC effects in iridates, it is crucial to quantify the strength of such interaction. In this sense, XANES provides a direct probe of the spin–orbit interactions, since the branching ratio, defined as $BR = I_{L3}/I_{L2}$ (where $I_{L2,\,3}$ are the XANES white line intensities) is proportional to the ground–state expectation value of the angular part of the SOC, $\langle \mathbf{L}\cdot\mathbf{S} \rangle$, via [178]:

$$BR = \frac{2 + \langle \boldsymbol{L}\cdot\boldsymbol{S} \rangle / n}{1 - \langle \boldsymbol{L}\cdot\boldsymbol{S} \rangle / n} \tag{4.1}$$

where n is the number of holes. Additionally, the XANES spectrum is very sensitive to the local bonding environment of the absorbing atom, so it can provide information with regard to oxidation state or density of states. High–energy resolution fluorescence detected XANES (HERFD–XANES) is used to optimize the sensitivity to modifications in the electronic state.

The normalized HERFD–XANES spectra recorded at the Ir $L_{2,\,3}$ edges are compared in Figs. 4.5–4.8 for representative samples with different crystallinity, thickness, probed direction and strain, respectively. Additionally, the BR and the $\langle \mathbf{L}\cdot\mathbf{S} \rangle$ product calculated for each sample are given in Table 4.2. At first glance, very similar spectral profiles can be observed in all the figures. In all the cases, the HERFD–XANES data show strong white lines at both absorption edges independently on the structural details, indicative of a large local density of 5*d* states [81]. Note that this result is in stark contrast with the classical idea of largely extended 5*d* orbitals, broad 5*d*–bandwidth and metallic behavior. In addition, the BR is found to be around 4 in all the samples (see Table 4.2). These experimental values, approximately two times larger than the statistical BR = 2, imply the presence of a large and robust SOC in all the cases [81]. This result agrees well with the SOC robustness (and $BR \approx 4$) already observed in other Ir^{4+} iridates, such as in Sr_2IrO_4 [179] or in $BaIrO_3$ [180, 181].

Looking carefully at the $\langle \mathbf{L}\cdot\mathbf{S} \rangle$ values, some small, yet interesting differences can be discerned, indicating deviations in the electronic structure among these

samples. First, in Fig. 4.5(a) a representative comparison between the spectra recorded on samples with **different crystallinity** is displayed. A small shift in the L_3 edge (~0.4 eV) towards lower energies and a reduction in the intensity of the L_2 white line can be discerned as the sample crystallinity is worsened. Moreover, whereas little differences are observed in the $\langle \mathbf{L}\cdot\mathbf{S} \rangle$ values for polycrystallines and epitaxial films (< 3% difference), represented in Fig. 4.5(b), a noticeable increase in the SOC is observed in the amorphous sample (around 10%). The energy shift could be tentatively associated to the presence of a significant amount of metallic Ir. However, this would be accompanied by a decrease of the white line intensities and in the SOC, as shown by *Clancy et al.* [81]. Since this is not case, the presence of an important amount of metallic Ir can be ruled out. Such energy shift could also be associated to the larger Ir–O distances observed in the amorphous samples in Fig. 4.4(b) [122, 182, 183]. This could explain, at least in part, such SOC enhancement in the amorphous samples. The increment of the Ir–O distances would reduce the orbital overlap and, in turn, the more atomic (less hybridized) character of the orbitals results in a higher SOC. Furthermore, as the SOC is one of the main factors involved in the spin–detection process, this could partially explain why *K. Fujiwara et al.* [7] found a better response for IrO_2 as a spin–detector material in the amorphous state.

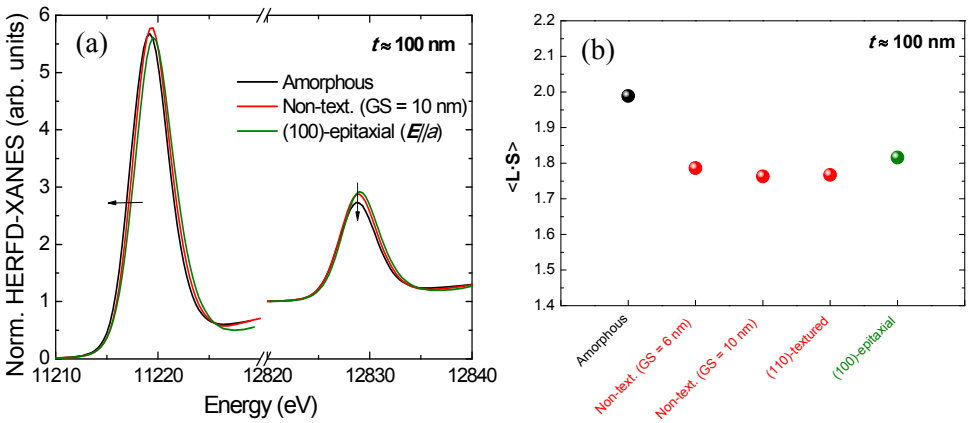

Figure 4.5 (a) Representative comparisons between the normalized Ir $L_{2,3}$–edges HERFD–XANES spectra recorded on samples with different crystallinity. Panel (b) plots the values of the SOC ($\langle \mathbf{L}\cdot\mathbf{S} \rangle$ product) in units of $\hbar^2$ obtained from the XANES data.

Representative spectra recorded on samples with **different thickness** are depicted in Figs. 4.6(a), 4.6(c) and 4.6(e) for the amorphous, polycrystalline and epitaxial sample series, respectively. The values of **⟨L·S⟩** obtained from the XANES data are conveniently represented in Figs. 4.6(b), 4.6(d) and 4.6(f).

As displayed by the solid symbols in Fig. 4.6(b), when the layer thickness of the amorphous films is reduced from ~100 to ~5 nm, the **⟨L·S⟩** values remain constant (< 1% variation). It should be noticed, however, the noticeable effect of metallic Ir, see open symbols in panel (b). The presence of metallic phase in these samples, which can be inferred from the clear reduction in the intensity and the shift towards lower energies, of around 0.5 eV between the $t \approx 100$ nm and $t \approx 2$ nm samples; causes the SOC to be reduced around 7%. On the other hand, in the polycrystalline non–textured samples, represented in Figs. 4.6(c) and 4.6(d), the intensity of both white lines is reduced as the layer thickness decreases from $t \approx 100$ to $t \approx 2$ nm. In this case, the SOC slightly increases (~4%). Similarly, for the epitaxial samples the intensity of both white lines decreases as the layer thickness is reduced (Fig. 4.6(e)) and the SOC slightly increases (Fig. 4.6(f)). Although the differences are in general smaller than 5%, the tendency seems to be robust, as it has been observed in the three probed directions within the same sample, as represented in Fig. 4.6(f); and in the rest of the samples measured (see Table 4.2).

As proved by XRD measurements, all these samples are single crystals, so a SOC enhancement due to a poorer crystallinity can be ruled out. As mentioned in the introduction, by reducing the layer thickness the coordination of constituent ions at the interfaces is reduced. This yields a decrease of both, the orbital overlap and W [184], thus increasing the SOC. In fact, recent angle–resolved photoemission spectroscopy (ARPES) studies have reported narrower W in ultrathin IrO_2 films [185]. Besides, angle–integrated measurements of the valence bands present a small shift in energy, in agreement with the shift observed in Fig. 4.6 [87]. However, the effect of thickness and strain/lattice parameters can be "overlapped" in these samples and both contributions must be identified separately.

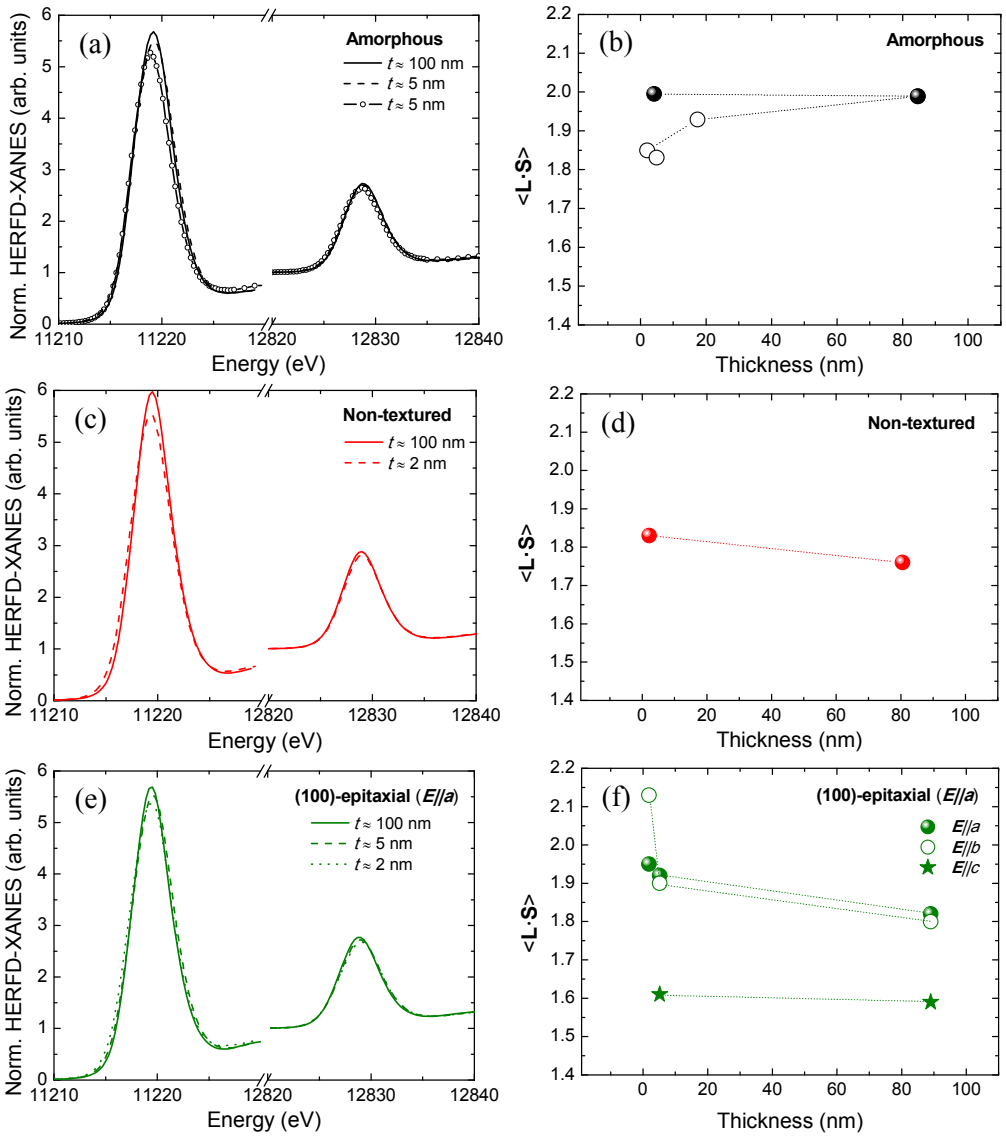

Figure 4.6 Representative comparisons of the normalized Ir $L_{2,\ 3}$–edges HERFD–XANES spectra recorded on samples with different thickness in (a) amorphous, (c) non–textured and (e) epitaxial samples. Panels (b), (d) and (f) plot the values of the SOC ($\langle \mathbf{L}\cdot\mathbf{S} \rangle$ product) in units of $\hbar^2$ obtained from the XANES data. In panels (a) and (b), samples prepared under two different pre–sputtering atmospheres, Ar + O_2 (open symbols) or Ar (solid symbols), are compared (see section 2.1.2.).

Dipole selection rules impose a strong dependence of the absorption cross–section on the photon polarization, which makes the absorption spectra dependent on

the orientation of orbitals relative to the X–ray beam polarization (of the electric vector, ***E***). Therefore, if linearly polarized light is used in single crystals, the directional dependence of the density of states (or the orbital occupancy or the direction of chemical bonds) of the atom selected by its absorption edge can be probed by varying the crystallographic alignment of the crystal with respect to the incident X–ray polarization vector [186–190]. Hence, during the experiments data were collected along **different directions** for the epitaxial samples. As a representation of the differences observed when probing an epitaxial film along different directions, Fig. 4.7(a) shows the spectra recorded in the $t \approx 5$ nm (100)–epitaxial sample with the electric vector oriented along [100] (***E***//*a*), [010] (***E***//*b*) and [001] (***E***//*c*). Here, only a subtle yet robust difference is observed: the threshold shifts ~0.3 eV towards higher energy when the [001] direction is probed, and the intensity of the Ir L_2 white line increases respect to the other directions. This is translated into an important reduction of the SOC, as represented in Fig. 4.7(b), around 10–15%. Since the same effect is observed in all the ~100 and ~5 nm–thick samples (see Table 4.2), a strain–induced effect can be ruled out. The shift observed with the electric vector oriented along [001] (***E***//*c*) relative to [100] (***E***//*a*), agrees well with the strong polarization dependence of the O K–edge XAS at low energy, where the intensity of π polarization (π//*c*) becomes strongly suppressed compared to that of σ polarization (σ//*b*) [191]. Besides, ab–initio calculations performed by Dr. J. Chaboy confirmed the small displacement (~0.3 eV experimental/~0.2 eV theoretic) of the threshold towards higher energies when the [001] direction is probed, as shown in Fig. 4.7(c).

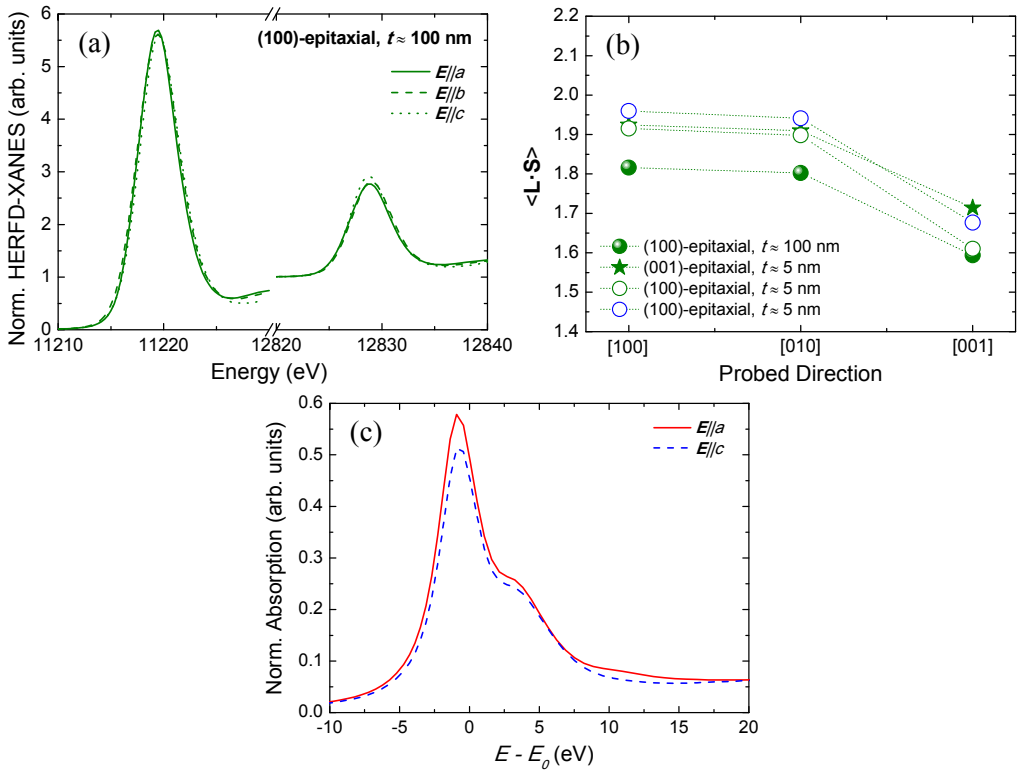

Figure 4.7 (a) Representative comparison between the normalized Ir $L_{2,3}$–edges HERFD–XANES spectra recorded on different directions. Panel (b) plots the values of the SOC (⟨**L**·**S**⟩ product) in units of $\hbar^2$ obtained from the XANES data in representative samples measured along different directions. (c) Theoretical computations corresponding to the Ir L_3–edge XANES of IrO_2 (bulk lattice parameters) with the electric vector oriented along [100] (***E*//*a***) and [001] (***E*//*c***).

Finally, Fig. 4.8(a) shows the spectra recorded in three representative samples with **different degree of strain**, showing negligible differences between them. In the same way, there seems not to be a clear tendency in the values of the SOC (⟨**L**·**S**⟩ product) with the different degree of strain (Fig. 4.8(b)). The (100)–textured sample, which presented unusual large lattice parameters respect to powder IrO_2, also shows a value of ⟨**L**·**S**⟩ (1.83) similar to other ~100 nm–thick samples (Table 4.2). Ab–initio calculations displayed in Fig. 4.8(c) and 4.8(d), indicate that there is a complex response of the polarization–dependent XANES spectra to strain. This is a consequence of the fact that the orientation of the *d* orbitals does not bear a direct

relationship with the lattice axes ([100], [010] and [001]) [84]. As shown in Fig. 4.8(c), the absorption along *a* is strongly modified, not only when stretching the lattice parameter *a* in 5%, but also when *b* and *c* increase. Something similar happens when probing the absorption along *c* (Fig. 4.8(d)). As a result of this combined effect, and the smallness of the differences measured, fine details of the strain–dependence of absorption spectra cannot be easily accounted for.

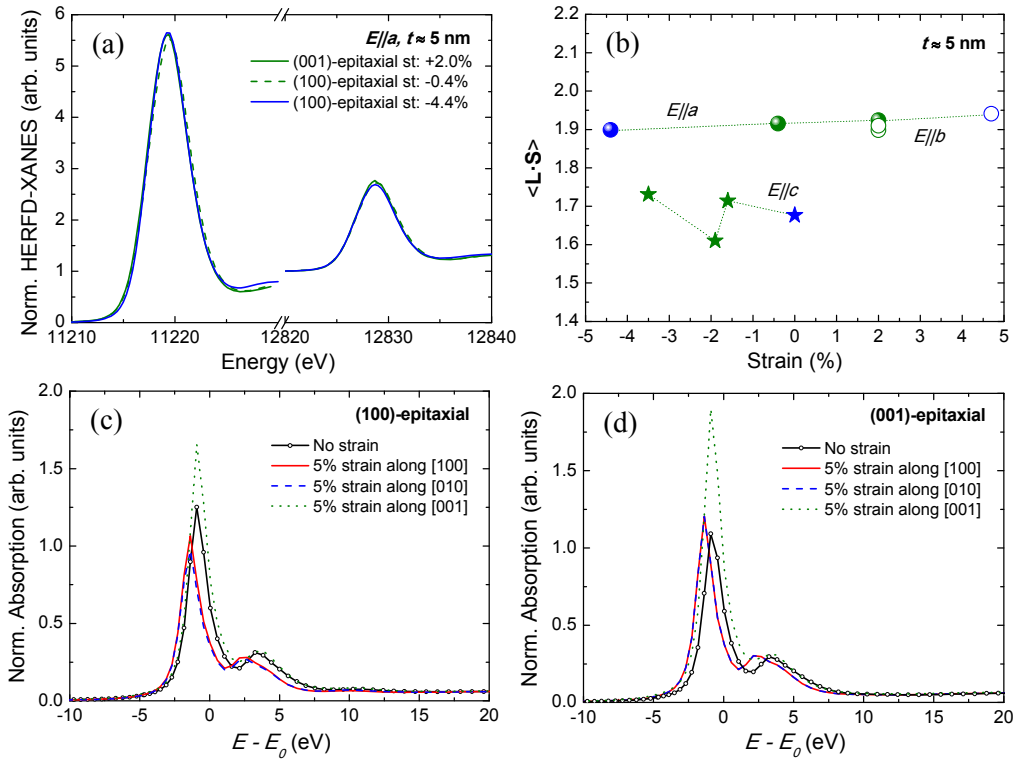

Figure 4.8 (a) Representative comparisons between the normalized Ir $L_{2,3}$–edges HERFD–XANES spectra recorded on samples with different degree of strain. Panel (b) plots the values of the SOC ($\langle \mathbf{L}\cdot\mathbf{S} \rangle$ product) in units of $\hbar^2$ obtained from the XANES data. Panels (c) and (d) show theoretical computations corresponding to the Ir L_3–edge XANES of (100)– and (001)–epitaxial IrO_2 with 5% strain applied along [100], [010] and [001].

Table 4.2: Electronic characterization of the studied samples: integrals of the white lines ($IL_{3,2}$, branching ratio (BR) and ground–state expectation value of the angular part of the SOC ($\langle \mathbf{L}\cdot\mathbf{S} \rangle$ in units of $\hbar^2$).

Sample Crystallinity	*t* (nm)	Probed Direction	IL_3	IL_2	BR	$\langle \mathbf{L}\cdot\mathbf{S} \rangle$
Amorphous	84.7		20.66	5.19	3.98	1.99
	17.4*		20.13	5.18	3.88	1.93
	5.0		21.41	5.36	3.99	1.99
	4.1*		18.82	5.04	3.73	1.83
	2.0*		18.22	4.85	3.76	1.85
Non–text. (GS = 6 nm)	88.1		21.83	5.95	3.67	1.79
Non–text. (GS = 10 nm)	80.5		21.63	5.95	3.63	1.76
	2.1		21.16	5.68	3.73	1.83
(110)–textured	106.5		21.25	5.84	3.64	1.77
(100)–textured	104.4		20.89	5.60	3.73	1.83
(001)–epitaxial	96.0	[100]	21.40	5.71	3.75	1.84
		[010]	21.53	5.62	3.83	1.89
		[001]	20.49	5.81	3.53	1.69
	23.4	[010]	21.45	5.56	3.86	1.91
		[001]	20.81	5.93	3.51	1.67
	5.7	[100]	21.45	5.53	3.88	1.92
		[010]	21.35	5.54	3.85	1.91
		[001]	20.71	5.81	3.56	1.71
(100)–epitaxial	89.0	[100]	20.79	5.60	3.71	1.82
		[010]	21.64	5.86	3.69	1.80
		[001]	20.98	6.16	3.40	1.59
	5.1	[100]	21.42	5.54	3.86	1.92
		[010]	21.58	5.63	3.84	1.90
		[001]	20.70	6.04	3.43	1.61
	2.0	[100]	21.39	5.46	3.92	1.95
		[010]	23.16	5.49	4.22	2.13
(110)–epitaxial	92.2	[001]	21.18	6.09	3.48	1.65
	5.3	[001]	20.73	5.78	3.59	1.73
(100)–epitaxial	5.1	[100]	20.52	5.35	3.84	1.90
		[010]	21.84	5.60	3.90	1.94
		[001]	21.02	5.98	3.51	1.68

*Samples prepared using a pure Ar atmosphere during the pre–sputtering (see section 2.1.2.).

In view of these results, it can be concluded that **the SOC in IrO_2 is very high** and mainly independent on crystallinity, thickness, measuring direction or strain. However, a small yet robust increment of the SOC can be observed for the amorphous (~10%) and the finest (~1–10%) samples. Similarly, within epitaxial films, the SOC shows clearly smaller values when probed along the [001] direction (~10–15%).

Finally, it is pertinent to note that the small differences observed in IrO_2 are in contrast to the case of other widely studied spintronic oxides, such as wurtzite–ZnO [186, 192]. In the latter, the uniaxial crystal symmetry with fairly directional bonding of (strong covalent) ionic–like character leads to a clear directional dependence of the density of (unoccupied final) states probed by XANES, resulting in a large X–ray linear dichroic signal at the Zn K edge. Other rutile structures, such as TiO_2 and SnO_2, have also been reported to show X–ray linear dichroism [187–189]. Furthermore, this practically direction–independent electronic structure in IrO_2 seems to be in disagreement with the predictions by *J. K. Kawasaki et al.* [87] mentioned in the introduction.

4.4. Electrical Characterization

The electrical characterization of the samples was carried out by measuring the temperature–dependent electrical resistivity, ρ(T). Fig. 4.9(a) shows the ρ(T) curves recorded for the ~100 nm–thick samples with differentiated **crystallinity**. At first glance it can be easily seen that: (i) ρ(T) is scarcely dependent on the temperature in all the samples, (ii) there is a trend in the resistivity to increase as the disorder increases (greater electron scattering at grain boundaries [193]), and (iii) the response of the amorphous sample is different from the monotonically increasing resistivity with the temperature observed in the crystalline films.

All the non–amorphous samples present the typical metallic behavior of IrO_2 characterized by a slightly increasing electrical resistivity with the temperature over the whole temperature range. The values of the electrical resistivity in these samples are also within the same order of magnitude than those previously reported for

polycrystalline or epitaxial IrO_2 films, as it may apply [7, 56, 58, 140, 141, 143–146, 194].

In metals, resistivity arises due to collisions of the conduction electrons with vibrating lattice atoms (phonons), impurities and defects. As the temperature increases, the atoms vibrate with greater amplitude, making it more likely that a moving electron collide with them. This impedes the movement of the electrons and is translated into an increase of the electrical resistivity. This can be mathematically described as:

$$\rho_{TOTAL} = \rho(0) + \rho(T) \tag{4.2}$$

where ρ_{TOTAL} states for the total resistivity, $\rho(0)$ is the residual resistivity due to defects, impurities, size effects, and grain boundary scattering, which is essentially temperature–independent and its value is the electrical resistivity when the temperature approaches zero; and $\rho(T)$ is a temperature–dependent contribution which generally follows the Bloch–Grüneisen (B–G) semi–empirical relationship [195]. So that, Eq. 4.2 is written as follows:

$$\rho_{TOTAL} = \rho(0) + A\left(\frac{T}{\theta_R}\right)^n \int_0^{\theta_R/T} \frac{x^n}{(e^x-1)(1-e^{-x})}\,dx \tag{4.3}$$

where A is a constant depending on the electrons velocity at the Fermi surface and their density in the metal, θ_R is the Debye temperature characteristic of each material, and n is an integer that depends upon the nature of the interactions: n = 5 implies that the resistance is mainly due to scattering of electrons by phonons, n = 3 implies that the resistance is due to *s–d* electron scattering, and n = 2 implies that the resistance is due to electron–electron interactions.

As an example of the fits carried out in the samples showing a metallic–like behavior, in Fig. 4.9(b) the fits for the ~100 nm–thick non–textured sample with GS = 10 nm are displayed for the three possible values of n in Eq. 4.3. The excellent fitting curves obtained for n = 2 indicate that the electron–electron scattering dominates the

temperature dependent part of the electrical resistivity, *i.e.*, a Fermi liquid behavior ($\rho \propto T^2$).

As for the electrical resistivity of the amorphous sample, it is found to be ~10 times greater than in the representative epitaxial film, which can be attributed to the disorder of amorphous materials that hinders the conductive electrons in the film, increasing thereby their electrical resistivity. Although it remains largely unchanged (from 670 μΩ cm at RT to 690 μΩ cm at 10 K), two different behaviors can be distinguished: $d\rho/dT > 0$ for low temperatures (T < 200 K), and $d\rho/dT < 0$ in the high temperature range (T > 200 K). This behavior is typically found in amorphous samples [143, 195–198] and it is discussed below.

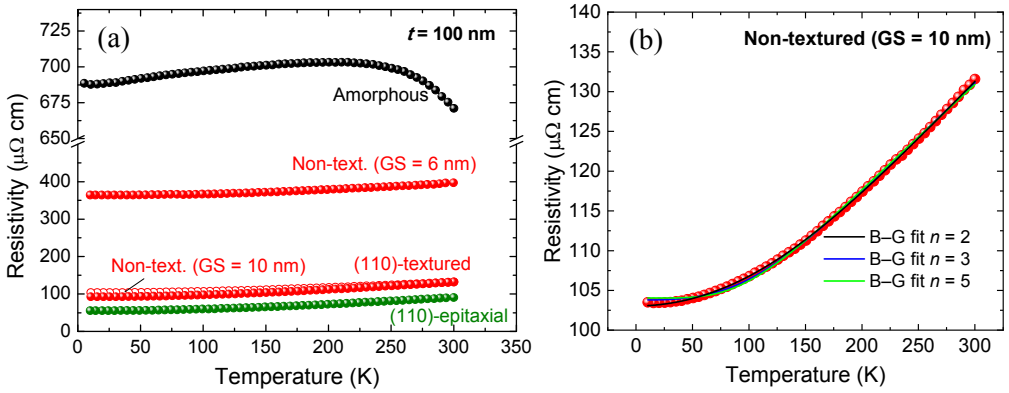

Figure 4.9 (a) ρ(T) curves measured in the ~100 nm–thick samples with different crystallinity. (b) B–G fit for different values of n in the 100 nm–thick non–textured sample (GS = 10 nm).

Regarding the effect of **thickness**, it is observed that the resistivity of the crystalline IrO_2 films increase when decreasing the layer thickness, as represented in Fig. 4.10(a)–(e), for non–textured, (110)–textured, (001)–epitaxial, (100)–epitaxial, and (110)–epitaxial samples, respectively. In general, three different regimes can be identified:

(i) For the thickest samples, *i.e.*, for 5 nm ≤ t ≤ 100 nm (nominal), the electrical resistivity remains, roughly speaking, around 10^2 μΩ cm, showing a metallic behavior in the whole range of temperatures.

(ii) In the $t \approx 2$–3 nm range, the electrical resistivity increases around one order of magnitude respect to the previous case. Moreover, in these samples the resistance decreases when decreasing temperature until T_{min} (marked with arrows in Fig. 4.10), below which an upturn occurs (see inset in Fig. 4.10(b)). This kind of low temperature upturns in resistivity is often observed when a system approaches a MIT from the metallic side [67, 199–201]. In addition, the upturn is located at increasingly higher temperatures as the thickness is reduced.

(iii) Finally, for the thinnest samples ($t < 2$ nm), a $d\rho/dT < 0$ response (semiconductor–like behavior) in the whole temperature range is observed.

Therefore, it is apparent that **the IrO_2 crystalline films undergo a MIT in the 1.5–2.0 nm range**.

As for the amorphous series (Fig. 4.10(f)), the $t \approx 20$ nm sample displays a similar profile to that already observed for $t \approx 100$ nm, though with slightly larger values of electrical resistivity and also with a maximum at ~200 K. As the layer thickness decreases, the "high temperature mechanism", which leads to $d\rho/dT < 0$, becomes progressively more dominant, and for $t \approx 2$ nm the slope of the resistivity curve remains negative over the whole temperature range. Roughly speaking, it can be seen that the "low temperature mechanism" ($d\rho/dT > 0$) sets the electrical resistivity around 10^3 μΩ cm, while the "high temperature mechanism" lowers the resistivity almost one order of magnitude in the $t \approx 2$ nm sample. The complex behavior of the electrical resistivity with the film thickness in amorphous materials was already observed by *Y. Fu et al.* [196]. Moreover, added to the amorphous state of these films, there are at least other two contributions that should be taken into account: the presence of Ir metal, with $\rho \approx 10$ μΩ cm at 5 K; and the possible existence of a conducting channel switching between the upper IrO_2 film and the inversion layer at the SiO_2–Si interface underneath [202–204].

In conclusion, it is clear that, in the amorphous films, the different contributions to the electrical resistivity lead to a complex response. Notwithstanding

this, it should be noted that the total variation of resistivity is very small, as it practically remains in the same order of magnitude regardless of the layer thickness. Hence, a deep study of these effects is beyond the aim of this chapter and the scope of the thesis.

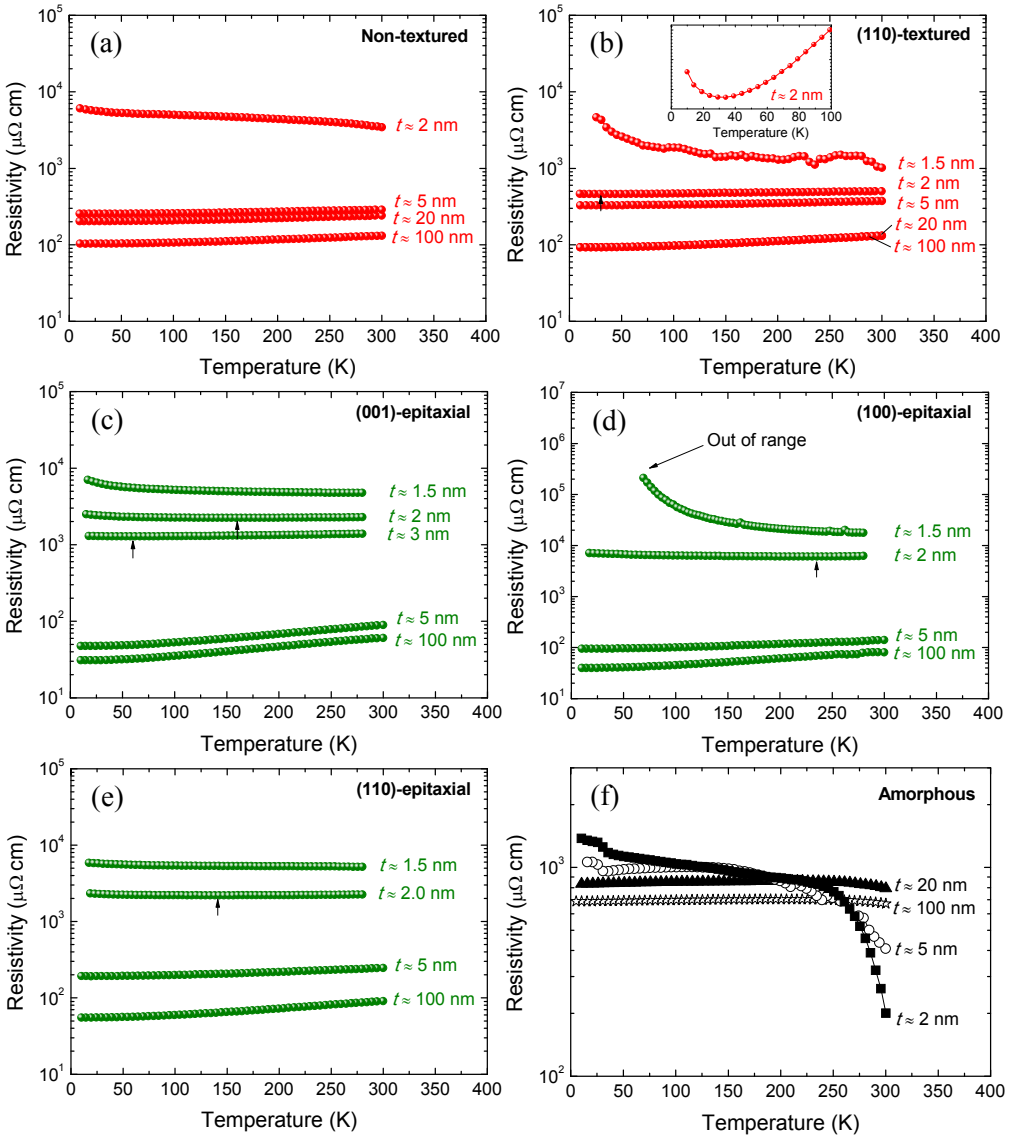

Figure 4.10 ρ(T) curves for (a) non–textured, (b) (110)–textured, (c) (001)–epitaxial, (d) (100)–epitaxial, (e) (110)–epitaxial and (f) amorphous samples with different thickness. Vertical arrows mark the position of upturns.

Trying to shed some light into the origins of the MIT observed in the crystalline samples, Fig. 4.11(a) shows the sheet resistance, R_s, as a function of the temperature for representative epitaxial samples (R_s is defined as $R_s = R\pi/ln(2)$, being R the electrical resistance). It can be seen that R_s continuously increases as the film thickness is reduced. For relatively low R_s values (samples with $t \geq 5$ nm) the Fermi liquid behavior was already proved (not included here). On further reducing t to the 3–2 nm range, a strong upturn occurs. Then, it is important to realize that the change in the electrical behavior corresponds to $R_s \approx 25$ kΩ. *Ioffe* and *Regel* pointed out that the simple kinetic theory of conductivity has to break down when the particle wavelength is longer than the mean free path, l. When $k_F l$ is close to unity, being k_F the Fermi wave–vector, a MIT is expected. In very thin films (~2D), R_s is related to $k_F l$ by [205]:

$$k_F l = \frac{h/e^2}{R_S} \approx \frac{25\ \text{k}\Omega}{R_S} \tag{4.4}$$

Therefore, the above criterion defines a crossover region between weak and strong localization [205].

Trying to elucidate the type of insulator, the resistivity curves were fitted to several theoretical models. The low temperature upturns can be explained by weak localization. Weak localization is a disorder–driven effect (Anderson type) due to quantum interference of the conducting charge carriers at defect sites, which increases the resistivity [206]. Fig. 4.11(b) illustrates that the R_s in the low temperature upturn region is well fitted to [174, 207]:

$$\rho = \rho(0) - \alpha T^{3/4} + \beta T^{3/2} \tag{4.5}$$

where $\rho(0)$, α, and β state for the remnant resistance, three–dimensional weak localization, and inelastic scattering due to electron–boson interactions, respectively. The weak localization coefficient for the $t \approx 3$ nm (001)–epitaxial film is found to be $\alpha/\rho(0) = 0.004$, which is practically identical to that found on $SrIrO_3$ deposited on $SrTiO_3$ ($\alpha/\rho(0) = 0.003$) [175].

On the other hand, the resistivity of the (001)–epitaxial film with $t \approx 2$ nm has a sheet resistance very close to h/e^2 at RT, resulting in $k_F l \approx 1$, and an insulating behavior is found in the temperature range. For this strongly localized regime, a variable range hopping (VRH) type of conduction is expected. In this case, at low temperatures, electrons hop between localized states and the resistivity is given by [208, 209]:

$$\rho = C\ exp\left(\frac{T_o}{T}\right)^n \tag{4.6}$$

where C is a constant and T_0 is the characteristic temperature of the compound, which depends on the density of localized states and the spread of their wave functions [210]. The fitting shown in Fig. 4.11(c) for the (001)–epitaxial sample with $t \approx 2$ nm yields an exponent $n = 0.46$, being in good agreement with the Efros–Shklovskii VRH (ES–VRH) model ($n = 0.5$). Such model assumes a Coulomb gap opening in the density of states near the Fermi level brought in by interactions between localized electrons, *i.e.*, a Mott–insulator [211].

Finally, as shown in Fig. 4.11(d), the behavior of the (100)–epitaxial film with $t \approx 1.5$ nm (sample with the highest electrical resistivity) is well described by an Arrhenius type behavior given by:

$$\rho = C\ T\ exp\left(\frac{E_g}{2k_B T}\right) \tag{4.7}$$

where C is a constant, E_g is the energy gap and k_B is the Boltzmann constant. The fit yields to $E_g \approx 30$ meV, which again suggests a Mott–insulator.

Therefore, it is concluded that the electrical resistivity of crystalline IrO_2 thin films is highly dependent on the thickness, up to the point where **a clear MIT occurs in the 1.5–2.0 nm range**. Such layer thickness corresponds to 3–5 unit cells, being quite in agreement with the theoretical predictions [82, 83]. It has to be noted that the superlattices are distinctly different from IrO_2 single films, since the first may be affected by interlayer coupling. In particular, the superlattices could be affected by

additional hopping channels between the IrO_2 layers, as observed in $SrIrO_3$ superlattices [212]. This could be the reason why *J. K. Kawasaki et al.* [87] could not find this MIT. By studying single IrO_2 layers of different thicknesses, the effect of dimensionality (3D–2D) on IrO_2 is directly addressed. By fitting the resistivity curves to different models, in the t = 2–3 nm range, signs of weak/Anderson localization emerge (upturns at low temperature), revealing an important role of disorder. However, on further reducing the layer thickness the hopping (ES–VRH) and thermal activation mechanisms suggest a gap opening, and hence, a major role of correlations (Mott–insulator). It is worth mentioning here that the same models were used by *D. J. Groenendijk et al.* [65] to study the MIT observed in $SrIrO_3$ thin films deposited on $SrTiO_3$, suggesting similar underlying mechanisms in both materials.

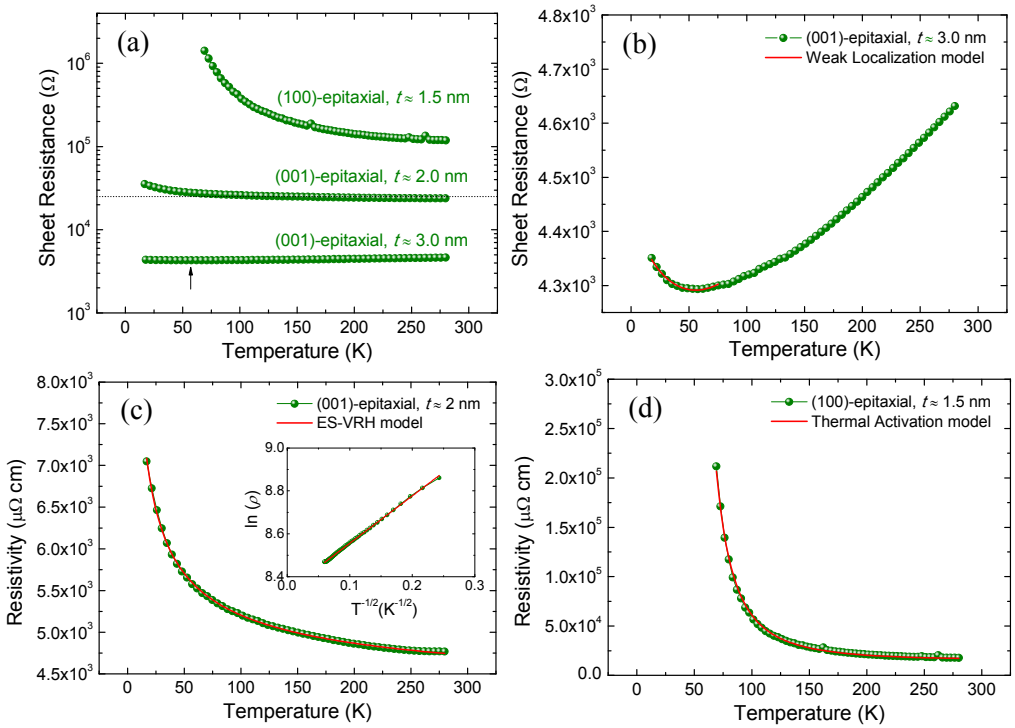

Figure 4.11 (a) Sheet resistance calculated for the thinnest (001)– and (100)–epitaxial films. (b) ρ(T) curve for the $t \approx 3$ nm (001)–epitaxial sample fitted to a weak localization model at low temperature. (c) ρ(T) curve for the $t \approx 2$ nm (001)–epitaxial sample fitted to a ES–VRH model. (d) ρ(T) curve for the $t \approx 1.5$ nm (100)–epitaxial sample fitted to a thermal activation model.

Therefore, these initial results suggest the contribution of both, disorder and correlations in inducing a MIT in IrO_2 when reducing the film thickness. It has to be noted that revealing the origins of a MIT is an intricate work, where, as proved in previous research carried out on $SrIrO_3$ and Sr_2IrO_4, several mechanisms might coexist [65, 67, 72–74, 175]. Although further work is needed to fully clarify this issue in IrO_2, to the best of our knowledge this research is pioneer in finding a MIT in such iridate and starting to study its origins.

Given the structural anisotropy of IrO_2, the difference in resistivity when the current (*I*) is applied along **different directions** was also studied. It has to be noted that in this case, the van der Pauw method (section 2.6) does not apply, but a standard four probe configuration has been used for each direction separately ($\rho = R\pi t/ln(2)$, where R is the electrical resistance). In addition, samples with nominal $t < 5$ nm cannot be taken into account due to the strong influence of the thickness below this limit, as proved above. Despite these facts, some proper comparisons can be made. Fig. 4.12 shows the resistivity curves for the ~100 and ~5 nm–thick epitaxial films with *I* applied along different directions: *I//a* and *I//c*. It can be seen that, for both layer thicknesses, the electrical resistivity is 2–3 times greater when *I//c*. As mentioned above, this reflects the anisotropy in the crystal structure and could be due to the reduced hybridization of the t_{2g} orbitals of Ir with the O–2*p* orbitals along [001] relative to the hybridization along [100] and [010] directions [191]. Compared to other structurally anisotropic iridates such as $BaIrO_3$ or Sr_2IrO_4, the rutile iridate presents lower anisotropy of ρ(T), *i.e.*, lower ρ_a/ρ_c [213, 214]. More importantly, the differences observed are negligible compared with those obtained when varying the layer thickness.

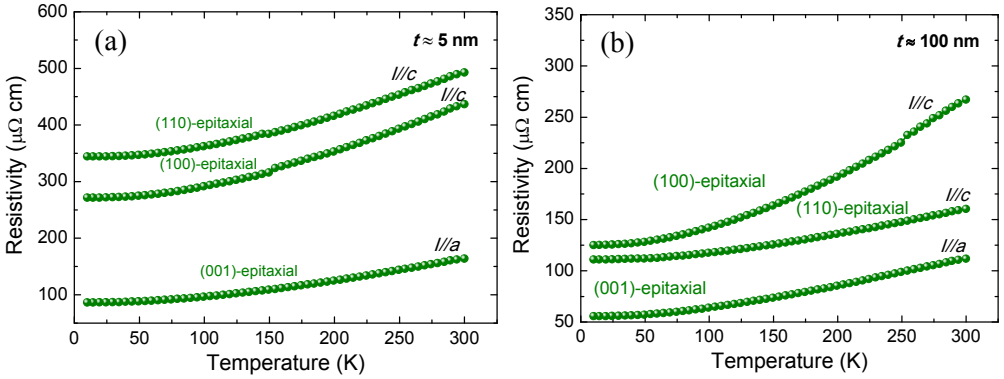

Figure 4.12 ρ(T) curves measured with *I* applied along different directions: *I//a* and *I//c*; for epitaxial films with (a) $t \approx 100$ nm and (b) $t \approx 5$ nm.

Finally, no clear tendencies which could be attributed to a **strain**–driven effect are observed in Fig. 4.13, since samples with large differences in their lattice parameters display very similar resistivity curves. Compare for instance in Fig. 4.13(a) the (100)–epitaxial sample deposited on TiO_2 (ε_a = -0.4%, ε_b = 2.0% and ε_c = -1.9%) and the (100)–epitaxial sample deposited on SnO_2 (ε_a = -4.4%, ε_b = 4.7% and ε_c = 0.0%). This behavior is noticeably different from that observed in $SrIrO_3$, where a 35 nm–thick film deposited on $NdGaO_3$ (with ε_a = +2.5% and ε_c = -2.7%) results in $d\rho/dT < 0$ in the whole temperature range [67, 175]. Such different response to the substrate–driven strain could be related to the structural differences of these iridates: while the IrO_6 octahedra in IrO_2 share corners and edges, in $SrIrO_3$ they are only corner–sharing. This results in an initially broader bandwidth (*W*) as well as in a more rigid structure for IrO_2 [80]. Remember that $W \propto cos\varphi/d$ (where φ is the angle formed by Ir–O–Ir atoms, and *d* the Ir–O bond length). The MIT induced by the substrate–driven strain observed in $SrIrO_3$ is associated to a tilt in φ, while it is assumed that the bond length remains constant [67, 175]. Although a similar substrate–driven strain in IrO_2 has been achieved, it seems not to be enough to significantly distort its structure and in turn, to reduce *W*. Therefore, this approach is certainly not a feasible method to find a MIT in IrO_2.

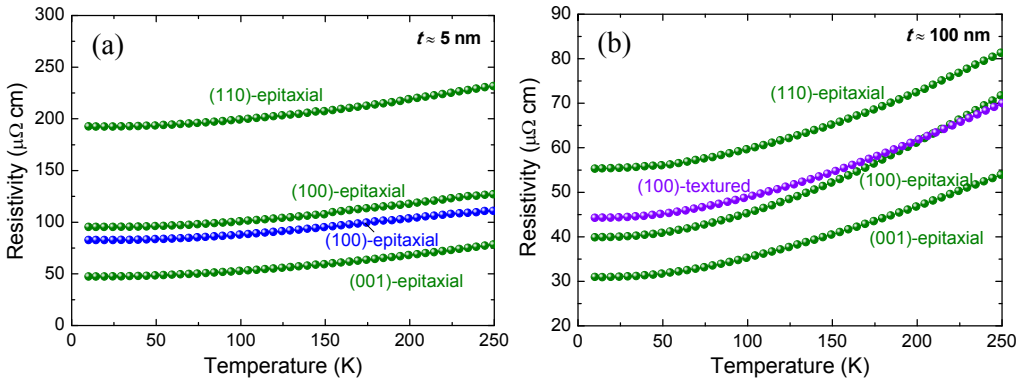

Figure 4.13 Comparison of the ρ(T) curves measured in samples with different substrate–driven strain with (a) $t \approx 5$ nm and (b) $t \approx 100$ nm.

4.5. Magnetic Characterization

Once experimental evidence of the predicted MIT has been proved in previous section, it is mandatory to search also for the expected nonmagnetic–magnetic transition induced in IrO_2 by structural modifications [82, 83].

4.5.1. SQUID Magnetometry

Fig. 4.14(a) shows the field dependent, M(H), curves measured in the ~100 nm–thick films with different **crystallinity**. It can be observed that all the samples show a negligible response to the magnetic field regardless of their crystallinity, with a maximum magnetic moment at 5 K and 50 kOe (M_{max}) in the order of 10^{-5} emu/cm^2. No hint of magnetic order is observed. The very small negative slope can be associated to a slightly imperfect correction of the substrate or to the silver paste diamagnetic contribution.

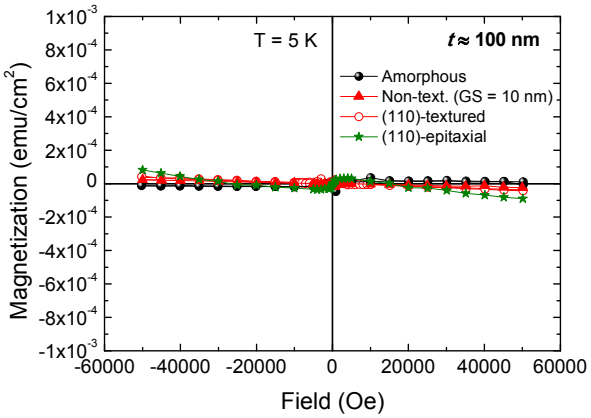

Figure 4.14 M(H) curves for the ~100 nm–thick amorphous, non–textured (GS = 10 nm) and (110)–textured samples, measured at 5 K.

Similarly, Fig. 4.15 shows the M(H) curves measured in representative samples of the epitaxial series deposited on TiO_2, at both 5 K (left panels) and 300 K (right panels). Again, no hint of magnetic order is detected regardless of the **thickness**, **direction** or **strain**, since the M(H) curves remain within the error bar extracted in Chapter 2. Therefore, even in the cases where a positive slope is observed, this signal cannot be undoubtedly associated to the presence of magnetic order. Note also that the apparent signal observed in the $t \approx 1.5$ nm (100)–epitaxial sample in panel (c) is not real, at least in magnitude, since when associating the magnetic moment measured to the IrO_2 layer, non–sense values up to 8 μ_B/at. Ir at H = 50 kOe are obtained. This is probably due small differences in the substrates employed (such as more Ti^{3+} impurities).

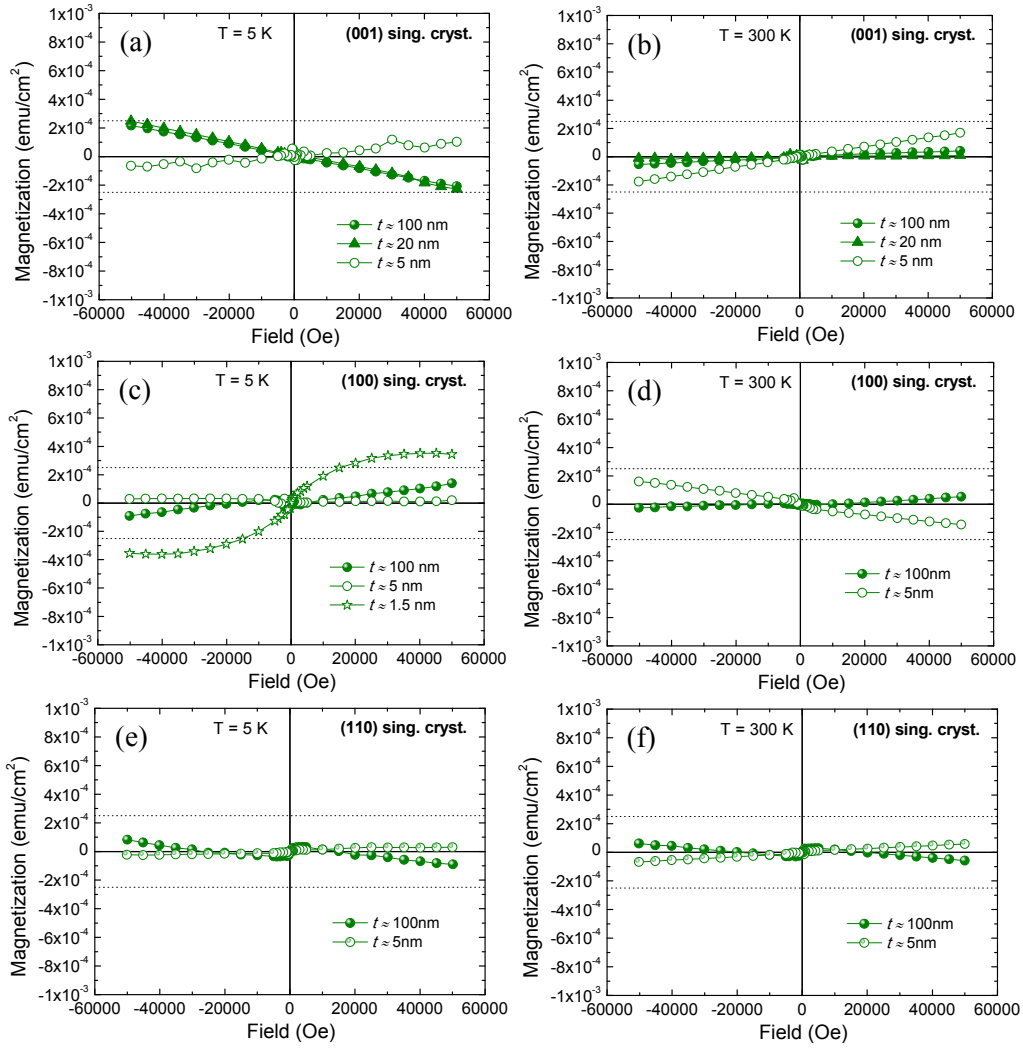

Figure 4.15 M(H) curves for representative samples of the epitaxial IrO_2 series on TiO_2 substrates, measured at 5 K (left panels) and 300 K (right panels). Two dotted lines at $\pm 2.5 \times 10^{-4}$ emu/cm^2 mark the limit of the reliable magnetic response as explained in Chapter 2. In other words, any signal within these lines is in the order of the spurious/undesired effects.

In order to elucidate what could be expected from the magnetometry measurements, Fig. 4.16(a) shows the M(H) curve recorded in powder IrO_2 at 5 K. In Fig. 4.16(b) the curve is normalized to a 100 nm–thick film, *i.e.*, this would be the expected signal for a pure 100 nm–thick IrO_2 thin film. It shows a paramagnetic behavior with $M_{max} = 8.5 \times 10^{-6}$ emu/cm^2. This value is, roughly speaking, one order of

magnitude smaller than the signals observed in Figs. 4.14 and 4.15 and the spurious or undesired effects introduced in the SQUID.

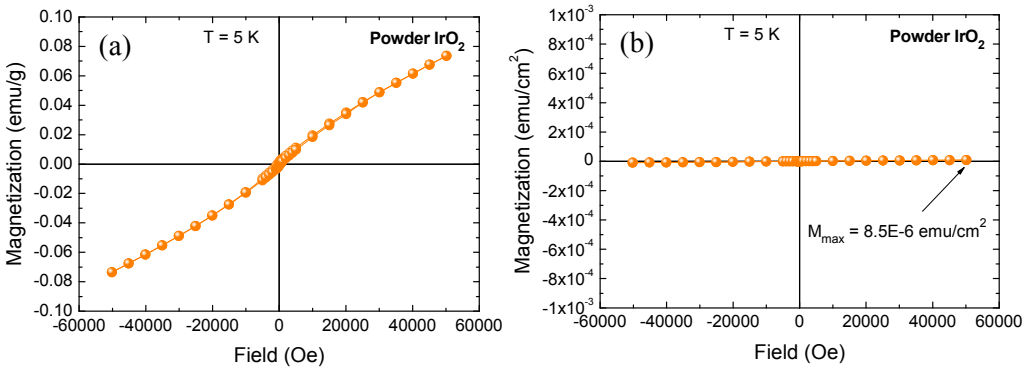

Figure 4.16 M(H) curve measured in powder IrO_2 and normalized to a 100 nm–thick film.

On the other hand, if some of the structural modifications in the films were able to trigger a paramagnetic–to–ferromagnetic transition with an atomic magnetic moment of 1.0 μ_B/at. Ir (0.1 μ_B/at. Ir), then a M_{max} in the 1–30x10^{-4} (0.1–3x10^{-4}) emu/cm^2 range should be expected in the films, as displayed in Table 4.3. Note that these values could be even smaller for a canted antiferromagnetic ordering.

Table 4.3 Expected IrO_2 magnetization values, $M_{max,\ IrO2}$, for an effective magnetic moment of 1.0 and 0.1 μ_B/at. Ir, for a 100 and 5 nm–thick films.

Sample	**Expected $M_{max,\ IrO2}$ (x10^{-4} emu/cm^2)**	
	For 1.0 μ_B/at. Ir	For 0.1 μ_B/at. Ir
IrO_2 film t = 100 nm	29.0	2.9
IrO_2 film t = 5 nm	1.5	0.2

Thus, the M(H) curves measured in the ~100 nm–thick samples in Figs. 4.14 and 4.15, seem to rule out a ferromagnetic ground state regardless of the degree of **crystallinity**. However, (canted) antiferromagnetism is still compatible with these results. Regarding the layer **thickness**, as showed in Table 4.3, the maximum expected magnetization for a t = 5 nm film is just on the limit of the reliable magnetic response, as explained in Chapter 2. Something similar happens with the analysis of the **direction** or **strain**, since all the signals in Fig. 4.15 are in the order or smaller than

the spurious/undesired effects. Therefore, the presence of a magnetically ordered state cannot be unambiguously neither confirmed nor discarded by the M(H) curves.

On the other hand, Figs. 4.17(a) and 4.17(b) show the temperature–dependent magnetization curves, M(T), measured in the thinnest films from the (001)– and (100)–epitaxial sample series, respectively. While the curve recorded in the (001)–epitaxial film shows a typical weak paramagnetic behavior, a small ferromagnetic–like transition is observed in the (100)–epitaxial film at T_c = 130 K. Also a paramagnetic contribution seems to be overlapped with such weak ferromagnetic signal. Zero–field–cooled (ZFC) and field–cooled (FC) curves split at a temperature slightly below T_c. This fact indicates that the weak ferromagnetism might arise from a canted antiferromagnetic order, as occur in Sr_2IrO_4 [215] or in Sn–doped $SrIrO_3$ [70, 71], and also in agreement with the theoretical predictions on IrO_2 [82, 83]. Moreover, it can also be observed that this transition appears approximately in the same temperature range at which the electrical resistivity shows a drastic increase, in agreement with the Slater theory (Slater insulator). Therefore, without losing sight of the relatively high uncertainty of these results, which hinders extracting more conclusive results, this should be seen as a first hint of the possibility of inducing magnetic ordering in IrO_2 through structural modifications (thickness).

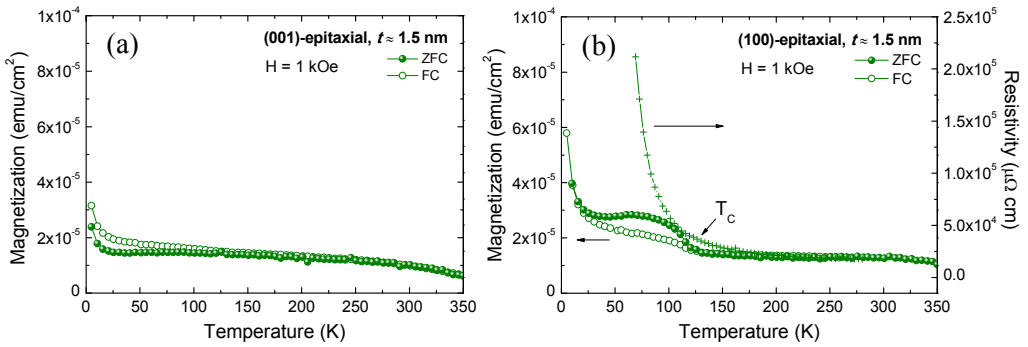

Figure 4.17 M(T) curves measured on the thinnest ($t \approx 1.5$ nm) (a) (001)–epitaxial and (b) (100)–epitaxial films.

Finally, it has to be said that for the sample grown on SnO_2 (100), having this substrate a "natural growth", it contains large and uncontrolled magnetic impurities that hindered any analysis of the magnetic signal of the deposited IrO_2 layer.

4.5.2. X–Ray Magnetic Circular Dichroism (XMCD)

In view of the results obtained above, trying to disentangle any possible magnetic ordering of the Ir atoms, Fig. 4.18(a) shows the XMCD spectrum recorded at the Ir $L_{2,3}$ edges on the $t \approx 1.5$ nm (100)–epitaxial sample, *i.e.*, the sample exhibiting the largest electrical resistivity and traces of magnetic ordering in the M(T) curves at low temperatures. Although the signal to noise ratio is relatively big, a small XMCD signal (~0.2%) can be inferred in the Ir L_3 edge. Regarding the Ir L_2 edge the presence of an XMCD signal is ambiguous. If any, its size is much smaller than that at the L_3 edge. The position, shape and sign of the small signal observed agrees well with previous XMCD measurements carried out in other Ir^{4+}–based compounds, such as in Sr_2IrO_4 [179], Sr_2TiIrO_6 [216] or $BaIrO_3$ [180]. This suggests that such small signal may indeed be associated to magnetic ordering of the Ir^{4+} cations. In addition, the XMCD measurements on powder IrO_2 present a much smaller intensity (Fig. 4.18(b)). Even when this commercial sample contains ~4% of metallic Ir (which explains the low intensity of the white line), the comparison points out, at least, to an enhanced paramagnetic signal in the film. Unfortunately, there is not a good reference on pure IrO_2 available in the literature, neither in thin film nor even in bulk.

Hence, this is another hint suggesting that magnetic ordering can be achieved in IrO_2 through structural modifications (thickness), in agreement with theoretical predictions [82, 83]. However, these initial results need for complementary measurements to extract irrefutable conclusions, such as XMCD measurements as a function of the temperature, or X–ray magnetic scattering, for instance. These experiments entail long allocation time at large facilities such as synchrotrons or muon sources, and hence, they had to be left out from the scope of this thesis.

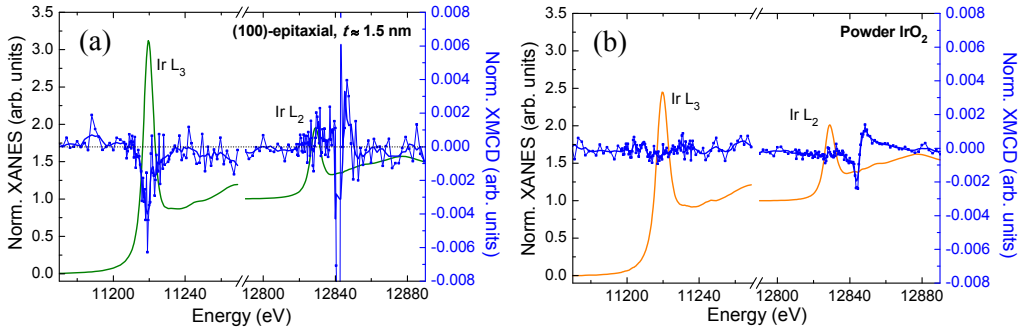

Figure 4.18 (a) Normalized XANES and XMCD spectra recorded in fluorescence mode at the Ir $L_{2,3}$ edges at T = 10 K and H = ±50 kOe on the $t \approx 1.5$ nm (100)–epitaxial sample. (b) Normalized XANES and XMCD spectra measured in transmission mode at the Ir $L_{2,3}$ edges at T = 10 K and H = ±35 kOe on powdered IrO_2. The lower intensity of the white line is due to a ~4% of metal Ir phase. Solid blue lines are guides to the eye.

4.6. Conclusions

The relationships between the structure of IrO_2 thin films and their electronic description and electrical and magnetic properties have been studied.

The structural characterization allowed confirming that the samples under study present indeed, relevant differences in their crystallinity (from amorphous to epitaxial films), thickness (from ~100 to ~1.5 nm), growing orientation ((001)–, (100)– and (110)–oriented); and lattice parameters/strain (from -5 to +5% difference, approximately, respect to the powder IrO_2). In addition, the EXAFS measurements revealed that the Ir–O bond lengths are slightly greater in amorphous samples.

The SOC in IrO_2 is very large and robust, being mainly independent on the structural details. A small but reproducible increment of the SOC is observed for the amorphous (~10%) and the finest (~1–10%) samples. Similarly, within the epitaxial films the SOC is slightly reduced when probed along the [001] direction (~10–15%). The differences observed are qualitatively well explained in terms of bandwidth reduction.

Regarding the electrical characterization, upon reducing the IrO_2 film thickness, the response evolves from a metallic ground state ($t \geq 5$ nm) to a strongly localized behavior (in the 1.5–2.0 nm range) as the RT sheet resistance approaches $h/e^2 \approx 25$ kΩ. A transition region between the metallic and the strongly localized states is observed around 2–3 nm–thickness, where the films show upturns in the resistivity at low temperatures explained by the theory of weak localization (Anderson/disorder). On further reducing the thickness of the deposited layer, in the 1.5–2.0 nm range a small band gap is opened (Mott/correlations). Thus, a **thickness–dependent MIT has been found in IrO_2 thin films**. On the other hand, modification of the lattice parameters or the degree of crystallinity does not result in any significant modification of the electrical transport response (same order of magnitude). The resistivity is found to present only a slight anisotropy.

As for the magnetic properties, the SQUID magnetometry gives ambiguous results in most cases, so that the presence of a magnetically ordered state cannot be neither confirmed nor discarded. However, the temperature magnetization curves suggest some (anti)ferromagnetic ordering at low temperature in the finest samples. The transition seems to occur at the same temperature at which the resistivity shows a strong increase (Slater insulator). In addition, the XMCD measurements also point out the presence of some magnetic ordering of the Ir^{4+} cations in the same sample at low temperature. However, the uncertainty of these results is not negligible and more experimental work is needed to confidently assert and better understand such magnetic ordering.

Therefore, this research highlights ultrathin IrO_2 films as a novel platform for tuning the electrical and magnetic response of this material. The main advantage over other iridates is the much easier synthesizing methods. A systematic study of the magnetotransport properties near the MIT and further XMCD measurements would be highly desirable to better characterize the transitions and have a deeper knowledge of this complex system.

2nd Approach

Negative Chemical Pressure

Chapter 5

$Ir_{1-x}Sn_xO_2$ Thin Films

5.1. Introduction

An alternative route to that probed in the preceding chapter to **tune the electrical and magnetic properties of IrO_2** thin films consists on applying a negative chemical pressure **by substitutional doping**. Choosing **Sn** as the dopant element is especially promising, since it conforms the Hume–Rothery rules for the formation of a substitutional solid solution phase: (i) IrO_2 and SnO_2 have the same rutile crystal structure; (ii) in such structure, the Ir and Sn cations have the same valence state (4+); (iii) the size of the Sn^{+4} cation is only slightly larger than the Ir^{4+} (0.69 *vs.* 0.63 Å [217]); and (iv) the electronegativities of Ir and Sn are similar (2.20 *vs.* 1.96, according to Pauling scale [218]). Therefore, the formation of a stable $Ir_{1-x}Sn_xO_2$ solid solution is envisaged, even when phase separation and very low solubility have also been reported [219]. Regarding the electrical transport, the larger size of Sn^{4+} should result in a volume increase, which in turn may produce a decrease of the orbital overlap, thus favoring an increase in the electrical resistivity. Moreover, the closed–shell electron configuration of the Sn^{4+} cation should also contribute to enhance the resistivity of the compound. In fact, bulk SnO_2 (with Sn^{4+}: [Kr]$4d^{10}$ and O^{2-}: [Ne]) presents an insulating behavior [220, 221]. Finally, Sn^{4+} doping will not modify the electronic configuration of Ir, which will remain as Ir^{4+} irrespective of the doping content. Therefore, the modification of the resistivity due to a change in the Ir cation can be ruled out. On the other hand, given the robustness of the spin–orbit coupling (SOC) in Ir^{4+} systems [179–181], there is a reasonable likelihood that the $Ir_{1-x}Sn_xO_2$ compound also remains in a high SOC regime.

From the applied point of view, the main motivation of the work described along this chapter is related to the potential of IrO_2 in the development of pure spin–current spintronic devices [7]. In particular, the main goal is to **optimize the response of IrO_2 as a spin–current detector material**. To this end, special attention is paid to the main factors involved in the spin–current detection process, namely: the spin Hall angle, α_{SH}, and the electrical resistivity, ρ. The spin Hall resistivity, given by $\rho_{SH} = \alpha_{SH}\rho$, determines the efficiency of spin–current detection [222, 223]. This means that a sensitive detection of spin currents would be achieved in materials with both, large α_{SH} and high ρ. The large α_{SH}, owed to the strong SOC, is typically found in heavy transition metals. However, such materials typically present very low ρ. Although the resistivity of IrO_2 is relatively high, it still belongs to the family of electrically conductive transition metal oxides, with $\rho \approx 10^2$ μΩ cm [7, 56, 58, 140, 141, 143–146, 194]. Therefore, in order to improve the usability of IrO_2 as spin current detector, it is necessary to **increase its electrical resistivity while keeping its high SOC**.

So far, the study of $Ir_{1-x}Sn_xO_2$ compounds has been limited to powder samples and nanoparticles in the field of catalysis [224–230] and prepared by chemical methods such as sol–gel [224, 225], Adams fusion [226, 227] or surfactant–assistant methods [228]. Nevertheless, no attention has been paid to the potential of these dilutions in the field of spintronics and, to the best of our knowledge, this is the first time that $Ir_{1-x}Sn_xO_2$ thin films have been grown by means of sputtering techniques. Thus, along this chapter the fabrication and characterization of sputtered Sn–doped IrO_2 thin films with different doping content and microstructure is described. Section 5.2 is devoted to the sample preparation. The structural properties are presented in section 5.3, and the electronic, electrical and magnetic characterization is discussed in sections 5.4, 5.5 and 5.6, respectively.

5.2. Sample Fabrication

$Ir_{1-x}Sn_xO_2$ thin films of ~100 nm (x = nominal Sn concentration) were prepared by reactive co–sputtering deposition (see Fig. 2.3) on Si substrates at room temperature (RT) from metallic Ir and SnO_2 targets. The same Ir target employed in

the previous chapters for growing sputtered IrO_2 films was connected to a DC–source, while the SnO_2 target,[10] due to its insulating behavior, was connected to a RF–source. In order to avoid the formation of metallic Ir in significant amounts, which would suppose a decrement in the SOC [81], the sputtering power supplied to the Ir target was set to ~8 W and the gas flows at 13 ml Ar/min and 2 ml O_2/min, according to the previous study shown in Chapter 3. As for the SnO_2 target, the sputtering power was accordingly varied from 18 to 29 W to obtain dilutions with different Ir/Sn proportions, ranging from 10 to 50 at.% Sn. Additionally, pure SnO_2 (x = 1) films fabricated under the same conditions, and analogous IrO_2 (x = 0) films from Chapters 3 (synthesis) and 4 (characterization) were used as reference materials.

After studying the properties of the as–grown films, *i.e.*, amorphous samples, they were subsequently annealed in air at 600 ºC during 6 h to obtain polycrystalline samples. Additionally, as the optimal annealing temperature for SnO_2 is greater (around 1100 ºC from our experience), one amorphous $Ir_{0.5}Sn_{0.5}O_2$ sample was annealed in air at 900 ºC during 6 h (labeled as $Ir_{0.5}Sn_{0.5}O_2(2)$). It has to be noted that this is above the temperature at which the volatile IrO_3 phase is formed (see section 3.2.4).

5.3. Structural and Compositional Characterization

5.3.1. X–Ray Reflectivity (XRR)

Fig. 5.1 shows the XRR curves measured to determine the thickness of the as–grown samples. The values obtained from such curves, given in Table 5.1, are within the 100 ± 20 nm range. Additionally, looking at Fig. 5.1 the decay rate of the reflectivity curves is similar in all the samples, indicating a similar surface roughness, around 2.5 nm according to the fittings (except ~1.3 nm for x = 0.3 sample). Moreover, it can also be observed in this figure how the critical angle, θ_c, shifts towards lower 2θ values as the Sn content increases, consistent with the lower density

[10] Home–made SnO_2 target provided by Dr. C. Prieto from *Instituto de Ciencia de Materiales de Madrid* (ICMM).

of SnO_2 (6.95 g/cm^3) against IrO_2 (11.66 g/cm^3). On the annealed samples, unfortunately, the signal to noise ratio of the XRR curves (not shown) did not allowed a reliable determination of the layer thickness due to a relatively great roughness which hinders the X–ray interference created by the substrate and film surfaces. Nevertheless, from the results extracted in Chapter 3 and the absence of a volatile SnOx phase, the annealing treatment at 600 ºC is expected to reduce the film thickness less than 10% (the sample annealed at 900 ºC will be discussed in the next section).

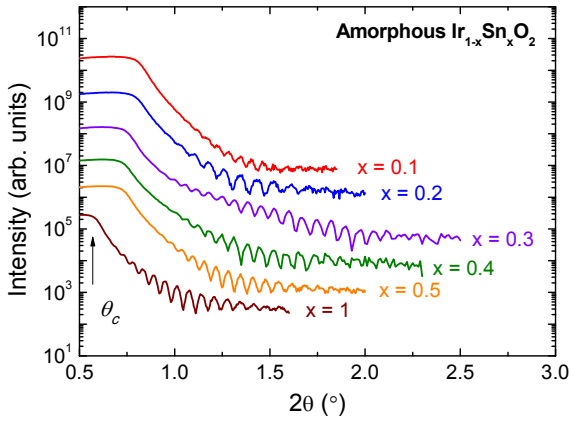

Figure 5.1 XRR measurements on as–grown $Ir_{1-x}Sn_xO_2$ samples.

5.3.2. Field–Emission Scanning Electron Microscopy (FE–SEM)

In order to study the effects of the annealing treatment on the morphology and thickness, cross–sectional FE–SEM images were taken on representative samples. Figs. 5.2(a) and 5.2(b) compare the $Ir_{0.5}Sn_{0.5}O_2$ sample after the annealing treatment at both, 600 and 900 ºC, respectively. For the first, a homogeneous layer thickness of ~105 nm is observed. That is ~7% lower than the thickness of the amorphous sample measured by XRR and in agreement with the results extracted from Chapter 3. As for the sample annealed at 900 ºC, a layer thickness of ~95 nm is measured, *i.e.*, a ~16% reduction respect to the amorphous sample. In consequence, while the annealing treatment at 600 ºC seems to produce the typical compaction by reducing internal defects in the film, it is likely that, at 900 ºC, the formation of volatile IrO_3 contribute to further reduce the layer thickness.

Table 5.1: Structural and compositional properties of $Ir_{1-x}Sn_xO_2$ thin films. Layer thickness measured by XRR in as–grown samples, Sn concentration determined by EDX (relative to the total Ir + Sn) in polycrystalline samples, and lattice parameters extracted from XRD and Rietveld analyses.

Sample	Thickness (nm)	Sn Content (%) ±2%	Lattice Parameters (Å)		Cell Volume (Å^3)
			$a = b$	c	
$Ir_{0.9}Sn_{0.1}O_2$	114	9	4.495(2)	3.142(2)	63.5(1)
$Ir_{0.8}Sn_{0.2}O_2$	80	19	4.510(4)	3.149(4)	64.1(1)
$Ir_{0.7}Sn_{0.3}O_2$	109	26	4.547(9)	3.151(9)	65.2(3)
$Ir_{0.6}Sn_{0.4}O_2$	111	42	4.590(4)	3.148(3)	66.3(1)
$Ir_{0.5}Sn_{0.5}O_2$	114/105*	46	4.583(6)	3.176(6)	66.7(2)
$Ir_{0.5}Sn_{0.5}O_2$(2)	95*	63	4.605(4)	3.171(3)	67.2(1)
SnO_2	114	100	4.736(1)	3.185(1)	71.4(1)

*Measured on polycrystalline samples by FE–SEM.

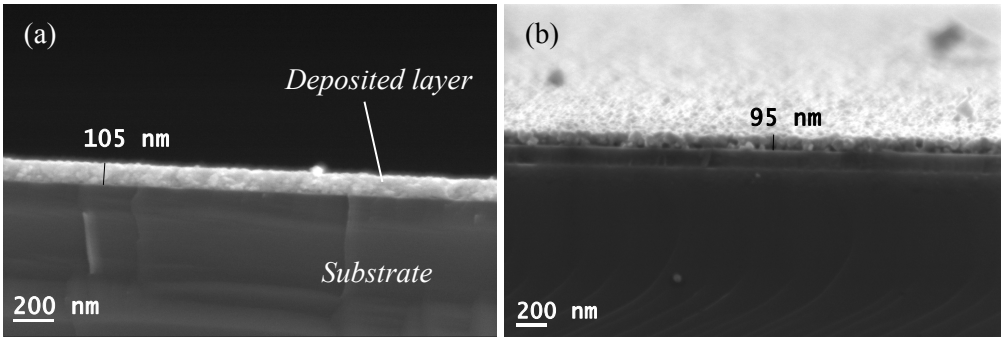

Figure 5.2 Cross–sectional FE–SEM images taken on $Ir_{0.5}Sn_{0.5}O_2$ samples annealed at (a) 600 ºC and (b) 900 ºC.

5.3.3. Energy–Dispersive X–ray spectroscopy (EDX)

To determine the composition of the films, EDX analyses were performed in the annealed samples. Additionally, in order to gain a deeper knowledge about the annealing effects, the $Ir_{0.5}Sn_{0.5}O_2$ sample was measured before the annealing process, and after being annealed at 600 and 900 ºC.

The Sn percentages (relative to the total Ir + Sn) obtained from these experiments, displayed in Table 5.1, are found to be close to the nominal values (≤ 4

% difference). Moreover, negligible differences in the Sn content (< 1%) were found between the as–grown $Ir_{0.5}Sn_{0.5}O_2$ sample (not shown in the table) and that annealed at 600 ºC. On the contrary, a 63 at.% of Sn was measured on the $Ir_{0.5}Sn_{0.5}O_2$ sample annealed at 900 ºC (labeled as $Ir_{0.5}Sn_{0.5}O_2(2)$). This fact confirms the formation of the volatile IrO_3 phase.

5.3.4. X–Ray Diffraction (XRD)

Diffraction measurements were systematically performed on all the samples. In the as–grown films no diffraction patterns are revealed (not shown), indicating an amorphous character. On the other hand, Fig. 5.3(a) shows the corresponding diffractograms of the annealed $Ir_{1-x}Sn_xO_2$ samples, in which diffraction patterns arise. All of them exhibit a rutile–like polycrystalline non–textured microstructure, whose Bragg peaks position progressively shift from an IrO_2–like to a SnO_2–like structure as the Sn concentration is increased. Diffraction peaks corresponding to IrO_2 or SnO_2 single phases are not discerned in any sample, *i.e.*, phase separation is not observed. The peak width indicates a progressive reduction of the grain size, from 10 nm in the pure IrO_2 film to 7 nm in the $Ir_{0.5}Sn_{0.5}O_2$ sample (worse crystallized). Then, it slightly increases for $Ir_{0.5}Sn_{0.5}O_2(2)$. This is probably due the greater crystallization temperature needed for SnO_2, as mentioned above.

The calculated lattice parameters from Rietveld analyses are included in Table 5.1 along with the cell volume. Even though the peak width is relatively large, a nearly linear increase of the cell volume with the Sn content is obtained (Fig. 5.3(b)). Therefore, the XRD experiments suggest that, when grown by the co–sputtering technique, **Ir and Sn form a substitutional solid solution phase**. The $Ir_{0.5}Sn_{0.5}O_2(2)$ sample is the only one considerably shifted from this linear tendency. In fact, its cell volume is only slightly larger than that found in the $Ir_{0.5}Sn_{0.5}O_2$ sample (~0.7% difference). Taking into account that at 900 ºC volatile IrO_3 is formed, the lattice parameters seem to indicate the presence of a great amount of Ir vacancies, rather than a "$Ir_{0.4}Sn_{0.6}O_2$–like" dilution with the atomic sites fully occupied.

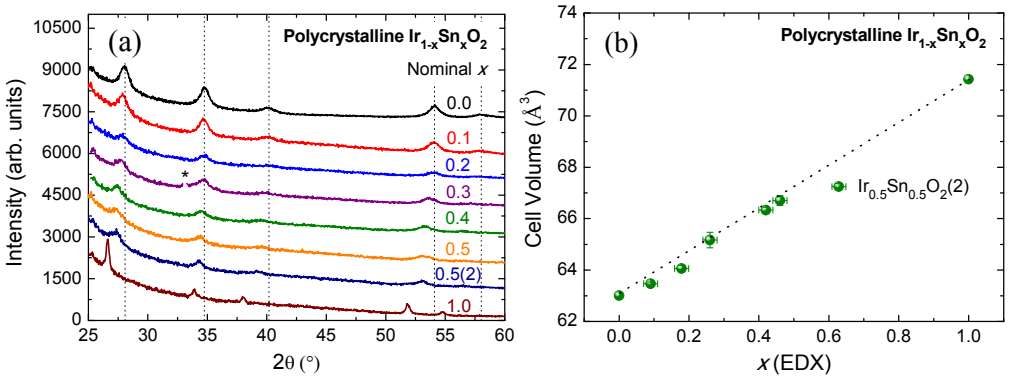

Figure 5.3 (a) XRD profiles for annealed $Ir_{1-x}Sn_xO_2$ thin films. *Substrate peak removed for clarity. A polycrystalline non–textured pure IrO_2 film (x = 0) is included as reference. The dotted lines mark the position of the diffraction peaks measured on bulk IrO_2 in Chapter 3. (b) Dependence of the cell volume with the Sn–concentration (EDX). The dotted line is a guide to the eye.

5.3.5. Extended X–ray Absorption Fine Structure (EXAFS)

In order to gain a deeper insight into the structural differences of the fabricated samples, EXAFS spectra were collected on the amorphous and polycrystalline films with the greatest Sn content. The recorded Ir L_3–edge EXAFS signals are displayed in Fig. 5.4(a) and compared to amorphous and polycrystalline pure IrO_2 films. To correlate the spectral features with specific structural changes, the Fourier transform of the EXAFS signal is shown in Fig. 5.4(b). It can be seen in such figure that both amorphous samples exhibited no order beyond the first shell (nearest neighbors), while the polycrystalline samples presented features due to scattering from ordered second nearest neighbors (features in the $R \approx 3$–4 Å range, no phase correction applied). On closer examination of Fig. 5.4(b), the position of the main peak (marked with a solid line), which indicates the distance of the nearest neighbors, is slightly shifted towards larger R values for amorphous and doped samples, indicative of **larger Ir–O distances**. Fig. 5.4(c) helps to see the evolution of the main peak with the Sn content. The larger Ir–O distances in samples with poorer crystallinity were already observed and discussed in section 4.2.3 As far as the influence of the Sn doping, this

result supports the XRD analyses, indicating a unit cell expansion which, in turn, produces an enlargement in the Ir–O distances.

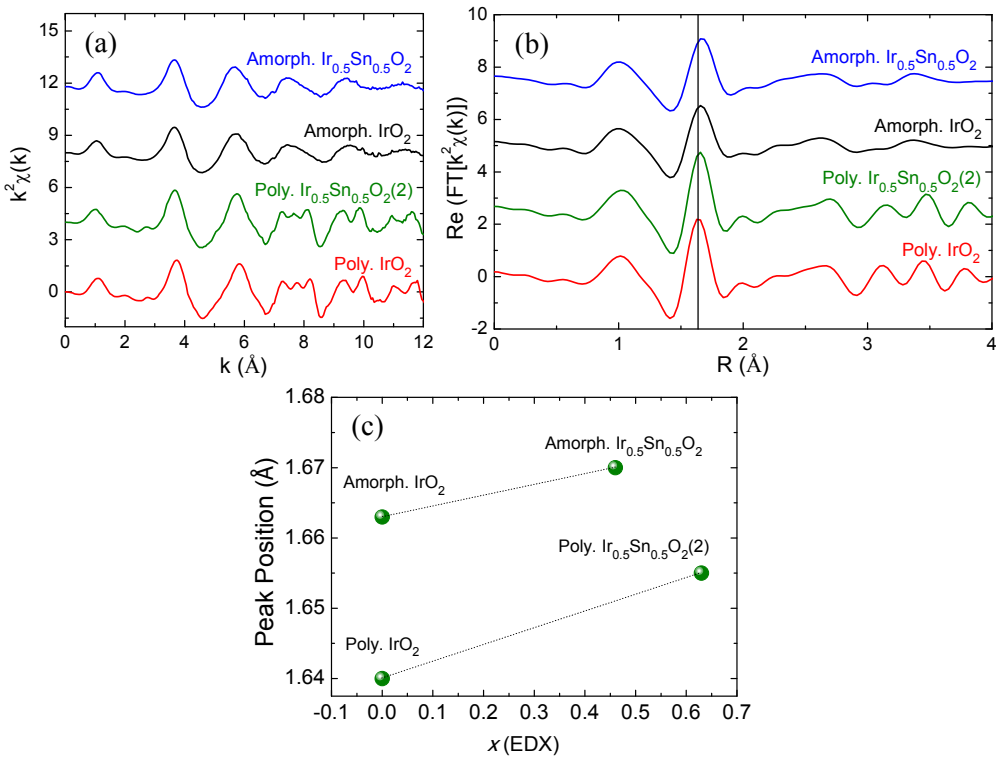

Figure 5.4 (a) EXAFS spectra recorded at the Ir L_3 edge at RT on representative $Ir_{1-x}Sn_xO_2$ films. (b) Fourier transform (real part) of the k^2–weighted Ir L_3–edge EXAFS signal in the range from 3 $Å^{-1}$ to 12 $Å^{-1}$. The solid line is a guide to the eye. (c) Evolution of the main peak position with the Sn content obtained from EDX experiments. The dotted lines are guides to the eye.

5.4. Electronic Characterization

Given the importance of the SOC in the spin–current–detection processes, it is crucial to quantify such interaction. In this way, the X–ray absorption near edge spectroscopy (XANES) provides a direct probe of the spin–orbit interactions [178], as explained in section 4.3.

Figs. 5.5(a) and 5.5(b) show the normalized HERFD–XANES spectra recorded at the Ir $L_{2,3}$ edges on the end members of the amorphous and polycrystalline series, respectively. In all the cases, the HERFD–XANES data show strong white lines at both absorption edges, indicative of a large local density of 5*d* states [180]. At first glance, very similar spectral profiles can be observed regardless of the Sn amount, revealing very similar electronic structure and SOC for Sn–doped and pure IrO_2 samples.

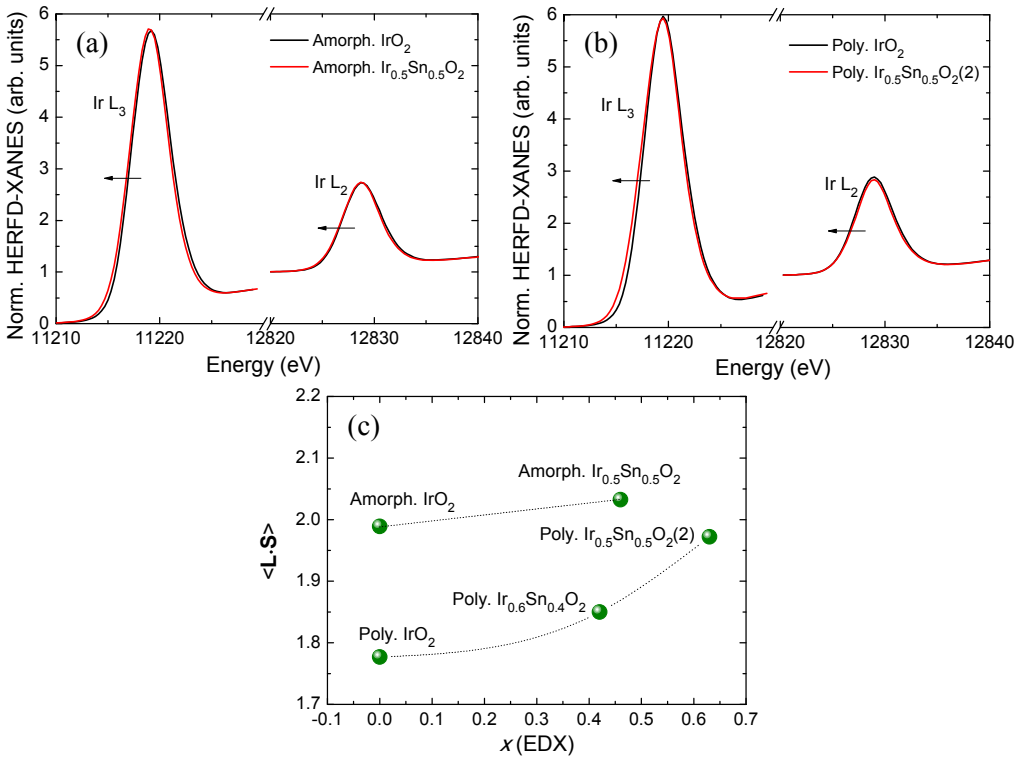

Figure 5.5 Comparisons between the normalized Ir $L_{2,3}$–edges HERFD–XANES spectra recorded at RT on representative (a) amorphous and (b) polycrystalline $Ir_{1-x}Sn_xO_2$ thin films. Panel (c) plots the values of the SOC ($\langle \mathbf{L}\cdot\mathbf{S} \rangle$ product in units of $\hbar^2$) obtained from the XAS.

More quantitatively, Fig. 5.5(c) shows the ground–state expectation value of the angular part of the SOC, $\langle \mathbf{L}\cdot\mathbf{S} \rangle$, calculated via the branching ratio as explained in section 4.3. **Large and robust SOC is found in all the cases**. Looking carefully at that figure, some small yet interesting differences can be noticed. The greater SOC measured on amorphous samples, compared to those of polycrystalline films, was

already discussed in Chapter 4. As far as the Sn doping is concerned, not only does the SOC not get worse, but it seems to increase. The value calculated for the amorphous $Ir_{0.5}Sn_{0.5}O_2$ sample is around 2% greater than that found in the amorphous IrO_2 thin film. The same tendency, even more evident, is observed in the polycrystalline samples. Here, the SOC is ~10% greater in the $Ir_{0.5}Sn_{0.5}O_2$(2) sample than in pure IrO_2. Therefore, in view of these results it can be said that the first condition mentioned in the introduction for an optimized spin–current detector is fulfilled (high SOC regime).

As in the amorphous *vs.* polycrystalline comparison, discussed in Chapter 4, the small SOC enhancement observed after Sn doping can be associated to structural changes. In this case, the small shift (~0.2 eV) of the XANES threshold towards lower energies observed in the doped samples relative to pure IrO_2 can be hardly seen in Figs. 5.5(a) and 5.5(b). Nevertheless, both XRD and EXAFS experiments do point out larger Ir–O distances in the doped samples. Assuming a homogeneous volume expansion, a ~1.8% increase, or in other words a ~0.04 Å increase in the Ir–O distance can be roughly estimated from the XRD data. This value should be seen as a maximum length increase, as the expansion is expected to be mainly due to the larger size of the Sn–octahedra. On the other hand, the EXAFS data indicate a ~0.02 Å and ~0.01 Å Ir–O length increase for polycrystalline and amorphous samples, respectively. This is a very small change that can be hardly detected in the XANES spectra, but it might be related to the SOC increase. The mechanism can be tentatively explained as follows: the increment of the Ir–O distances reduces the orbital overlap and, in turn, the more atomic (less hybridized) character of the orbitals naturally results in a higher SOC. Moreover, the [Kr]$4d^{10}$ electronic configuration of the Sn^{4+} cation, is also expected to contribute to enhance the atomic character of the Ir 5*d* orbitals. Finally, the certain resemblance of the trend observed in Fig. 5.5(c) to that observed in Fig. 5.4(c) agrees with the hypothesis that an increase of the Ir–O bond distances is translated into higher SOC values.

5.5. Electrical Characterization

Once proved the high SOC regime of the fabricated samples, it is mandatory to measure the other key property involved in a spin–current detection process, *i.e.*, the electrical resistivity. Thus, temperature–dependent electrical resistivity curves, ρ(T), were systematically collected on all the amorphous and polycrystalline samples.

First, the insulating behavior of pure SnO_2 films (x = 1) was probed by measuring the corresponding ρ(T) curve. Fig. 5.6 shows the measurement carried out on the amorphous SnO_2 sample synthesized as reference (see Table 5.1). A semiconductor–like behavior is observed (dρ/dT < 0) with an electrical resistivity of ~2x10^7 μΩ cm at RT. The ρ(T) curve goes out of the PPMS range (> 10^8 μΩ cm) when cooling down below 155 K.

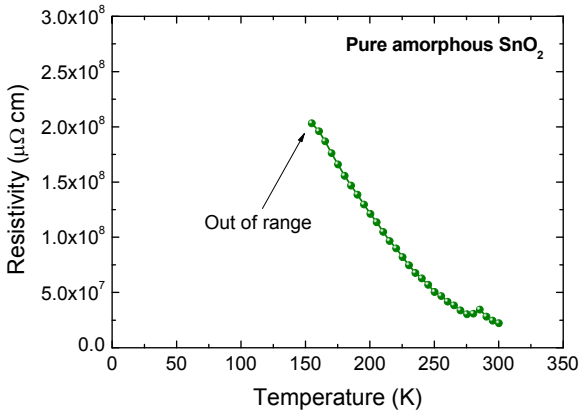

Figure 5.6 Electrical resistivity of an amorphous pure–SnO_2 thin film.

Figs. 5.7(a) and 5.7(b) show the ρ(T) curves measured on the amorphous and polycrystalline $Ir_{1-x}Sn_xO_2$ samples, respectively (the electrical response of pure IrO_2 films were already discussed in Chapter 4 and are taken as references for x = 0). It can be seen in those figures that, as Sn atoms replaces Ir in the sample structure, there is an evident change in the slope of the ρ(T) curves. Such change takes place in the x = 0.2–0.3 range for the amorphous films, and in the x = 0.3–0.4 range for the polycrystalline ones, turning from a metallic–like (dρ/dT > 0, for low x values) to semiconductor–like (dρ/dT < 0, for high x values) behavior. In addition, as shown in

Figs. 5.7(c) and 5.7(d), at RT there is an exponential increment in the electrical resistivity with the Sn concentration, increasing a factor 50 in both sample series, approximately. The differences are even more evident at low temperature (T = 10 K), where the resistivity increases more than five orders of magnitude (from ~$7x10^2$ μΩ cm to > 10^8 μΩ cm, out of the PPMS range) in the amorphous samples, and two orders of magnitude (from ~$1x10^2$ μΩ cm to ~$1x10^4$ μΩ cm) in the polycrystalline films.

All the films are around 100 nm thick, not having very different surface roughness, microstructure or grain sizes. Hence, a relevant contribution due to size–effects, surface or boundaries scattering can be ruled out. On the other hand, Sn doping can give rise to an increase of the electron scattering due to a larger number of defects and impurities (considering Sn as impurities) in the sample, which increases the residual resistivity ($\rho(0)$ in Eq. 4.2). However, this effect alone would maintain a linear increase at higher temperature (as it happens for instance in the case of Ni impurities in Cu metal [231]). The drastic change of the thermal dependence indicates a change in the electronic structure. Such change is subtle as indicates the fact that HERFD–XANES data have not enough resolution to reveal this information, but clearly modifies the transport response towards the semiconducting–like behavior. Two possible mechanisms may contribute to this. On the one hand, the closed–shell electron configuration of the Sn^{4+} ions, [Kr]$4d^{10}$, compared to the [Xe] $4f^{14}5d^5$ half–filled shells of the Ir^{4+} ions, implies a reduction of the orbital hybridization along the sample. In other words, as the Sn^{4+} ions substitute Ir^{4+} in the sample structure the electronic bands become progressively narrower, and hence, the overlap between conduction and valence band decreases. Another possible mechanism could be the gradual increase of the volume, which also decreases the spatial overlap of the orbitals, thus contributing to narrowing the bands. Obviously, both effects can take place simultaneously, being both responsible for the huge increase in the electrical resistivity.

In consequence, these results indicate that by suitably choosing the Sn content, it is possible to **significantly tune the electrical response** of the $Ir_{1-x}Sn_xO_2$ films, thus

accomplishing the second condition mentioned in the introduction for an optimized spin–current detector.

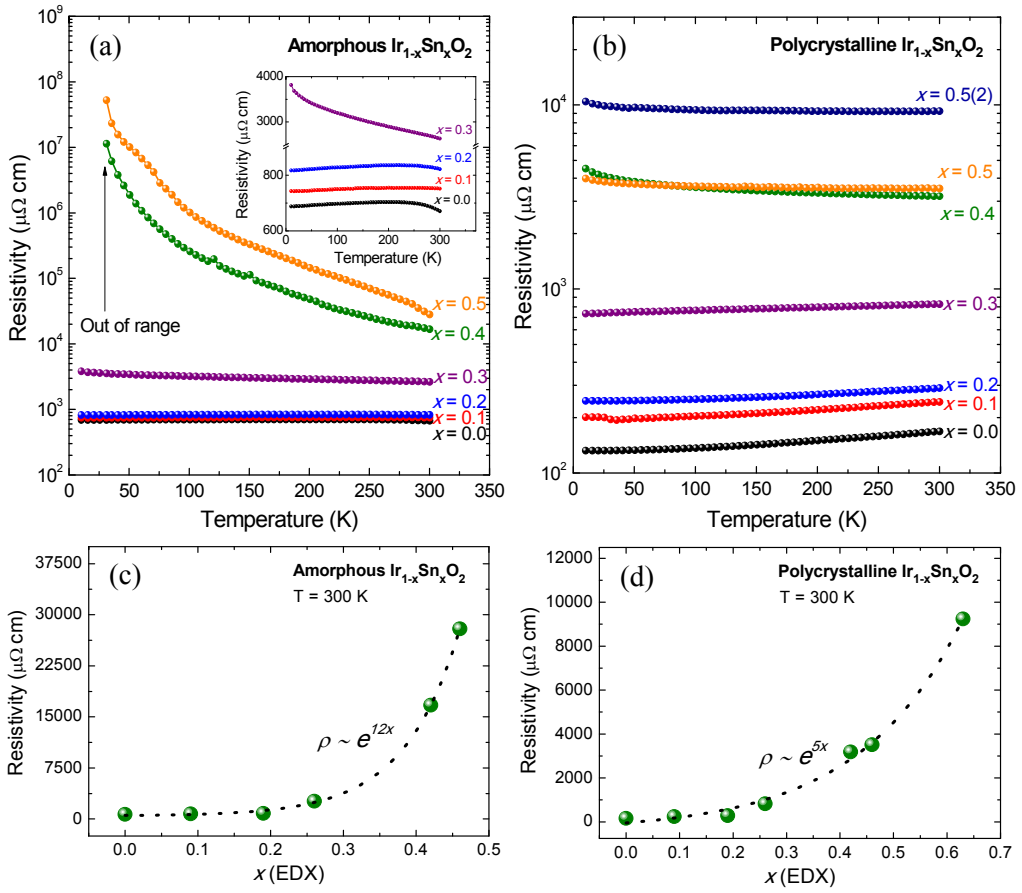

Figure 5.7 Electrical resistivity of (a) amorphous and (b) polycrystalline $Ir_{1-x}Sn_xO_2$ thin films. The inset in panel (a) allows seeing the details of samples with $x \leq 0.3$. The evolution of the resistivity measured at 300 K is plotted in panels (c) and (d) for amorphous and polycrystalline samples, respectively.

The resistivity curves of samples showing a metallic–like behavior ($x \leq 0.2$ for the amorphous films and $x \leq 0.3$ for the polycrystalline samples) can be explained with the same models employed for pure IrO_2 in Chapter 4 (Bloch–Grüneisen formula with $n = 2$), though with increasing values of residual resistivity.

As for the semiconductor amorphous samples (x = 0.4 and 0.5), a thermal activation model provides a good fit of the resistivity curves even for T > 100 K, as

illustrated in Fig. 5.8(a). The band gap provided by such fit is $E_G \approx 64$ meV. This relatively small band gap between the occupied and unoccupied energy levels indicates that the system is situated on the verge of the metallic state (fits performed in the $x = 0.4$ amorphous sample or in other temperature range give similar values of E_G).

Regarding the behavior of the polycrystalline samples, the ρ(T) curve of the $Ir_{0.5}Sn_{0.5}O_2$(2) film, shown in Fig. 5.8(b), presents a more complex response. It shows a transition from "bad metal" (relatively high resistivity) to "weak insulator" at $T_C \approx$ 245 K. When cooling down below this temperature, the ρ(T) curve shows a "shoulder" (marked with an asterisk in the figure) preceding a rapid increase in the resistivity. Looking at the relatively small variation of ρ with temperature, it is obvious that models such as the thermal activation do not provide good fits. Contrary, in this sample, as well as in the polycrystalline $Ir_{0.5}Sn_{0.5}O_2$ film, a 3D Mott's variable range hopping (Mott–VRH) model ($\rho(T) = Cexp[(T_0/T)^{1/4}]$, where C is a constant and T_0 is the characteristic temperature of the compound [232]) provides a good fit (see inset in the figure). However, according to the Mott theory on VRH the average hopping distance, R_M, must be larger than the localization length, a, which is $R_M/a = 3/8\,(T_0/T)^{1/4} > 1$. This condition is not fulfilled in our case ($T_0 \approx 0.02$). This could be due to the presence of competing conducting mechanisms (metallic and semiconductor) in the system for being on the verge of the metal–insulator transition (MIT). In fact, in the three polycrystalline samples showing a semiconductor–like behavior ($x \geq 0.4$), the increment of the resistivity when decreasing the temperature is relatively subtle. This further confirms that the system is on the verge of the MIT.

At this point, it is instructive to make a comparison with the $SrIrO_3$ perovskite. *J. Cheng et al.* [70] and *Q. Cui et al.* [71] studied the bulk Sn–doped $SrIr_{1-x}Sn_xO_3$ compound, while *M. Negishi et al.* [233] investigated the same material though in the thin film structure (~15 nm thick). A similar behavior was observed, either in bulk or in thin film, finding a concentration, $x = 0.1$, where a thermal MIT is observed. Above this concentration, the resistivity curves present a semiconductor–like behavior, with a transition temperature T_C located at around 280 K for $x = 0.2$, and a "shoulder" preceding the rapid increase in the resistivity. Additionally, it is found that the $x = 0.2$

sample well–followed a VRH model [208, 209]. The higher "transition concentration" found in the $Ir_{1-x}Sn_xO_2$ system relative to that found in the perovskite could be tentatively associated to the different arrangement of the Ir octahedra in both cases: corner–sharing in the perovskite *vs*. a combination of corner– and edge–sharing in the rutile structure (see Fig. 1.4). The latter favors shorter distances and higher orbital overlap [80]. Indeed, undoped $SrIrO_3$ has an electrical resistivity in the order of 10^3 μΩ cm [234, 235], which is 1 order of magnitude greater than in IrO_2.

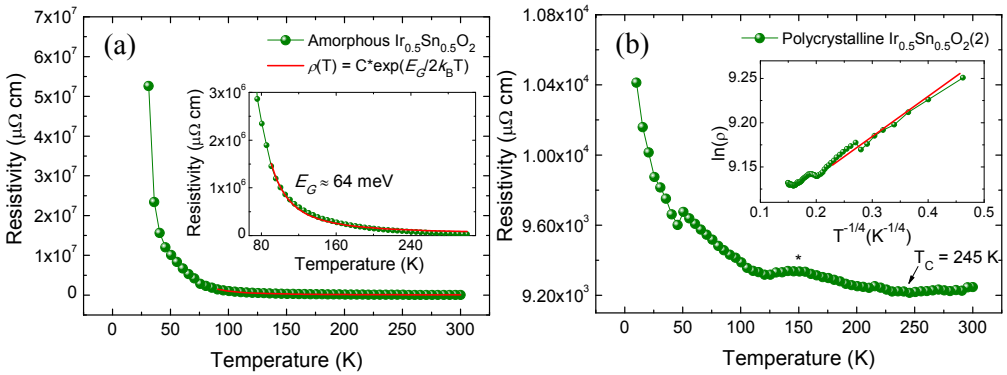

Figure 5.8 Detailed temperature–dependent electrical resistivity of (a) amorphous $Ir_{0.5}Sn_{0.5}O_2$ and (b) polycrystalline $Ir_{0.5}Sn_{0.5}O_2$(2) thin films. The inset in panel (a) shows a detailed region fitted to a thermal activation model (red solid line) and in panel (b) the inset shows the resistivity plotted as ln(ρ) *vs*. $T^{-1/4}$.

5.6. Magnetic Characterization

As mentioned in Chapter 1, *Panda et al.* [82] predicted that IrO_2 can be made insulating as well as magnetic upon reducing the direct overlap between the Ir 5*d* orbitals, for instance by increasing the unit cell volume, as in this case. Experimentally, the MIT observed in the $SrIr_{1-x}Sn_xO_3$ perovskite series has been proved to be accompanied by a weak ferromagnetism below T_C [70, 71, 233], attributed to canted antiferromagnetism of the Ir^{4+} cations for analogy to the Sr_2IrO_4 compound [215] (Slater–type MIT). Therefore, one could expect a similar behavior (magnetic ordering) in the $Ir_{1-x}Sn_xO_2$ material, especially for those Sn contents which give samples with the greatest electrical resistivity.

5.6.1. SQUID magnetometry

Figs. 5.9(a) and 5.9(b) show the field–dependent magnetization curves, M(H), recorded in the amorphous and polycrystalline $Ir_{0.5}Sn_{0.5}O_2$ samples, respectively, which exhibited the largest electrical resistivity (see Fig. 5.7). M(H) curves for pure IrO_2 (x = 0) and SnO_2 (x = 1) films are also included as references. As can be seen, a negligible magnetic response is obtained in all the cases, with absolute maximum magnetization values under $3x10^{-4}$ emu/cm^2. Thus, the measurements on Fig. 5.9 allow discarding the presence of a substantial net magnetic moment in the samples.[11] In fact, the M(H) curves seem to indicate a main diamagnetic character, resembling the magnetic response of SnO_2.

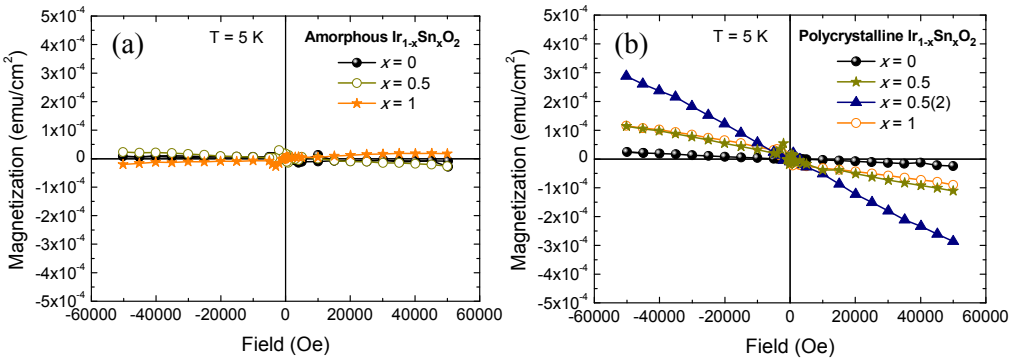

Figure 5.9 M(H) curves for (a) amorphous and (b) polycrystalline $Ir_{0.5}Sn_{0.5}O_2$ samples measured at T = 5 K. Substrate background removed.

Therefore, at first sight the magnetization measurements seem to rule out the appearance of magnetic order in the Sn–doped IrO_2 films. However, it should be recalled that *Panda et al.* [82] predicted an antiferromagnetic arrangement. Therefore, whether there is an antiferromagnetic ordering fully collinear or a very small canting, the magnetic response of such samples could be hidden in these measurements. In addition, as shown in Chapter 2, the error bar at 50 kOe introduced by subtracting the Si substrate background is around $3.5x10^{-5}$ emu/cm^2 (~$1x10^{-4}$ emu/cm^2 from electronic

[11] Temperature–dependent magnetization, M(T), curves were also recorded resulting in a negligible magnetic response as well (not shown).

noise). This introduces further uncertainty to the analysis of the M(H) curves. As a consequence, from the magnetization data the presence of magnetic ordering cannot be, neither confirmed nor discarded.

5.6.2. X–Ray Magnetic Circular Dichroism (XMCD)

Trying to shed more light on this question, Fig. 5.10(a) shows the XMCD spectrum recorded at the Ir L_3 edge on the polycrystalline $Ir_{0.5}Sn_{0.5}O_2$(2) sample. It can be seen in the figure that, although the signal to noise ratio is relatively big, a small XMCD signal (~0.6%) can be inferred at ~11217 eV. The position and intensity of this signal agrees well with previous XMCD measurements carried out in other Ir^{4+}–based compounds, such as in Sr_2IrO_4 [179], Sr_2TiIrO_6 [216] or $BaIrO_3$ [180]. In addition, the XMCD signal measured on powdered IrO_2 in Fig. 5.10(b) presents a much smaller intensity. In consequence, these preliminary results suggest that the relatively small signal observed in Fig. 5.10(a) can be indeed associated to the presence of magnetic ordering of the Ir^{4+} cations or, at least, to an enhanced paramagnetic signal in the film.

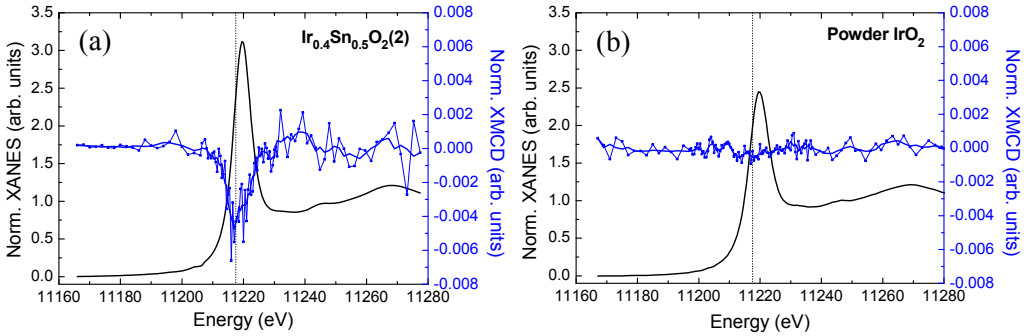

Figure 5.10 (a) Normalized XANES and XMCD spectra recorded at the Ir L_3 edge at T = 10 K and H = 50 kOe on polycrystalline $Ir_{0.5}Sn_{0.5}O_2$(2) sample. Solid blue line is a guide to the eye. (b) Ir L_3–edge XANES and XMCD spectra measured in transmission mode at T = 10 K and H = 35 kOe on powder IrO_2. The low intensity of the white line is due to a 4% of metallic Ir.

5.7. Conclusions

Sn–doped IrO_2 thin films, $Ir_{1-x}Sn_xO_2$ (x = 0.1–0.5), of ~100 nm have been successfully grown by reactive magnetron co–sputtering for the first time. The structural characterization shows that a single phase is formed in all the (crystalline) samples, confirming that Ir and Sn form a substitutional solid solution phase when grown by such technique.

The analysis of the HERFD–XANES data reveals very strong 5*d* SOC in all the samples. The spin–orbit interaction is found to be slightly enhanced in the amorphous state, also in the doped samples. This confirms the result obtained in the pure IrO_2 films from Chapter 4. Similarly, the SOC slightly increases when introducing the dopant element. From the XRD, HERFD–XANES, and EXAFS experiments, such SOC increase can be correlated, in both cases, to an enhanced atomic character of the Ir 5*d* orbitals.

The electrical properties have proven to be strongly dependent on the Sn concentration, **changing the metallic response of pure IrO_2 to semiconducting–like** for the highest Sn–doped samples. By changing the Sn content the electrical resistivity of the Sn–doped IrO_2 films can be tuned in a range of several orders of magnitude.

Regarding the magnetic properties, while the SQUID magnetometry gives ambiguous results, our initial XMCD measurements do point out the presence of **certain magnetic ordering of the Ir^{4+} cations**. Nevertheless, the uncertainty of this result is not negligible and more experimental work is needed to confidently assert and better understand such magnetic ordering. Unfortunately, the experiments required to confirm this preliminary result entail long allocation time at large facilities, such as synchrotrons or muon sources, and hence, they had to be left out from the scope of this thesis.

As a concluding remark, the two main factors involved in the spin–current detection process are optimized for IrO_2: (1) a nearly constant, or even slightly

enhanced, SOC (always in the high SOC regime); and (2) an increased electrical resistivity. Thus, **our results point to a new direction in the quest of optimized materials for spin–current detection.**

3rd Approach

IrO_2 Combined with Magnetic 3d Elements

Chapter 6

$Ir_{1-x}Cr_xO_2$ Thin Films

6.1. Introduction

In the preceding chapter, the formation of the sputtered substitutional solution phase $Ir_{1-x}Sn_xO_2$ was proved to be successful. This compound exhibited an enhanced electrical resistivity and spin–orbit coupling (SOC). Considering the good results achieved in tuning the electrical response of IrO_2 by Sn doping, now the attention is focused on **modifying the magnetic properties of IrO_2** through a similar doping route, though this time magnetic atoms are incorporated. Thus, this chapter aims at studying the magnetic properties of **Cr–doped IrO_2 thin films**, *i.e.*, a system where the high SOC of a 5*d* element (Ir) is combined with the high magnetic moment and Curie temperature (T_C) of a 3*d* element (Cr) to modify the magnetic properties of IrO_2, and in turn, to get a system with tunable magnetic properties.

Combining IrO_2 and CrO_2 is an interesting approach, not only for tuning the magnetic properties of IrO_2, but also for growing and manipulating the magnetism of CrO_2. Indeed, CrO_2 is a metastable phase and conventional film growing techniques, such as sputtering, pulsed laser deposition or molecular–beam epitaxy have not succeeded in synthesizing this compound. So far, chemical vapor deposition is the only successful technique in depositing CrO_2 thin films [236, 237], whereas only small advances are being achieved with other techniques [238]. In addition, the CrO_2 surface is thermodynamically unstable under atmospheric conditions with a tendency to decompose into the insulating, antiferromagnetic, and more stable phase, Cr_2O_3 [239]. Since both, IrO_2 and CrO_2, grow in the same rutile space group with similar lattice parameters, and IrO_2 is the only stable solid IrOx compound, Ir may be expected to

stabilize Cr in the rutile structure. Besides, Cr and Ir conform the Hume–Rothery rules for the formation of a substitutional solid solution phase (see Chapter 5). Thus, the formation of a stable $Ir_{1-x}Cr_xO_2$ compound is expected, where the oxidation state of Cr would remain as 4+ (ferromagnetic).

Regarding the magnetic properties, CrO_2 (in bulk form and in ~2 μm thin films) is reported to be a half–metallic ferromagnetic material with a T_C in the 385–400 K range, very small coercive field < 100 Oe, and a magnetic moment of 2 μ_B/at. Cr [240–244]. By virtue of this property, it has been proposed as a source of spin–polarized electrons for the fabrication of spintronic devices, such as magnetic tunnel junctions or spin valves [245–250]. Introducing high SOC Ir ions may result in an even more appealing material for spin–current manipulation. In addition, the use of high SOC elements is a key aspect in many of the current efforts devoted to optimize the control of the magnetic anisotropy (MA) in physical systems at the nanoscale [251–254]. Among the intrinsic ways of MA manipulation, one may cite the design of compounds including high single–ion anisotropy elements, such as Pt in Co and Fe nanostructures [255, 256], or more recently, Ir in several oxides [257, 258]. In this sense, huge coercivity (up to 550 kOe) has been reported on bulk $BaIrO_3$ and Sr_3NiIrO_6 [257, 258]. In addition, compared to rare earths elements, the broad spatial extension of the 5*d* orbitals may prove to be more efficient in inducing hardness on the neighboring 3*d*–transition metal. From an applied point of view, magnetic materials with large coercivity have broad applications ranging from permanent magnets and data storage media to high–frequency electromagnetic wave filters [259–261].

This scenario reveals the potential interest of IrO_2–CrO_2 systems for spintronics and in the development of new permanent magnets. Surprisingly enough, to the best of our knowledge there are no works published so far on this issue. Thus, as an initial approach to this new playground, along this chapter the fabrication and characterization of sputtered Cr–doped IrO_2 thin films with different doping content is described. Section 6.2 is devoted to the sample preparation. The structural properties are presented in section 6.3, and the electronic, electrical and magnetic characterization is shown in sections 6.4, 6.5, and 6.6, respectively.

6.2. Sample Fabrication

$Ir_{1-x}Cr_xO_2$ thin films of ~100 nm (x = nominal Cr concentration) were prepared by reactive magnetron co–sputtering deposition (see Fig. 2.3) on Si substrates at room temperature (RT) from metallic Ir and Cr targets. The same Ir target employed in the previous chapters for growing sputtered IrO_2 films was connected to a DC source, while the Cr target was connected to a pulsed DC source (frequency set at 25 kHz) to avoid "target poisoning" due to the formation of insulating Cr_2O_3 on top of the target [239].

To optimize the growth of IrO_2, the sputtering power supplied to the Ir target was set to ~8 W and the gas flows to 13 ml Ar/min and 2 ml O_2/min, according to the previous study shown in Chapter 3. As for the Cr target, the sputtering power was accordingly varied from 15 to 198 W to obtain dilutions with different Ir/Cr proportions, ranging from 10 to 80 at.% Cr. Pure IrO_2 (x = 0) films from Chapters 3 (synthesis) and 4 (characterization) were used as references. However, pure CrO_2 films could not be grown by reactive magnetron sputtering due to the formation of thermally more stable phases:[12] Cr_2O_3 and CrO_3 (boiling point: ~250 ºC [262, 263]). Hence, simulations and samples provided by other groups were used as references.[13]

Finally, the as–grown films (amorphous) were subsequently annealed in air at 600 ºC during 6 h to obtain polycrystalline samples.

[12] Several combinations of growing parameters and subsequent annealing treatments were probed in our sputtering chamber, obtaining in all the cases other chromium oxides but CrO_2. This study has not been included here for the sake of readability.

[13] Epitaxial CrO_2 films deposited on TiO_2(110) by chemical vapor deposition by the Nanotechnology of Surfaces group from *Instituto de Ciencia de Materiales de Sevilla* (ICMS) [244].

6.3. Structural and Compositional Characterization

6.3.1. X–Ray Reflectivity (XRR)

Figs. 6.1(a) and 6.1(b) show the XRR curves measured to determine the thickness of the as–grown and annealed films, respectively. The values obtained from such curves, given in Table 6.1, are within 90 ± 10 nm for the as–grown samples, and within 80 ± 10 nm for the annealed samples, which is valid for our purpose. In general, the surface roughness remains between 1.5 and 2.5 nm according to the fittings. Moreover, it can be seen in Fig. 6.1(a) and 6.1(b) how the critical angle, θ_c, shifts towards lower 2θ values as the Cr content increases, consistent with the lower density of CrO_2 (4.89 g/cm^3) against IrO_2 (11.66 g/cm^3).

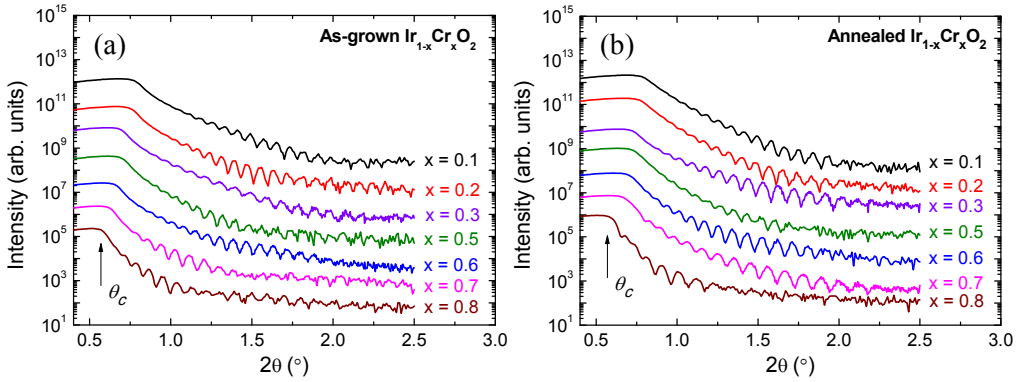

Figure 6.1 XRR measurements on (a) as–grown and on (b) annealed $Ir_{1-x}Cr_xO_2$ samples.

6.3.2. Energy–Dispersive X–ray spectroscopy (EDX)

The composition of the films was determined by EDX analyses performed on all the as–grown and annealed samples. The Cr percentages (relative to the total Ir + Cr content) obtained from these experiments are in general close to the nominal values (Table 6.1). They range from ~10–80 at.% Cr, being homogeneously spaced, which is valid for our purpose. Furthermore, the values obtained before and after the annealing treatment showed remarkable similarities, with differences in the at.% Cr ≤ 3%. This suggests that volatile CrO_3 is not formed during the annealing treatment.

Table 6.1: Structural and compositional properties of $Ir_{1-x}Cr_xO_2$ thin films: layer thickness (t) measured by XRR and Cr concentration determined by EDX (relative to the total Ir + Cr content) in as–grown and annealed films. Lattice parameters and cell volume calculated by XRD and Rietveld analyses.

Sample	t (nm)		Cr (%) ±2%		Lattice parameters (Å)		Cell Vol.
	As–grown	Ann.	As–grown	Ann.	$a = b$	c	(Å^3)
$Ir_{0.9}Cr_{0.1}O_2$	95	89	12	14	4.482(5)	3.118(4)	62.6(1)
$Ir_{0.8}Cr_{0.2}O_2$	95	89	22	25	4.488(5)	3.106(4)	62.5(1)
$Ir_{0.7}Cr_{0.3}O_2$	96	90	32	33	4.482(6)	3.091(5)	62.1(2)
$Ir_{0.5}Cr_{0.5}O_2$	92	90	46	46	4.466(6)	3.059(4)	61.0(1)
$Ir_{0.4}Cr_{0.6}O_2$	96	83	58	57	4.472(8)	3.056(8)	61.1(2)
$Ir_{0.3}Cr_{0.7}O_2$	83	71	70	68	4.42(1)	3.00(1)	58.6(4)
$Ir_{0.2}Cr_{0.8}O_2$	86	71	76	77	4.42(3)	2.98(3)	58.2(8)

6.3.3. X–Ray Diffraction (XRD)

Diffraction measurements were systematically performed on all the samples to determine their crystallinity. In the as–grown films, no diffraction patterns are revealed (not shown), indicating the amorphous character of these samples. In contrast, all the annealed films exhibited a rutile–like polycrystalline non–textured microstructure whose Bragg peaks position progressively shift from an IrO_2–like to a CrO_2–like structure as the Cr content is increased (Fig. 6.2(a)). Diffraction peaks corresponding to IrO_2 or CrO_2 single phases are not discerned in any sample, *i.e.*, phase separation is not observed.

The peak width indicates a roughly constant grain size of around 9 nm (Eq. 2.1) regardless of the Cr content. On the other hand, for $x \geq 0.6$ the diffraction peaks becomes less intense. The fact that the peak width is roughly constant and its intensity decreases with the Cr content, suggests the presence of differentiated crystalline and amorphous regions. This could be seen as crystalline clusters in an amorphous matrix, with greater relative weight of the latter as the Cr content is increased.

The calculated lattice parameters from Rietveld analyses are included in Table 6.1 along with the cell volume. The fact that the diffraction peaks become less intense with increasing the Cr concentration makes the error bar larger for the greatest Cr percentages. Despite of that, a nearly linear decrease of the cell volume with the Cr content is obtained, as represented in Fig. 6.2(b). This suggests that the crystalline and amorphous regions do not present a big disparity of Ir/Cr percentages. Contrary to the unit cell expansion observed in Sn–doped IrO_2 films in the previous chapter (negative chemical pressure), a unit cell contraction is observed with Cr doping (positive chemical pressure) driven by the smaller size of the Cr–octahedra. Such contraction is found to be up to ~10% in the $Ir_{0.2}Cr_{0.8}O_2$ sample respect to pure IrO_2. In view of all of this, the XRD experiments suggest that, when grown by the co–sputtering technique, **Ir and Cr form a substitutional solid solution phase**.

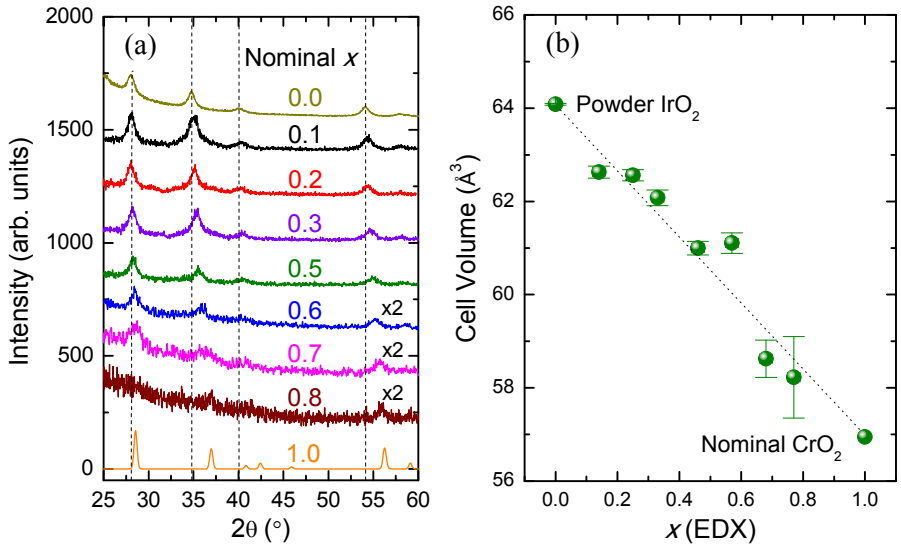

Figure 6.2 (a) XRD patterns for annealed $Ir_{1-x}Cr_xO_2$ thin films. A polycrystalline non–textured pure IrO_2 film ($x = 0$) from Chapter 3, and a simulated pattern of polycrystalline pure CrO_2 ($x = 1$) are included as references. The dashed lines mark the position of the diffraction peaks measured on bulk IrO_2 in Chapter 3. (b) Dependence of the cell volume with the Cr–concentration obtained from EDX experiments. The dotted line is a guide to the eye.

6.4. Electronic Characterization

The XANES spectra recorded at the Ir $L_{2,3}$ edges and Cr K edge provided information about the SOC and oxidation state of Ir and Cr. Fig. 6.3(a) shows the normalized XANES spectra at the Ir $L_{2,3}$ edges measured on the $Ir_{0.4}Cr_{0.6}O_2$ sample and compared to those of a pure IrO_2 film. Practically identical profiles are obtained, indicating a similar ground–state expectation value of the angular part of the SOC, $\langle \mathbf{L}\cdot\mathbf{S} \rangle$, which is found to be 2.0 (in units of $\hbar^2$). Although more samples of the series should be measured, it seems reasonable to affirm that all the $Ir_{1-x}Cr_xO_2$ dilutions remain in a **high SOC regime**. In this figure, it can also be discerned a small shift (~0.5 eV) in the spectra of the $Ir_{0.4}Cr_{0.6}O_2$ sample to higher energies respect to pure IrO_2. Upon reducing the first neighboring interatomic distance of the absorbing atom a shift in the absorption threshold towards higher energies is expected. Therefore, the experimentally observed shift suggests smaller Ir–O distances as Cr is incorporated in the IrO_2 framework. This is in agreement with the gradual reduction in the size of the lattice, induced by Cr doping, observed in the XRD experiments. While this reduction is rooted at the smaller size of the CrO_6 octahedra, a concomitant reduction of the IrO_6 octahedra may also be expected (compared to perovskites, the rutile structure is quite rigid and not so susceptible to distort via inter–octahedral Ir–O–Ir tilting). Note that the shift is comparable to that observed in Chapter 5 with Sn doping, though obviously of opposite sign (opposite variation in the distances). Although the experiments strongly suggest that the shift is due to a reduction in the interatomic distances, the presence of a certain amount of Ir^{5+}, which should also present a ~0.5 eV shift [216], cannot be yet discarded from this data. Finally, it should be noted that the IrO_2 film here measured corresponds to a ~1.5 nm thick (100)–epitaxial sample. As discussed in Chapter 4 (from the data displayed in Fig. 4.7) this shift could be, at least partially, explained in terms of the thickness difference.

On the other hand, the normalized XANES spectrum recorded at the Cr K edge is given in Fig. 6.3(b) compared to that of a pure CrO_2 film (~1 μm thick). Some notable differences can be observed between the two spectra. The amplitude and width

of the XANES oscillations is modified. Besides, regarding the near–edge region, the $Ir_{0.4}Cr_{0.6}O_2$ film presents a worse defined shoulder–like feature at ~6003 eV and the raising edge looks, somehow, less sharp. As a result, in some parts of the threshold a small shift of ~0.6 eV towards lower energies is observed. To explain the changes of the profile one may propose the presence of Cr_2O_3, the most stable chromium oxide. However, Cr_2O_3 has a 3+ oxidation state and presents a shift in the threshold energy around 3 eV towards lower energies respect to the spectrum of pure CrO_2 [264]. In consequence, the presence of a considerable amount of Cr^{3+} (Cr_2O_3–like) can be discarded.

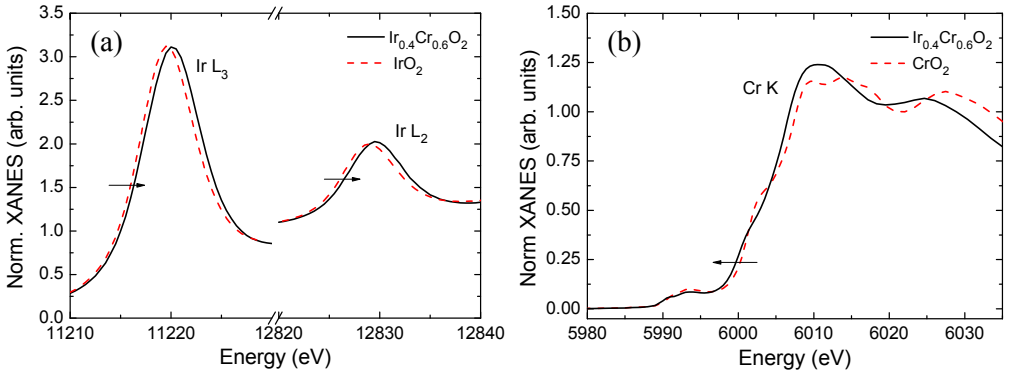

Figure 6.3 Normalized (a) Ir $L_{2,3}$–edges and (b) Cr K–edge XANES spectra recorded at 10 K on the $Ir_{0.4}Cr_{0.6}O_2$ sample accordingly compared to those of pure IrO_2 and CrO_2 films.

Trying to verify whether the observed shift is associated to larger Cr–O distances than those of CrO_2, XANES simulations were performed by Dr. J. Chaboy. Details about the calculations (references, cluster size, potential used, treatment of the core–hole and experimental resolution, etc.) can be found elsewhere [265, 266]. Fig. 6.4(a) shows three calculations corresponding to: CrO_2, CrO_2 simulated using the atomic distances of $Ir_{0.4}Cr_{0.6}O_2$, and $Ir_{0.5}Cr_{0.5}O_2$ simulated using the atomic distances of $Ir_{0.4}Cr_{0.6}O_2$.[14] In addition, in Fig. 6.4(b) the profile calculated for two different clusters sizes of CrO_2 is displayed to illustrate the effect of disorder. As can be seen in Fig.

[14] In the spectra shown in Fig. 6.4 half of the Cr atoms in the cluster have been substituted by Ir atoms in an alternating manner. Choosing different positions for the Ir atoms slightly modifies the amplitude of the main peak, but the overall profile remains invariable.

6.4(a), modifiying the Cr–O distances to those of $Ir_{0.4}Cr_{0.6}O_2$ has an important effect on the profile. In fact, the threshold is slightly shifted and the XANES oscillations are modified, so that the profile reproduces the experimental spectrum of the $Ir_{0.4}Cr_{0.6}O_2$ sample. From these simulations it is also established that substitution of Cr by Ir and the increase of structural disorder seem to have a smaller effect on the threshold, being in accordance with the observed experimental spectrum. Therefore, it can be concluded that the Cr ions in the $Ir_{0.4}Cr_{0.6}O_2$ film are actually in a rutile crystal structure and present a **4+ oxidation state.** This also confirms the 4+ oxidation state for Ir ions.

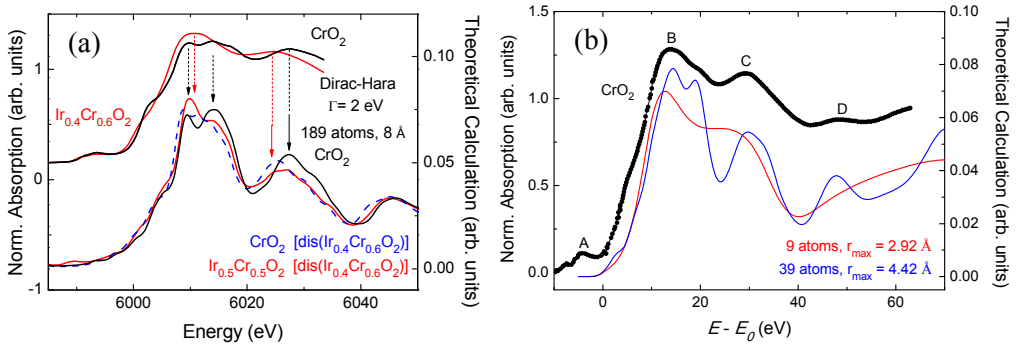

Figure 6.4 (a) Normalized Cr K–edge XANES spectra of the $Ir_{0.4}Cr_{0.6}O_2$ and pure CrO_2 films compared to the theoretical spectra of CrO_2, CrO_2 with the atomic distances of $Ir_{0.4}Cr_{0.6}O_2$, and $Ir_{0.5}Cr_{0.5}O_2$ with the atomic distances of $Ir_{0.4}Cr_{0.6}O_2$. In panel (b) the effect of disorder is illustrated by simulating two different cluster sizes (9 and 39 neighbors) compared with a CrO_2 reference.

6.5. Electrical Characterization

CrO_2 is a good metal at low temperatures with a residual resistivity in thin films ($t \geq 100$ nm) in the order of 10 μΩ cm and a poor metal at room temperature with a resistivity in the 10^2–10^3 μΩ cm range [236, 243, 267, 268]. Bearing this in mind, and the fact that IrO_2 films of this thickness have also a metallic ground state (see section 4.4), one would naively expect the $Ir_{1-x}Cr_xO_2$ films to be metallic regardless of the Cr content. However, the ρ(T) curves measured in the polycrystalline samples, displayed in Fig. 6.5(a), show a surprising behavior. In contrast to the pure–

metallic curves observed in IrO_2 and CrO_2 films, clear upturns in the resistivity appear at low temperatures for relatively small values of x (marked with arrows in the figure). Such upturn is observed at increasing temperatures as the Cr content is increased, up to the point where, for $x = 0.8$, $d\rho/dT < 0$ in the whole range of temperatures (semiconductor–like behavior).

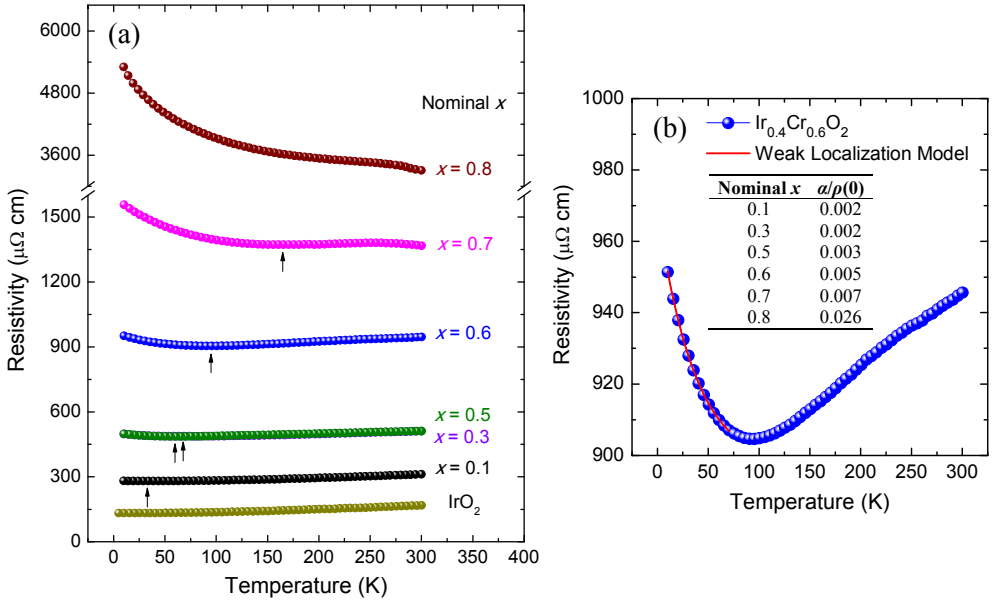

Figure 6.5 (a) ρ(T) curves measured in the annealed $Ir_{1-x}Cr_xO_2$ films. (b) ρ(T) curve of the $Ir_{0.4}Cr_{0.6}O_2$ sample fitted to a weak localization model. The table gives the $\alpha/\rho(0)$ values obtained from the fittings for each sample.

One could tentatively associate the change in the slope to the insulating and more stable phase, Cr_2O_3. However, the presence of Cr_2O_3 (or Cr^{3+} in any other oxide) is neither observed in the XRD measurements nor in the XANES experiments. It is thus more likely the presence of localization mechanism(s) hindering the movement of the electrons. Following the same scheme from previous chapters, the possible mechanisms include those associated to enhanced correlations, disorder, and/or magnetism. Besides, given the large compression of the lattice observed in section 6.3.3, structural distortions (in particular greater Ir–O–Ir tilting) reducing the bandwidth should also be taken into account. Although the detailed study of this

behavior is beyond the scope of this thesis (for instance, a more detailed structural characterization is currently not possible), a preliminary analysis can be made. On the one hand, typical resistivity models, such as thermal activation or Mott–hopping, are not able to reproduce the electrical response observed in Fig. 6.5(a). This fact suggests that neither correlations (Mott insulator) nor magnetism (Slater insulator) are responsible for the localization. Similarly, the shape of the curves seems not to be compatible (solely) with a Kondo effect (scattering mechanism of conduction electrons in a metal due to magnetic impurities) [269–272]. On the other hand, the response is similar to that observed by *J. H. Gruenewald et al.* [175] in compressed $SrIrO_3$ thin films, who attributed the metal–insulator transition (MIT) to a weak localization effect (disorder). Fig. 6.5(b) shows a representative fit of the semiconducting region to a weak localization model (Eq. 4.5) in the sample with x = 0.6, and the $\alpha/\rho(0)$ values (weak localization term in Eq. 4.5) obtained for each sample. Excellent fits are obtained in all the samples, giving increasing values of $\alpha/\rho(0)$ as the Cr content is increased. This points out to an important role of disorder as the underlying mechanism inducing the MIT in $Ir_{1-x}Cr_xO_2$ samples.

6.6. Magnetic Characterization

6.6.1. SQUID magnetometry

As–grown $Ir_{1-x}Cr_xO_2$ films display a negligible response to the magnetic field with a maximum magnetic moment at 5 K and 50 kOe (M_{max}) in the order of 10^{-5} emu/cm^2 (not shown). No hint of magnetic order is observed in these samples. In contrast, very interesting phenomena arise after the thermal treatment.

In annealed samples, the temperature–dependent zero–field–cooled (ZFC) and field–cooled (FC) M(T) curves, displayed in Fig. 6.6, show a very strong temperature dependence of magnetization, which also depends on the Cr content. In all the doped samples the FC magnetization increases with decreasing temperature. Differently, the ZFC magnetization increases gradually until it reaches a maximum at the peak temperature, T_P. Then, it decreases monotonically as the temperature decreases.

Moreover, a pronounced bifurcation between the FC and ZFC curves occurs at the irreversibility temperature, T_{irr}.

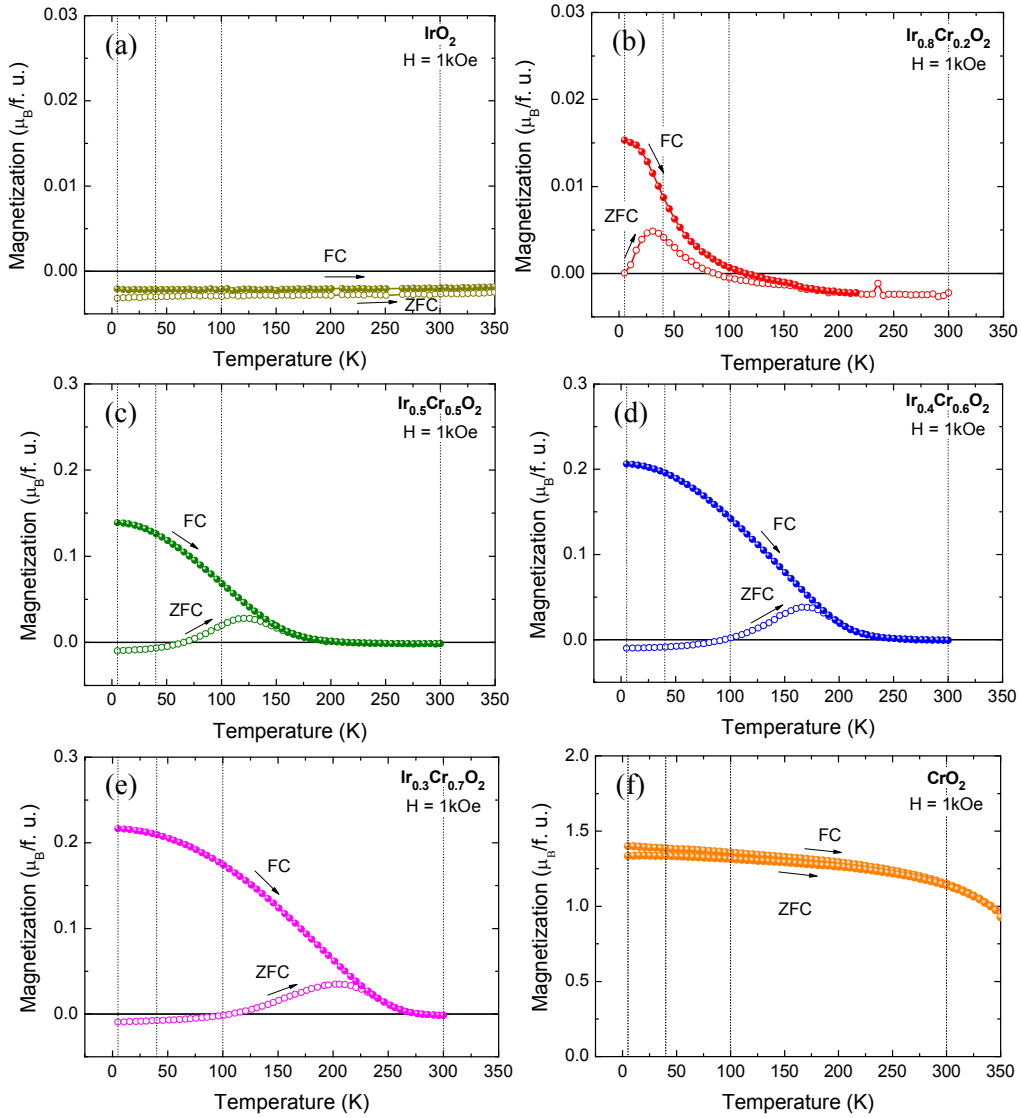

Figure 6.6 ZFC and FC M(T) curves recorded on representative annealed $Ir_{1-x}Cr_xO_2$ samples with H = 1 kOe (0.1 kOe for CrO_2). Pure IrO_2 and CrO_2 films are included for comparison. Dotted lines are relevant for the discussion.

The maximum values reached by the FC and ZFC magnetization are represented in Fig. 6.7(a) as a function of the Cr content. In a similar manner, the Cr

content dependence on T_P and T_{irr} are displayed in Fig. 6.7(b). These four parameters show a progressive increase up to $x = 0.7$ and then decrease for $x = 0.8$.

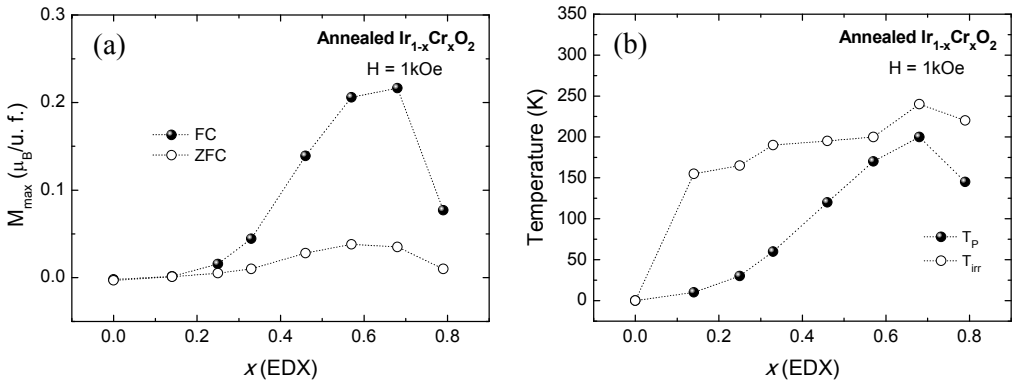

Figure 6.7 (a) Maximum magnetization measured in the FC and ZFC curves and (b) evolution of T_P and T_{irr} with the Cr content extracted from EDX. Dotted lines are guides to the eye.

In view of these results, M(H) curves were recorded in all the annealed samples at 300, 100, 40 and 5 K. In the representative curves displayed in Fig. 6.8, three different regions can be distinguished depending on the temperature:

(i) When $T > T_P$, *i.e.*, T = 300 K, a paramagnetic–like behavior is observed in all the samples, with a relative small maximum magnetic moment irrespective of the Cr content.

(ii) The temperatures at which $T_P < T < T_{irr}$ depend on the Cr content (see Fig. 6.6). For instance, for $x = 0.1$, 0.2 and 0.3, T = 100 K lies between T_{irr} and T_P. In these cases, a small ferromagnetic–like (or nearly saturated) component appears in the M(H) curves and small coercive fields (H_C) are revealed.

(iii) Finally, when $T < T_P$ the shape of the M(H) curves changes drastically: M_{max} increases and **huge coercive fields** are observed.

These results suggest a scenario where magnetically ordered clusters are formed in the $T_P < T < T_{irr}$ range, giving rise to the saturated (ferromagnetic–like) component observed in this range of temperatures. When $T < T_P$, it is evident the appearance of an anisotropy source.

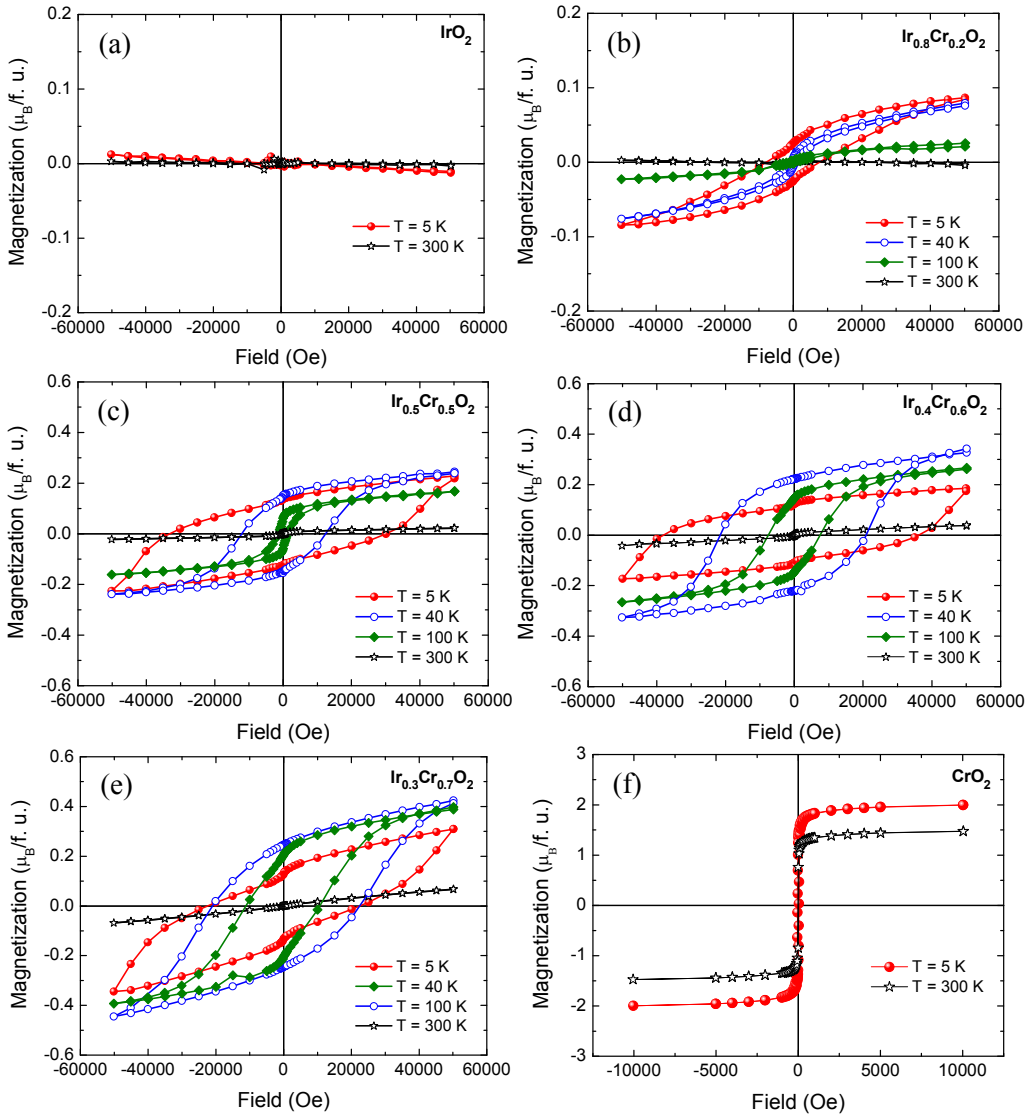

Figure 6.8 M(H) curves recorded on representative annealed $Ir_{1-x}Cr_xO_2$ samples at 5, 40, 100 and 300 K. Pure IrO_2 and CrO_2 films are included for comparison.

The evolution of M_{max} (magnetization at T = 5 K and H = 50 kOe) with the Cr content is shown in Fig. 6.9(a) for the four temperatures probed. It can be seen in this figure that the net magnetic moment increases up to the sample with $x = 0.7$ and then decreases for $x = 0.8$. In all cases, the $Ir_{1-x}Cr_xO_2$ films present a relatively high magnetic moment at low T, up to ~0.4 μ_B/f. u. in the $Ir_{0.3}Cr_{0.7}O_2$ sample. It is somehow

unexpected that M_{max} decreases for x = 0.8. This could be due to the less crystalline structure of this film, as observed in the XRD experiments.

Similarly, the dependence of H_C on x is displayed in Fig. 6.9(b). It can be seen in this figure that H_C increases up to the sample with x = 0.6 and then decreases. It is remarkable the observed **giant coercive fields** in these compounds, greater than 40 kOe in the $Ir_{0.4}Cr_{0.6}O_2$ film at 5 K (maximum H_C measured). It is important to note that for $0.4 \leq x \leq 0.8$, the large hysteresis loops are actually minor loops and remain far from saturating up to 50 kOe. This indicates that the actual H_C for these samples is even larger, as well as the magnetic moment. Applying a field cooling from RT before measuring the loops increases the values of the magnetization (up to a factor ~2 has been observed at high fields in $Ir_{0.4}Cr_{0.6}O_2$). However this magnetic state is found to be metastable and it rapidly relaxes.

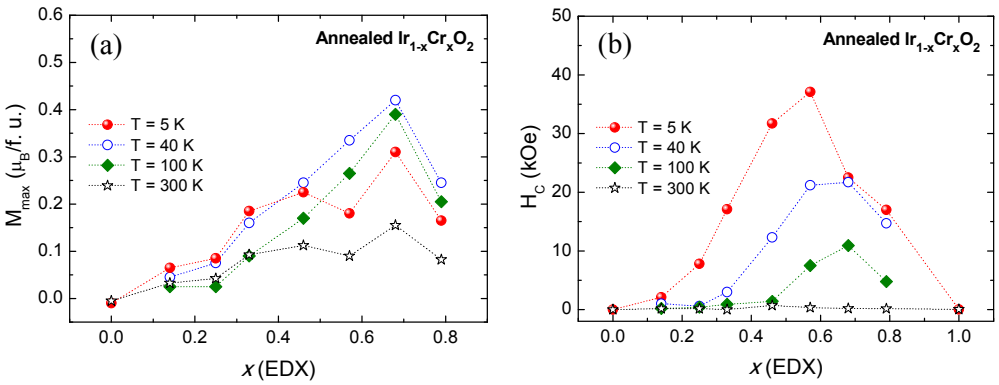

Figure 6.9 (a) Magnetization at H = 50 kOe and (f) and H_C as a function of the Cr content. Dotted lines are guides to the eye.

It is relevant to make a comparison with the magnetic response of pure CrO_2 (Fig. 6.8(f)). In this sense, the $Ir_{1-x}Cr_xO_2$ films present a relatively high magnetization, though obviously not as large as in bulk CrO_2 (~2 μ_B/f. u.). On the other hand, the coercivity of these systems is remarkably different, from an almost negligible H_C (< 100 Oe) in bulk CrO_2 to the huge H_C (> 40 kOe) observed in the dilutions.

6.6.2. X–Ray Magnetic Circular Dichroism (XMCD)

After the very interesting macroscopic magnetic response observed in the annealed $Ir_{1-x}Cr_xO_2$ films, XMCD is needed to microscopically disentangle the magnetic contributions coming from Ir and Cr atoms. Thus, XMCD spectra were recorded at the Ir $L_{2,3}$ edges and at the Cr K edge[15] of the sample exhibiting the largest coercive field at 5 K, *i.e.*, the $Ir_{0.4}Cr_{0.6}O_2$ sample.

Ir $L_{2,3}$ edges

Fig. 6.10(a) shows the XMCD spectra recorded at the Ir $L_{2,3}$ edges on the polycrystalline $Ir_{0.4}Cr_{0.6}O_2$ sample. Contrary to the spectra measured in previous chapters, a **clear and indubitable XMCD signal is revealed** at both absorption edges, of similar magnitude (~2%), and of opposite sign. This demonstrates an important magnetic contribution coming from the Ir atoms to the magnetic response of the $Ir_{1-x}Cr_xO_2$ films. The results derived from sum rule analysis [135, 136] indicate that the net magnetic moment of Ir is **antiferromagnetically coupled to Cr** and basically of spin nature: $m_s \approx -0.11$, $m_l = 0.01$ μ_B/at. Ir, and $m = (m_l + m_s) = -0.10$ μ_B/at. Ir.[16] This is quite an unexpected and important result, since usually Ir XMCD signals observed in other Ir^{4+} iridates at the L_2 edge are very small, leading to comparable m_s and m_l moments [179, 216, 273–275]. In this case, however, the nature of the magnetic moment is completely different. From this large XMCD signal the formation of Ir^{5+}, which is a non–magnetic $J = 0$, is ruled out [276]. That is, this result further confirms that the shift observed in Fig. 6.3 is not due to charge transfer.

In addition, Figs. 6.10(b) and 6.10(c) show the field– and temperature–dependent XMCD signals, respectively, recorded in the same sample. The XMCD(H) measurement reveals a clear hysteresis loop with a coercive field $H_C = 5$ kOe, which is

[15] The K edge ($1s \rightarrow 4p$ transitions) provides magnetic information of the *d* states indirectly through the 3*d*–4*p* hybridization [277, 278].

[16] These values are obtained assuming $T_z = 0$. While the precise values depend on T_z, the almost pure spin nature remains invariant.

relatively large but far from the H_C > 40 kOe observed in macroscopic measurements (Fig. 6.8(d)). On the contrary, the XMCD(T) curve (Fig. 6.10(c)) presents a transition at ~225 K coincident with the macroscopic M(T) curve recorded with the SQUID.

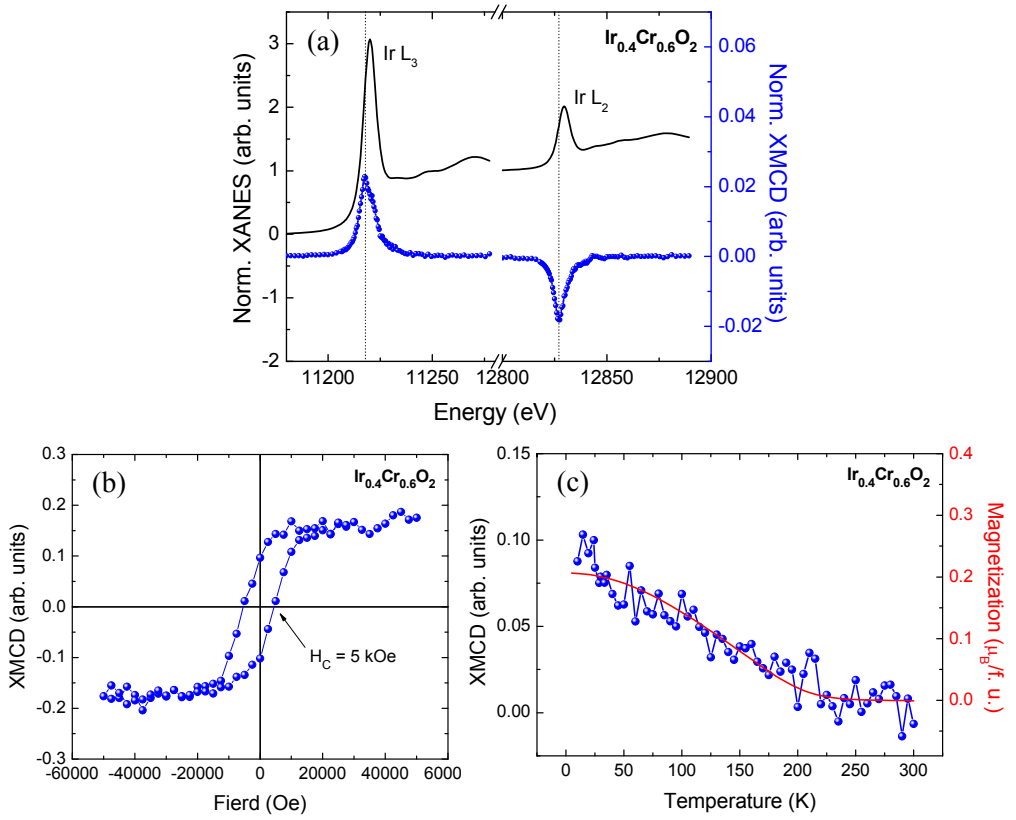

Figure 6.10 (a) Normalized XANES and XMCD spectra recorded at the Ir $L_{2,3}$ edges at T = 10 K and H = 50 kOe on polycrystalline $Ir_{0.4}Cr_{0.6}O_2$ sample. (b) Ir L_3–edge field–dependent XMCD curve at T = 10 K and *E* = 11218 eV. (c) Ir L_3–edge temperature–dependent XMCD curve with H = 1kOe. The FC–M(T) is also included for comparison.

Cr K edge

Figs. 6.11(a) and 6.11(b) show the XMCD spectra recorded at the Cr K edge on the polycrystalline $Ir_{0.4}Cr_{0.6}O_2$ sample and on the pure CrO_2 film, respectively. Both samples show similar XMCD signals. The similar size of both XMCD spectra indicates that in $Ir_{0.4}Cr_{0.6}O_2$ the value of the Cr magnetic moment is similar to that found in CrO_2 (~2 μ_B/at. Cr) and that it orders ferromagnetically within the Cr

sublattice. This is a rather puzzling result as it is not in agreement with the macroscopic magnetization data, which indicates a noticeably smaller net moment of Cr. The origin of such an apparent contradiction is not clear and point to a complex magnetic behavior, whose clarification would require further extensive work. On the other hand, the spectral profile of $Ir_{0.4}Cr_{0.6}O_2$ film shows a feature at 6010 eV that is not observed in CrO_2. The small differences in the profile can be tentatively associated to differences in the structure (as observed in the case of the XAS profile) and/or hybridization with the Ir atoms.

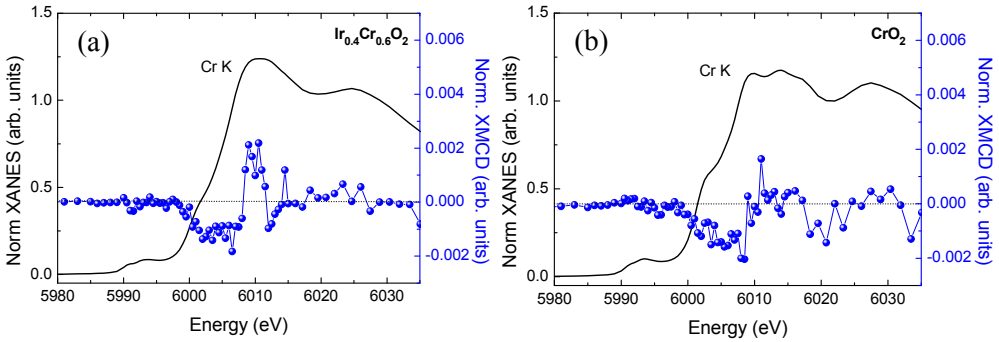

Figure 6.11 (a) Normalized XANES and XMCD spectra recorded at the Cr K edge at T = 10 K and H = 50 kOe on the polycrystalline $Ir_{0.4}Cr_{0.6}O_2$ sample. (b) Normalized XANES and XMCD spectra recorded at the Cr K edge at T = 10 K and H = 10 kOe on the epitaxial CrO_2 film.

It is thus clear that the magnetic characterization of the $Ir_{1-x}Cr_xO_2$ samples has revealed a very interesting, yet intriguing scenario. These systems present high magnetization and, at the same time, huge coercive fields.

In an initial approach, one could tentatively associate the increment in coercivity to the presence of small antiferromagnetic Cr_2O_3 clusters, where the existence of CrO_2/Cr_2O_3 heterostructures would lead to an enhanced H_C in a similar way to that observed for Fe/Fe_2O_3 and Co/CoO [279, 280]. However, as mentioned above the presence of Cr_2O_3 (or Cr^{3+} in any other oxide) is neither observed in the XRD measurements nor in the XANES experiments. In addition, negligible H_C in Cr_2O_3/CrO_2 nanoparticles and nanorods have been previously reported [281, 282].

Hence, this scenario can be reasonably discarded. On the other hand, other Cr–doped rutile structures (TiO_2) have also proven to show negligible H_C [283, 284].

Another source of magnetic frustrations could be RKKY or dipolar exchange interactions between crystallographically ordered regions (clusters) in a disordered matrix, which would agree with the XRD experiments. Nevertheless, these kinds of inter–cluster exchange interactions are too weak to be (solely) responsible for the huge coercivity and stronger short range interactions should be considered.

In view of this, it seems that Ir could be the key ingredient. In this sense, two different pictures can be envisaged. One can propose the high SOC of Ir to be at the origin of the huge H_C observed in the M(H) loops in a similar manner to that proposed in $BaIrO_3$ and Sr_3NiIrO_6 [257, 258, 285]. According to these works, the huge H_C would be linked to the unusual spin–orbit–entangled local state of the Ir^{4+} ion and its potential for anisotropic exchange interactions. Alternatively, one can propose an Ir–driven exchange coupled core–shell–like heterostructure where the structural disorder at the surface (shell) of the cluster gives rise to a spin glass behavior that blocks the magnetic response of the whole cluster in a similar way to that observed in Fe_2O_3 nanoparticles [286]. In this picture, the antiparallel coupling between Cr and Ir would be a key factor. Both scenarios, however, have also some drawbacks. In particular, the small orbital magnetic moment of Ir and the smaller H_C found in the Ir L_3–edge XMCD hysteresis loop do not seem to agree well with an Ir–induced anisotropy.

The nature of the magnetic moment of Ir itself is rather puzzling. To the best of our knowledge, all the L–edge XMCD spectra reported so far for iridates with IrO_6 octahedra consist of a large signal at the L_3 edge and a much smaller signal at the L_2 edge. In our case, however, the XMCD experiments indicate a drastic quenching of the Ir orbital magnetic moment with $\langle m_l \rangle / \langle m_s \rangle = 0.09$. This fact discards a $j_{eff} = 1/2$ state, which should lead to $\langle m_l \rangle / \langle m_s \rangle \approx 2$ predicted for a purely ionic $j_{eff} = 1/2$ model [27]. This result cannot be explained in terms of charge transfer either, since it would require having a majority of Ir^{6+} ions [216]. On the other hand, the $j_{eff} = 1/2$ state of Ir^{4+} relies on a nearly cubic crystal field, and substantial distortions of the IrO_6

octahedra are expected to destroy such state, leading to a quenched orbital moment. Thus, one could speculate that the quenched $\langle m_l \rangle$ here observed occurs due to Ir^{4+} ions placed in highly distorted octahedra. However, the high $\langle \mathbf{L} \cdot \mathbf{S} \rangle$ is difficult to reconcile with a quenched $\langle m_l \rangle$.

Finally, a Cr–induced magnetic moment should also be considered. While such an origin is frequent in intermetallics and in metallic multilayers through direct orbital overlap [287, 288], it is quite controversial in oxides, where just a few cases of neighbor–induced XMCD signals have been only recently reported [289]. If verified, this would be a remarkable result that would clearly tilt the balance in this discussion, openning a new route to engineer the magnetic properties of oxides, thus contributing to future applications.

It should be noted that all the factors mentioned above could be playing a certain role in the macroscopic response of these compounds depending on the Ir/Cr content. A systematic study (future work) is needed to clarify the relative weigh of each of them.

6.7. Conclusions

Polycrystalline $Ir_{1-x}Cr_xO_2$ (x = 0.1–0.8) thin films of ~100 nm have been successfully grown by reactive magnetron co–sputtering followed by an annealing treatment at 600 ºC. The structural characterization shows that a rutile single phase is formed in all the samples, confirming that Ir and Cr form a substitutional solid solution phase.

The analysis of the XANES spectra of the $Ir_{0.6}Cr_{0.4}O_2$ sample reveals very strong 5*d* SOC and further confirms the oxidation state of both, Ir and Cr, to be 4+.

In contrast to the metallic ground state of IrO_2 and CrO_2, the electrical characterization of the $Ir_{1-x}Cr_xO_2$ samples reveals a clear upturn in the resistivity. This upturn appears at increasing temperatures for greater values of x, up to the point where

a semiconductor–like response is observed in the sample with x = 0.8. Disorder is proposed to be at the origin of this MIT.

Contrary to CrO_2, the $Ir_{1-x}Cr_xO_2$ samples present **giant coercive fields** (greater than 40 kOe). At low temperatures the hysteresis loops are minor loops and remain far from saturating up to 50 kOe. Besides, compared to other iridates with high coercivity like Sr_3NiIrO_6, in the $Ir_{1-x}Cr_xO_2$ films very large coercive fields are observed at relatively high temperatures (up to ~200 K in the case of x = 0.7). Our results suggest that the presence of Ir is at the origin of this giant coercivity. Moreover, we have found that by changing the Cr content, both **the magnetization and the coercive field can be widely tuned**.

The XMCD experiments show that **Ir has a sizable magnetic moment** in this samples, m = 0.10 μ_B/at. Ir. Surprisingly enough for a Ir^{4+} iridate, the orbital contribution to the magnetic moment is negligible. Our data so far suggest that the magnetic moment of Ir is induced by Cr, which is a remarkable result for an oxide. The magnetic measurements also reveal a complex magnetic structure, where the net magnetic moment of Cr is antiferromagnetically coupled to the net magnetic moment of Ir.

This work is the first report on the synthesis of $Ir_{1-x}Cr_xO_2$ samples. From the applied point of view, this material has huge potential for spintronics as it combines a half metal with the high SOC required for spin–current to charge–current conversion. In addition, it provides a new route to grow the thermally unstable CrO_2 structure and even tune its magnetic response by dilution. The initial research carried out in this chapter has led to a very interesting yet intriguing scenario, in which further work is needed to confirm the origin of both, the electrical and the magnetic response of this new compound.

Chapter 7

Ir(IrO_2)/Fe(FeOx) multilayers

7.1. Introduction

The growth of structures based on 3*d*/iridate bilayers offers a promising approach in the development of new spintronics devices. One can envisage the fabrication of controlled 3*d*/5*d* structures where the high SOC of the 5*d* (Ir oxide) is combined with the high magnetic moment and Curie temperature (T_C) of the 3*d* compound to obtain, for instance, a system with tunable magnetic properties. Pioneer works have recently shown, for instance, the capability of paramagnetic iridates, such as $SrIrO_3$, to extrinsically manipulate the magnetic anisotropy of a neighbor $La_{2/3}Sr_{1/3}MnO_3$ film [26]. The strong SOC of iridates has been reported to give rise to anisotropic magnetoresistance in $La_{2/3}Sr_{1/3}MnO_3/Sr_2IrO_4$ [25] and anomalous Hall effect in $Sr_2MnO_3/SrIrO_3$ [290]. In addition, the enhanced thermospin effects in Fe_3O_4/Pt multilayers [291] suggest an interesting thermoelectric performance also in the Fe_3O_4/IrO_2 systems.

The growth of 3*d*/iridate heterostructures is, however, at a very early stage and it is still necessary to find these optimized 3*d*–transition metal oxide (TMO)/iridate structures aimed at creating spin–polarized currents and/or manipulating nanomagnets. In view of this, the current chapter aims at **exploring $IrO_2/Fe_3O_4(Fe_2O_3)$ and IrO_2/Fe heterostructures (multilayers)**. To the best of our knowledge, no previous work on IrO_2/3*d*–TMO or IrO_2/3*d*–metal systems has been published to date. Therefore, as a first step, we focus on the synthesis and characterization of samples prepared by conventional sequential magnetron sputtering at room temperature (RT) and with no

further thermal treatment, *i.e.*, the simplest conditions, and in turn, the most interesting from the practical point of view (the most favorable industrial production conditions).

For the sake of completeness Ir/Fe multilayers are also studied. While binary thin films and heterostructures based on combinations of Fe and Ag, W, Pt, or Au have attracted lot of attention for practical spintronic applications [288, 292–300], the Ir/Fe systems have been barely explored [301–306]. The lack of research on Ir/Fe systems is surprising taking into account that Ir also exhibits a strong SOC that could result in high magnetocrystalline anisotropy [307].

Thus, section 7.2 is devoted to the sample fabrication; the structural and compositional characterization is presented in section 7.3; and the magnetic response of such heterostructures is provided in section 7.4. Finally, the effect of annealing a few selected samples is described in section 7.5.

7.2. Sample Fabrication

Conventional (reactive) magnetron sputtering in a pure Ar atmosphere (Ar/O_2 mixture gas ~24% O_2–rich) was used for depositing metallic (oxide) layers in a sequential way. All the samples were grown on Si(100) substrates at RT starting with an Ir–based layer. On top of the multilayer an Ir–based layer was also deposited to protect the last Fe–based layer from the environment. As schematized in Fig. 7.1, the samples studied along this chapter are classified within three groups regarding their nominal composition, namely: oxide/metallic (**O/M**), oxide/oxide (**O/O**) and metallic/metallic (**M/M**). IrO_2 and FeOx (as shown below the phase is not well defined) stand for layers grown in an oxygen–containing atmosphere. The samples are also labeled according to the nominal thickness (in nm) of the Ir– and Fe–based layers, *t* and *t'*, respectively; and the number of bilayers, *n*.

The sputtering parameters employed in the synthesis of the films are given in Table 7.1. The thickness of the Ir– and Fe–based single layers making up the multilayers was varied in the 0.3 to 10 nm range to study its influence in the magnetic

response. In some cases, samples with same bilayer structure but variable number of repetitions were grown to optimize the signal to noise ratio in the different experiments.

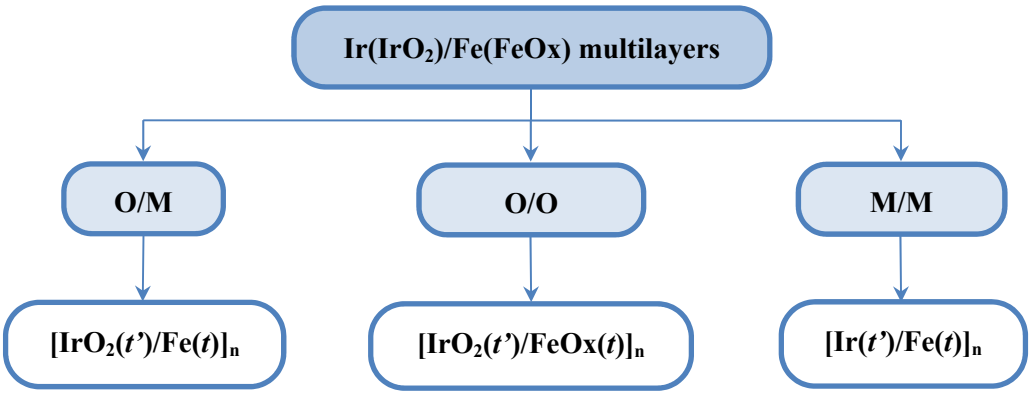

Figure 7.1 Scheme of the samples studied along this chapter.

7.3. Structural and Compositional Characterization

7.3.1. X–Ray Reflectivity (XRR)

The XRR curves displayed in Figs. 7.2(a), 7.2(b) and 7.2(c) for the O/M, O/O and M/M sample series, respectively, provide information about the total and bilayer thickness, and about the interface quality (roughness) of the multilayers. The values of the total and bilayer thickness, calculated by means of the Eq. 2.4, are given in Table 7.1. As shown in such table, the total thicknesses values are in good agreement with the nominal ones. Note that in the multilayers with a total nominal thickness of ~200 nm, the actual total thickness could not be estimated by XRR because of being such value on the verge of the detection limit of the technique [308, 309]. This is reflected in Fig. 7.2 in the fact that the *Kiessig fringes*, which indicate the total layer thickness (see section 2.4.2), cannot be so clearly discerned in these samples. On the other hand, the deviations in the bilayer thickness are below 10% in the **O/M** and **O/O groups**, and around 20% in the **M/M group**.

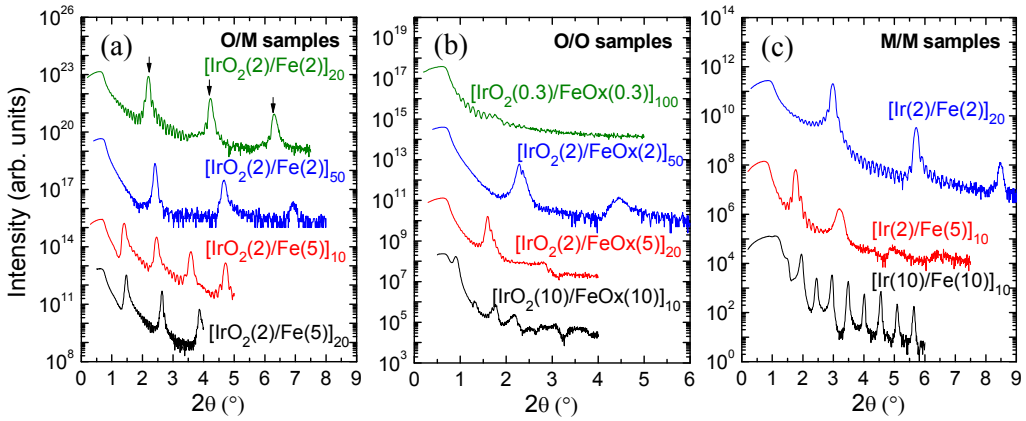

Figure 7.2 XRR measurements for the (a) O/M, (b) O/O and (c) M/M sample series.

Concerning the structural quality, *satellite maxima* (which indicate the bilayer thickness) can be discerned in a broad angular range in the **O/M** and **M/M samples**, indicative of well–defined layered structures with clean interphases. For instance, the *satellite maxima* are visible in the $[IrO_2(2)/Fe(2)]_{50}$ sample up to $2\theta \approx 7.0^{\circ}$ (marked with vertical arrows in Fig. 7.2(a)), and in the $[Ir(2)/Fe(2)]_{20}$ sample up to $2\theta \approx 8.5^{\circ}$. Contrary, the poorer–resolved XRR profiles of the **O/O samples** are indicative of a worse layered structure. In fact, *satellite maxima* are well resolved only for $2\theta < 4.5^{\circ}$ in the $[IrO_2(2)/FeOx(2)]_{50}$ sample. Furthermore, the curve of the $[IrO_2(0.3)/FeOx(0.3)]_{100}$ sample looks more similar to a single layer than to a multilayer, since no *satellites* are discerned.

One possible explanation for such worse structural quality observed in the O/O sample series respect to the other groups is an intermixing at the interface, since XRR cannot distinguish interface compositional grading or diffuseness from interface roughness. Additionally, an effect due to the density difference in the layers should also be considered. In this sense, XRR is sensitive to the density difference along the surface normal direction. Hence, a better–defined profile should be expected for higher density differences between the layers, that is, for O/M and M/M samples. Obviously, both situations can take place simultaneously.

Table 7.1 Sputtering parameters employed in the synthesis of the multilayers and structural and compositional information: bilayer and total multilayer thickness calculated from XRR data, individual and total multilayer thickness according to TEM (in nm, ±0.5nm); and total multilayer thickness and relative abundance of elements obtained from RBS measurements. RBS experiments were carried out and analyzed by Dr. J. García López at *Centro Nacional de Aceleradores* (Sevilla, Spain) and were used to normalize the SQUID data (in section 7.4.1). More information about the RBS experiments can be found in Ref. [310].

Sample	**Power Source**	**Power (W)**	**XRR Thickness (nm)**		**TEM Thickness (nm)**		**Atoms (10^{15} at/cm^2)**	**Elemental Composition**
			Bilayer	**Total**	**Bilayer**	**Total**		
$[IrO_2(2)/Fe(2)]_{20}$	RF/DC	5.0/3.4	4.2	87.0	1.5/2.7	87	750	$Ir_{10}Fe_{31}O_{58}Ar_1$
$[IrO_2(2)/Fe(2)]_{50}$	RF/DC	5.0/3.5	3.9	*	1.5/1.8	173	1620	$Ir_{16}Fe_{30}O_{53}Ar_1$
$[IrO_2(2)/Fe(5)]_{10}$	DC/DC	4.0/6.0	7.7	79.5	1.6/5.8	84	660	$Ir_7Fe_{42}O_{51}Ar_0$
$[IrO_2(2)/Fe(5)]_{20}$	DC/DC	4.0/5.8	6.9	145.3	1.7/4.5	136	1150	$Ir_{10}Fe_{44}O_{45}Ar_1$
$[IrO_2(0.3)/FeOx(0.3)]_{100}$	RF/DC	5.5/28.8	–	65.0	–	65	520	$Ir_{12}Fe_{18}O_{70}Ar_0$
$[IrO_2(2)/FeOx(2)]_{50}$	DC/DC	4.0/28.0	4.0	*	1.9/1.0	153	1780	$Ir_{17}Fe_{13}O_{69}Ar_1$
$[IrO_2(2)/FeOx(5)]_{20}$	DC/DC	4.0/27.7	–	122.0	2.5/3.0	118	1040	$Ir_{11}Fe_{22}O_{66}Ar_1$
$[IrO_2(10)/FeOx(10)]_{10}$	DC/DC	3.6/28.3	20.3	148.4	9.4/7.0	151	1605	$Ir_{34}O_{65}Ar_1/Fe_{29}O_{70}Ar_1$
$[Ir(2)/Fe(2)]_{20}$	DC/DC	3.4/3.1	3.2	66.2	1.8/1.2	67	460	$Ir_{48}Fe_{51}Ar_1$
$[Ir(2)/Fe(5)]_{10}$	RF/DC	3.1/3.4	5.3	61.0	2.1/3.0	58		–
$[Ir(10)/Fe(10)]_{10}$	DC/DC	3.3/6.0	16.1	*	9.0/6.7	176	1096	$Ir_{98}Ar_2/Fe_{98}Ar_2$

*The actual total thickness could not be estimated because of being on the verge of the detection limit of the technique (~200 nm) [308, 309].

7.3.2. Transmission Electron Microscopy (TEM)

Further structural information was obtained by TEM microscopy. Illustrative cross–sectional TEM images are given in Fig. 7.3, showing the full layer; and in Fig. 7.4, showing the bilayer structure in detail. Clear layered structures can be discerned in all the **O/M** and **M/M** samples, while a poorer defined (rougher) microstructure is observed in the **O/O** multilayers, in agreement with the XRR experiments. In fact, the layered structure disappears in the sample with the thinnest monolayers, $[IrO_2(0.3)/FeOx(0.3)]_{100}$. The relative roughness and the thickness values of each layer measured on the TEM images, shown in Table 7.1, are also in agreement with the XRR data.

It is noticeable that the experimentally–obtained thickness of the Fe layer in **O/M** samples is considerably larger than that obtained in **M/M** samples with the same nominal thickness. On the other hand, the IrO_2 layer in **O/M** samples is smaller than in **O/O** systems. This suggests some kind of "expansion" of the Fe layer at the expense of the IrO_2 layer.

Inside each individual layer, small regions of different shades of gray can be discerned. This could be due to different phases within the layer and/or different crystal orientation. On the one hand, the clusters observed inside the Fe layers of O/M samples look similar to a cluster/matrix biphasic system (see arrows in Fig. 7.4(g), for instance). On the other hand, in the M/M multilayers the sharp contrast observed inside most of the individual layers (Fig. 7.4(i)) suggests different grain orientations. Indeed, some crystalline planes are observable in most of the samples displayed in Fig. 7.4 and in the Fourier transform (FT) in panel (l). This proves the existence of certain order (polycrystallinity) even when no annealing treatment was performed. However, on the $[IrO_2(2)/Fe(2)]_{20}$, $[IrO_2(2)/Fe(5)]_{10}$, $[IrO_2(0.3)/FeOx(0.3)]_{100}$, and $[IrO_2(2)/FeOx(2)]_{50}$ samples, no crystalline planes can be distinguished, which suggests higher degree of disorder probably due to the smaller size of the layer.

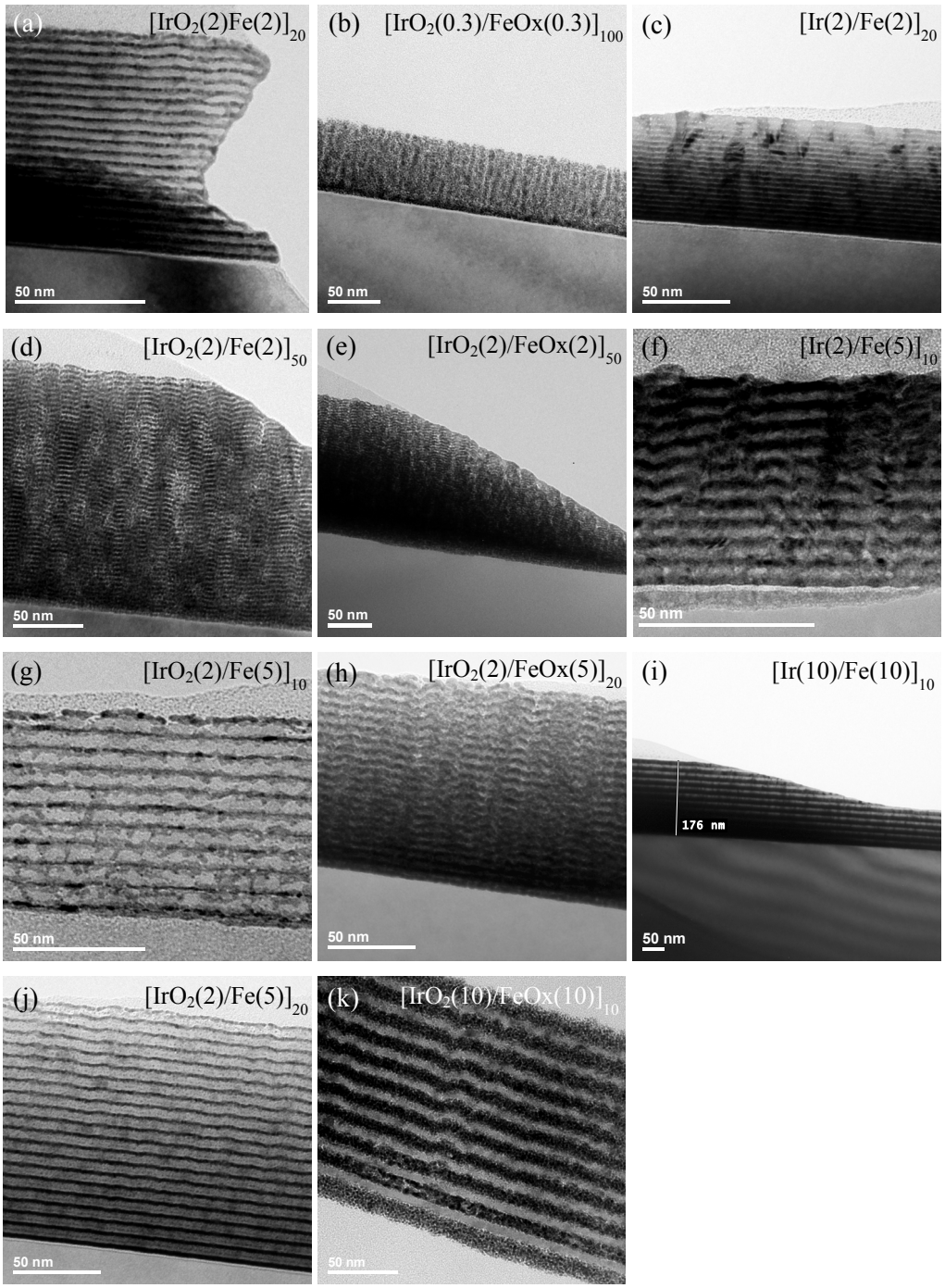

Figure 7.3 Illustrative TEM images of O/M (left), O/O (middle) and M/M (left) samples showing the full cross–section. Darkest (lightest) layers are assigned to Ir–based [Z = 77] (Fe–based, Z = 26) layers.

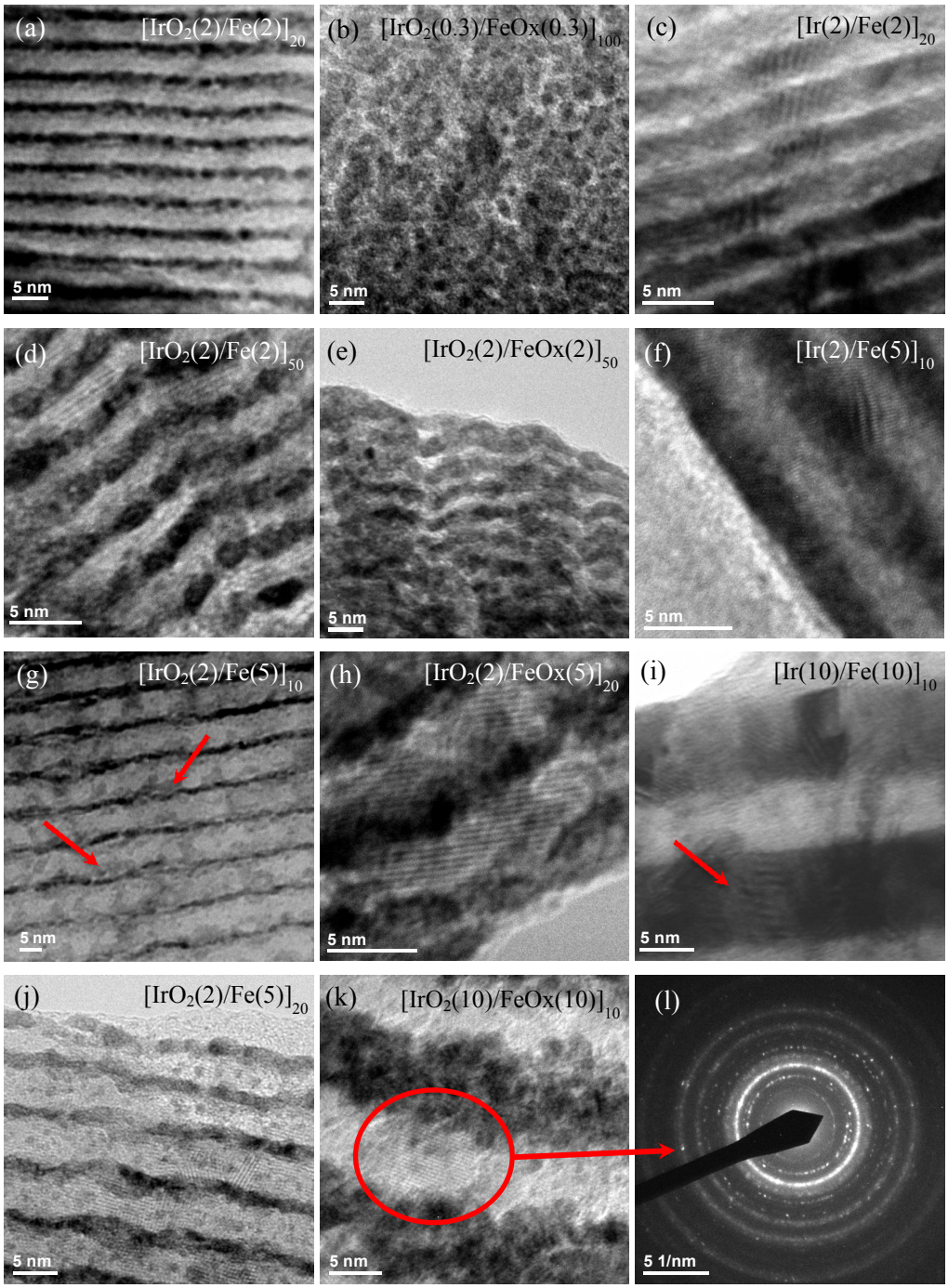

Figure 7.4 Illustrative TEM images of O/M (left column), O/O (middle column) and M/M (left column) samples showing the bilayer structure in detail. The panel (l) shows the FT corresponding to the selected area of the $[IrO_2(10)/FeOx(10)]_{10}$ sample.

7.3.3. X–Ray Absorption (XAS)

In general, the magnetic response of systems containing Fe oxides is strongly dependent on the nature of the Fe phase [311, 312]. It has been demonstrated that the XAS technique is a powerful tool to elucidate the nature of such kind of phases [313, 314]. Hence, a thorough XAS study was performed in representative samples. Both, X–ray absorption near edge structure (XANES) and extended X–ray absorption fine structure (EXAFS), were recorded at the Ir L_3 edge and at the Fe K edge.

Ir L_3 edge

Figs. 7.5(a) and 7.5(b) show the XANES and the EXAFS spectra, respectively, measured at the Ir L_3 edge of representative samples.

It can be seen that the XANES spectra of the **O/M samples** show an intermediate profile between the spectra of the M/M and the O/O samples (pure Ir and IrO_2, respectively, as proved below), indicating a phase mixture (Fig. 7.5(a)). Moreover, in the case of the $[IrO_2(2)/Fe(5)]_{20}$ sample, such profile is closer to that of M/M samples than in the case of $[IrO_2(2)/Fe(2)]_{20}$ multilayers, indicative of a greater amount of metallic phase in the first. In fact, the FT of the EXAFS signal in Fig. 7.5(c) confirms that the Ir–based layers in $[IrO_2(2)/Fe(5)]_{20}$ (practically) correspond to Ir metal, even when they were grown as IrO_2. On the other hand, the spectrum of the $[IrO_2(2)/Fe(2)]_{50}$ sample indicates a significant contribution of both, metallic and oxide phases, in agreement with the results from the XANES analysis.

In order to get a rough estimation of the percentages of each phase in these samples, a linear combination fitting of the XANES profiles was carried out. The corresponding fits are displayed in Fig. 7.5(d) and the phase percentages obtained from such fits are given in Table 7.2. The $[IrO_2(2)/FeOx(2)]_{50}$ and $[Ir(2)/Fe(2)]_{20}$ multilayers are used as references for pure oxide and metal phases (proved below),

respectively.[17] From such analyses, the greater percentage of metallic Ir in the $[IrO_2(2)/Fe(5)]_{20}$ sample than in $[IrO_2(2)/Fe(2)]_{50}$ is confirmed: ~94% in $[IrO_2(2)/Fe(5)]_{20}$ and ~67% in $[IrO_2(2)/Fe(2)]_{50}$.

Table 7.2: Estimated percentages of each phase in the multilayers from a linear combination fit (fitting range -15 to 150 eV from E_0) using $[IrO_2(2)/FeOx(2)]_{50}$ and $[Ir(2)/Fe(2)]_{20}$ multilayers as references for pure oxide and metal phases, respectively.

Sample	Fe		Ir	
	Metal (%)	**Oxide (%)**	**Metal (%)**	**Oxide (%)**
$[IrO_2(2)/Fe(2)]_{50}$	17	83	67	33
$[IrO_2(2)/Fe(5)]_{20}$	38	62	94	6

As for the **O/O samples**, both $[IrO_2(2)/FeOx(2)]_{50}$ and $[IrO_2(0.3)/FeOx(0.3)]_{100}$ multilayers show the expected XANES spectrum for IrO_2 (Fig. 7.5(a)) [81]. The small differences in the profile can be addressed to small structural differences. The EXAFS signals of these samples, given in Fig. 7.5(b) compared to that of a bulk IrO_2 reference, confirm that the Ir–based layers correspond to IrO_2. The relative reduction of the FT at higher R values indicates that the local order in the multilayer is not as good as in the reference (Fig. 7.5(c)). Nevertheless, the sample keeps a certain degree of local structural order up to R = 5 Å (no phase correction applied).

Regarding the representative sample from the **M/M group** ($[Ir(2)/Fe(2)]_{20}$), it displays both XANES and EXAFS profiles practically identical to metallic Ir (Figs. 7.5(a) and 7.5(c), respectively) [81]. The similarity of the EXAFS spectra also indicates that the Ir layers present a remarkable structural order taking into account that the thickness is only 2 nm. This was further confirmed by fitting the spectrum of the $[Ir(2)/Fe(2)]_{20}$ sample to the theoretical spectrum of Ir metal (details in Ref. [310]).

[17] It should be noted that the multilayer is not made of well-defined phases, so there is always an error inherent to the employed references in this procedure. Nevertheless, similar percentages and the same conclusions are drawn regardless of the chosen references: maghemite and Fe foil, or $[IrO_2(2)/FeOx(2)]_{50}$ and $[Ir(2)/Fe(2)]_{20}$ multilayers.

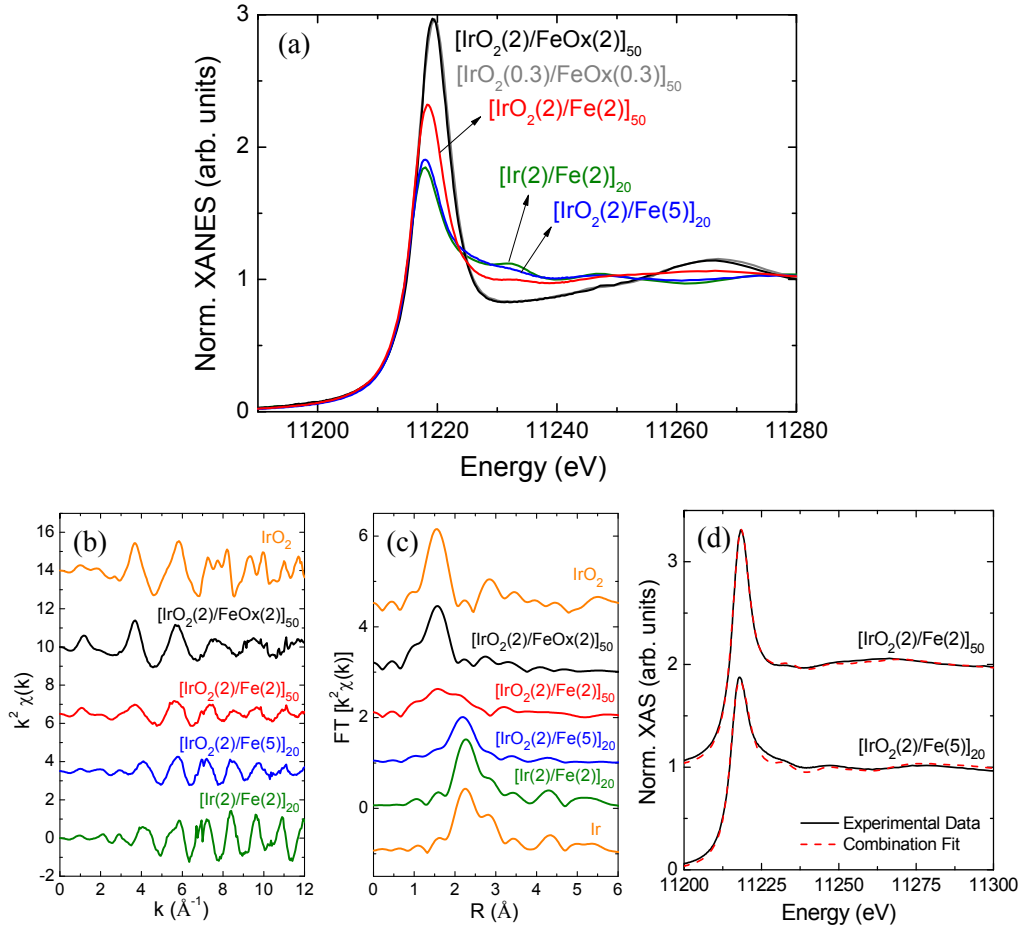

Figure 7.5 Comparison of the Ir L_3–edge (a) XANES and (b) EXAFS spectra recorded on representative O/M, O/O and M/M samples. Panel (c) shows the FTs (k^2–weighted, range from 3.0 $Å^{-1}$ to 10 $Å^{-1}$) of the EXAFS signals. For the sake of clarity the spectra have been shifted. Due to the lack of a good experimental metallic Ir reference, a simulated spectrum (Artermis software) of Ir metal has been used for comparison in panel (c). Panel (d) shows the linear combination fits of the XANES spectra at the Ir L_3 edge in the samples from the O/M group (fitting range -15 to 150 eV from E_0) using $[Ir(2)/Fe(2)]_{20}$ and $[IrO_2(2)/FeOx(2)]_{50}$ samples as references for pure metal and oxide phases, respectively.

Fe K edge

The XAS spectra of two representative (nominal) **O/M samples** are displayed in Fig. 7.6 and compared to bulk maghemite (γ–Fe_2O_3), the most frequent iron oxide; and to bcc Fe references. Regarding the $[IrO_2(2)/Fe(5)]_{20}$ sample, in the XANES

spectrum (Fig. 7.6(a)) the energy position of the threshold, E_0, the height of the pre–edge at ~7115 eV and the profile just above the edge, can only be accounted for by a mixture of metallic and oxidized phases. Moreover, in the FT of the EXAFS signal, the peak at ~2 Å in the real part (dotted line in Fig. 7.6(d)) also reveals a metallic contribution added to the main oxide phase. Thus, both the XANES and the EXAFS signals indicate a mixture of metal and oxide phases in this sample, even when, according to the growing conditions, the Fe–based layer should be pure Fe metal. As for the crystallinity, the presence of a second peak at $R \approx 2.7$ Å on the FT (Fig. 7.6(c)) indicates the formation of a second coordination shell in the oxide. However, the reduced intensity of the peaks relative to the bulk references, and the fact that this reduction is larger for the second peak, indicates a certain degree of crystallographic disorder. Such disorder, along with the presence of two phases, prevents the oxide in the Fe layer from being identified as a specific crystallographic phase.

Similar conclusions are drawn for the (nominally) $[IrO_2(2)/Fe(2)]_{50}$ sample: there is a mixture of metal and oxide phases, both of them structurally disordered. However, the XANES and the EXAFS signals are found to be more similar to those of the γ–Fe_2O_3 reference, indicating a smaller amount of metallic Fe respect to the $[IrO_2(2)/Fe(5)]_{20}$ sample. Moreover, based on the comparisons of the FT in Fig. 7.6(c), the reduced intensity of the features respect to the $[IrO_2(2)/Fe(5)]_{20}$ sample indicates higher degree of disorder, as one could expect from the smaller thickness of the Fe–based layers.

By applying a linear combination fit to the XANES region (Fig. 7.6(e)), similar to that followed for the Ir L_3 edge, the greater percentage of metallic phase in the $[IrO_2(2)/Fe(5)]_{20}$ sample than in $[IrO_2(2)/Fe(2)]_{50}$ is confirmed (Table 7.2): around 60% of the Fe atoms are found to be in an oxide phase in the $[IrO_2(2)/Fe(5)]_{20}$ sample, and ~85% in the $[IrO_2(2)/Fe(2)]_{50}$ multilayer.

Therefore, it can be concluded that, in **O/M samples**, the resulting actual heterostructures are significantly different from the nominal (deposited) ones. In particular, the XAS spectra evidence strong oxygen diffusion from the Ir layers to the

Fe ones, rooted at the disparate affinity of Ir and Fe atoms for oxygen. The result is diverse oxide–metal structures depending on the Ir/Fe ratio. It should also be noted that the migration of oxygen from the IrO_2 layers to the Fe ones explains well the thicknesses observed in the TEM images. The Fe layers thickness in the O/M samples is relatively higher that in M/M samples due to oxygen atoms transferring to the Fe layers. Accordingly, the IrO_2 layers in O/M samples is thinner than in O/O.

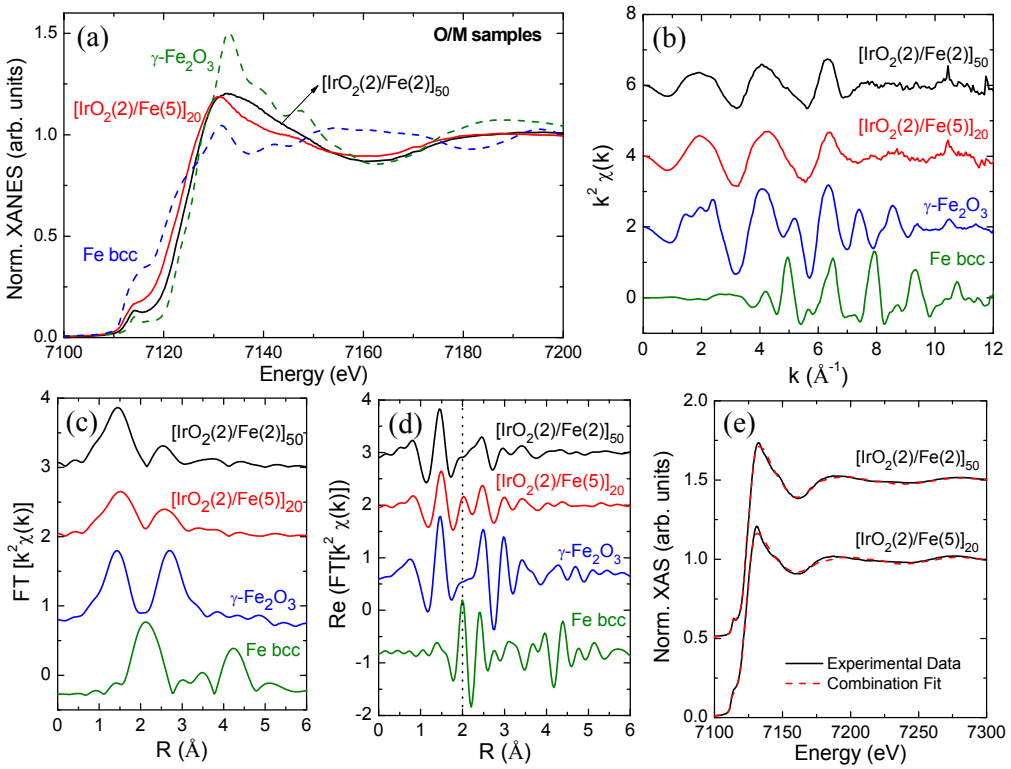

Figure 7.6 (a) Fe K–edge XANES spectra recorded on the $[IrO_2(2)/Fe(2)]_{50}$ and $[IrO_2(2)/Fe(5)]_{20}$ samples and comparted to bulk γ–Fe_2O_3 and Fe foil references. (b) EXAFS spectra recorded at the Fe K edge on the same samples from panel (a). In panels (c) and (d), the FTs (modulus and real part, respectively) of the k^2–weighted Fe K–edge EXAFS signal in the range from 3 $Å^{-1}$ to 10 $Å^{-1}$ are depicted. For the sake of a better comparison, the FT of the Fe foil has been multiplied by a factor of 0.3. The dotted line is a guide to the eye. It helps to identify the contribution of Fe metal phase in the mainly oxidized samples. Panel (e) shows the linear combination fit of the XAS spectra of these samples (fitting range -15 to 150 eV from E_0) using $[IrO_2(2)/FeOx(2)]_{50}$ and $[Ir(2)/Fe(2)]_{20}$ multilayers as references for pure oxide and metal phases, respectively.

For the sake of coherence Table 7.3 shows the notable agreement between the percentage for each element (Ir, Fe, and O) estimated form the combination of TEM (Table 7.1) and XANES (Table 7.2) data, and that obtained by RBS.

Table 7.3: Estimated atomic percentages of each component from XANES combination fittings and layer thickness from TEM microscopy compared with results from RBS.

Sample	Fe (%)		Ir (%)		O (%)	
	TEM & XANES	**RBS**	**TEM & XANES**	**RBS**	**TEM & XANES**	**RBS**
$[IrO_2(2)/Fe(2)]_{50}$	35	30	15	16	50	54
$[IrO_2(2)/Fe(5)]_{20}$	51	45	7	10	42	45

In Fig. 7.7(a) the XANES spectrum of a representative **O/O sample**, $[IrO_2(2)/FeOx(2)]_{50}$, is compared to bulk γ–Fe_2O_3 and Fe_3O_4 references. As the position of the threshold, E_0, is determined by the bond lengths, which in turn gives a hint on the oxidation state [122, 182, 315], this comparison has been used to estimate the Fe oxidation state to be 2.85+ in such multilayer. Besides, the poor structure of the XANES spectrum indicates a highly distorted local structure around Fe. Note that the XANES profile of this sample is less structured than that of the ferrihydrite (Fig. 7.7(b)), which is typically considered a structurally disordered iron oxide itself. In fact, the XANES spectrum resembles that found on very short range coordinated Fe–O arrangements, such as mesoporous aluminosilicates with a tiny 0.5 wt.% load of Fe or simple Fe^{3+} aqueous solutions [313, 316]. Further confirmation of the high structural disorder around Fe in the $[IrO_2(2)/FeOx(2)]_{50}$ sample is obtained from the barely perceivable second peak of the EXAFS FT represented in Fig. 7.7(d) (marked with an asterisk).

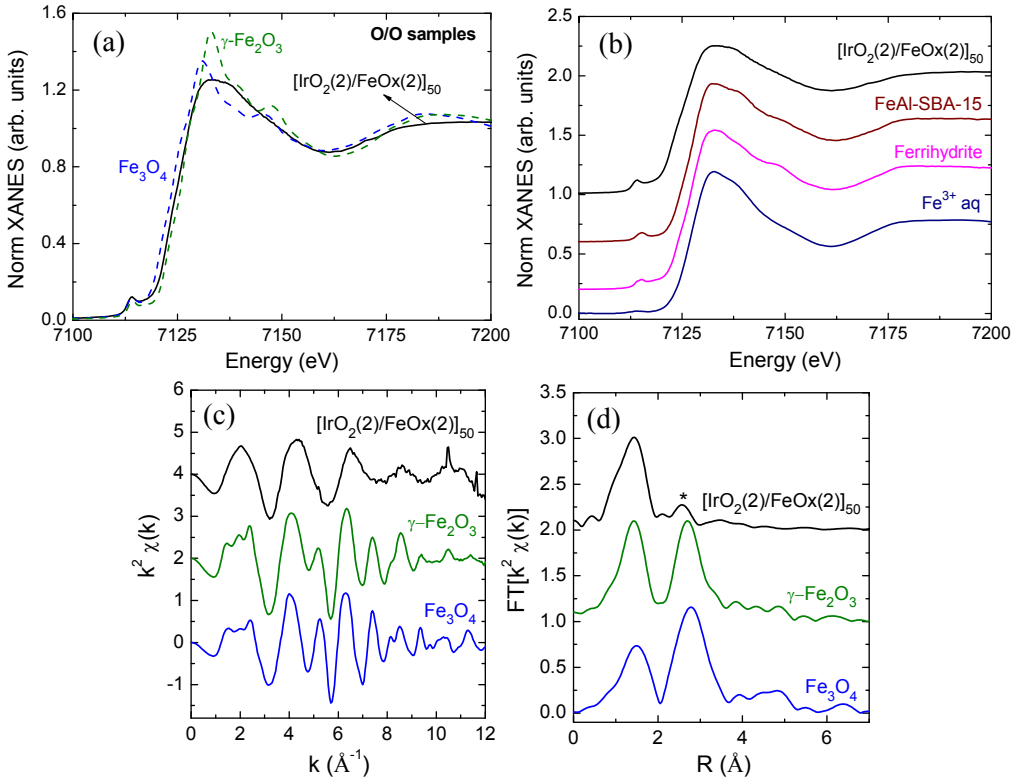

Figure 7.7 Fe K–edge XANES spectrum of the $[IrO_2(2)/FeOx(2)]_{50}$ sample and compared to (a) bulk γ–Fe_2O_3 and Fe_3O_4 references, and to (b) ferrihydrite, Fe–doped aluminosilicate and Fe^{3+} aqueous solution [313, 316]. (c) Comparison of the Fe K–edge EXAFS spectrum recorded on the $[IrO_2(2)/FeOx(2)]_{50}$ sample and bulk γ–Fe_2O_3 and Fe_3O_4 references. (d) FTs of the k^2–weighted EXAFS signal in the 3–10 $Å^{-1}$ range.

Finally, the normalized XAS spectrum recorded at the Fe K edge on the representative $[Ir(2)/Fe(2)]_{20}$ **M/M sample**, is shown in Fig. 7.8(a) along with bulk bcc Fe and γ–Fe_2O_3 references. It can be seen that the energy position of the threshold, E_0, is located at the same energy that bulk bcc Fe (~7112 eV), indicating that the Fe layers are fully metallic as expected. However, as shown in Fig. 7.8(b), the details of the profile, *i.e.*, position and width of the features, do not match the profile of bulk bcc Fe, bulk fcc Ni (universal fcc reference) nor fcc Fe nanoparticles references [296, 317]. Similarly, clear differences are observed between the EXAFS spectral profile of this sample and those of the references (Fig. 7.8(c)). More clearly, the FT of the EXAFS spectrum shows that at higher *R* values (4–5 Å range, no phase correction applied), the

intensity of the main peak is reduced relative to the bulk references, indicative of structural disorder (Fig. 7.8(d)). Moreover, at first sight the position and width of the first peak of the FT looks more similar to the fcc than to bcc references, whereas at higher *R* values the profile resembles more closely the bcc one. All this hampers a clear identification of the crystallographic structure.

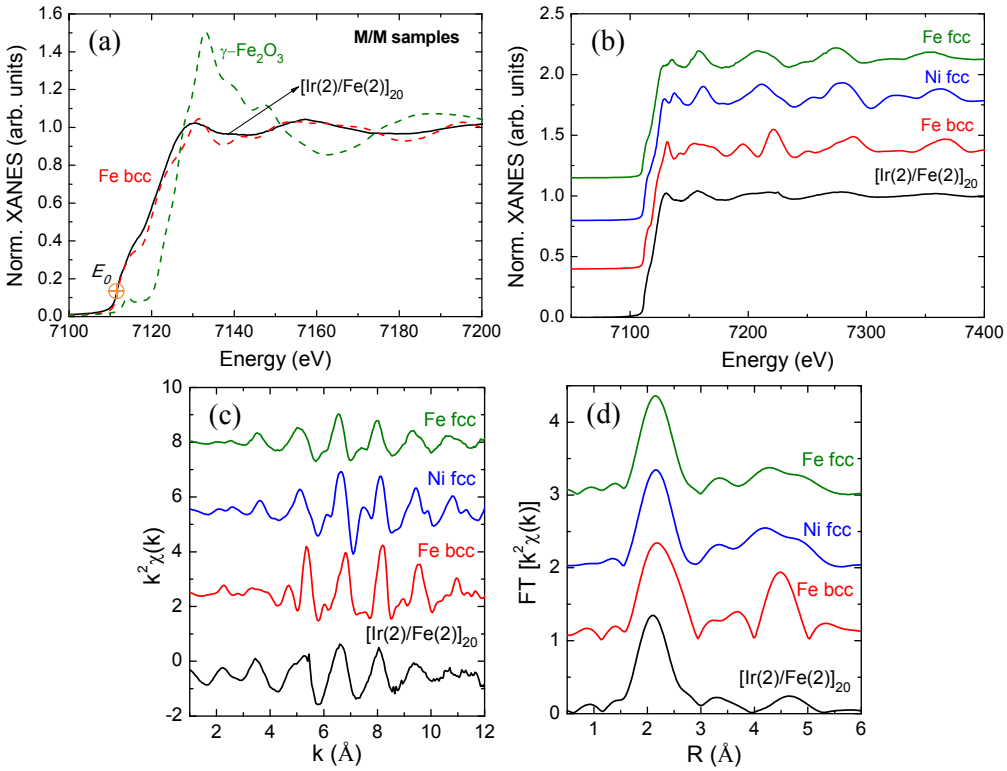

Figure 7.8 (a) Fe K–edge XAS spectrum recorded on $[Ir(2)/Fe(2)]_{20}$ sample at RT and compared to (a) bulk Fe and γ–Fe_2O_3 references and to (b) bulk Fe bcc, bulk fcc Ni and Fe fcc nanoparticles [296, 317]. (c) Fe K–edge EXAFS spectrum recorded on $[Ir(2)/Fe(2)]_{20}$ sample along with the same references from panel (b). In panel (d), the FTs of the k^2–weighted Fe K–edge EXAFS signals in the 3–10 $Å^{-1}$ range is represented. For the sake of a better comparison the references have been multiplied by a factor of 0.3.

Trying to elucidate whether the crystalline Fe phase is a disordered bcc or fcc phase, the EXAFS spectrum of the $[Ir(2)/Fe(2)]_{20}$ sample was fitted using the bcc and fcc crystal structures and the standard EXAFS formula (Eq. B.12). The results from the best fits are displayed in Fig. 7.9 and the corresponding parameters are given in

Table 7.4. As can be seen in the figure, the best fit is obtained when the bcc model is used. Moreover, the interatomic distances (R_j) are very similar to those found for a Fe foil. The only difference is the larger Debye–Waller factors indicating higher disorder. It is noted that a fit using the crystal bct structure [301–303] does not result in any improvement (not shown). Attempts to refine the EXAFS signal using the fcc model gave an unsatisfactory fit, as shown in Fig. 7.9(b). Notably, the values of R_j tend to be slightly smaller than those found for bulk Ni, while slightly larger values should be expected [317]. Therefore, the EXAFS analysis indicates that the Fe layer of the M/M sample can be accounted for in terms of a disordered bcc structure and discards the formation of disordered fcc or bct structures. This agrees well with the XANES simulations performed by Dr. J. Chaboy showing an optimal match with two coordination shells of a bcc structure [310].

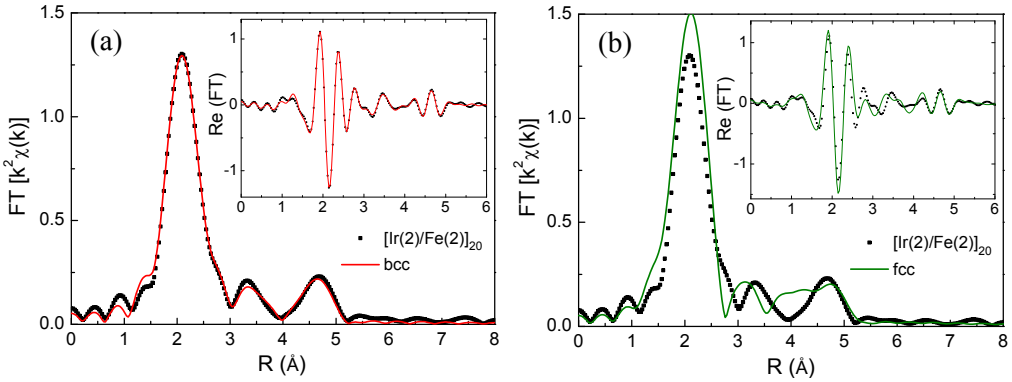

Figure 7.9 FT of the Fe K–edge EXAFS spectrum (k–range from 3.0 A^{-1} to 10.0 A^{-1}; k^2–weighted) recorded on the $[Ir(2)/Fe(2)]_{20}$ sample compared to the best fits obtained for (a) bcc and bct and for (b) fcc structures. The real part is shown in the corresponding insets.

Table 7.4 Values of the structural parameters obtained from the best fits: interatomic distances (R_j) and Debye–Waller factors (σ^2). The number of atoms at mean distances R_j around the absorbing atom (N_j) are fixed in the model (8, 6, 12, 14 and 8 for bcc, and 12, 6, 24 and 12 for fcc). To have good references for the analysis of the EXAFS spectra, the experimental data of well–crystallized Fe and Ni foils were also fitted.

Sample	**Fe foil**	**[Ir(2)/Fe(2)]$_{20}$**	**Ni foil**	**[Ir(2)/Fe(2)]$_{20}$**
Crystal structure	**Fe bcc**	**Fe bcc**	**Ni fcc**	**Fe fcc**
S_0^2	0.85	0.83	0.79	0.79*
ΔE_0	4.28	4.09	6.61	6.61*
R_1(Å)	2.46	2.51	2.49	2.51
R_2(Å)	2.84	2.85	3.49	3.41
R_3(Å)	4.04	4.07	4.33	4.27
R_4(Å)	4.69	4.38	5.01	5.01
R_5(Å)	4.98	4.97	–	–
R_6(Å)	–	–	–	–
R_7(Å)	–	–	–	–
σ_1^2(Å^2)	0.005	0.013	0.006	0.018
σ_2^2(Å^2)	0.005	0.020	0.008	0.023
σ_3^2(Å^2)	0.008	0.025	0.006	0.052
σ_4^2(Å^2)	0.007	0.041	0.006	0.024
σ_5^2(Å^2)	0.004	0.020	–	–
σ_6^2(Å^2)	–	–	–	–
σ_7^2(Å^2)	–	–	–	–

*Fixed value

7.4. Magnetic Characterization

7.4.1. SQUID Magnetometry

To analyze the magnetic response of these systems, Fig. 7.10 shows the temperature–dependent magnetization curves, M(T), for the O/M, O/O and M/M samples. Both zero–field–cooled (ZFC) and field–cooled (FC) data were collected at 100 Oe (left column) and 1000 Oe (right column). Similarly, Fig. 7.11 shows the field–dependent magnetization curves, M(H), recorded at 5 K (left column) and 300 K (right column).

The M(T) curves of the **O/M samples** (Figs. 7.10(a) and 7.10(b)) behave similarly irrespectively of the number of layers or their thickness. When decreasing the temperature, the ZFC and FC magnetization increases gradually up to a maximum value at T_P, (see Fig. 7.10(b)). On further decreasing the temperature, the magnetization decreases monotonically in both branches. Besides, a clear bifurcation between the ZFC and FC curves occurs at the irreversibility temperature, $T_{irr.}$. This behavior agrees well with a structural model consisting of magnetic clusters (metallic Fe phase) embedded in a non–magnetic matrix (Fe oxide phase). The maximum at T_p and the irreversibility between the ZFC and FC branches are indicative of magnetically frustrated interactions, *i.e.*, the system behaves as a cluster spin glass (or superspin glass) [318, 319]. Moreover, the decay in the FC magnetization for $T < T_p$ is probably reflecting some kind of reentrant cluster glass behavior. Supporting this hypothesis, it can be seen that the maximum magnetization (M_{max}) and T_P are higher for the $[IrO_2(2)/Fe(5)]_n$ samples than for $[IrO_2(2)/Fe(2)]_n$, indicating that the clusters formed in the $[IrO_2(2)/Fe(5)]_n$ films are greater. Finally, it should be noted that the differences observed between samples of the same nominal thickness can be explained by the small structural and compositional differences.

The M(H) curves of these samples show a diverse behavior (Figs. 7.11(a) and 7.11(b)). The values of M_{max} at 5 K range from 0.05 μ_B/at. Fe in the $[IrO_2(2)/Fe(2)]_{50}$ sample (~85% of Fe oxide according to XAS) up to 0.4 μ_B/at. Fe in $[IrO_2(2)/Fe(5)]_{10}$ (~60% of Fe oxide according to XAS). These data agree well with the structural model previously inferred from the behavior of the ZFC–FC M(T) curves. When the thickness of the Fe layer is 2 nm or less (as in $[IrO_2(2)/Fe(2)]_{50}$), the Fe layer is fully (or almost fully) oxidized, resulting in a linear M(H) response similar to that found in the O/O samples (shown below in Fig. 7.11(c)). Contrary, in the $[IrO_2(2)/Fe(5)]_{10}$ multilayer, with an actual Fe thickness of 5.8 nm according to TEM, the amount of oxygen is not enough to fully oxidize the Fe layers. A significant amount of Fe remains metallic and M_{max} at 5 K rises up to 0.4 μ_B/at. Fe. The other two samples show intermediate M(H) curves in agreement with the relative amount of metallic Fe. In addition, at low temperature these samples present high coercivity (H_C). The values of

H_C, in the 4–6 kOe range, are among the highest reported for Fe–based systems [286, 314, 320, 321]. Notwithstanding the high H_C, no exchange–bias is observed. As expected in a granular system, at RT the M(H) curves show the typical behavior of a superparamagnetic or cluster glass system.

Regarding the **O/O multilayers**, the magnetization values measured are very small ($M_{max} \leq 0.10$ μ_B/at. Fe) compared to those of the other families. The M(T) curves are almost flat (Figs. 7.10(c) and 7.10(d)), whereas a linear M(H) response is observed in all the samples (Figs. 7.11(c) and 7.11(d)). These results discard the formation of well–defined maghemite–like phases that should display hysteresis loops with a sizable magnetic moment. In contrast, this response indicates a paramagnetic–like behavior. However, taking into account that most of the disordered iron oxides, such as goethite or ferrihydrite, are antiferromagnets in the bulk form, and the antiferromagnetic nature of the superexchange interaction between Fe atoms in all the Fe oxides, the random formation of small regions with antiferromagnetic or frustrated behavior cannot be ruled out. Finally, the behavior of all the samples in this group is very similar, with only small differences that can be ascribed to the particular microstructural details of each sample.

The M(T) curves of the **M/M samples** measured at relatively low field (100 Oe, Fig. 7.10(e)) behave similarly irrespective of the number of layers or their thickness. A clear bifurcation between the ZFC and FC curves occurs at T_{irr}. Below this temperature, the FC magnetization remains almost constant, while the ZFC branch decreases as the temperature is decreased. The maximum irreversibility is observed in the sample with more relative Fe content, $[Ir(2)/Fe(5)]_{10}$. For higher measuring fields (1 kOe, in Fig. 7.10(f)) the irreversibility between the ZFC and FC curves disappears, and only a small reminiscence is observed in the $[Ir(2)/Fe(5)]_{10}$ sample.

As for the M(H) curves, all the samples show ferromagnetic–like M(H) loops with a significant magnetic moment (Figs. 7.11(e) and 7.11(f)). On closer examination, however, they present some features indicating a deviation from standard ferromagnetic behavior as the Fe layer thickness decreases. First, the M(H) curves for

the $[Ir(10)/Fe(10)]_{10}$ sample show a squared hysteresis loop with a very low H_C (125 Oe at 5 K and ≤ 20 Oe at 300 K) and a magnetic moment of 2.16 μ_B/at. Fe at 5 K, *i.e.*, very close to that of bulk Fe (2.20 μ_B/at. Fe). That means that a thickness of 6.7 nm (10 nm nominal) is enough to show a behavior similar to that found in bulk bcc Fe. As the thickness of the Fe layer decreases, the profile of the hysteresis loop at 5 K becomes less squared, the magnetic moment decreases down to 1.20 μ_B/at. Fe and H_C increases up to 700 Oe ($[Ir(2)/Fe(2)]_{20}$ sample). These results, together with the irreversibility found in the ZFC–FC curves measured at 100 Oe, indicate an evolution from a magnetically percolated system (*i.e.*, strongly interacting grains) for the $[Ir(10)/Fe(10)]_{10}$ sample towards a weakly interacting granular system when decreasing the Fe thickness [322]. The granular structure in these samples can be associated to better crystallized bcc magnetic regions (clusters) separated by more disordered regions (matrix) that inhibit the magnetic percolation.

Finally, note that, in both O/M and M/M sample series, we are dealing with similar clusters: magnetically–ordered Fe atoms embedded in an oxide (paramagnetic) matrix in the O/M case, or in a ferromagnetic matrix in the M/M samples. Hence, the different behavior observed in each series

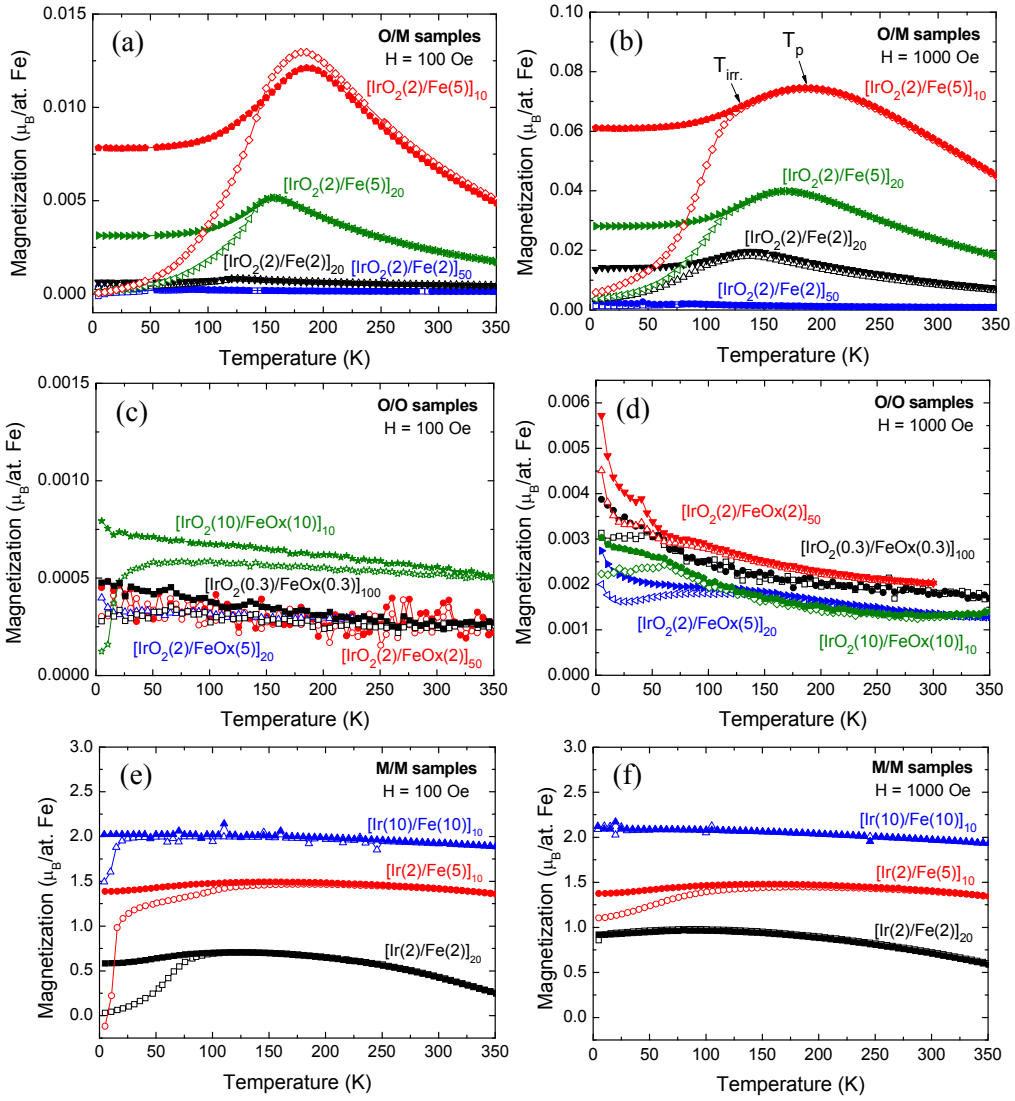

Figure 7.10 M(T) FC (solid symbols) and ZFC (open symbols) curves at H = 100 Oe (left column) and H = 1000 Oe (right column) for the O/M (panels (a) and (b)), O/O (panels (c) and (d)) and M/M samples (panels (e) and (f)). To normalize per Fe atom, the elemental thickness obtained by RBS (Table 7.1) has been used.

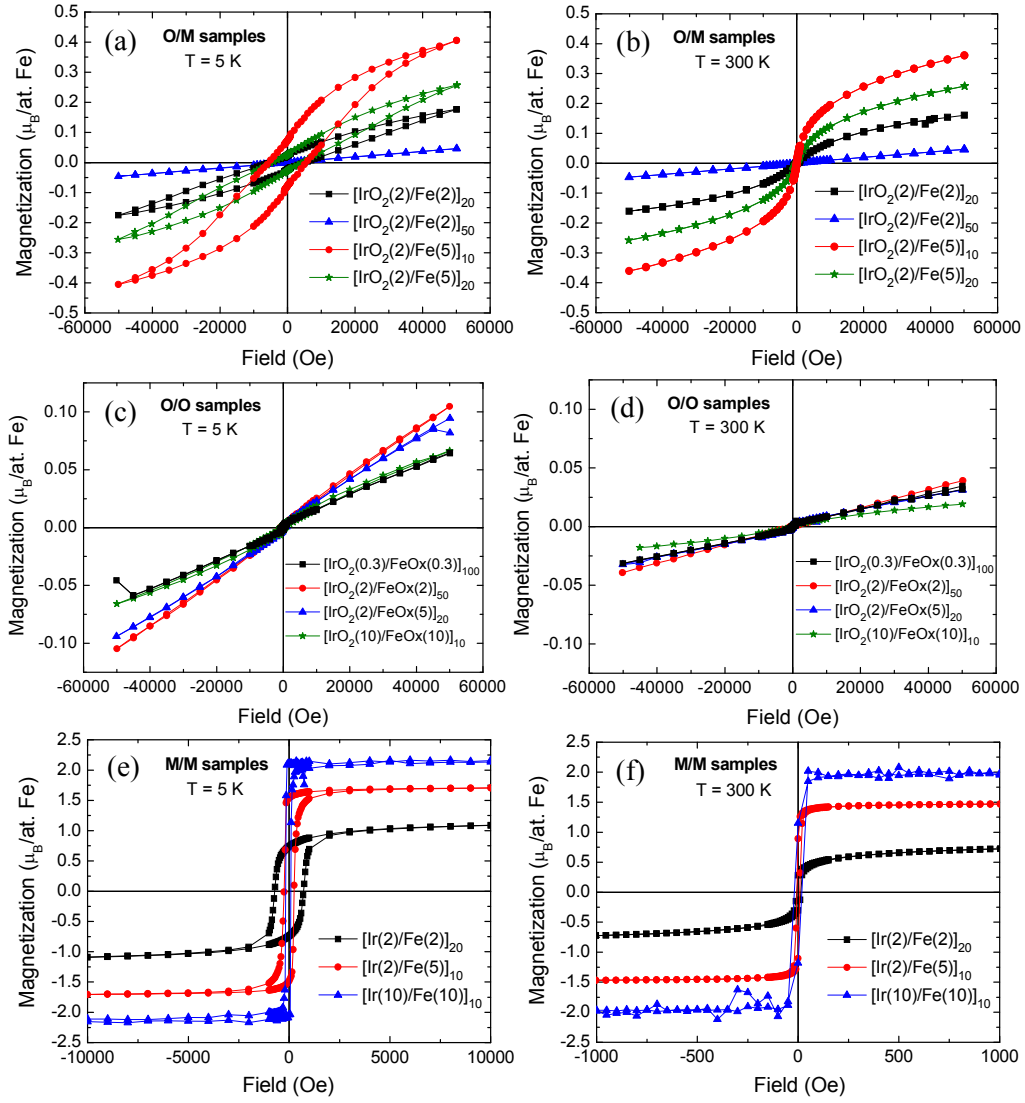

Figure 7.11 M(H) curves recorded at 5 K (left column) and 300 K (right column) on the O/M (panels (a) and (b)), O/O (panels (c) and (d)) and M/M samples (panels (e) and (f)). To normalize per Fe atom, the elemental thickness obtained by RBS (Table 7.1) has been used.

7.4.2. X–Ray Magnetic Circular Dichroism (XMCD)

Finally, to elucidate if there is any contribution of Ir to the magnetic response, XMCD measurements were recorded at the Ir $L_{2,3}$ edges at 10 K and under an applied magnetic field of 35 kOe in representative samples from each group.

As for the measurements performed in the **O/M series**, no XMCD signal (if any, is within the noise level, ~0.4%) is observed in the $[IrO_2(2)/Fe(2)]_{20}$ sample (Fig. 7.12(a)). Contrary, a small but clear XMCD signal is revealed in the $[IrO_2(2)/Fe(5)]_{10}$ multilayer (Fig. 7.12(b)). Such signal is of opposite sign at both absorption edges and resembles of those reported for Fe–Ir intermetallic compounds [323, 324]. Regarding the $[IrO_2(0.3)/FeOx(0.3)]_{100}$ sample from the **O/O group**, displayed in Fig. 7.12(c), no XMCD signal can be discerned (the relative high level of noise should be noted). Eventually, the $[Ir(2)/Fe(2)]_{20}$ sample from the **M/M group** (Fig. 7.12(d)) exhibits a similar XMCD signal, in shape and magnitude, to that observed in the $[IrO_2(2)/Fe(5)]_{10}$ sample.

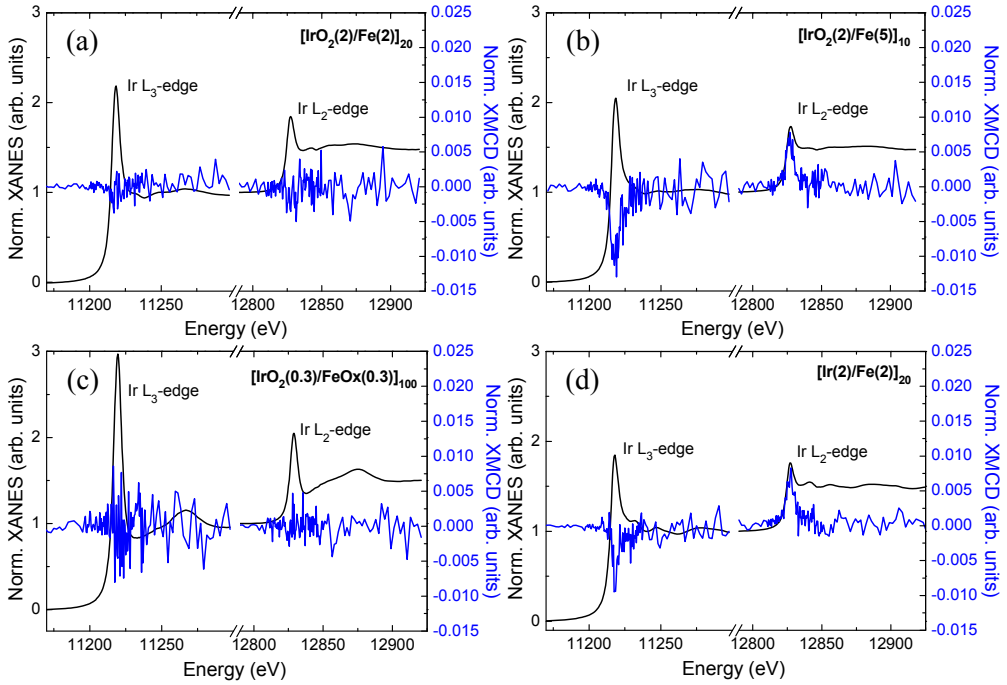

Figure 7.12 Normalized XAS and XMCD spectra recorded at the Ir $L_{2,3}$ edges at T = 10 K and H = 35 kOe on four representative samples: (a) $[IrO_2(2)/Fe(2)]_{20}$, (b) $[IrO_2(2)/Fe(5)]_{10}$, (c) $[IrO_2(0.3)/FeOx(0.3)]_{100}$ and (d) $[Ir(2)/Fe(2)]_{20}$.

Hence, from the similar XMCD signals observed in Ir–Fe intermetallics and in our $[Ir(2)/Fe(2)]_{20}$ and $[IrO_2(2)/Fe(5)]_{10}$ multilayers, it can be concluded that this XMCD signal corresponds to the magnetic moment induced in metallic Ir by metallic

Fe at the interfaces. Indeed, in the (nominally) $[IrO_2(2)/Fe(5)]_{10}$ sample, the Ir layer is almost fully metallic (~94% according to XAS combination fittings) and at least part of the metallic Fe clusters are located in the vicinity of the Ir layer. On the other hand, in the (nominally) $[IrO_2(2)/Fe(2)]_{20}$ sample, it is reasonable to assume that there is not metal/metal interfaces, since the amount of metallic Fe is very small (~17%) and the Ir layer is not fully metallic (~67%). Accordingly, the XMCD, if any, is much smaller and cannot be distinguished from the noise.

Sum rules gives $m_s \approx 0.019$ and $m_l = 0.004$ μ_B/at. Ir in the $[IrO_2(2)/Fe(5)]_{10}$ sample and $m_s \approx 0.015$ and $m_l = 0.000$ μ_B/at. Ir in the $[Ir(2)/Fe(2)]_{20}$ sample. The results derived from sum rule analysis [135, 136] indicate that the induced magnetic moment is ferromagnetically coupled to Fe and basically of spin nature. This is in agreement with the results observed in bulk intermetallics and with the calculations performed by *I. A. Campbell* [325]. However, the values of the magnetic moment are one order of magnitude smaller than those found by *V. V. Kristnamurthy et al.* in Ir–Fe alloys [323]. This can be explained by the fact that only Ir at the interfaces is expected to have a significant induced magnetic moment. Besides, it has been observed that the moment in the $[Ir(2)/Fe(2)]_{20}$ sample is reduced relative to the bulk value (Fig. 7.10(a)). This reduction of the Fe moment will, in turn, result in a smaller induced moment on Ir.

7.5. Effect of the Annealing Treatment

As shown in the previous sections, the as–grown **O/M samples** display a very small magnetic response whose behavior is associated to the migration of oxygen and the formation of Fe/FeOx core–shell heterostructures. The Ir layer does not seem to play any relevant role. In this case no annealing treatment is expected to revert the oxygen migration and result in an IrO_2–based structure with potential spintronic interest.

The as–grown **O/O samples** show no magnetic order. Since this is addressed to the mainly amorphous and paramagnetic nature of the FeOx layer, an annealing

treatment has been attempted trying to transform the FeOx layer in a magnetic phase (maghemite–like). In particular, two sequential treatments were followed: first, the sample was annealed for 1 hour at 300 ºC under a H_2 (2%) + Ar (98%) mixture atmosphere to promote the hematite–like to magnetite transition. Then, the sample was annealed for 6 hours at 300 ºC in air to get the maghemite phase. This procedure is based on those typically followed in nanoparticles to transform hematite into maghemite.

After annealing the $[IrO_2(2)/FeOx(2)]_{50}$ multilayer, the two weak XRD peaks observed in Fig. 7.13(a) indicate that the annealing treatment transforms IrO_2 into metal Ir. On the other hand, no information about the Fe phase can be inferred. As for the magnetic response, the M(H) curve of this annealed sample, represented in Fig. 7.13(c), shows that the application of a thermal treatment to convert the FeOx layer into γ–Fe_3O_2 or Fe_3O_4 results in a ferromagnetic behavior with a remarkable increase in the magnetization, up to ~0.3 μ_B/at. Fe and H_C = 550 Oe. This fact could indicate that, indeed, (some of) the FeOx has transformed into γ–Fe_3O_2 or Fe_3O_4. However, from these results the formation of metallic Fe centers cannot be ruled out.

Regarding the **M/M multilayers**, the low magnetic coercivity is the most striking result, especially when compared to the extremely high H_C, up to 63 kOe, observed in $L1_0$–ordered Pt/Fe films [326]. Although no diffraction peaks were detected in the XRD patterns (not shown), likely due to the smallness of the samples along with their polycrystalline character (observed by TEM), a multilayer structure with fcc–Ir and bcc–Fe layers separated by a clean interface has been identified. Trying to increase the coercivity of these samples, the $[Ir(2)/Fe(2)]_{10}$ multilayer was annealed during 4 hours at 500 ºC under a He flow to prevent it from oxidizing and under a magnetic field of 5 kOe applied in the in–plane direction.

As for the structural effects of the thermal treatment, no diffraction peaks were detected in the annealed $[Ir(2)/Fe(2)]_{10}$ sample (not shown), while the XRR curve shown in Fig. 7.13(b) reveals that the layered structure is practically lost likely due to intermixing between layers. As for the magnetic response, it can be seen in Fig.

7.13(d) that the thermal treatment in the M/M sample leads to a magnetization reduction and a small increase of the coercivity up to 1.5 kOe (much smaller than that found on Fe/Pt films). This can be associated to the fact the Fe and Ir may only form a disordered fcc (A1) or disordered hcp (A3) phase [327], in contrast to the ordered $L1_0$ phase in Fe/Pt multilayers.

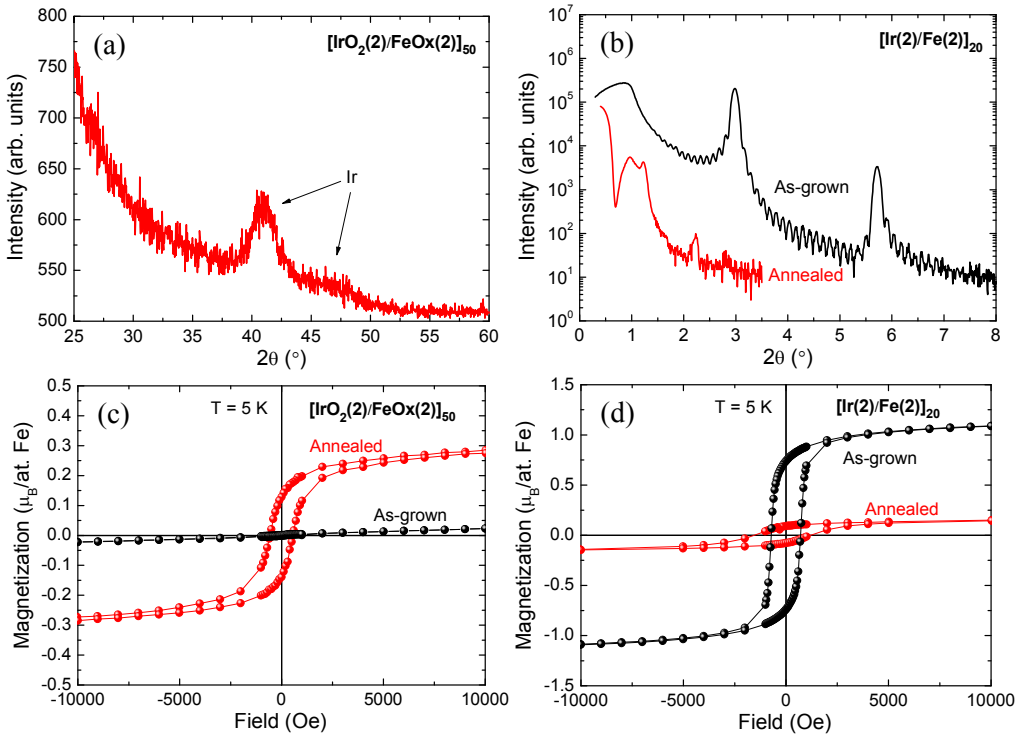

Figure 7.13 (a) XRD measurement on $[IrO_2(2)/FeOx(2)]_{50}$ after being annealed. (b) XRR measurement recorded on $[Ir(2)/Fe(2)]_{20}$ sample before and after the annealing treatment. Panels (c) and (d) show the M(H) curves recorded on $[IrO_2(2)/FeOx(2)]_{50}$ and $[Ir(2)/Fe(2)]_{20}$ samples before and after the annealing treatment.

7.6. Conclusions

Nominal IrO_2/Fe (**O/M**), IrO_2/FeOx (**O/O**) and Ir/Fe (**M/M**) multilayers have been prepared by magnetron sputtering. Clear layered structures are distinguished by XRR and TEM for layer thicknesses greater than 1 nm. Both, the structure and the

magnetic response of the samples are found to be highly dependent on the preparation method conditions.

As for the **O/M samples**, the resulting heterostructures are significantly different from the nominal ones. The different affinity of Ir and Fe for oxygen is able to displace the oxygen from the Ir–based layers and form diverse metal–oxide structures depending on the Ir/Fe ratio. For the thinnest Fe layers (2 nm), the oxygen initially in the Ir layers is enough to (almost) fully oxidize the Fe layers. At the same time, a biphasic metal–oxide structure is formed in the Ir layers. On the other hand, for thicker Fe layers (5 nm) there is not enough oxygen in the Ir–based layers to fully oxidize the Fe ones. In this case the initial IrO_2 layers become purely metallic.

The magnetic characterization of these samples indicate the presence of metallic magnetic Fe clusters embedded in a mainly paramagnetic FeOx matrix, giving rise to a cluster spin glass behavior. The size of these clusters and their magnetic response (M_{max} and H_C) depend on the initial thickness ratios of the IrO_2 and Fe layers. A large coercivity up to ~6 kOe and a negligible exchange bias is found in these samples. On the other hand, the XMCD experiments point to a purely induced Ir moment associated to the presence of metallic–Ir/metallic–Fe interfaces. The formation of complex metal–oxide structures at the Fe layer might be hampering a more relevant role of Ir.

Regarding the **O/O samples**, the Ir phase is identified as IrO_2 and the Fe–based layer is found to be a highly disordered oxide phase with an oxidation state close to Fe^{3+}.

The magnetization measurements undoubtedly discard the formation of a ferro– or ferrimagnetic phase and indicate a paramagnetic behavior, which seems in accordance with an ill–defined iron oxide phase.

Standard thermal treatments to convert hematite into maghemite cause also the reduction of IrO_2 to Ir metal. Therefore, annealing is not a good way for the

fabrication of IrO_2/Fe_3O_4 or IrO_2/γ–Fe_3O_2 samples. Given their vast potential for spintronics, alternative routes should be explored.

Finally, in the as–grown **M/M samples**, the XANES and EXAFS experiments allowed identifying the Ir and Fe phases as fcc and bcc structures, respectively.

The magnetic response is that expected for a Fe percolated system when the thickness of the Fe layer is ~7 nm. The thickness decrease results in a granular cluster glass–like behavior and in a slight increase of the coercivity at 5 K. In this case, the clusters can be associated to better–defined ferromagnetic bcc regions dispersed in crystallographically disordered regions (acting as a matrix between the clusters). The XMCD measurements prove the presence of induced Ir magnetic moments at the interface ferromagnetically aligned to Fe and mainly of spin nature. Nevertheless, the contribution of Ir to the total magnetization is found to be negligible and the proposed increase of H_C is not observed.

Attempts to increase the coercivity by thermal treatments were also unsuccessful, likely due to the formation of a disordered fcc (A1) or disordered hcp (A3) phase, in contrast to the ordered $L1_0$ phase in Fe/Pt multilayers.

Concluding Remarks and Outlook

This thesis was focused on the study of IrO_2 motivated by the interesting predictions suggesting tunable physical properties added to its enormous potential for spintronic applications. In particular, this dissertation had the general goal aimed at finding experimental evidence of the predicted tunable electrical transport and magnetic properties of IrO_2–based systems. For this purpose to be achieved, three different approaches were followed: (1) growing IrO_2 thin films with relevant structural differences as far as thickness (dimensionality), crystallinity and lattice parameters (substrate–induced strain) are concerned; (2) applying a negative chemical pressure via substitutional doping; and (3) combining IrO_2 with magnetic 3*d* elements.

The diverse set–up operations and implementations carried out in our recently mounted sputtering chamber allowed optimizing the performance of the equipment. A subsequent comprehensive and systematic work carried out to optimize the film growth allowed depositing samples of disparate structure in a controlled manner by means of this technique. In combination with high O_2 pressure sputtering and pulsed laser deposition techniques, IrO_2 films with relevant differences in their thickness (from ~100 to ~1.5 nm), crystallinity (from amorphous to epitaxial), growing orientation ((001)–, (100)– and (110)–oriented); and strain (from -5 to +5%, approximately) were successfully synthesized. Moreover, the co–sputtering configuration of our chamber was used to grow novel $Ir_{1-x}A_xO_2$ compounds, with A = Sn, Cr.

1st Approach: Structure of IrO_2 Thin Films

The spin–orbit coupling (SOC) in all the IrO_2 thin films is found to be very large and robust, being mainly independent on structural details. A small, but reproducible increment of the SOC is observed in the amorphous (~10%) and finest (~1–10%) samples. Similarly, within the epitaxial films the SOC is slightly reduced when probed along the [001] direction (~10–15%).

Upon reducing the IrO_2 film thickness, the electrical response evolves from the metallic ground state ($t \geq 5$ nm) to a strongly localized behavior (in the 1.5–2.0 nm range), so that a clear **thickness–dependent metal–insulator transition (MIT)** is revealed. The analysis of the resistivity curves indicates a gap opening and the relevant role of effective correlations. Modification of the lattice parameters or the degree of crystallinity does not yield to any significant variation of the electrical transport response, which remains within the same order of magnitude.

The initial measurements suggest antiferromagnetic ordering of the Ir^{4+} cations at low temperature in the finest samples. The ordering transition seems to occur at the same temperature at which the resistivity shows a strong increase. Hence, the insulating IrO_2 is likely to be located in an intermediate region between a Slater– and a Mott–type insulator.

2nd Approach: Negative Chemical Pressure

Sn–doped IrO_2 thin films, $Ir_{1-x}Sn_xO_2$ (x = 0.1–0.5), of ~100 nm were grown by reactive magnetron co–sputtering for the first time.

A nearly constant or even slightly enhanced SOC is observed in these compounds.

The electrical response is strongly dependent on the Sn content, changing the metallic ground state of IrO_2 to semiconducting–like for the highest Sn–doped samples. By changing the Sn concentration **the electrical resistivity can be tuned in a range of several orders of magnitude**.

The two main factors involved in the spin–current detection process are thus optimized for Sn–doped IrO_2: high SOC and increased electrical resistivity; pointing to a **new direction in the quest of optimized materials for spin–current detection**.

The preliminary measurements also point out the presence of certain magnetic ordering of the Ir^{4+} cations in the most resistive samples.

3rd Approach: IrO_2 Combined with Magnetic 3d Elements

Cr–doped IrO_2 thin films, $Ir_{1-x}Cr_xO_2$ (x = 0.1–0.8), of ~100 nm and nominal IrO_2/Fe and IrO_2/FeOx multilayers were synthesized by magnetron sputtering.

As for the novel $Ir_{1-x}Cr_xO_2$ samples, the experiments reveal a very strong 5*d* SOC and confirm the oxidation state of both, Ir and Cr, to be 4+, thus providing a new route to grow the thermally unstable CrO_2 structure.

In contrast to the metallic ground state of IrO_2 and CrO_2, the electrical characterization of the $Ir_{1-x}Cr_xO_2$ samples reveals a clear upturn in the resistivity. This upturn appears at increasing temperatures for greater values of x, up to the point where a **semiconductor–like response** is observed for x = 0.8. Disorder seems to be at the origin of this MIT.

By changing the Cr content, both the **magnetization and the coercive field can be widely tuned**, reaching both its maximum in the x = 0.6–0.7 range. Giant coercive fields (greater than 40 kOe) are revealed in these dilutions.

In these samples, **Ir has a clear sizable magnetic moment**, m = 0.10 μ_B/at. Ir. Surprisingly enough for a Ir^{4+}–iridate, the orbital contribution to the magnetic moment is negligible. In addition, our data so far suggest that this magnetic moment is related to the presence of Cr^{4+} ions (*i.e.*, Cr–induced). The magnetic measurements also reveal a complex magnetic structure, where the net magnetic moment of Cr is antiferromagnetically coupled to the net magnetic moment of Ir.

Regarding the nominal IrO_2/Fe multilayers, the different affinity of Ir and Fe for oxygen results in actual heterostructures where the oxygen is displaced and form diverse metal–oxide structures depending on the Ir/Fe ratio. Magnetically, the resulting system can be seen as metallic magnetic Fe clusters embedded in a mainly paramagnetic FeOx matrix, giving rise to a cluster spin glass behavior. Large coercivity up to ~6 kOe is found in these samples. The lack of clear IrO_2/Fe interfaces hinders studying the effect of a neighbor magnetic layer on IrO_2.

With respect to the IrO_2/FeOx samples, the as–grown Fe–based layers consist of highly disordered and non–magnetic oxide phase. Application of conventional thermal treatments to convert FeOx into Fe_3O_4/γ–Fe_3O_2 causes also the reduction of IrO_2 to Ir metal. As a result, no IrO_2/Fe_3O_4 (IrO_2/γ–Fe_3O_2) interfaces are obtained to study of the effect of a neighbor magnetic layer on IrO_2.

Outlook

This dissertation has provided a deep insight into the actual experimental conditions that make it possible to tune the electrical and magnetic response of IrO_2–based systems. The **pioneering experimental observation of metal–insulator and nonmagnetic–magnetic transitions in this iridate** leads to several opened questions and opens the door to future research.

While our results on IrO_2 and $Ir_{1-x}Sn_xO_2$ films suggest the combined role of correlations and magnetism to be at the origin of the MITs (Mott *vs*. Slater), further work is desirable to confirm our results and provide a deeper knowledge about the underlying mechanisms triggering such MITs. In this sense, it is important to recall that this open question concerns not only IrO_2, but iridates in general. A systematic study based on magnetotransport properties near the MIT and further XMCD experiments could be of help.

As for the $Ir_{1-x}Cr_xO_2$ system, our pioneer research has shown exciting properties and revealed a promising scenario. To better understand the origin of such a giant coercive field, it would be desirable to synthesize better crystallized (and even epitaxial) films. HR–TEM and EXAFS measurements would provide a deeper knowledge about the growth of these compounds. XMCD experiments carried out in several samples of the series could provide the information necessary to understand the complex magnetic response observed in this system. Similarly, the puzzling nature of the magnetic moment of Ir in these films deserves further consideration. Provided the hypothesis of a Cr–induced magnetism is confirmed, it would open the door to a new route for engineering the magnetic properties of oxides, thus contributing to

future applications. In this sense, theoretical calculations added to the experiments mentioned above could give a boost to this hypothesis.

Finally, given their vast potential in spintronics, alternative routes to synthesize IrO_2/Fe_3O_4 or $IrO_2/\gamma–Fe_3O_2$ structures should be explored.

Appendices

Appendix A

Sputtering Implementations

This appendix contains further information to that provided in Chapter 2 about the implementation of certain components carried out in our sputtering chamber which could be of help to other groups looking into a similar project.

A.1. RF Source

Regarding the RF–source installation, to control the input parameters from the front panel (Front Panel Operation mode) a contact closure between pins 2 and 15 (external interlock) in the corresponding 25–pin "D" sub–miniature connector must be made before the RF output can be enabled. This fact is mentioned because usually it is not a straightforward information which can be extracted from the user manual. Similarly, to install the sensor located in the refrigeration system (*poka–yoke* mechanism which allows operating the source only when water flows through the tubes towards the magnetrons) it was also necessary to make a contact closure between pins 1 and 14 (in the same connector mentioned above), which control the status of the power supply.

It is also important to note that, in order to initialize the discharge, the gas pressure must be considerably increased (e.g., increasing the Ar flux, in our case up to 80 ml/min). Once the plasma is stable, the gas pressure can be set to that desired.

A.2. Substrate Heater

A substrate heating system, exposed in Fig. A.1, was implemented to grow samples at temperatures up to 950 ºC. A 2"–diameter SU–200–HH substrate heater (1)

from *Meivac* is placed over an additional designed arm (2) which allows the heater to move from one position to another. The designed arm drawn with AutoCAD is shown in Fig. A.2. A cylindrical–shape counterweight (3) of ~380 g (approximately the heater mass) is placed at the other end of the arm to prevent the motor axis from bending. The substrate temperature is measured by means of a K–type thermocouple (4) embedded in the substrate holder beneath the substrate mounting area. Temperature programs with heating and cooling ramps can be set up with a homemade temperature controller directly connected to the heater. A 220/40 V transformer was installed to avoid arcing in the electrical contacts inside the chamber during the process. The power cables are protected with ceramic (alumina) beads (5) and rolled up around the motor axis in order not to hinder the arms movement. Before installation, the heater had to be operated in air at 700 ºC for an hour in order to produce an oxide passivation layer on the surface, thus preventing any contamination of the process.

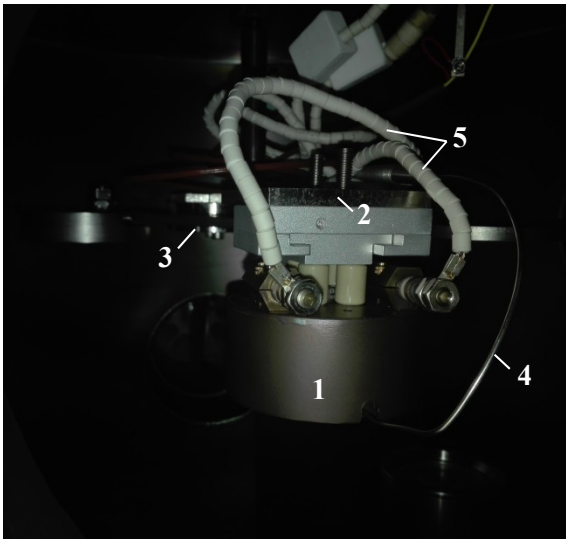

Figure A.1 Photograph of the substrate heating system implemented in our sputtering chamber.

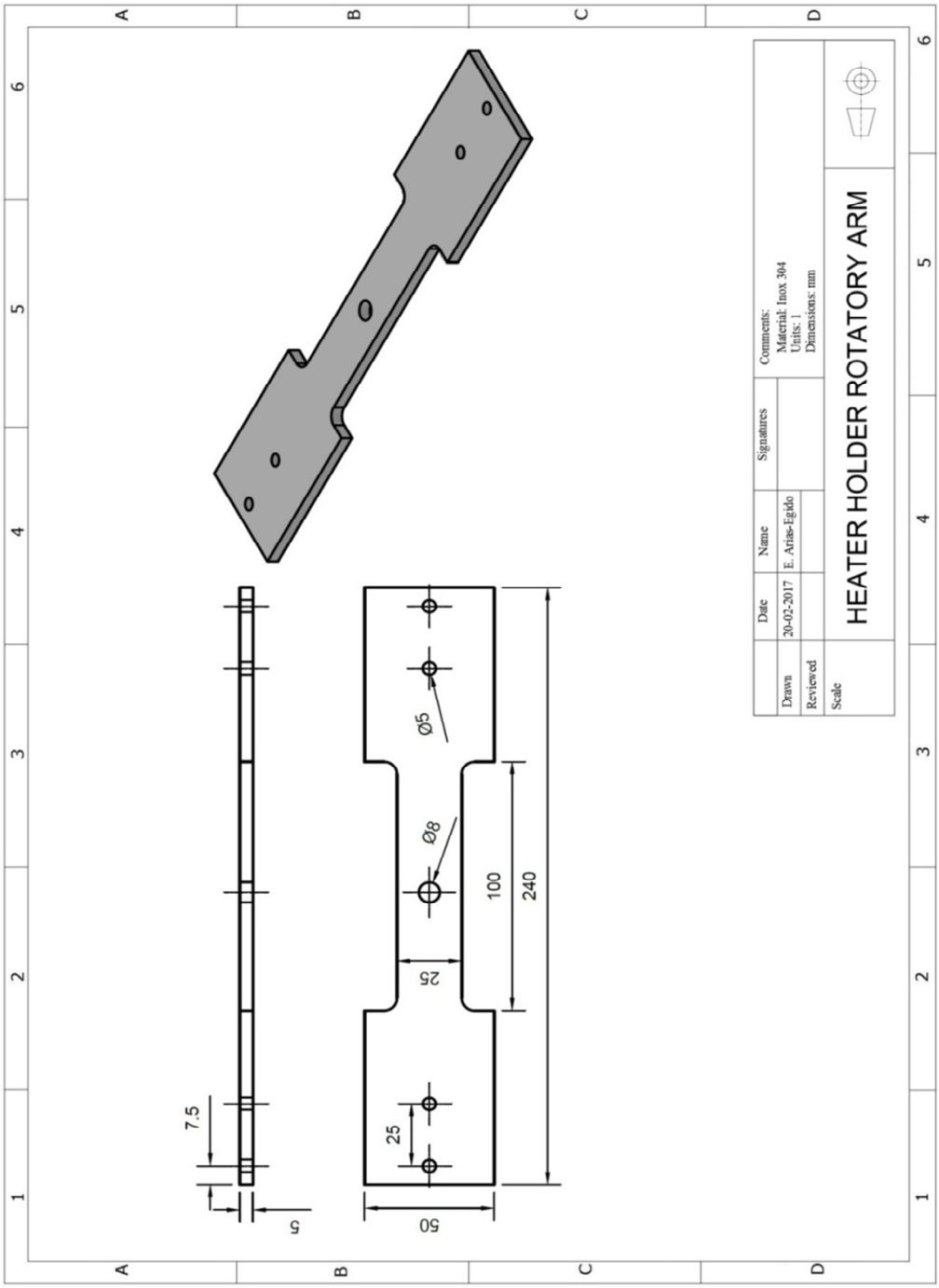

Figure A.2 Heater holder rotatory arm design.

Appendix B

Basic Concepts

This appendix provides complementary information about basic concepts of the characterization techniques employed in this thesis.

B.1. X–Ray Diffraction (XRD)

X–rays are electromagnetic waves with a wavelength (0.1–10 nm range) in the order of magnitude of interatomic distances in crystalline materials. Because of this, and thanks to its periodic structure, crystals elastically scatter the X–ray beams in certain directions and amplify them by constructive interference. The outcome is a **diffraction pattern** whose interference condition, schematized in Fig. B.1(a), is given by the Bragg's law [328]:

$$n\lambda = 2d_{hkl}\, sin\theta \tag{B.1}$$

where n is the order of a reflection, λ the wavelength of the X–ray source, d_{hkl} the distance between parallel planes of the network, and θ the angle between the incident beam and the plane of the crystal. The diffraction pattern contains information about the atomic arrangement within the crystal. For a polycrystalline sample, as that shown in Fig. B.1(b), each diffraction peak is attributed to the scattering from a specific set of parallel planes of atoms, identified by the Miller indices (*hkl*). Similarly, amorphous solids, which do not have long–range atomic order, will not produce a diffraction pattern but only broad scattering features; and single crystals only produce peaks from a family of planes.

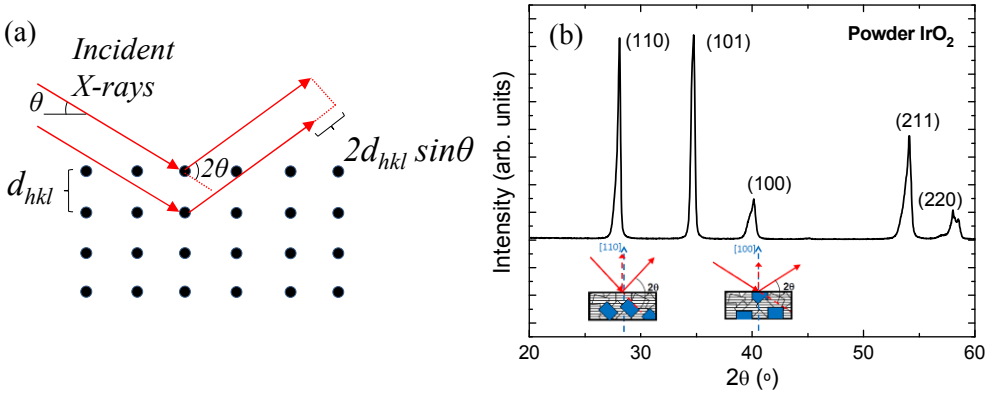

Figure B.1 (a) Bragg's law description and (b) XRD pattern example from a powder IrO_2.

The height, width and position of these reflections generated by the emerging X–ray beam can be used to determine many aspects of the material's structure:

The relative intensity of the peaks provides information about directions of **preferred orientation**. While the absolute intensity can vary due to instrumental and experimental parameters, the relative intensities of the diffraction peaks are instrument–independent [329]. Peaks with relative intensities greater than those standards (*i.e.*, those obtained for a given sample with randomly oriented crystallites) indicate that a preferred orientation is present in the material. A texture coefficient, *TC*(*hkl*), is calculated using the Harris analysis shown in Eq. B.2, where a *TC*(*hkl*) > 1 indicates a preferential orientation/texture [330].

$$TC(hkl) = \frac{I(hkl)/I_0(hkl)}{1/N \sum_{i=1}^{N} I(hkl)/I_0(hkl)} \tag{B.2}$$

where *I(hkl)* and $I_0(hkl)$ state for the measured and standard integrated intensity of the *(hkl)* reflection, respectively; and *N* is the number of reflections observed.

The full width half maximum (FWHM) of the diffraction peaks is directly related to the **crystallite size** through the Scherrer equation [107]:

$$GS = \frac{K\lambda}{B(2\theta)cos\theta} \tag{B.3}$$

where *GS* is the mean grain size in the direction perpendicular to a given plane, λ is the wavelength of the X–ray source, *B* is the FWHM of the specific peak (in radians), θ is the Bragg angle of such peak and *K* is the Scherrer constant (0.94). However, peak broadening may also be indicative of more stacking faults (microstrain and/or other defects in the crystal structure) or an inhomogeneous composition in a solid solution or alloy. Besides, different instrument configurations can change the peak width. In consequence, a careful evaluation is required to separate all the different potential causes of peak broadening.

The **unit cell dimensions** (lattice parameters) can be correlated to the position of diffraction peaks. Anything that changes the unit cell dimensions (temperature, substitutional doping, strain, etc.) will be translated into a peak shift. In the tetragonal structure of IrO_2, where $a = b \neq c$ and $\alpha = \beta = \gamma = 90^{o}$, next expression applies:

$$\frac{1}{d_{hkl}^2} = \left[h^2 + k^2 + l^2\left(\frac{a}{c}\right)^2\right]\frac{1}{a^2} \tag{B.4}$$

where *hkl* are the Miller indices and the *d*–values (interplanar spacing) are calculated with Eq. B.1.

B.1.1.1. Rietveld Analyses

Peak–overlapping, displacement error, significant background difficult to define or preferred orientations, among other things, usually hinder a straightforward analysis of the diffractograms. The Rietveld method is a refinement technique which has the ability to accurately determine structural parameters of the sample from the construction of a theoretical model that fits the experimental pattern by the least squares method [104].

Most of the diffraction patterns measured in this dissertation have been analyzed with the Rietveld method using the FullProf code [103]. As a representative example, the analysis carried out in a diffractogram measured on an IrO_2 film is given in Fig. B.2. Here, values of χ^2 between 1–2 are obtained, indicative of good fits.

According to the Rietveld analysis the lattice parameters are: $a = b = 4.493$ Å and $c = 3.145$ Å; while when using Eq. B.4 the calculated parameters are: $a = b = 4.488$ Å and $c = 3.141$ Å; which is < 0.2% difference. On the other hand, in the FullProf code the preferred orientation can be quantified by means of the *Pref.* parameter. A *Pref.* ≠ 1 means that the sample has grown with a preferred orientation. If the *Pref.* parameter is < 1, it indicates a platy habit, and if it is > 1, a needle–like habit [105, 106]. In the sample from Fig. B.2, *Pref.* = 0.97, which is consistent with the TC ≈ 1 (non–textured) obtained when using equation B.2 for all the reflections observed (the standard intensities have been obtained from the powder IrO_2 diffractogram in Fig. B.1(b)). In addition, the refinements allow discerning the presence of a small amount of metallic Ir (< 1%), which otherwise would easily go unnoticed.

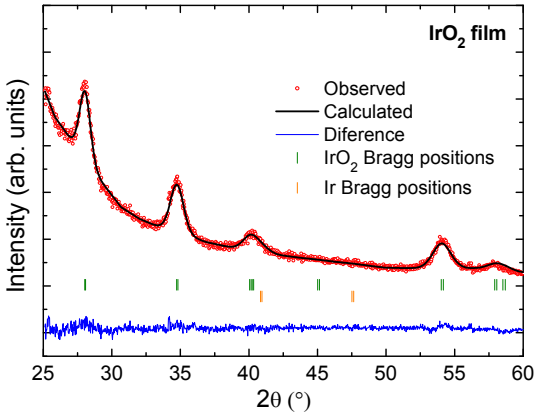

Figure B.2 XRD pattern measured in an IrO_2 film and Rietveld analysis using the FullProf code [103]. Red dots correspond to the experimental data and the black solid line is the calculated pattern. The difference between them is represented by a blue line. Small vertical green and orange lines mark the Bragg positions of IrO_2 and Ir phases, respectively.

B.1.1.2. Reciprocal Space Mapping

Reciprocal space maps are commonly used to study and determine structural properties of epitaxial thin films, such as lattice parameters or structural quality [108]. In real space the crystal unit cell can be defined by three basis vectors: $\boldsymbol{a_1}$, $\boldsymbol{a_2}$ and $\boldsymbol{a_3}$; so that any lattice point can be described by a vector that is a linear combination of them:

$\boldsymbol{R_n} = n_1\boldsymbol{a_1} + n_2\boldsymbol{a_2} + n_3\boldsymbol{a_3}$, where n_1, n_2 and n_3 are integers. The reciprocal space (also known as Fourier space) is defined by a set of basis vectors $\boldsymbol{a_1}^*$, $\boldsymbol{a_2}^*$ and $\boldsymbol{a_3}^*$, with:

$$\boldsymbol{a_1^*} = \boldsymbol{2\pi}\frac{\boldsymbol{a_2}\times\boldsymbol{a_3}}{\boldsymbol{a_1}\cdot\boldsymbol{a_2}\times\boldsymbol{a_3}} \quad \boldsymbol{a_2^*} = \boldsymbol{2\pi}\frac{\boldsymbol{a_3}\times\boldsymbol{a_1}}{\boldsymbol{a_1}\cdot\boldsymbol{a_2}\times\boldsymbol{a_3}} \quad \boldsymbol{a_3^*} = \boldsymbol{2\pi}\frac{\boldsymbol{a_1}\times\boldsymbol{a_2}}{\boldsymbol{a_1}\cdot\boldsymbol{a_2}\times\boldsymbol{a_3}} \tag{B.5}$$

In terms of a crystallographic plane (*hkl*) in real space, the reciprocal space vector is defined as $\boldsymbol{\sigma_{hkl}} = h\boldsymbol{a}^* + k\boldsymbol{b}^* + l\boldsymbol{c}^*$. It is easy to prove that this vector is perpendicular to the (*hkl*) plane and of magnitude the inverse of the inter–planar distance d_{hkl}, *i.e.*, $|\boldsymbol{\sigma_{hkl}}| = 1/d_{hkl}$ [108]. Therefore, when *a, b* and *c* are orthogonal, as in a tetragonal crystalline structure of IrO_2, from Eq. B.4 next expression is fulfilled:

$$|\boldsymbol{\sigma_{hkl}}| = \sqrt{\frac{h^2}{a^2} + \frac{k^2}{b^2} + \frac{l^2}{c^2}} \tag{B.6}$$

The determination of $\boldsymbol{\sigma_{hkl}}$ is carried out by the so–called reciprocal space maps, which consists of 2θ–ω scans for different values of ω, being 2θ the angle between the incident beam and the detector (detector angle), and ω the angle between the X–ray source and the sample (incident angle), as illustrated in Fig. B.3(a). In order to determine the in–plane and the out–of–plane parameters, it is useful to define $\boldsymbol{\sigma_{//}}$ and $\boldsymbol{\sigma_{\perp}}$ as the parallel and perpendicular components of the $\boldsymbol{\sigma_{hkl}}$ vector to the sample surface, respectively. Considering *a* and *b* the in–plane and *c* the out–of–plane lattice parameters in an orthogonal base, then from Eq. B.6:

$$\boldsymbol{\sigma}_{//} = \sqrt{\frac{h^2}{a^2} + \frac{k^2}{b^2}} \qquad \boldsymbol{\sigma}_{\perp} = \frac{l}{c} \tag{B.7}$$

A (*h0l*)–type reflection tends to be used here to have Eq. B.7 simplified in the form:

$$\boldsymbol{\sigma}_{//} = \frac{h}{a} \qquad \boldsymbol{\sigma}_{\perp} = \frac{l}{c} \tag{B.8}$$

Therefore, the RSMs allow the determination of $\boldsymbol{\sigma_{//}}$ and $\boldsymbol{\sigma_{\perp}}$ of the Bragg spots ($\boldsymbol{\sigma_{substrate}}$ and $\boldsymbol{\sigma_{film}}$ in Fig. B.3(b)) and hence, to determine the in–plane and the out–of–

plane lattice parameters of the film and the substrate as in Fig. B.3(b). That is why this technique is widely used in the characterization of epitaxially grown films.

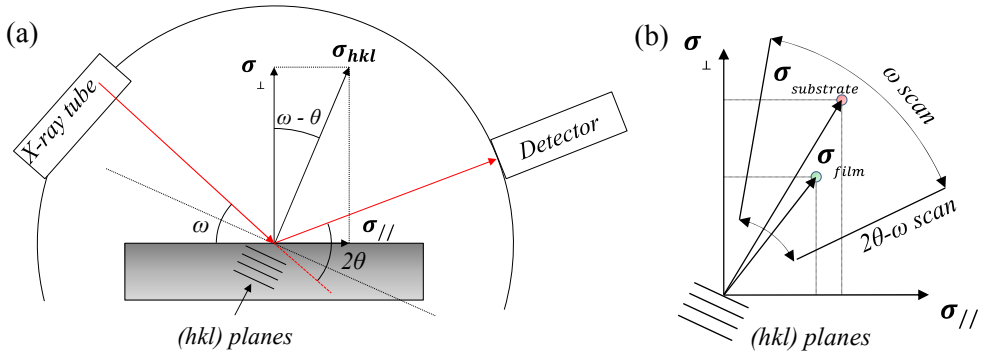

Figure B.3 (a) Reciprocal space vector σ_{hkl} and relations with θ and ω angles. (b) Schematic description of a RSM measurement.

B.2. X–Ray Reflectivity (XRR)

X–ray reflectivity (XRR) is a non–destructive and non–contact technique for thickness determination in the 2–200 nm range with a precision of about 1–3 Å. This technique can also be employed to estimate the density and roughness of films and multilayers [309, 308]. The physical phenomenon on which this technique is based is the same as that already explained for XRD, with the difference that in this case the interference pattern is obtained after the diffraction produced between two surfaces delimiting a film, as represented in Fig. B.4.

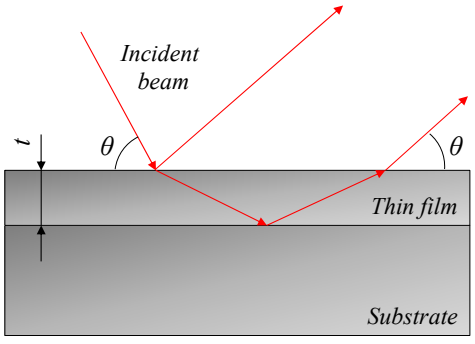

Figure B.4 Schematic representation of reflected and refracted beams in thin films. The X–rays scattered from the different interfaces produce an interference pattern.

Consider the well–known Snell equation. Since the refractive index, n, of the film is smaller than that of the air ($n_{air} = 1$), there is an angle, known as critical angle, θ_c, under which the X–rays are totally reflected. Above such angle, due to the interference between the X–ray beams scattered from the different interfaces, it is possible to record a scan consisting of the so–called *Kiessig fringes*, *i.e.*, intensity maxima corresponding to constructive interferences and minima due to destructive interferences. The position of these fringes is directly related to the thickness of the layer (t) [109]:

$$2t\sqrt{sin^2\theta_m - sin^2\theta_c} = m\lambda \tag{B.9}$$

where m is an integer.

Considering the incident angle θ sufficiently small, Eq. B.9 has the form:

$$\theta_m^2 - \theta_c^2 = m^2\left(\frac{\lambda}{2t}\right)^2 \tag{B.10}$$

For a periodic multilayer containing N periods, each consisting of a layer A, with thickness t_A, and a layer B, with thickness t_B; and considering the incident angle θ sufficiently small, Eq. B.9 is written as [109]:

$$\theta_m^2 - \theta_c^2 = m^2\left(\frac{\lambda}{2D}\right)^2 \tag{B.11}$$

where $D = t_A + t_B$.

B.3. X–Ray Absorption Spectroscopy (XAS)

X–ray absorption spectroscopy (XAS) is a well–established analytical technique for structural determination (namely: the local environment of an atom). This technique is based on the electron excitation from deep core levels of a selected atom by the absorption of an X–ray photon. In general, the X–ray absorption coefficient smoothly varies with the photon energy. However, when the incident photons have enough energy to excite a core electron, an abrupt increase in the X–ray

absorption occurs, known as absorption edges. After a short time (~10^{-15} s), the generated core–hole is occupied by an electron from higher–energy states and the corresponding energy difference is commonly released via X–ray fluorescence or Auger electron emission. For these transitions to happen certain requirements called electric dipole selection rules must be met:

1) Transitions are mono–electronic, *i.e.*, only one electron is involved in each transition.
2) The relative orientations of the spin of a complex cannot be modified.
3) The only allowed transitions are those that involve a change in parity.

In other words, these rules imply that $\Delta s = 0$ and $\Delta l = \pm 1$ [110, 331]. As the inner shell absorption occurs at characteristic energies with a considerable difference between each other, by properly tuning the X–ray energy it is possible, not only to select a specific element in the sample (**element–selective**), but also a specific shell within the same atom, *i.e.*, **shell–selective**.

As shown in Fig. B.5, these allowed transitions are characterized by the initial and final states of the excited electron and are usually labeled by the spectroscopic name: *1s* is called K edge and *2s* is called L_1 edge. For the two spin–orbit split shells $2p_{1/2}$ and $2p_{3/2}$ the edge names are L_2 and L_3 edge, respectively; and so on.

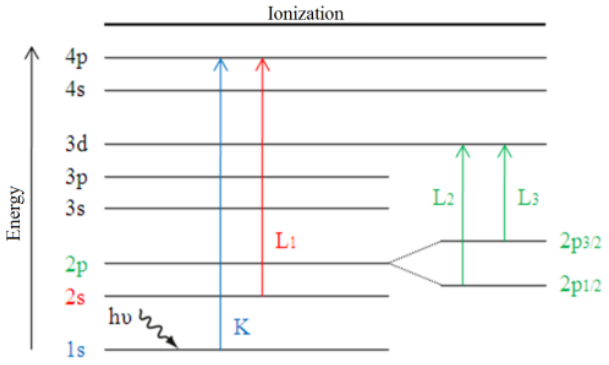

Core State	Spectroscopic Name
1*s*	K
2*s*, 2*p*	L_1, $L_{2,3}$
3*s*, 3*p*, 3*d*	M_1, $M_{2,3}$, $M_{4,5}$
4*s*, 4*p*, 4*d*, 4*f*	N_1, $N_{2,3}$, $N_{4,5}$, $N_{6,7}$

Figure B.5 Scheme of the excitation of an electron by the absorption of an X–ray photon.

Once an allowed transition occurs, a photoelectron is emitted and its wave is backscattered by the surrounding atoms. As a result, constructive and destructive interferences are created between the outgoing photoelectron wave and the backscattered wave that extends beyond the edge by an amount typically of the order of 1 keV. Hence, the absorption spectrum is usually divided into two main regions, as shown in Fig. B.6: (i) the **XANES** (X–ray absorption near edge structure) region, which extends about 20 eV below the edge to ~30–100 eV beyond the edge. In certain XANES spectra, depending on the details of the density of states, the rising absorption edge might lead to a sharp intense peak, usually referred to as "white line". (ii) And the **EXAFS** (extended X–ray absorption fine structure) region, which extends from ~30–100 eV to ~600–1000 eV beyond the edge.

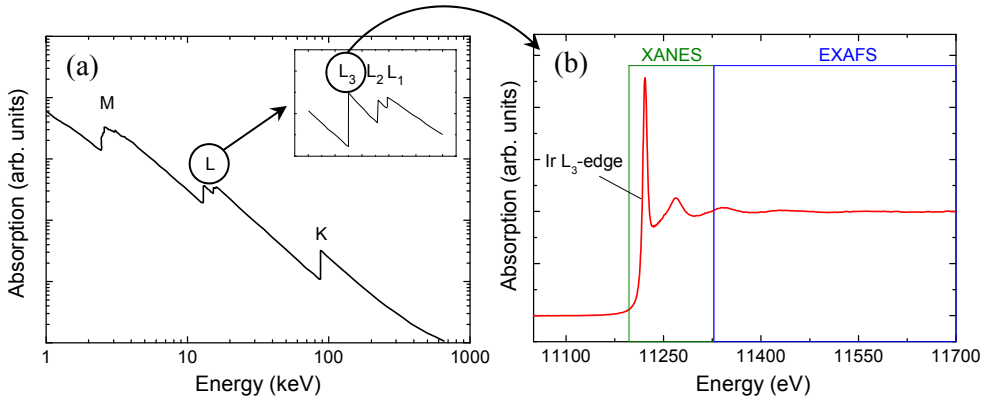

Figure B.6 (a) Low resolution XAS spectrum example [332] where three major transitions can be discerned (K, L, and M edges), corresponding to excitation of an electron from n = 1, 2, and 3 shells, respectively. At higher resolution (inset) both the L and the M edges are split. (b) Typical regions in a XAS spectrum.

The spectral shape of the XANES region is characterized by transitions of the photoelectron to unoccupied bound states. The XANES is thus sensitive to the chemical bonding and local bonding environment of the absorbing atom, exhibiting, for instance, characteristic features for different oxidation states of the absorbing atom. The XANES features are also influenced by strong multiple scattering effects (Fig. B.7(a)), which depend on the three–dimensional geometry of the crystal structure. This provides a way of distinguishing between different crystal phases or

different coordination. Although theoretical complex calculations are possible, typical (simpler) analyses are based on comparing the measured spectra to those of known standards. Quantitative values are commonly obtained by linear combination fittings.

As far as the EXAFS region is concerned, single scattering events of the outgoing electron on the neighboring atoms domain, as schematized in Fig. B.7(b). This gives information about the local atomic structure around the absorbing site: coordination number, interatomic distances, structural disorder, etc. The EXAFS oscillations for a Gaussian distribution of N_j atoms at mean distances R_j around the absorbing atom, considering single scattering and plane–wave approximation, are described by next expression [333]:

$$\chi(k) = S_0^2 \sum_j \frac{N_j}{kR_j^2} e^{\left(-2k^2\sigma_j^2\right)} e^{\left(-\frac{2R_j}{\lambda(k)}\right)} f_j(k) \times sin\left(2kR_j + \phi_j(k)\right) \qquad \text{(B.12)}$$

where S_0^2 is an intrinsic loss factor, N_j is the average coordination number for the Gaussian distribution of distances centered at the R_j value, σ_j is the Debye–Waller factor, and $\phi_j(k) = 2\delta(k) + \varphi_j(k)$ is the phase shift, being $\delta(k)$ and $\varphi_j(k)$ the central and backscattering atom phase shifts, respectively. $f_j(k)$ is the magnitude of the backscattering amplitude of the j^{th}–neighbour atom, and λ is the mean free path of the photoelectron traveling from the absorbing atom to the backscatterer in the j^{th}–shell and the life time of the core hole.

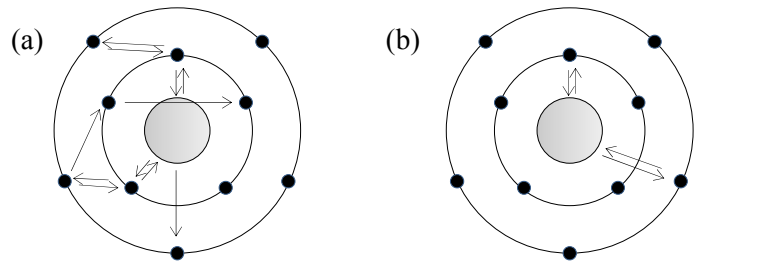

Figure B.7 Multiple and single scattering contributions dominating in (a) XANES and (b) EXAFS regions, respectively.

B.3.1. Transmission *vs.* Fluorescence Measurements

Due to the manner X–rays interacts with matter, schematized in Fig. B.8, X–ray absorption spectra are usually recorded on transmission or fluorescence mode. The choice of carrying out one measurement or another depends solely on the type of sample.

In the **transmission mode**, the absorption is recorded by measuring what is transmitted through the sample (see Fig. B.8). An X–ray beam with intensity I_0 will be attenuated when it passes through a sample with a thickness t according to the Lambert equation:

$$I = I_0 e^{-\mu t} \tag{B.13}$$

where μ is the absorption coefficient and I the X–ray beam intensity after passing through the sample. If a transmission measurement can be made, it is relatively easy and gives excellent data. For transmission measurements, a uniform sample free from pinholes is needed. It is commonly used for concentrated samples in which the element of interest is above ~10 wt. %, and a thin enough sample can be prepared. It is noted that sample preparation is more stringent for transmission measurements than for fluorescence measurements.

In the **fluorescence mode**, the photons emitted during the re–filling of the deep core–hole are detected and it holds that:

$$\mu(E) \propto I_f / I_0 \tag{B.14}$$

being I_f the intensity of the fluorescence X–rays (see Fig. B.8). This kind of measurement is employed in thin films deposited on a substrate and in dilute samples in which the element of interest is below ~10 wt. %. For concentrated samples that cannot be made thin enough for transmission the fluorescence mode can be used, but special attention must be payed to the re–absorption of the fluorescence photons by the same species before the photons leave the sample (self–absorption effects).

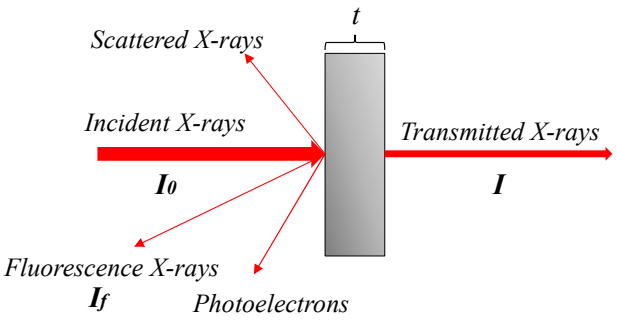

Figure B.8 Scheme of the X–ray radiation and matter interactions.

B.3.2. Spectra Normalization

Once a XAS spectrum has been experimentally recorded, a normalization procedure is necessary before data can be compared. The procedure, schematized in Fig. B.9, has the following steps [178, 135, 136, 334, 81]:

1) Convert the recorded intensities to $\mu(E)$, correcting systematic measurement errors such as self–absorption effects and detector dead time (time after each event during which the system is not able to record another event).

2) Subtract a smooth pre–edge function from $\mu(E)$ to get rid of any instrumental background and absorption from other edges. Typically, the background $\mu_0(E)$ can be approximated by a linear function.

3) Identify the threshold energy, E_0, typically as the energy of the maximum of the first derivative of $\mu(E)$.

4) The intensity of the post–edge region varies from one sample to another due to thickness differences. To remove such dependence, $\mu(E)$ is normalized so that the average absorption coefficient at high energy is equal to 1 at the L_3 (and K) edge and 0.5 at the L_2 edge. This normalization scheme reflects the number of initial core–electron states available for the L_2 and L_3 absorption processes, since the ratio of occupied $2p_{1/2}$ and $2p_{3/2}$ states is 1:2 [81].

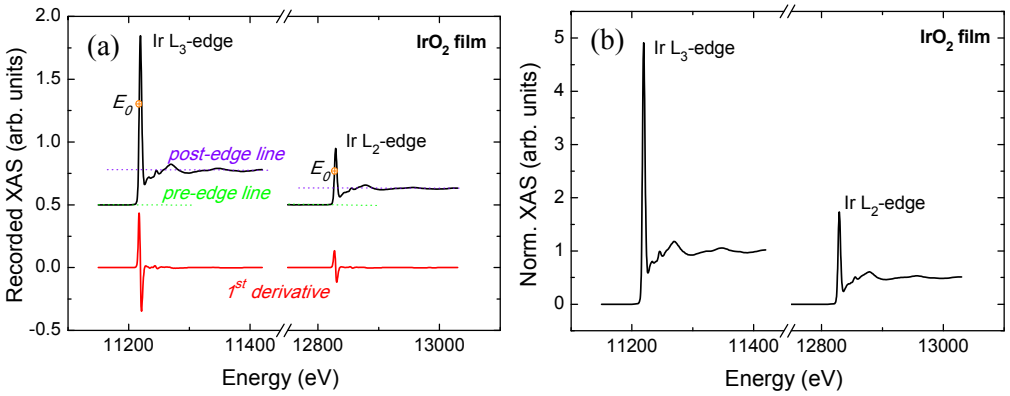

Figure B.9 XAS spectra (a) as–recorded and (b) after background subtraction and normalization.

B.3.3. Synchrotron Facility and Synchrotron Radiation

XAS experiments were performed at synchrotron facilities due to the requirement of high X–ray intensities and a continuous energy spectrum. Classically, any charged particle moving in a curved path or accelerated in a straight line emits electromagnetic radiation. Synchrotron radiation is electromagnetic radiation generated by charged particles (electrons) moving along a curve path at relativistic velocities in a magnetic field. In a typical synchrotron facility, as that shown in Fig. B.10(a), the electrons emitted from a thermionic electron gun (1) are first accelerated in a linear accelerator (2). Then, the electrons get inside a circular accelerator (booster ring) where they are boosted by electric fields (3). The electrons are subsequently injected into the storage ring (4), where they travel through different types of magnets making them deflect from their straight path by several degrees. This fact causes them to emit a synchrotron radiation that will be used in the beamlines (5) to perform different kind of experiments (6).

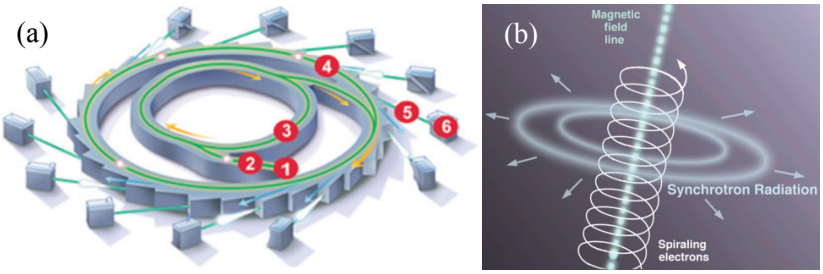

Figure B.10 (a) scheme of a synchrotron facility and (b) synchrotron radiation illustration.

B.4. Transmission Electron Microscopy (TEM)

In the transmission electron microscopy (TEM) a beam of electrons is transmitted through an ultra–thin specimen and the images are formed from the interaction of the electrons transmitted through it. That makes it necessary a prior (non–trivial) sample preparation to thin it down in order to enable electrons to pass through it.

The electrons are first produced either thermoionically by heating a W or LaB_6 cathode, or by a field emission electron gun. The electron beam is then accelerated and confined onto the sample by a magnetic lens system. After going through an optical set, the transmitted electrons are gathered and collected in the image plane and the image is formed on the screen. These microscopes usually incorporate a "diffraction mode" which allows recording a diffraction pattern of selected regions from the sample.

B.5. Field–Emission Scanning Electron Microscopy (FE–SEM)

The scanning electron microscope (SEM) scans a sample with a focused electron beam over its surface to create an image. The signals derived from the electron–sample interactions reveal information about the external morphology, chemical composition or crystalline structure and orientation of materials making up the sample.

In conventional SEM, the electrons are produced thermionically by heating a W or LaB_6 cathode. In field–emission scanning electron microscopes (FE–SEM), the electrons are emitted from the surface of a conductor by means of a strong electric field, producing a much smaller–diameter electron beam, which allows recording much higher–resolution images. Once the electrons have been produced, the electron beam is focalized onto the sample by electromagnetic lenses. When the electron beam hits the sample, both electron and photon signals are emitted. The signals most commonly used are the so–called secondary electrons, backscattered electrons and X–rays. The secondary electrons come from atoms of the sample that have been ionized by the impact of the primary electrons (electron beam); the backscattered electrons are primary electrons that have been elastically backscattered; and the production of X–rays is due to electron transitions of the atoms of the sample excited by the primary electrons. Both, the secondary and the backscattered electrons are used to form the image, and the X–rays give compositional information.

B.6. Energy Dispersive X–Ray Spectroscopy (EDX)

The energy dispersive X–ray spectroscopy (EDX) technique is based on the X–ray spectrum emitted by a solid bombarded with a focused beam of electrons to obtain a localized chemical analysis. Each element produces X–rays corresponding to characteristic electronic transitions which allow its identification.

This compositional analysis is commonly combined with the morphologic study provided by SEM, and hence, it is usually incorporated in such microscopes.

B.7. Rutherford Backscattering Spectroscopy (RBS)

Rutherford backscattering spectrometry (RBS) is a quantitative and non–destructive technique employed for precise determination of stoichiometry, elemental surface density and distribution of impurities in the surface region of solids [335, 336]. This technique is based on the measurement of the number and energy distribution of the elastically backscattered ions due to the Coulomb repulsion effect between

positive beam particles and nuclei in the sample [337, 338]. From the energy spectrum of the backscattered particles, elemental concentration and depth profiles can be calculated.

In a RBS experiment, the sample is bombarded with light ions (typically H^+ or He^{2+}) perpendicularly directed to it with typical energies between 0.4 and 3 MeV (Fig. B.11). These particles collide elastically with the atoms of the sample, being dispersed with a characteristic energy which depends on the mass of the scattering center (the larger the mass of the collided atom, the greater the energy of the particle to be detected). The dispersed particles are then detected in certain directions with silicon barrier detectors.

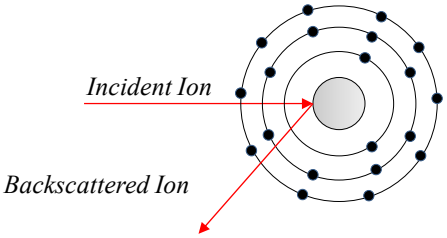

Figure B.11 RBS fundamentals.

B.8. Electrical Resistivity (Van der Pauw)

The electrical resistivity, ρ, is an intrinsic property that quantifies how strongly a material opposes the flow of an electric current. It is usually calculated as:

$$\rho = \frac{RA}{L} \tag{B.15}$$

where R states for the electrical resistance, A is the cross–sectional area, and L is the length of the sample.

To measure the electrical resistivity in thin films the Van der Pauw technique is commonly used [125]. The typical scheme of such experiment has 4 electrical contacts (A to D) at the four corners of a roughly square sample, as that shown in Fig.

B.12. The sample resistivity is calculated using the voltage measured between two adjacent contacts while applying a current between the two opposite adjacent contacts.

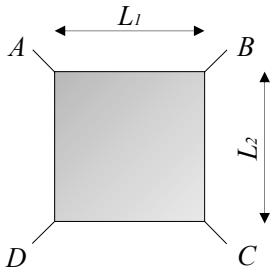

Figure B.12 Van der Pauw typical geometry.

This method is applicable for an arbitrary sample as long as its thickness is known and uniform and the contact areas are small and placed on the perimeter of the sample. In such case, it holds that [125]:

$$e^{-\frac{\pi R_{AB,CD} t}{\rho}} + e^{-\frac{\pi R_{BC,DA} t}{\rho}} = 1 \tag{B.16}$$

where t is the thickness of the sample, ρ the resistivity, $R_{AB,CD}$ is the resistance determined by dividing the potential difference V_D - V_C by the current going from A to B, and $R_{BC,\,DA}$ is defined similarly.

Assuming $L_1 = L_2$ (square samples) and $R_{AB,\,CD} = R_{BC,\,DA}$; Eq. B.16 can be simplified by:

$$\rho = \frac{\pi R t}{\ln(2)} \tag{B.17}$$

However, when this approximation cannot be made, a mathematical software is needed to solve Eq. B.16. In this dissertation, Mathematica software has been used for solving equations in the form:

$$e^{-\frac{\alpha}{\rho}} + e^{-\frac{\beta}{\rho}} = 1 \tag{B.18}$$

where $\alpha = -\frac{\pi R_{AB,CD} t L_2}{L_1}$ and $\beta = -\frac{\pi R_{BC,DA} t L_1}{L_2}$.

B.9. Superconducting QUantum Interference Device (SQUID)

The SQUID is one of the most sensitive devices currently available for measuring the magnetization of different types of samples. As schematized in Fig. B.13, the measurement is carried out by displacing the sample, typically inserted in a straw, along a series of pick–up coils. The variations in the electric current induced in such coils by the magnetic moment of the sample are recorded, converted into voltage by a Josephson junction (insulating barrier between two superconductor materials), and eventually transmitted as an electric signal proportional to the magnetic moment of the sample.

Two different modes are available in the device to perform the experiments: "no–overshoot" and "hysteresis". In the no–overshoot mode, when the magnetic field is changed the field is ramped quickly at the beginning, but as the field approaches the target value, the field changes much more slowly to avoid overshooting the requested value. In contrast, in the hysteresis mode the magnet is charged directly to the final field and the magnet current is maintained during the measurements. Thus, this last mode allows measuring sequential field settings much more rapidly than the no–overshoot mode, but the sensitivity of such measurements is substantially reduced due to the increased magnetic noise from the magnet supply current [127].

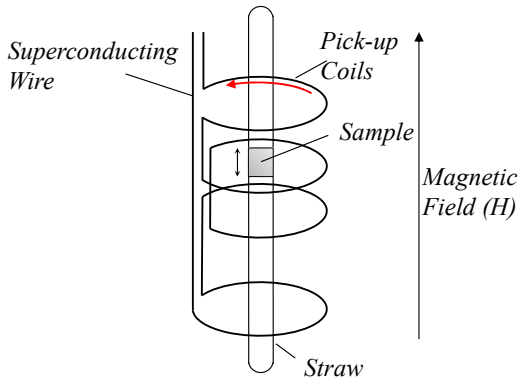

Figure B.13 Operating diagram of the SQUID magnetometer.

B.10. X–ray Magnetic Circular Dichroism (XMCD)

The X–ray magnetic circular dichroism (XMCD) is a powerful tool for the study of magnetic materials, capable to provide element and shell specific information about orbital and spin magnetic moments [133, 134]. This technique is based on the fact that the absorption of X–rays in magnetic materials depends on the polarization of light. Measuring the absorption coefficient (XAS) of a sample under an applied magnetic field for both circular polarizations, *i.e.*, left (μ^-) and right (μ^+), and subtracting both signals, an XMCD spectra is obtained: $\mu_c = \mu^- - \mu^+$.

XMCD became more powerful as a tool for the element–selective magnetic characterization of materials with the derivation of the magneto–optical sum rules by *B. T. Thole et al.* [135] and *P. Carra et al.* [136]. Via these sum rules it is possible to determine both, the orbital ($m_l = -\langle L_z \rangle$, in units of μ_B/atom), and spin ($m_s = -2\langle S_z \rangle$, in μ_B/atom) magnetic moments of the probed (X–ray absorbing) atom from the integrated intensities of the measured XMCD. In the case of XMCD measured at $L_{2,3}$ edges, the first sum rule states that the orbital magnetic moment $\langle L_z \rangle$ is proportional to:

$$\langle L_z \rangle = -2\, n_h \frac{\int_{L_3+L_2} (\mu^- - \mu^+) dE}{\int_{L_3+L_2} (\mu^- + \mu^+ + \mu^0) dE} \tag{B.19}$$

where n_h is the number of holes and μ^0 states for the absorption of X–rays linearly polarized along the magnetization direction, usually approximated by $(\mu^+ + \mu^-)/2$.

The sum rule for the expectation value of the spin momentum is:

$$\frac{2}{3}\langle S_z \rangle + \frac{7}{3}\langle T_z \rangle = -\, n_h \frac{\int_{L_3} (\mu^- - \mu^+) dE - 2\int_{L_2} (\mu^- - \mu^+) dE}{\int_{L_3+L_2} (\mu^- + \mu^+ + \mu^0) dE} \tag{B.20}$$

where $\langle T_z \rangle$ is the magnetic dipole operator.

It is common in the XMCD literature [133, 339, 340] to refer to the first integral in the numerator of Eq. B.20 as “A”, the second integral as “B”, and the

denominator as "3C" (see Fig. B.14). Therefore, the sum rules can be re–expressed in the following manner (in units of $\hbar$/atom):

$$\langle L_z \rangle = -2n_h \frac{A+B}{3C} \qquad \langle S_z \rangle = -n_h \frac{A-2B}{2C} - \frac{7}{2}\langle T_z \rangle \tag{B.21}$$

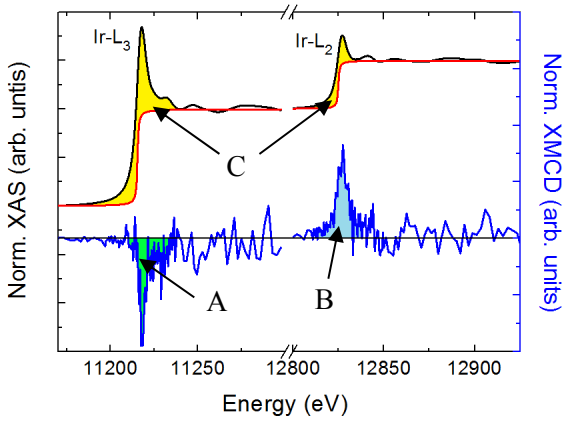

Figure B.14 Necessary integrals for the determination of the orbital and spin magnetic moments. Black lines: XAS at Ir $L_{2,3}$ edges, red lines: steps for background removal, and blue lines: Ir XMCD signals at Ir $L_{2,3}$ edges.

Appendix C

Film Synthesis

This last appendix contains further non–systematic experiments carried out to optimize the growth of IrO_2 thin films in our sputtering chamber.

C.1. Substrate Adherence

It was observed that a few days after being deposited, some kind of "spots" appeared on the surface of some non–annealed samples visible with the naked eye, as shown in Fig. C.1(a). In the same figure, the diffractograms of one sample affected with such "spots" (labeled as NOK) and another one not affected (labeled as OK) grown under the same conditions are compared. These diffractograms and the results obtained from Rietveld analyses (not shown) proved that there is no appreciable difference in the structure of these two samples.

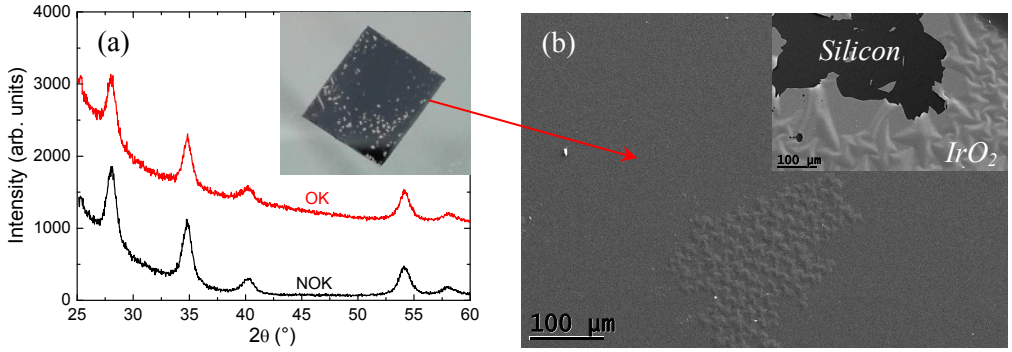

Figure C.1 (a) XRD experiments carried out in samples with (NOK) and without (OK) "spots". The inset shows an image of one sample affected with such "spots". In panel (b) illustrative FE–SEM images from this affected sample are displayed.

Affected samples with such "spots" were observed under a FE–SEM (Fig. C.1(b)). The images reveal that these "spots" are in fact due to bad adherence of the IrO_2 layers to the silica substrate. It is known that high–thickness films can accumulate stress and hence induce the film to separate from the substrate.

C.2. Influence of the Substrate

In the work presented in section 3.2 Si substrates were used. Such substrates have an amorphous naturally passivated SiO_2 layer of ~2–5 nm on their surface. Trying to improve the crystallinity (GS mainly) of the films, polycrystalline (non–textured) SnO_2[18] substrates, which have the same crystalline structure and similar lattice parameters than IrO_2, were used. An IrO_2 layer was deposited on Si/SnO_2 using growing conditions that yield to polycrystalline non–textured and (110)–textured samples after annealing. The diffractograms measured in these systems are given in Fig. C.2(a) and compared to the respective IrO_2 films grown Si substrates.

It can be seen in that figure that no appreciable changes occur when using "non–textured conditions". Contrary, for the "(110)–textured conditions" the crystal orientation of the IrO_2 film is lost, indicative of a worse crystallinity. Such poorer crystallinity could be due to the relatively high surface roughness observed in the SnO_2 substrates (see Fig. C.2(b)).

These results indicate that an amorphous smooth surface is better than a relatively rough polycrystalline one (even if it presents the same crystal structure and similar lattice parameters) for growing better crystallized IrO_2 films.

[18] ~80 nm-thick amorphous $Si(SiO_2)/SnO_2$ films were provided by Dr. Ana Cueva from Univ. of Zaragoza, and annealed at 1100 ºC in air during 6 h to obtain polycrystalline films.

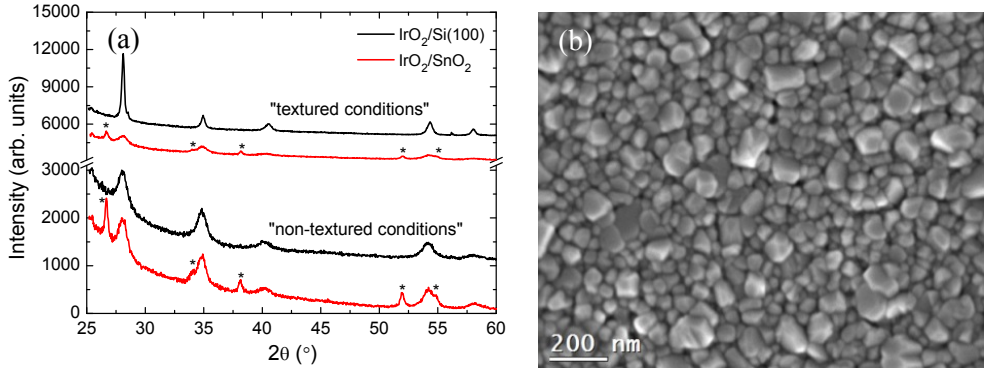

Figure C.2 (a) XRD measurements in IrO_2 films deposited on polycrystalline SnO_2 substrates using growing conditions which give polycrystalline non–textured (IO_39) and (110)–textured (IO_23) samples from Table 3.1. *SnO_2 peaks. (b) Illustrative surface FE–SEM image from one of the SnO_2 substrates employed.

C.3. Effect of Quenching

It is well known that a rapid cooling of a sample after annealing (quenching) can result in different material properties and commonly stress is induced [341–343]. This could have an important effect on the macroscopic properties of IrO_2, as explain in Chapter 1. Thus, three cooling procedures were compared in a (110)–textured film. The samples were first heated up to 600 ºC in air atmosphere. After 4 hours, one of the samples was air quenched (removed from the furnace) and another sample was water quenched (without agitation). The third sample was annealed at 600 ºC in air atmosphere for 6 hours and cooled down to RT at 5 ºC/min. Fig. C.3 compares the diffractograms of these samples, showing negligible differences. In view of this results, the typical "slow" cooling (5 ºC/min) was used for all the samples.

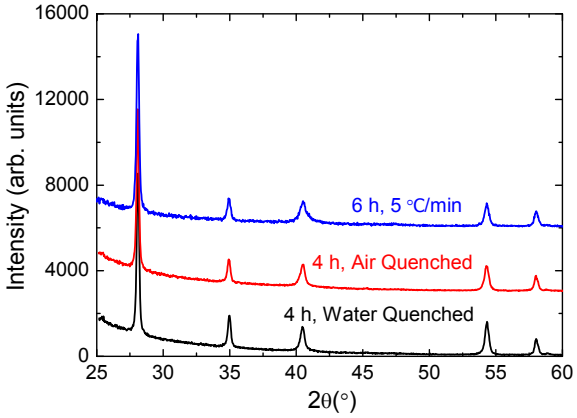

Figure C.3 Diffractogram of IO_23 sample (Table 3.1) cooled at 5 ºC/min, and quenched in air and water.

Bibliography

[1] S. Hackwood, G. Beni, M. A. Bösch, K. Kang, L. M. Schiavone, and J. L. Shay, Phys. Rev. B **26**, 7073(R) (1982).

[2] C. G. Granqvist, E. Avendaño, and A. Azens, Thin Solid Films **442**, 201 (2003).

[3] S.–W. Kim, S.–H. Kwon, D.–K. Kwak, and S.–W. Kang, J. Appl. Phys. **103**, 023517 (2008).

[4] G. Shi, M. Luo, J. Xue, Y. Xian, L. Jin, and J. Y. Jin, Talanta **55**(2), 241 (2001).

[5] P. Kurzweil, Sensors **9**(6), 4955 (2009).

[6] S. D. Tilley, M. Cornuz, K. Sivula, and M. Grätzel, Angew. Chem. Int. Ed. **49**(36), 6405 (2010).

[7] K. Fujiwara, Y. Fukuma, J. Matsuno, H. Idzuchi, Y. Niimi, Y. Otani, and H. Takagi, Nat. Commun. **4**, 2893 (2013).

[8] G. A. Prinz, Science **282**, 1660 (1998).

[9] M. D. Asham, and A. H. Phillips, Physica E Low Dimens. Syst. Nanostruct. **113**, 97 (2019).

[10] J. Sinova, S. O. Valenzuela, J. Wunderlich, C. H. Back, and T. Jungwirth, Rev. Mod. Phys. **87**, 1213 (2015).

[11] T. Jungwirth, J. Wunderlich, and K. Olejnik, Nat. Mater. **11**(5), 382 (2012).

[12] A. Manchon, H. C. Koo, J. Nitta, S. M. Frolov, and R. A. Duine, Nat. Mater. **14**(9), 871 (2015).

[13] A. Soumyanarayanan, N. Reyren, A. Fert, and C. Panagopoulos, Nature **539**(7630), 509 (2016).

[14] S. A. Wolf, D. D. Awschalom, R. A. Buhrman, J. M. Daughton, S. von Molnár, M. L. Roukes, A. Y. Chtchelkanova, and D. M. Treger, Science **294**(5546), 1488 (2001).

[15] J. Hirsch, Phys. Rev. Lett. **83**, 1834 (1999).

[16] S. Zhang, Phys. Rev. Lett. **85**, 393 (2000).

[17] Y. K. Kato, R. C. Myers, A. C. Gossard, and D. D. Awschalom, Science **306**, 1910 (2004).

[18] S. O. Valenzuela, M. Tinkham, Nature **442**, 176 (2006).

[19] M. Cubukcu, O. Boulle, N. Mikuszeit, and C. Hamelin, Spintec. **1–23** 1509.02375v1 (2015).

[20] K. Jabeur, G. Di Pendina, F. Bernard–Granger, and G. Prenat, IEEE Electron Device Lett. **35**(3), 408 (2014).

[21] I. M. Miron, K. Garello, G. Gaudin, P. J. Zermatten, M. V. Costache, S. Auffret, S. Bandiera, B. Rodmacq, A. Schuhl, and P. Gambardella, Nature **476**(7359), 189 (2011).

[22] M. Jiang, H. Asahara, S. Sato, T. Kanaki, H. Yamasaki, S. Ohya, and M. Tanaka, Nat. Commun. **10**, 2590 (2019).

[23] H. Wang, W. Wang, N. Hu, T. Duan, S. Yuan, S. Dong, C. Lu, and J.–M. Liu, Phys. Rev. Appl. **10**, 014025 (2018).

[24] B. G. Park, J. Wunderlich, X. Martí, V. Holy, Y. Kurosaki, M. Yamada, H. Yamamoto, A. Nishide, J. Hayakawa, H.Takahashi, *et al.*, Nat. Mater. **10**(5), 347 (2011).

[25] I. Fina, X. Marti, D. Yi, J. Liu, J. H. Chu, C. Rayan–Serrao, S. Suresha, A. B. Shick, J. Zelezny, T. Jungwirth, *et al.*, Nat. Commun. **5**, 4671 (2014).

[26] D. Yi, J. Liu, S. L. Hsu, L. Zhang, Y. Choi, J W. Kim, Z. Chen, J. D. Clarkson, C. R. Serrao, E. Arenholz, *et al.*, Proc. Natl. Acad. Sci. **113**(23), 6397 (2016).

[27] B. J. Kim, H. Jin, S. J. Moon, J.–Y. Kim, B.–G. Park, C. S. Leem, J. Yu, T. W. Noh, C. Kim, S.–J. Oh, *et al.*, Phys. Rev. Lett. **101**, 076402 (2008).

[28] B. J. Kim, H. Ohsumi, T. Komesu, S. Sakai, T. Morita, H. Takagi, and T. Arima, Science **323**(5919), 1329 (2009).

[29] D. Pesin, and L. Balents, Nat. Phys. **6**, 376 (2010).

[30] M. Kargarian, J. Wen, and G. A. Fiete, Phys. Rev. B **83**, 165112 (2011).

[31] Y. K. Kim, O. Krupin, J. D. Denlinger, A. Bostwick, E. Rotenberg, Q. Zhao, J. F. Mitchell, J. W. Allen, and B. J. Kim, Science **345**(6193), 187 (2014).

[32] H. Luo, T. Klimczuk, L. Müchler, L. Schoop, D. Hirai, M. K. Fuccillo, C. Felser, and R. J. Cava, Phys. Rev. B **87**, 214510 (2013).

[33] X. Wan, A. M. Turner, A. Vishwanath, and S. Y. Savrasov, Phys. Rev. B **83**, 205101 (2011).

[34] W. Witczak–Krempa, and Y. B. Kim, Phys. Rev. B **85**, 045124 (2012).

[35] Y. Machida, S. Nakatsuji, S. Onoda, T. Tayama, and T. Sakakibara, Nature **463**(7278), 210 (2010).

[36] Y. Okamoto, M. Nohara, H. Aruga–Katori, and H. Takagi, Phys. Rev. Lett. **99**, 137207 (2007).

[37] Y. Hirata, K. Ohgushi, J.–I. Yamaura, H. Ohsumi, S. Takeshita, M. Takata, and T.–H. Arima, Phys. Rev. B **87**, 161111(R) (2013).

[38] S. Sugano, Y. Tanabe, and H. Kamimura, *Multiplets of Transition–Metal Ions in Crystals* (Academic Press, New York, 1970).

[39] L. Balents, Nature **464**, 199 (2010).

[40] F. Hund, Z. Phys. **33**, 345 (1925).

[41] S. Maekawa, T. Tohyama, S. E. Barnes, S. Ishihara, W. Koshibae, and G. Khaliullin, *Physics of Transition Metal Oxides* (Springer–Verlag, Berlin, 2004).

[42] B. Keimer, A. Aharony, A. Auerbach, R. J. Birgeneau, A. Cassanho, Y. Endoh, R. W. Erwin, M. A. Kastner, and G. Shirane, Phys. Rev. B **45**, 7430 (1992).

[43] P. W. Atkins, and R. S. Friedman, *Molecular Quantum Mechanics* (Oxford University Press, New York, 1999).

[44] B. Andlauer, J. Schneider, and W. Tolksdorf, Phys. Stat. Sol. B **73**(2), 533 (1976).

[45] K. W. Blazey and F. Levy, Solid State Commun. **59**(6), 335 (1986).

[46] Y. Tokura, and N. Nagaosa, Science **288**(5465), 462 (2000).

[47] G. Cao, J. Bolivar, S. McCall, J. E. Crow, and R. P. Guertin, Phys. Rev. B **57**, R11039(R) (1998).

[48] G. Cao, Y. Xin, C. S. Alexander, J. E. Crow, P. Schlottmann, M. K. Crawford, R. L. Harlow, and W. Marshall, Phys. Rev. B **66**, 214412 (2002).

[49] I. Nagai, Y. Yoshida, S. I. Ikeda, H. Matsuhata, H. Kito, and M. Kosaka, J. Phys. Condens. Matter **19**, 136214 (2007).

[50] S. J. Moon, H. Jin, K. W. Kim, W. S. Choi, Y. S. Lee, J. Yu, G. Cao, A. Sumi, H. Funakubo, C. Bernhard, *et al.*, Phys. Rev. Lett. **101**, 226402 (2008).

[51] M. K. Crawford, M. A. Subramanian, R. L. Harlow, J. A. Fernandez–Baca, Z. R. Wang, and D. C. Johnston, Phys. Rev. B **49**, 9198 (1994).

[52] N. F. Mott, Proc. Phys. Soc. A **62**, 416 (1949).

[53] Coordination Compounds. http://www.rsc.org/pdf/tct/df–chapter.pdf, pp 54–70 (2005).

[54] M. Mochizuki, and M. Imada, New J. Phys. **6**(1), 154 (2004).

[55] G. Zhou, X. Gu, X. Yang, X. Gao, K. Wang, J. Peng, F. Zhang, and X. S. Wub, AIP Adv. **7**, 055823 (2017).

[56] M. Uchida, W. Sano, K. S. Takahashi, T. Koretsune, Y. Kozuka, R. Arita, Y. Tokura, and M. Kawasaki, Phys. Rev. B **91**, 241119(R) (2015).

[57] W. K. Zhu, C.–K. Lu, W. Tong, J. M. Wang, H. D. Zhou, and S. X. Zhang, Phys. Rev. B **91**, 144408 (2015).

[58] W. D. Ryden, and A. W. Lawson, J. Chem. Phys. **52**, 6058 (1970).

[59] J. C. Slater, Phys. Rev. **82**, 538 (1951).

[60] P. W. Anderson, Phys. Rev. **109**, 1492 (1958).

[61] G. Cao, V. Durairaj, S. Chikara, L. E. DeLong, S. Parkin, and P. Schlottmann, Phys. Rev. B **76**, 100402(R) (2007).

[62] L. Zhang, B. Pang, Y. B Chen, and Y. Chen, Crit. Rev. Solid State Mater. Sci. **43**(5), 367 (2018).

[63] V. Singh, and J. J. Pulikkotil, J. Phys. Condens. Matter **31**, 425501 (2019).

[64] J. Kim, D. Casa, M. H. Upton, T. Gog, Y.–J. Kim, J. F. Mitchell, M. van Veenendaal, M. Daghofer, J. van den Brink, G. Khaliullin, *et al.*, Phys. Rev. Lett. **108**, 177003 (2012).

[65] D. J. Groenendijk, C. Autieri, J. Girovsky, M. C. Martinez–Velarte, N. Manca, G. Mattoni, A. M. R. V. L. Monteiro, N. Gauquelin, J. Verbeeck, A. F. Otte, *et al.*, Phys. Rev. Lett. **119**, 256403 (2017).

[66] Y. F. Nie, P. D. C. King, C. H. Kim, M. Uchida, H. I. Wei, B. D. Faeth, J. P. Ruf, J. P. C. Ruff, L. Xie, X. Pan, *et al.*, Phys. Rev. Lett. **114**, 016401 (2015).

[67] A. Biswas, K.–S. Kim, Y. H. Jeong, J. Appl. Phys. **116**, 213704 (2014).

[68] S. Chikara, O. Korneta, W. P. Crummett, L. E. DeLong, P. Schlottmann, and G. Cao, Phys. Rev. B **80**, 140407(R) (2009).

[69] I. Qasim, B. J. Kennedy, and M. Avdeev, J. Mater. Chem. A **1**, 3127 (2013).

[70] J. Cheng, J. Zhou, J. B. Goodenough, K. Matsubayashi, and Y. Uwatoko, JPS Conf. Proc. **3**, 013014 (2014).

[71] Q. Cui, J.–G. Cheng, W. Fan, A. E. Taylor, S. Calder, M. A. McGuire, J.–Q. Yan, D. Meyers, X. Li, Y. Q. Cai, *et al.*, Phys. Rev. Lett. **117**, 176603 (2016).

[72] J. S. Lee, Y. Krockenberger, K. S. Takahashi, M. Kawasaki, and Y. Tokura, Phys. Rev. B **85**, 035101 (2012).

[73] C. R. Serrao, J. Liu, J. T. Heron, G. Singh–Bhalla, A. Yadav, S. J. Suresha, R. J. Paull, D. Yi, J.–H. Chu, *et al.*, Phys. Rev. B **87**, 085121 (2013).

[74] J. Nichols, J. Terzic, E. G. Bittle, O. B. Korneta, L. E. De Long, J. W. Brill, G. Cao, and S. S. A. Seo, Appl. Phys. Lett. **102**, 141908 (2013).

[75] J. Hubbard, Proc. R. Soc. A **276**, 238 (1963).

[76] D. Yanagishima, and Y. Maeno, J. Phys. Soc. Jpn. **70**, 2880 (2001).

[77] S. Zhao, J. M. Mackie, D. E. MacLaughlin, O. O. Bernal, J. J. Ishikawa, Y. Ohta, and S. Nakatsuji, Phys. Rev. B **83**, 180402(R) (2011).

[78] H. J. Koo, M. H. Whango, and B. J. Kennedy, J. Solid State Chem. **136**(2), 269 (1998).

[79] N. Taira, M. Wakeshima, and Y. Hinatsu, J. Phys. Condens. Matter **13**, 5527 (2001).

[80] J. K. Kawasaki, M. Uchida, H. Paik, D. G. Schlom, and K. M. Shen, Phys. Rev. B **94**, 121104(R) (2016).

[81] J. P. Clancy, N. Chen, C. Y. Kim, W. F. Chen, K. W. Plumb, B. C. Jeon, T. W. Noh, and Y.–J. Kim, Phys. Rev. B **86**, 195131 (2012).

[82] S. K. Panda, S. Bhowal, A. Delin, O. Eriksson, and I. Dasgupta, Phys. Rev. B. **89**, 155102 (2014).

[83] X. Ming, K. Yamauchi, T. Oguchi, and S. Picozzi, arXiv preprint arXiv:1702.04408 (2017).

[84] J. M. Kahk, C. G. Poll, F. E. Oropeza, J. M. Ablett, D. Céolin, J.–P. Rueff, S. Agrestini, Y. Utsumi, K. D. Tsuei, Y. F. Liao, *et al.*, Phys. Rev. Lett. **112**, 117601 (2014).

[85] M.–S. Miao, and R. Seshadri, J. Phys. Condens. Matter **24**, 215503 (2012).

[86] Y. Ping, G. Galli, and W. A. Goddard, J. Phys. Chem. C **119**(21), 11570 (2015).

[87] J. K. Kawasaki, D. Baek, H. Paik, H. P. Nair, L. F. Kourkoutis, D. G. Schlom, and K. M. Shen, Phys. Rev. Mater. **2**, 054206 (2018).

[88] D. Depla, and S. Mahieu, *Reactive Sputter Deposition* (Springer, New York, 2008).

[89] E. Slavcheva, R. Vitushinsky, W. Mokwa, and U. Schnakenberg, J. Electrochem. Soc. **151**(7), E226 (2004).

[90] A. Okamoto, and T. Serikawa, Thin Solid Films **137**(1), 143 (1986).

[91] X. Chu, S. A. Bamett, M. S. Wong, and W. D. Sproul, J. Vac. Sci. Technol. A **14**(6), 3124 (1996).

[92] N. Martin, and C. Rousselot, Surf. Coat. Tech. **110**(3), 158 (1998).

[93] R. Cremer, M. Witthaut, D. Neuschutz, G. Erkens, T. Leyendecker, and M. Feldhege, Surf. Coat. Tech. **120–121**, 213 (1999).

[94] R. Cebulla, R. Wendt, and K. Ellmer, J. Appl. Phys. **83**, 1087 (1998).

[95] M. Ohring, *The Materials Science of Thin Films* (Academic Press, London, 1992).

[96] G. Este, and W. D. Westwood, J. Vac. Sci. Technol. A **6**, 1845 (1988).

[97] M. Jambunathan, K. Karakaya, R. Elfrink, R. Vullers, and R. Van Schaijk, presented at International Symposium on Applications of Ferroelectrics, Vancouver (2011).

[98] M. Varela, Ph.D. thesis, Universidad Complutense de Madrid (2001).

[99] J. Tornos, Ph.D. thesis, Universidad Complutense de Madrid (2014).

[100] F. Y. Bruno, Ph.D. thesis, Universidad Complutense de Madrid (2011).

[101] L. Guan, D. M. Zhang, X. Li, and Z. H. Li, Nucl. Instrum. Methods Phys. Res. B **266**(1), 57 (2008).

[102] P. Jiménez, End–of–master work, Universidad de Zaragoza (2015).

[103] J. Rodríguez–Carvajal, Physica B Condens. Matter **192**, 55 (1993).

[104] M. L. Ramón García, *Introducción al Método Rietveld* (Centro de Investigación en Energía Universidad Nacional Autónoma de México, 2007).

[105] J. Rodríguez–Carvajal, *An Introduction To The Program FullProf* (Laboratoire Léon Brillouin CEA–CNRS, 2001).

[106] A. Pereira, Ph.D. thesis, Universidade de Coimbra (2016).

[107] A. L. Patterson, Phys. Rev. **56**, 978 (1939).

[108] P. F. Fewster, Crit. Rev. Solid State **22**(2), 69 (1996).

[109] E. Céspedes, Ph.D. thesis, Universidad Autónoma de Madrid (2009).

[110] M. A. Laguna–Marco, Ph.D. thesis, Universidad de Zaragoza (2006).

[111] K. Hämäläinen, D. P. Siddons, J. B. Hastings, and L. E. Berman, Phys. Rev. Lett. **67**, 2850 (1991).

[112] F. M. F de Groot, M. H. Krisch, and J. Vogel, Top. Catal. **10**, 179 (2000).

[113] P. Glatzel, and U. Bergmann, Coord. Chem. Rev. **249**, 65 (2005).

[114] S. Hayama, G. Duller, J. P. Sutter, M. Amboage, R. Boada, A. Freeman, L. Keenan, B. Nutter, L. Cahill, P. Leicester, *et al.*, J. Synchrotron Radiat. **25**(Pt 5), 1556 (2018).

[115] H. H. Johann, Z. Phys. **69**, 185 (1931).

[116] R. Plackett, I. Horswell, E. N. Gimenez, J. Marchal, D. Omar, and N. Tartoni, J. Instrum. **8**, C01038 (2013).

[117] D. E. Sayers, and B. Bunker, *X–Ray Absorption: Principles, Applications, Techniques of EXAFS, SEXAFS, and XANES* (Wiley, New York, 1988).

[118] K. V. Klementiev, XANES dactyloscope for Windows, freeware: http://xafs.org/Software/ViperAndXandawww.cells.es/old/Beamlines/CLAESS/software/.

[119] C. R. Natoli, D. K. Misemer, S. Doniach, and F. W. Kutzler, Phys. Rev. A **22**, 1104 (1980).

[120] M. Benfatto, and S. D. Longa, J. Synchrotron Radiat. **8**(4), 1087 (2001).

[121] J. Chaboy, and S. Quartieri, Phys. Rev. B **52**, 6349 (1995).

[122] J. Chaboy, J. Synchrotron Radiat. **16**, 533 (2009).

[123] J. Chaboy, A. Muñoz–Páez, F. Carrera, P. Merkling, and E. Sánchez–Marcos, Phys. Rev. B **71**, 134208 (2005).

[124] A. Espinosa, Ph.D. thesis, Universidad Autónoma de Madrid (2009).

[125] L. J. van der Pauw, Philips Res. Repts. **13**, 1 (1958).

[126] J. García Barriocanal, Ph.D. thesis, Universidad Complutense de Madrid (2007).

[127] M. McElfresh, S. Li, and R. Sager, *Effects of Magnetic Field Uniformity on the Measurement of Superconducting Samples* (Quantum Design, San Diego) .

[128] M. A. García, E. Fernández Pinel, J. de la Venta, A. Quesada, V. Bouzas, J. F. Fernández, J. J. Romero, M. S. Martín González, and J. L. Costa–Krämer, J. Appl. Phys. **105**, 013925 (2009).

[129] M. Sawicki, W. Stefanowicz, and A. Ney, Semicond. Sci. Technol. **26**, 064006 (2011).

[130] A. Singh, K. Baur, S. Brennan, T. Homma, N. Kubo, and P. Pianetta, AIP Conf. Proc. **652**, 472 (2003).

[131] L.–B. Xiong, J.–L. Li, B. Yang, and Y. Yu, J. Nanomater. 2012, 831524 (2011).

[132] M. Buchner, K. Höfler, B. Henne, V. Ney, and A. Ney, J. Appl. Phys. **124**, 161101 (2018).

[133] J. Stöhr, and H. König, Phys. Rev. Lett. **75**, 3748 (1995).

[134] D. Weller, Y. Wu, J. Stöhr, M. G. Samant, B. D. Hermsmeier, and C. Chappert, Phys. Rev. B **49**, 12888 (1994).

[135] B. T. Thole, P. Carra, F. Sette, and G. van der Laan, Phys. Rev. Lett. **68**, 1943 (1992).

[136] P. Carra, B. T. Thole, M. Altarelli, and X. Wang, Phys. Rev. Lett. **70**, 694 (1993).

[137] T. J. Park, D. S. Jeong, C. S. Hwang, M. S. Park, and N.–S. Kang, Thin Solid Films **471**(1–2), 236 (2005).

[138] A. Karthigeyan, R. P. Gupta, K. Scharnagl, M. Burgmair, S. K. Sharma, and I. Eisele, Sens. Actuators B Chem. **85**, 145 (2002).

[139] A. Karthigeyan, R. P. Gupta, K. Scharnagl, M. Burgmair, M. Zimmer, T. Sulima, S. Venkataraj, S. K. Sharma, and I. Eisele, IEEE Sens. J. **4**(2), 189 (2004).

[140] R. H. Horng, D. S. Wuu, L. H. Wu, and M. K. Lee, Thin Solid Films **373**(1–2), 231 (2000).

[141] C. U. Pinnow, I. Kasko, C. Dehm, B. Jobst, M. Seibt, and U. Geyer, J. Vac. Sci. Technol. B **19**, 1857 (2001).

[142] H.–J. Cho, H. Horii, C. S. Hwang, J.–W. Kim, C. S. Kang, B. T. Lee, S. I. Lee, Y. B. Koh, and M. Y. Lee, Jpn. J. Appl. Phys. **36**, 1722 (1997).

[143] Y. Liu, H. Masumoto, and T. Goto, Mater. Trans. **45**(10), 3023 (2004).

[144] M. A. El Khakani, M. Chaker, and E. Gat, Appl. Phys. Lett. **69**, 2027 (1996).

[145] L. M. Zhang, Y. S. Gong, C. B. Wang, Q. Shen, and M. X. Xia, Thin Solid Films **496**(2), 371 (2006).

[146] Y. Gong, C. Wang, Q. Shen, and L. Zhang, Mater. Chem. Phys. **116**(2–3), 573 (2009).

[147] K. Nishio, T. Tsuchiya, Sol. Energy Mater. Sol. Cells **68**(3–4), 279 (2001).

[148] I. A. Ges, B. L. Ivanov, D. K. Schaffer, E. A. Lima, A. A. Werdich, and F. J. Baudenbacher, Biosens. Bioelectron. **21**(2), 248 (2005).

[149] H. Yang, S. K. Kang, C. A. Choi, H. Kim, D.–H Shin, Y. S. Kim, Y. T. Kim, Lab Chip **4**, 42 (2004).

[150] Y.–L. Chen, C.–C. Hsu, Y.–H. Song, Y. Chi, A. J. Carty, S.–M. Peng, and G.–H. Lee, Chem. Vap. Deposition **12**(7), 442 (2006).

[151] M. Asadian, JCPT **3**(3), 75 (2013).

[152] J. Tiilikainen, M. Mattila, T. Hakkarainen, and H. Lipsanen, J. Phys. D **41**, 115302 (2008).

[153] M. Ramamoorthy, D. Vanderbilt, and R. D. King–Smith, Phys. Rev. B **49**, 16721 (1994).

[154] R. Daniel, and J. Musil, *Novel Nanocomposite Coatings: Advances and Industrial Applications* (Pan Stanford, New York, 2014).

[155] Y. Niimura, and M. Naoe, J. Magn. Magn. Mater. **54–57**(3), 1687 (1986).

[156] E. Slavcheva, G. Topalov, G. Ganske, I. Radev, E. Lefterova, and U. Schnakenberg, Electrochim. Acta **55**(28), 8992 (2010).

[157] G. Vijaya, M. M. Singh, M. S. Krupashankara, and R. S. Kulkarni, J. Phys. Conf. Ser. **149**, 012075 (2016).

[158] S. Rahmane, M. A. Djouadi, M. S. Aida, and N. Barreau, presented at 13th International Conference on Plasma Surface Engineering, Garmisch–Partenkirchen (2012).

[159] C.–C. Lin, and P.–Y. Lin, J. Electrochem. Soc. **157**(7), A753 (2010).

[160] M. A. Borysiewicz, M. Wzorek, M. Mysliwiec, J. Kaczmarski, and M. Ekiels, Superlattices Microstruct. **100**, 1213 (2016).

[161] L. R. Damiani, and R. D. Mansano J. Phys. Conf. Ser. **370**, 012019 (2012).

[162] P. A. Nwofe, K. T. Ramakrishna Reddy, G. Sreedevi, J. K. Tan, I. Forbes, and R. W. Miles, Energy Procedia **15**, 354 (2012).

[163] I. M. Fisher, and D. A. Smith, Texture Microstruct. **13**, 91 (1991).

[164] C.–L. Tien, H.–Y. Lin, C.–K. Chang, and C.–J. Tang, Adv. Condens. Matter Phys. **2018**, 2647282, (2018).

[165] D. W. Hoffman, J. Vac. Sci. Technol. A **12**, 953 (1994).

[166] H. Windischmann, Crit. Rev. Solid State **17**(6), 547 (1992).

[167] T. I. Selinder, G. Larsson, U. Helmersson, and S. Rudner, J. Appl. Phys. **69**(1), 390 (1991).

[168] R. H. Horng, D. S. Wuu, L. H. Wu, and M. K. Lee, Thin Solid Films **373**, 231 (2000).

[169] Y. Liu, H. Masumoto, and T. Goto, Mater. Trans. **45**, 3023 (2004).

[170] P. C. Liao, C. S. Chen, W. S. Ho, Y. S. Huang, and K. K. Tiong, Thin Solid Films **301**, 7 (1997).

[171] G. Sanchez–Santolino, J. Tornos, D. Hernandez–Martin, J. I. Beltran, C. Munuera, M. Cabero, A. Perez–Muñoz, J. Ricote, F. Mompean, M. Garcia–Hernandez, *et al.*, Nat. Nanotechnol. **12**, 655 (2017).

[172] Y. Niu, R. Frisenda, S. A. Svatek, G. Orfila, F. Gallego, P. Gant, N. Agraït, C. León, A. Rivera–Calzada, and D. P. de Lara, 2D Mater. **4**, 034002 (2017).

[173] M. Cabero, K. Nagy, F. Gallego, A. Sander, M. Rio, F. A. Cuellar, J. Tornos, D. Hernandez–Martin, N. M.Nemes, F. Mompean, *et al.*, APL Mater. **5**, 096104 (2017).

[174] F.–X. Wu, J. Zhou, L. Y. Zhang, Y. B. Chen, S.–T. Zhang, Z.–B. Gu, S.–H. Yao, and Y.–F. Chen, J. Phys. Condens. Matter **25**(12), 125604 (2013).

[175] J. H. Gruenewald, J. Nichols, J. Terzic, G. Cao, J. W. Brill, and S. S. A. Seo, J. Mater. Res. **29**, 2491 (2014).

[176] H. Fitouri, M. M. Habchi, and A. Rebey, *High-Resolution X-Ray Diffraction of III–V Semiconductor Thin Films* (IntechOpen, London, 2016).

[177] H. J. Koo, M. H. Whango, and B. J. Kennedy, J. Solid State Chem. **136**, 269 (1998).

[178] G. van der Laan, and B. T. Thole, Phys. Rev. Lett. **60**, 1977 (1988).

[179] D. Haskel, G. Fabbris, M. Zhernenkov, P. P. Kong, C. Q. Jin, G. Cao, and M. van Veenendaal, Phys. Rev. Lett. **109**, 027204 (2012).

[180] M. A. Laguna–Marco, D. Haskel, N. Souza–Neto, J. C. Lang, V. V. Krishnamurthy, S. Chikara, G. Cao, and M. van Veenendaal, Phys. Rev. Lett. **105**, 216407 (2010).

[181] M. A. Laguna–Marco, G. Fabbris, N. M. Souza–Neto, S. Chikara, J. S. Schilling, G. Cao, and D. Haskel, Phys. Rev. B **90**, 014419 (2014).

[182] P. Glatzel, G. Smolentsev, and G. Bunker, J. Phys. Confer. Ser. **190**, 012046/1 (2009).

[183] M. Tromp, J. Moulin, G. Reid, and J. Evans, presented at 13th Int. Conf. X–ray Absorption Fine Structure, Stanford (2006).

[184] D. E. McNally, X. Lu, J. Pelliciari, S. Beck, M. Dantz, M. Naamneh, T. Shang, M. Medarde, C. W. Schneider, V. N. Strocov, *et al.*, npj Quant. Mater. **4**, 6 (2019) .

[185] J. K. Kawasaki, C. H. Kim, J. N. Nelson, S. Crisp, C. J. Zollner, E. Biegenwald, J. T. Heron, C. J. Fennie, D. G. Schlom, and K. M. Shen, Phys. Rev. Lett. **121**, 176802 (2018).

[186] A. Ney, Materials **3**(6), 3565 (2010).

[187] Q. Zhu, Q. Ma, D. B. Buchholz, R. P. H. Chang, M. J. Bedzyk, and T. O. Mason, App. Phys. Lett. **103**, 031913 (2013).

[188] T. C. Rossi, D. Grolimund, M. Nachtegaal, O. Cannelli, G. F. Mancini, C. Bacellar, D. Kinschel, J. R. Rouxel, N. Ohannessian, D. Pergolesi, Phys. Rev. B **100**, 245207 (2019).

[189] T. C. Kaspar, A. Ney, A. N. Mangham, S. M. Heald, Y. Joly, V. Ney, F. Wilhelm, A. Rogalev, F. Yakou, and S. A. Chambers, Phys. Rev. B **86**, 035322 (2012).

[190] M. Hegde, I. D. Hosein, and P. V. Radovanovic, J. Phys. Chem. C **119**(30), 17450 (2015).

[191] W. J. Kim, S. Y. Kim, C. H. Kim, C. H. Sohn, O. B. Korneta, S. C. Chae, and T. W. Noh, Phys. Rev. B **93**, 045104 (2016).

[192] S.–W. Han, Int. J. Nanotechnology **33**(3), 396 (2006).

[193] A. F. Mayadas, and M. Shatzkes, Phys. Rev. B **1**, 1382 (1970).

[194] J. Hämäläinen, M. Kemell, F. Munnik, U. Kreissig, M. Ritala, and M. Leskelä, Chem. Mater. **20**(9), 2903 (2008).

[195] L. M. Ziman, Electrons and Phonons: *The Theory of Transport Phenomena in Solids* (Oxford University Press, New York, 1960).

[196] Y. Fu, Q. P. Cao, X. D. Wang. D. X. Zhang, and J. Z. Jiang, Thin Solid Films **672**, 182 (2019).

[197] Y. P. Krasny, N. P. Kovalenko, V. T. Shvets, and J. Krawczyk, J. Mol. Liq. **93**, 207 (2001).

[198] D. Korn, W. Murer, and G. Zibold, Phys. Lett. **47**A, 117 (1972).

[199] L. Wang, L. Chang, X. Yin, A. Rusydi, L. You, Y. Zhou, L. Fang, and J. Wang, J. Phys. Condens. Matter **29**(2), 025002 (2017).

[200] X. Shen, X. Qiu, D. Su, S. Zhou, A. Li, and D. Wu, J. Appl. Phys. **117**, 015307 (2015).

[201] R. Scherwitzl, S. Gariglio, M. Gabay, P. Zubko, M. Gibert, and J.–M. Triscone, Phys. Rev. Lett. **106**, 246403 (2011).

[202] J. Tang, J. Dai, K. Wang, W. Zhou, N. Ruzycki, and Ulrike Diebold, J. Appl. Phys. **91**, 10 (2002).

[203] R. S. Markiewicz, and L. A. Harris, Phys. Rev. Lett. **46**, 1149 (1981).

[204] J. Dai, L. Spinu, K.–Y. Wang, L. Malkinski, and J. Tang, J. Phys. D **33**, L65 (2000).

[205] D. C. Licciardello, and D. J. Thouless, Phys. Rev. Lett. **35**, 1475 (1975).

[206] G. Bergmann, Phys. Rep. **107**(1), 1 (1984).

[207] N. Gayathri, A. K. Raychaudhuri, X. Q. Xu, J. L. Peng, and R. L. Greene, J. Phys. Condens. Matter **10**(6), 1323 (1998).

[208] N. F. Mott, and E. A. Davies, *Electron Processes in Non–Crystalline Materials* (Oxford, Clarendon, 1979).

[209] N. F. Mott, *Metal Insulator Transitions* (London, Taylor and Francis, 1990).

[210] W. Brenig, G. H. Döhle, and H. Heyszenau, Philos. Mag. **27**, 1093 (1973).

[211] A. L. Efros, and B. I. Shklovskii, J. Phys. C Solid State Phys. **8**, 4 (1975).

[212] L. Hao, D. Meyers, C. Frederick, G. Fabbris, J. Yang, N. Traynor, L. Horak, D. Kriegner, Y. Choi, J.–W. Kim, *et al.*, Phys. Rev. Lett. **119**, 027204 (2017).

[213] G. Cao, J. E. Crow, R. P. Guertin, P. F. Henning, C. C. Homes, M. Stronginc, D. N. Basov, and E. Lochner, Solid State Commun. **113**(11), 657 (2000).

[214] T. F. Qi, O. B. Korneta, S. Chikara, M. Ge, S. Parkin, L. E. De Long, P. Schlottmann, and G. Cao, J. Appl. Phys. **109**, 07D906 (2011).

[215] F. Ye, S. Chi, B. C. Chakoumakos, J. A. Fernandez–Baca, T. Qi, and G. Cao, Phys. Rev. B **87**, 140406R (2013).

[216] M. A. Laguna–Marco, P. Kayser, J. A. Alonso, M. J. Martínez–Lope, M. van Veenendaal, Y. Choi, and D. Haskel, Phys. Rev. B **91**, 214433 (2015).

[217] R. D. Shannon, Acta Cryst. A. **32**(5), 751 (1976).

[218] L. Pauling, J. Am. Chem. Soc. **54**(9), 3570 (1932).

[219] X. Wang, Q. Yin, Z. Tang, X. Liu, D. Tang and W. Lin, J. Eur. Ceram. Soc. **33**(15–16), 3045 (2013) and references therein.

[220] Z. M. Jarzebski, and J. P. Marten, J. Electrochem. Soc. **123**(9), 299C (1976).

[221] S. Muranaka, Y. Bando, and T. Takada, Thin Solid Films **86**(1), 11 (1981).

[222] K. Ando, and E. Saitoh, Nat. Comm. **3**, 629 (2012).

[223] L. Vila, T. Kimura, and Y. Otani, Phys. Rev. Lett. **99**, 226604 (2007).

[224] Y. Murakami, H. Ohkawauchi, M. Ito, K. Yahikozawa, and Y. Takasu, Electrochim. Acta **39**(17), 2551 (1994).

[225] S. Ardizzone, C. L. Bianchi, L. Borgese, G. Cappelletti, C. Locatelli, A. Minguzzi, S. Rondinini, A. Vertova P. C. Ricci, C. Cannas, *et al.*, J. Appl. Electrochem. 39, 2093 (2009).

[226] A. Marshall, B. Børresen, G. Hagen, M. Tsypkin, and R. Tunold, Mater. Chem. Phys. **94**(2), 226 (2005).

[227] E. Mayousse, F. Maillard, F. Fouda–Onana, O. Sicardy, and N. Guillet, Int. J. Hydrog. Energy **36**(17), 10474 (2011).

[228] G. Li, H. Yu, X. Wang, S. Sun, Y. Li, Z. Shao, and B. Yi, Phys. Chem. Chem. Phys. **15**, 2858 (2013).

[229] K. S. Kadakia, P. Jampani, O. I. Velikokhatnyi, M. K. Datta, S. J. Chung, J. A. Poston, A. Manivannan, and P. N. Kumta, J. Electrochem. Soc. **161**, F868 (2014).

[230] M. K. Datta, K. Kadakia, O. I. Velikokhatnyi, P. H. Jampani, S. J. Chung, J. A. Poston, A. Manivannane, and P. N. Kumta, J. Mater. Chem. A **1**, 4026 (2013).

[231] S. Kasap, C. Koughia, and H. E. Ruda, *Electrical Conduction in Metals and Semiconductors* (Springer, Berlin, 2017).

[232] N. F. Mott, *Conduction in non–crystalline materials* (Philosophical Magazine, Informa UK Limited, 1969).

[233] M. Negishi, N. Hiraoka, D. Nishio–Hamane, and H. Takagi, APL Mater. **7**, 121101 (2019).

[234] Y. Liu, H. Masumoto, and T. Goto, Mater. Trans. **46**(1), 100 (2005).

[235] X. Liu, Y. Cao, B. Pal, S. Middey, M. Kareev, Y. Choi, P. Shafer, D. Haskel, E. Arenholz, and J. Chakhalian, Phys. Rev. Mater. **1**, 075004 (2017).

[236] M. S. Anwar, and J. Aarts, Supercond. Sci. Technol. **24**, 024016 (2011).

[237] H. Ye, Q. Zhang, F. Saito, B. Jeyadevan, K. Tohji, and M. Tsunoda, J. Appl. Phys. **93**(10), 6856 (2003).

[238] N. F. Heinig, H. Jalili, and K. T. Leunga, Appl. Phys. Lett. **91**, 253102 (2007).

[239] D. de Cogan, and G. A. Lonergan, Solid State Commun. **15**(9), 1517 (1974).

[240] S. P. Lewis, P. B. Allen, and T. Sasaki, Phys. Rev. B **55**, 10253 (1977).

[241] J. M. D. Coey, M. Venkatesan, J. Appl. Phys. **91**, 8345 (2002) .

[242] P. Schlottmann, Phys. Rev. B **67**, 174419 (2003).

[243] S. M. Watt, S. Wirth, S. von Molnár, A. Barry, and J. M. D. Coey, Phys. Rev. B **61**, 9621 (2000).

[244] C. Aguilera, J. C. González, A. Borrás, D. Margineda, J. M. González, A. R. González–Elipe, J. P. Espinós, Thin Solid Films **539**, 1 (2013).

[245] J. S. Parker, S. M. Watts, P. G. Inanov, and P. Xiong, Phys. Rev. Lett. **88**, 196601 (2002).

[246] A. Sokolov, C. S. Yang, L. Yuan, S.–H. Liou, R. Cheng, H. K. Jeong, T. Komesu, B. Xu, C. N. Borca, P. A. Dowben, *et al.*, Europhys. Lett. **58**(3), 448 (2002).

[247] A. M. Bratkovsky, Phys. Rev. B **56**, 2344 (1997).

[248] J. D. M. Coey, A. E. Berkowitz, L. Balcells, F. F. Putris, and A. Barry, Phys. Rev. Lett. **80**, 3815 (1998).

[249] H. Y. Hwang, S. Cheong, Science **278**(5343), 1607 (1997).

[250] R. S. Keizer, S. T. Goennenwein, T. M. Klapwijk, G. Miao, G. Xiao, A. Gupta, Nature **439**(7078), 825 (2006).

[251] A. Hernando, P. Crespo, and M. A. García, Phys. Rev. Lett. **96**, 057206 (2006).

[252] H. Boschker, M. Mathews, P. Brinks, E. Houwman, A. Vailionis, G. Koster, D. H. A. Blank, Guus Rijnders, J. Magn. Magn. Mater. **323**(21), 2632 (2011).

[253] S. Valencia, Ll. Balcells, B. Martínez, and J. Fontcuberta, J. Appl. Phys. **93**(10), 8059 (2003).

[254] F. Tsui, M. C. Smoak, T. K. Nath, and C. B. Eom, Appl. Phys. Lett. **76**, 2421 (2000).

[255] S. Iwata, S.Yamashita, and S.Tsunashima, J. Magn. Magn. Mater. **198–199**, 381 (1999).

[256] S. Sun, C. B. Murray, D. Weller, L. Folks, and A. Moser, Science **287**(5460), 1989 (2000).

[257] J. Singleton, J. W. Kim, C. V. Topping, A. Hansen, E.–D. Mun, S. Chikara, I. Lakis, S. Ghannadzadeh, P. Goddard, X. Luo, *et al.*, Phys. Rev. B **94**, 224408 (2016).

[258] T. Kida, S, Yoshii, M. Hagiwara, T. Nakano, and I. Terasaki, J. Phys. Conf. Ser. **150**, 022037 (2009).

[259] S. Hirosawa, M. Nishino, and S. Miyashita, Adv. Nat. Sci: Nanosci. Nanotechnol. **8**, 013002 (2017).

[260] V. Pillai, and D. O. Shah, J. Magn. Magn. Mater. **163**(1–2), 243 (1996).

[261] Y. C. Wang, J. Ding, J. B. Yi, B. H. Liu, T. Yu, and Z. X. Shen, Appl. Phys. Lett. **84**, 2596 (2004).

[262] D. R. Lide, *CRC Handbook of Chemistry and Physics* (CRC Press, Boca Raton, 2005).

[263] N. Birks, and G. H. Meier, *Introduction to High Temperature Oxidation of Metals* (Edward Arnold, London, 1983).

[264] S. Ould–Chikh, O. Proux, P. Afanasiev, L. Khrouz, M. N. Hedhili, D. H. Anjum, M. Harb, C. Geantet, J. M. Basset, and E. Puzenat, ChemSusChem **7**(5), 1361 (2014).

[265] A. Kuzmin, and J. Chaboy, IUCrJ **1**, 571 (2014).

[266] J. Chaboy, and S. Díaz–Moreno (to be published).

[267] H. Yanagihara, and M. B. Salamon, Phys. Rev. Lett. **89**, 187201 (2002).

[268] A. Barry, J. M. D. Coey, and M. Viret, J. Phys. Condens. Matter **12**, L173 (2000).

[269] J. Kondo, Prog. Theor. Phys. **32**(1), 37 (1964).

[270] L. Liang, *Field effect controlled magnetism and magnetotransport in low dimensions* (University of Groningen, 2017).

[271] M. Lee, J. R. Williams, S. Zhang, C. D. Frisbie, d. Goldhaber–Gordon, Phys. Rev. Lett. **107**, 256601 (2011).

[272] W.-N. Lin, J.–F. Ding , S.–X. Wu , Y.–F. Li, J. Lourembam, S. Shannigrahi, S.–J. Wang, and Tom Wu, Adv. Mater. Interfaces **1**(1), 1300001 (2014).

[273] J.–W. Kim, Y. Choi, S. H. Chun, D. Haskel, D. Yi, R. Ramesh, J. Liu, P. J. Ryan, Phys. Rev. B **97**, 094426 (2018).

[274] S. Agrestini, C.–Y. Kuo, K. Chen, Y. Utsumi, D. Mikhailova, A. Rogalev, F. Wilhelm, T. Förster, A. Matsumoto, T. Takayama, *et al.*, Phys. Rev. B **97**, 214436 (2018).

[275] K. S. Pedersen, J. Bendix, A. Tressaud, E. Durand, H. Weihe, Z. Salman, T. J Morsing, D. N. Woodruff, Y. Lan, W. Wernsdorfer, *et al.*, Nat. Commun. **7**, 12195 (2016) .

[276] M. A. Laguna–Marco, E. Arias–Egido, C. Piquer, V. Cuartero, L. Hernández–López, P. Kayser, J. A. Alonso, J. A. T. Barker, G. Fabbris, C. A. Escanhoela, Jr., *et al.*, Phys. Rev. B **101**, 014449 (2020).

[277] J. Chaboy, M. A. Laguna–Marco, M. C. Sánchez, H. Maruyama, N. Kawamura, and M. Suzuki, Phys. Rev. B **69**, 134421 (2004).

[278] J. Chaboy, H. Maruyama, L. M. García, J. Bartolomé, K. Kobayashi, N.Kawamura, A. Marcelli, and L. Bozukov, Phys. Rev. B **54**, R15637(R) (1996).

[279] D. L. Peng, K. Sumiyama, T. Hihara, and S. Yamamuro, Appl. Phys. Lett. **75**, 3856 (1999).

[280] R. K. Zheng, G. H. Wen, K. K. Fung, and X. X. Zhang, J. Appl. Phys. **95**, 5244 (2004).

[281] P. Z. Si, X. L. Wang, X. F. Xiao, H. J. Chen, X. Y. Liu, L. Jiang, J. J. Liu, Z. W. Jiao, and H. L. Ge, J. Magn. **20**(3), 211 (2015).

[282] A. C. Gandhi, T. Y. Li, T. S. Chan, and S. Y. Wu, Nanomaterials **8**(5), E312 (2018).

[283] S. Larumbe, and C. Gómez–Polo, IEEE Trans. Magn. **51**, 11 (2015).

[284] S. K. S. Patel, and N. S. Gajbhiye, J. Magn. Magn. Mater. **330**, 21 (2013).

[285] E. Lefrancois, A.–M. Pradipto, M. Moretti Sala, L. C. Chapon, V. Simonet, S. Picozzi, P. Lejay, S. Petit, and R. Ballou, Phys. Rev. B **93**, 224401 (2016).

[286] J. Sánchez–Marcos, M. A. Laguna–Marco, R. Martínez–Morillas, E. Céspedes, F. Jiménez–Villacorta, N. Menéndez, and C. Prieto, J. Phys. Condens. Matter **23**, 476003 (2011).

[287] R. Boada, C. Piquer, M. A. Laguna–Marco, and J. Chaboy, Phys. Rev. B **81**, 100404(R) (2010).

[288] J. Alonso, M. L. Fdez–Gubieda, G. Sarmiento, J. Chaboy, R. Boada, A. G. Prieto, D. Haskel, M. A. Laguna–Marco, J. C. Lang, C. Meneghini, *et al.*, Nanotechnology **23**, 025705 (2012).

[289] C. Strohm, P. van der Linden, O. Mathon, and S. Pascarelli, Phys. Rev. Lett. **122**, 127204 (2019).

[290] J. Nichols, X. Gao, S. Lee, T. L. Meyer, J. W. Freeland, V. Lauter, D. Yi, J. Liu, D. Haskel, J. R. Petrie, *et al.*, Nat. Commun. **7**, 12721 (2016).

[291] R. Ramos, I. Lucas, P. A. Algarabel, L. Morellon, K. Uchida, E. Saitoh, and M. R. Ibarra, J. Phys. D: Appl. Phys. **51**, 224003 (2018).

[292] F. Wilhelm, P. Poulopoulos, H. Wende, A. Scherz, K. Baberschke, M. Angelakeris, N. K. Flevaris, and A. Rogalev, Phys. Rev. Lett. **87**, 207202 (2001).

[293] J. Balogh, Cs. Fetzer, D. Kaptás, L. F. Kiss, I. S. Szucs, I. Dézsi, and I. Vincze, Phys. Stat. Sol. (a) **205**(8), 1828 (2008).

[294] Q. Zhang, P. Li, Y. Wen, C. Zhao, J. W. Zhang, A. Manchon, W. B. Mi, Y. Peng, and X. X. Zhang, Phys. Rev. B **94**, 024428 (2016).

[295] T. L. Monchesky, A. Enders, R. Urban, K. Myrtle, B. Heinrich, X.–G. Zhang, W. H. Butler, and J. Kirschner, Phys. Rev. B **71**, 214440 (2005).

[296] D. Alba–Venero, L. Fernández–Barquin, J. Alonso, M. L. Fdez–Gubieda, L. Rodríguez–Fernández, R. Boada, and J. Chaboy, J. Phys. Condens. Matter **25**, 276001 (2013).

[297] Y.–S. Chen, C.–H. Lee, and H.–J. Lin, J. Vac. Sci. Technol. B **34**, 04J109 (2016).

[298] C. Chappert, A. Fert, and F. N. van Dau, Nat. Mater. **6**(11), 813 (2007).

[299] T. Seki, Y. Hasegawa, S. Mitani, S. Takahashi, H. Imamura, S. Maekawa, J. Nitta, and K. Takanashi, Nat. Mater. **7**, 125 (2008).

[300] S. Hussain, C. S. Bhatia, H. Yang, and A. J. Danner, Appl. Phys. Lett. **104**(11), 111107 (2014).

[301] E. Snoeck, S. Frechengues, M. J. Casanove, C. Roucau, and S. Andrieu, J. Cryst. Growth **167**(1–2), 143 (1996).

[302] Ph. Bauer, S. Andrieu, O. M. Lemine, and M. Piecuch, J. Magn. Magn. Mater. **165**(1–3), 220 (1997).

[303] S. Andrieu, F. L. Razafindramisa, E. Snoeck, H. Renevier, A. Barbara, J. M. Tonnerre, M. Brunel, and M. Piecuch, Phys. Rev. B **52**, 9938 (1995).

[304] K. Louzazna, and A. Haroun, Thin Solid Films **374**(1), 114 (2000).

[305] T.–H. Chuang, Kh. Zakeri, A. Ernst, Y. Zhang, H. J. Qin, Y. Meng, Y.–J. Chen, and J. Kirschner, Phys. Rev. B **89**, 174404 (2014).

[306] W.–H.Chen, P.–C. Jiang, C.–Y.Hsieh, and J.–S.Tsay, IEEE Trans. Magn. **50**(1), 2000304 (2014).

[307] A. B. Shick, S. Khmelevskyi, O. N. Mryasov, J. Wunderlich, and T. Jungwirth, Phys. Rev. B **81**, 212409 (2010).

[308] F. Jiménez–Villacorta, *Basic Principles of X–ray Reflectivity in Thin Films* (Northeastern University, 2011).

[309] M. Yasaka, Rigaku Journal **26**, 2 (2010).

[310] E. Arias–Egido, M. A. Laguna–Marco, J. Sánchez–Marcos, C. Piquer, J. Chaboy, M. Ávila and J. Garcia Lopez, Phys. Rev. Mater. **2**, 014402 (2018).

[311] A. S. Teja, and P.–Y Koh, Prog. Cryst. Growth Charact. Mater. **55**(1–2), 22 (2009).

[312] M. S. Islam, J. Kurawaki, Y. Kusumoto, M. Abdulla–Al–Mamun, and M. Z. Bin Mukhlish, J. Sci. Res. **4**(1), 99 (2012).

[313] C. Piquer, M. A. Laguna–Marco, A. G. Roca, R. Boada, C. Guglieri, and J. Chaboy, J. Phys. Chem. C **118**(2), 1332 (2014).

[314] M. A. Laguna–Marco, J. Sánchez–Marcos, N. Menéndez, J. Chaboy, E. Salas–Colera, and C. Prieto, Mater. Des. **93**, 388 (2016).

[315] F. Farges, Phys. Chem. Miner. **36**, 463 (2009).

[316] M. Benfatto, J. A. Solera, J. G. Ruiz, and J. Chaboy, Chem. Phys. **282**(3), 441 (2002).

[317] S. H. Baker, M. Roy, S. C. Thornton, and C. Binns, J. Phys. Condens. Matter **24**, 176001 (2012).

[318] M. Sasaki, P. E. Jönsson, H. Takayama, and H. Mamiya, Phys. Rev. B **71**, 104405 (2005).

[319] R. W. Chantrell, N. S. Walmsley, J. Gore, and M. Maylin, J. Appl. Phys. **85**, 4340 (1999).

[320] J. Nogués, J. Sort, V. Langlais, V. Skumryev, S. Suriñach, J. S. Muñoz, and M. D. Baró, Phys. Rep. **422**(3), 65 (2005).

[321] E. Mazario, P. Herrasti, M. P. Morales, and N. Menéndez, Nanotechnology **23**, 355708 (2012).

[322] F. Jiménez–Villacorta, Ph.D. thesis, Universidad Autónoma de Madrid (2017).

[323] V. V. Krishnamurthy, M. Suzuki, N. Kawamura, T. Ishikawa, and Y. Kohori, Hyperfine Interact. **136**, 361 (2001).

[324] V. V. Krishnamurthy, M. Suzuki, N. Kawamura, T. Ishikawa, and Y. Kohori, Physica B Condens. Matter **312–313**, 647 (2002).

[325] I. A. Campbell, J. Phys. F: Met. Phys. **2**, L47 (1972).

[326] L. Zhang, Y. K. Takahashi, A. Perumal, and K. Hono, J. Magn. Magn. Mater. **322**(18), 2658 (2010).

[327] B. Predel, *Fe–Ir (Iron–Iridium)* (Springer, Berlin, Heidelberg, 1995).

[328] W. L. Bragg, *The Crystalline State* (The Macmillan Company, New York, 1934).

[329] B. Hassler, *ABC's of Electrochemistry–Materials Characterization Techniques: XRD* (Ohio University, 2011).

[330] P. S. Patil, P. S. Chigare, S. B. Sadale, T. Seth, D. P. Amalnerkar, and R. K. Kawar, Mater. Chem. Phys. **80**(3), 667 (2003).

[331] B. E. Douglas, D. H. McDaniel, and J. J. Alexander, *Concepts and Models of Inorganic Chemistry* (Wiley, New York, 1994).

[332] J. E. Penner–Hahn, *X–ray Absorption Spectroscopy* (University of Michigan, USA).

[333] D. C. Koninsberger, and R. Prins, *X–Ray Absorption: Principles, Applications, Techniques of EXAFS, SEXAFS and XANES* (Wiley, New York, 1988).

[334] K. V. Klementiev, J. Phys. D: Appl. Phys. **34**, 209 (2001).

[335] J. R Tesmer, and M. Nastasi, *Handbook of Modern Ion Beam Materials Analysis* (Cambridge University Press, Cambridge, 2005).

[336] D. L. Smith, *Thin Film Deposition. Principles and Practice* (McGraw–Hill, New York, 1995).

[337] M. González Silveira, Ph. D. thesis, Universidad Autónoma de Barcelona (2005).

[338] Técnicas de Análisis. Espectrometría de Retrodispersión Rutherford (RBS) y Canalización Iónica. Capítulo 1. Folleto del Centro Nacional de Aceleradores (CNA).

[339] J. Stöhr, J. Electr. Spectr. and Rel. Phenom. **75**, 253 (1995).

[340] S. P. Cramer, J. Chen, S. J. George, J. van Elp, J. Moore, O. Tench, J. Colaresi, M. Yocum, O. C. Mullins, and C. T. Chen, Nucl. Instrum. Methods A **319**(1–3), 285 (1992).

[341] N. Chobaut, D. Carron, S. Arsène, P. Schloth, and J.–M. Drezet, J. Mater. Process. Technol. **222**, 373 (2015).

[342] J. K. Rai, A. Mishra, and U. R. K. Rao, Int. J. Mach. Tool Manu. **20**(1), 1 (1980).

[343] M. Schemmel, P. Prevedel, R. Schöngrundner, W. Ecker, and T. Antretter Adv. Mater. Sci. Eng. **2015**, 678056 (2015).